UNIVERSITY OF SOUTHAMPTON

Institute of Sound and Vibration Research

A MODEL FOR ROTOR BROADBAND NOISE PREDICTION

By

Qidou Zhou

Thesis for the degree of Doctor of Philosophy

October 2004

UNIVERSITY OF SOUTHAMPTON

ABSTRACT

INSTITUTE OF SOUND AND VIBRATION RESEARCH

Doctor of Philosophy

A MODEL FOR ROTOR BROADBAND NOISE PRODICTION

By Qidou Zhou

This thesis describes a frequency domain formulation for predicting the broadband self-noise due to an open rotor or propeller. The integration in the formulation can be evaluated on the real blade surface rather than on the projected disk or blade mean-chord surface, as has been done previously, thereby avoiding the commonly made assumption of flat plate geometry. It is assumed that the noise is predominantly due to trailing edge interaction of the hydrodynamic pressure associated with the turbulent boundary layer over the rotor blades (self-noise). The unsteady blade loading, which constitutes the aerodynamic sound source, is predicted using modifications to Amiet's thin aerofoil theory, and a prediction of the boundary layer surface pressure frequency– wavenumber spectrum. This is obtained by combining the wavenumber spectrum due to Corcos, the measured frequency spectrum due to Chou and George, and the boundary layer thickness measurements of Brooks.

A generalized frequency domain formulation has been developed for making rotor broadband noise predictions. It can be used for making broadband and tonal noise predictions, and is valid in both the near field and the far field. A simplified expression for making far-field self-noise prediction is presented. This far-field frequency-domain formulation is computationally far more efficient than the general formulation. It is shown to reduce to the classic Gutin solution of propeller tonal noise prediction when the steady surface pressure source is confined to the propeller-projected disc.

A numerical scheme for performing the source integration on an arbitrary blade surface has been presented. The validation is performed of predictions of the measured broadband noise from an R212 propeller. Good agreement between the measurement and predicted noise spectrum is obtained. It is shown that the broadband self-noise directivity is significantly different from the single-frequency directivities due to a steady blade surface pressure distribution. The main lobe of broadband self-noise directivity is in the direction of the propeller axis whereas the main lobe of the single-frequency directivity is normal to the propeller axial direction. The theory has been used to undertake a parameter study of the broadband noise radiation from the propeller. A prediction of the pressure spectrum in the plane of the propeller for various blade-setting angles shows that for each degree of increase in blade-setting angle, the sound pressure level increases by 1.4 dB. The predicted dependence of the broadband frequency spectrum on the blade tip Mach number is found to scale very closely with the fifth power of the blade tip Mach number. Effects due to chord, blade number and angle of attack are also discussed in this thesis.

To understand the basic mechanism of self-noise generation, a comprehensive study of airfoil self-noise generation is also presented in this thesis. Numerical results of airfoil broadband self-noise show reasonable agreement with Brook empirical prediction based on experimental data. Broadband self-noise predictions are made for both frozen and non-frozen boundary layer turbulence. Non-frozen turbulence is shown to generate higher noise radiation than frozen turbulence at high frequency. However, the difference is generally less than 3 dB, suggesting that the frozen-gust assumption is a reasonable assumption for broadband noise predictions

To Hu Jia, Zhou Dai and Shao Zijun

Contents

Acknowledgement

I would like to acknowledge my supervisor Dr. Phillip Joseph, for his excellent support and constant encouragement as well as for providing me with the opportunity to complete my studies at the ISVR. This thesis has benefited a lot from discussions with him.

I would like to thank my examiners, Professor Philip Nelson and Dr. Michael Carley for taking the time to evaluate this work. My gratitude also goes to Professor Christopher Morfey and Professor Jeremy Astley for their beneficial advice and the time spent on my review examinations.

I would like to acknowledge the financial support from Rolls-Royce University Technology Centre (UTC) at the ISVR.

Thanks you to all of my friends and workmates in Southampton, especially Alessandro Bassetti, Vincent Hii, Juan Battaner-Moro, Fabrice Castres, Emmet English, Munhun Park, Tze Pei Chong, Stefan Zimmermann, Sebastien Guerin.

Finally, my debts are owed to my Mum and Dad for their enduring love.

List of Symbols

$\overline{A}$ = complex amplitude of a Fourier component of a quantity A in frequency domain, defined as $A = \int_{-\infty}^{\infty} \overline{A} e^{-i\omega_0 \tau} d\omega_0$

$\hat{A}$ = complex amplitude of a Fourier component of a quantity A in frequency-wavenumber domain, defined as $A = \int_{-\infty}^{\infty}\int_{-\infty}^{\infty}\int_{-\infty}^{\infty} \hat{A} e^{i(k_s \eta_s + k_t \eta_t - \omega_0 \tau)} dk_s dk_t d\omega_0$

$\widetilde{A}$ = non-dimensional version of a quantity A

a = $i(K + \mu_0 M + k_s)$ for an airfoil, $a = i(K + \mu_0 M_0 + k_{sm})$ for a rotor

a_b = $b(K + \mu M + k_1)$, see Eq.(5.24)

b = airfoil semi-chord, $b = c/2$

B_j = steady body force component in the j - coordinate direction

c = airfoil chord length

c_0 = speed of sound

c_u = convective velocity coefficient, $c_u = 0.65 \sim 0.8$

C_l = lift coefficients at a blade section

C_{li} = design lift coefficient (ideal lift coefficient)

d = semi-span length of an airfoil; blade span in Chapter VIII

D = directivity if with argument (see Eqs.(6.3), (8.15) and (11.12)); rotor diameter if without argument

D_H = directivity function defined by Eq.(6.1)

E = $R + M(y_1 - x_1)$; $E[\cdots]$ denotes the expected value; $E(\cdots)$ denotes the Fresnel integral

$\mathbf{e}_i$ = unit vector in y_i direction

$\mathbf{e}_i'$ = unit vector in y_i' direction

e_{ij} = $(i, j)^{\text{th}}$ component of the viscous stress tensor

f = frequency in Hertz

f_c = correction factor for pressure coefficient Π

f_p = position-dependent function of the incident pressure, defined by Eq.(3.21) or Eq. (3.20)

f_j = the j^{th} component of the force per unit area exerted by the boundaries on the fluid, $\mathbf{f} = (f_1, f_2, f_3)$

f_T, f_R, f_D = forces per unit area exerted by the rotor blades in y_1, r_0, θ_0 directions

F_j = θ_0 -dependent terms defined by Eq. (7.27) or (9.14)

$\hat{F}_j^l$ = Fourier coefficients defined by Eq. (7.29) or Eq. (9.16)

g^m = term defined by Eq. (7.21)

G = Green function in time domain, defined by Eq.(2.13)

$\overline{G}$ = Green function in frequency domain, defined by Eq.(2.14)

H_s = transfer function from p_i to p_s, see Eqs.(4.22) and (4.27)

H_q = transfer function from p_i to p_t, see Eqs.(4.29) and (7.9)

H_p = transfer function from $\hat{p}_i$ to $\hat{p}$, see Eqs.(5.11), (7.24) and (9.8)

H_l = transfer function of m^{th} mode from $\hat{p}_i$ to $\hat{p}$, see Eqs.(7.34) and (9.26)

$H_0^{(1)}$ = zero order Hankel function of the first kind

h_p = a function defined by Eq.(9.A.3) for tonal noise computation

h_l = a function defined by Eq.(9.A.5) for tonal noise computation

i = unit of a complex number; subscript when it appears at a subscript field

I = term defined by Eq.(5.5) in Chapter V or by Eq.(9.28) in Chapter IX

I_n = a term defined by Eq.(5.35) for an airfoil or by Eq.(9.29) for a rotor

I_n^H = a term defined by Eq.(5.36) for an airfoil or Eq.(9.30) for a rotor

$I_n^{H_e}$ = an integration defined by Eq.(5.38)

$I_n^{H_f}$ = an integration defined by Eq.(5.39)

J_m = the m^{th} order Bessel function of the first kind

k_0 = an integral variable in Eq. (7.13)

k_2' = $\kappa x_2 / R_s$

(k_1, k_2) = streamwise wavenumber and spanwise wavenumber for a flat plate airfoil

(k_s, k_t) = streamwise wavenumber and spanwise wavenumber, $\mathbf{k} = (k_s, k_t)$, $k = |\mathbf{k}|$

k_b = $b(K + \mu x_1 / R_s)$, see Eq.(5.24)

k_{sm} = $k_s - m\cos(\beta_p - \vartheta)/r_0$, see Eq.(9.34)

K = $\sqrt{\mu_0^2 - (k_t/\beta_0)^2}$ for airfoil, $K = \sqrt{\mu_0^2 - (k_2/\beta_0)^2}$ for flat plate airfoil

K_0 = $\beta\sqrt{\mu^2 - k_0^2}$, see Eq. (7.15)

K_s = $b[k_1 + \mu(M - x_1/R_s)]$, see Eq.(5.24)

l = integer indicated the order of blade pass frequency, $l = 0, \pm 1, \pm 2, \pm 3, \cdots$

l_1 = boundary layer turbulence integral length-scale in streamwise direction

l_2 = boundary layer turbulence integral length-scale in spanwise direction

l_y = spanwise correlation length used by Amiet, $l_y \approx 2.1 U_c / \omega$

L_0 = $K_s L$

L = integration defined by Eq. (5.21)

L_{I0} = $K_s L_I$

L_I = contribution to L due to the incident boundary layer pressure, see Eq.(5.23)

L_{s0} = $K_s L_s$

L_s = contribution to L due to the scattered pressure, see Eq.(5.24)

L_p = sound pressure level defined by Eq.(6.2)

m = $N_b l$ in Chapters IX to XI, $m = -N_b l$ in Chapters VII and VIII

M = rotor axial Mach number, U/c_0

M_0 = airfoil or blade section Mach number, U_0/c_0

M_h = blade tip Mach numbers

$\mathbf{n}$ = unit normal vector pointing inwards from the blade surface, $\mathbf{n} = (n_1, n_2, n_3)$ in rectangular coordinates, $\mathbf{n} = (n_1, n_r, n_\theta)$ in cylindrical coordinates, $n = |\mathbf{n}|$

n = propeller rotational speeds in rev/min in Chapters X and XI; element sequence number where numerical scheme involved; amplitude of normal vector, $n = |\mathbf{n}|$

N_b = blade number

N_{ef} = total element number

p = radiated acoustic pressure

p_a = atmosphere pressure, $p_a = 10^5\ P_a$

p_i = incident pressure due to boundary layer turbulence

p_s = scattered pressure due to trailing edge

p_t = pressure on airfoil surface or blade surface, $p_t = p_i + p_r$

p_l = radiated tone pressure at the l^{th} blade passing frequency

p_{ref} = reference pressure, $p_{ref} = 2\times10^{-5}\ Pa$

$\overline{p}^{(0)}$ = pressure corresponding to $\phi^{(0)}$

$\overline{p}_I$ = pressure corresponding to ϕ_I

$\overline{p}_i$ = time-harmonic component of incident pressure, $\overline{p}_i = \overline{p}_I + \overline{p}^{(0)}$

r = radial coordinate of observation point in cylindrical coordinate system

r_0 = radial coordinate of source point in cylindrical coordinate system

$r_<$ = $\min\{r, r_0\}$

$r_>$ = $\max\{r, r_0\}$

r_d = radius of the blade root

r_t = radius of the blade tip

R = mean-flow corrected distance, $R = \sqrt{(y_1 - x_1)^2 + \beta^2[(y_2 - x_2)^2 + (y_3 - x_3)^2]}$ in rectangular system, $R = \sqrt{(y_1 - x_1)^2 + \beta^2[r^2 + r_0^2 - 2rr_0\cos(\theta_0 - \Omega\tau - \theta')]}$ in cylindrical coordinates

R_0 = $\beta\sqrt{r^2 + r_0^2 - 2rr_0\cos(\theta_0 - \Omega\tau - \theta')}$

R_s = $\sqrt{x_1^2 + \beta^2 r^2}$ in cylindrical coordinates, $R_s = \sqrt{x_1^2 + \beta^2(x_2^2 + x_3^2)}$ in rectangular coordinates

R_d = observation distance $R_d = |\mathbf{y} - \mathbf{x}|$, $R_d = \sqrt{x_1^2 + r^2}$ from Chapter VIII to XI

$\widetilde{R}_d$ = R_d / d in Chapter VIII

R_e = Reynolds number based on the distance, η_e, from leading edge

R_{qq} = cross-correlation function of the surface pressure

$S(\tau)$ = a boundary surface, such as airfoil surface

S_0 = boundary layer frequency spectrum of point wall pressure

S_1 = wavenumber spectra in streamwise direction

S_2 = wavenumber spectra in spanwise direction

S_i = i^{th} blade surface

S_n = area of n^{th} element facet

S_{pp} = sound pressure spectral density

S_{qq} = frequency-wavenumber spectral density of wall pressure, that is incident surface pressure spectrum $S_{qq}(\mathbf{k},\omega) = S_0(\omega_0)S_1(k_s)S_2(k_t)$

$\hat{S}_{qq}$ = frozen pressure spectrum, see Eq. (3.31)

S_{QQ} = surface pressure spectrum S_{QQ}, which includes the airfoil response

S_i^{yr} = projected area of the rotating volume around the blade in the $y_1 - r$ plane

SPL = sound pressure level referenced to p_{ref}

t = time associated with arrival of sound wave at observation point in the moving reference system; airfoil maximum thickness when written in ratio of t/c

T = large time interval (eventually put equal to infinite); intermediate variable

T'_{ij} = Lighthill's stress tensor based on velocity $\mathbf{v}'$, $T'_{ij} = \rho v'_i v'_j + e_{ij}$

u_3 = virtual velocity in y_3 direction that would be produced by the turbulent boundary layer if the airfoil surface were absent

U = rotor forward flight velocity

U_0 = airfoil velocity, blade section velocity at a blade radius

U_c = convective velocity, $U_c = c_u U_0$

$\mathbf{v}$ = velocity measured in the moving reference frame, $\mathbf{v} = (v_1, v_2, v_3)$

$\mathbf{v}'$ = velocity measured in the stationary coordinate system, $\mathbf{v}' = (v'_1, v'_2, v'_3)$, $v'_i = v_i - \delta_{1i}U$

V_n = normal velocity of the boundary surface $S(\tau)$ observed in the moving coordinate system

V'_n = normal velocity of the boundary surface $S(\tau)$ observed in the stationary

coordinate system, $V_n' = V_n - n_1 U$

v/U_0 = velocity distribution duo to the basic thickness form of an airfoil at zero angle of attack

$\mathbf{x}$ = coordinates associated with observation point in the moving reference frame, $\mathbf{x} = (x_1, r, \theta')$ for cylindrical coordinates, $\mathbf{x} = (x_1, x_2, x_3)$ for rectangular coordinate system

(x_u, y_u) = rectangle coordinates for airfoil upper-surface profile

(x_l, y_l) = rectangle coordinates for airfoil lower-surface profile

$\mathbf{y}$ = coordinates associated with source point in the moving reference frame, $\mathbf{y} = (y_1, r_0, \theta_0')$ for cylindrical coordinates, $\mathbf{y} = (y_1, y_2, y_3)$ for rectangular coordinate system

$\mathbf{y}'$ = coordinates in the stationary reference frame, $\mathbf{y}' = \mathbf{y}'(y_1', y_2', y_3')$

$\mathbf{y}^b$ = blade-fixed coordinates associated with source point, $\mathbf{y}^b = (y_1, r_0, \theta_0)$ for cylindrical coordinates, $\mathbf{y}^b = (y_1^b, y_2^b, y_3^b)$ for rectangular coordinate system

y_c = mean-line ordinate normalised on the chord

$\mathbf{y}_{TE}^b$ = coordinate value of $\mathbf{y}^b$ at the trailing edge

$\mathbf{y}_0$ = reference point for position-dependent function f_p on the airfoil or blade trailing edge

y_t = ordinate of the airfoil thickness distribution, normalised on the chord

$\mathbf{Y}$ = a intermediate coordinates in Chapter IV, $\mathbf{Y} = (Y_1, Y_2, Y_3)$

Z = $\kappa r_0 \sin\psi$

α = attack angle at a blade radius section, $\alpha = \beta_P - \beta_H$; airfoil attack angle

β = $\sqrt{1-M^2}$

β_0 = $\sqrt{1-M_0^2}$

β_P = geometric pitch angle of a blade, $\beta_P = \beta_T + \beta_S$

β_H = inflow angle at a blade radius section

β_T = blade twist angle relative to that at the 0.70 radius station

β_s = blade setting angle defined as the twist angle at 0.70 radius station

γ = sources term

Δp_s = scattered pressure jump across a flat plate airfoil

$\Delta v / U_0$ = velocity distribution duo to the load distribution of airfoil camber line

$\Delta v_a / U_0$ = velocity distribution over an airfoil due to the additional load distribution associated with non-zero angle of attack

δ = Dirac delta function; boundary layer thickness

δ^* = boundary layer displacement thickness

δ_0^* = boundary layer displacement at zero angle of attack

δ_s^* = boundary layer displacement on suction side

δ_p^* = boundary layer displacement on pressure side

δ_{ij} = Kronecker delta function

ε = decay factor defined in Eq. (3.20)

(η_s, η_t) = curvilinear coordinate system on airfoil or blade surface, η_s in streamwise direction, η_t in spanwise direction, $\boldsymbol{\eta} = (\eta_s, \eta_t)$

η_c = streamwise curvilinear coordinate η_s at the element centre

η_e = arc length distance along airfoil upper or lower profile from the leading edge

η_s' = $\eta_s - U_c \tau$

Π = pressure coefficient of the steady force over an airfoil

θ = azimuthal angle measured from x_2 axis; azimuthal angle of observation point in blade-fixed cylindrical coordinate system $\mathbf{x}^b = (x_1, r, \theta)$, $\theta' = \theta - \Omega\tau$

θ_0 = azimuthal angle of source point in blade-fixed cylindrical coordinate system $\mathbf{y}^b = (y_1, r_0, \theta_0)$, $\theta_0' = \theta_0 - \Omega\tau$ measured in airplane-fixed coordinate system

θ_a = semi- blade angles, $\theta_a = \pi / N_b$

θ_c = azimuthal angle θ_0 at the element center

ϑ = tangent angle of the airfoil profile, $\vartheta = \tan^{-1}(dy_u / dx_u)$

ϑ_0 = tangent angle of the camber line, $\vartheta_0 = \tan^{-1}(dy_c / d\xi)$

κ = ω / c_0

κ_0 = ω_0 / c_0

κ_1 = ω_0 / U_0

κ_c = ω_0 / U_c

μ = κ/β^2

μ_0 = κ_0/β_0^2

$v(\tau)$ = a volume of fluid region exterior to an surface $S(\tau)$

ξ = separation distance between two points on the airfoil surface, $\xi=(\xi_1,\xi_2)$, ξ_1 is streamwise separation distance and ξ_2 spanwise separation distance

ξ = airfoil profile abscissa normalized on chord; intermediate integral variable

ρ = density of fluid

ρ_0 = density of steady background flow

σ_1 = reduced frequency, $\sigma_1=\kappa_c b$.

τ = time associated with emission of sound wave at source point in the moving reference system

τ' = time associated with emission of sound wave at source point in the stationary reference system

Φ_I = velocity potential related to velocity u_3, $\Phi_I=\phi_I e^{-i\omega_0\tau}$

Φ_t = total velocity potential, $\Phi_t=\Phi_I+\Phi$

Φ = a decomposed velocity potential $\Phi=\Phi_t-\Phi_I$, $\Phi=\phi e^{-i\omega_0\tau}$

φ = velocity potential defined by $\varphi=\psi e^{-ik_2Y_2/\beta_0}$

φ_I = velocity potential defined by $\varphi_I=\psi_I e^{-ik_2Y_2/\beta_0}$

$\varphi^{(0)}$ = velocity potential reflected by an infinite plate boundary, $\varphi=\varphi^{(0)}+\varphi^{(1)}$

$\varphi^{(1)}$ = velocity potential scattered by the trailing edge, $\varphi=\varphi^{(0)}+\varphi^{(1)}$

$\phi^{(0)}$ = $\varphi^{(0)}e^{-iM_0\mu_0 y_1}e^{ik_2 y_2}$

ψ = $\cos^{-1}(x_1/R_s)$ in Chapter IX to XI, $\sin\psi=r/R_s$; a intermediate variable for velocity potential in Chapter IV, $\psi=\phi e^{iM_0\mu_0 Y_1}$

ψ_I = $\phi_I e^{iM_0\mu_0 Y_1}$

Ψ = polar angle measured from x_1 axis

ω = observation frequency in moving (forward flight) coordinate system

ω_0 = source frequency in blade-fixed coordinate system

Ω = angular speed of rotor

$\widetilde{\Omega}$ = $\Omega d/c_0$

Chapter I

Introduction

1.1 Overview

The problem of sound radiated from aircraft engines is of increasing importance to the aircraft community as ever more stringent environmental constraints are imposed by the regulation bodies. Over the years, aero-engine fan noise is growing in importance as the engine bypass-ratio has increased and hence jet noise is reducing. An effective acoustic analysis tool for making rotor noise predictions is most desirable in the engineering design process. The analysis should model the problem as realistically as possible, taking into account blade geometry, rotor design parameters, but should also compute the solution within realistic time scales. Moreover, the input parameters (such as pressure spectrum) to the prediction should be easily measurable.

The principal motivation of this work is to develop an engineering analysis tool for the prediction of the broadband self-noise from an open rotor or propeller. Noise generated by a rotor can be classified into three categories: BPF (Blade Passing Frequency) tone noise, broadband in-flow noise and broadband self-noise, as shown in Fig. 1.1.

Tonal noise is due to a steady pressure distribution over the blade surface, which forms the steady thrust and torque on the rotor blade surface. This rotation (Gutin) noise will occur at the blade passing frequency (BPF), which may be interpreted as the Doppler shift frequency from the blade-fixed reference frame to an observation reference frame fixed to the airplane. The tonal noise has been well understood since Gutin's classical theory of propeller noise (Gutin, 1936). Tonal noise will be discussed in this thesis by

way of validation of the frequency domain formulation presented in this thesis. This is because the steady surface pressure distribution can be predicted with much greater accuracy than the unsteady pressure due to boundary layer turbulence.

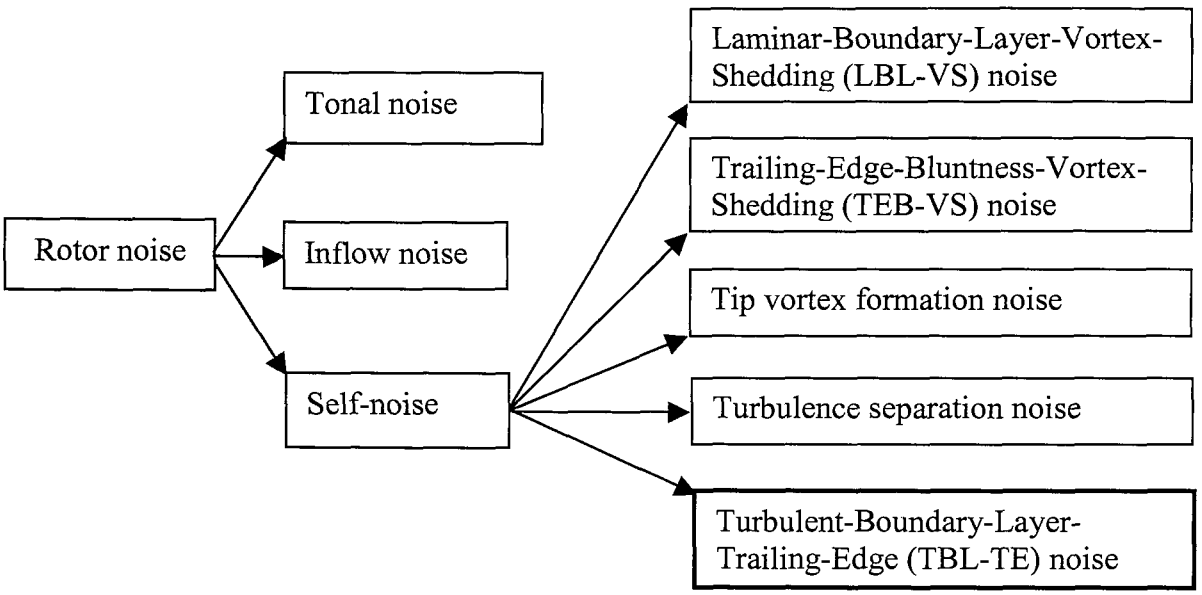

Figure 1.1. Rotor noise classification

Broadband inflow noise originates from the interaction between inflow turbulence with the rotating blades. The ingested turbulence may be atmospheric turbulence, ship-wake turbulence, or front flap wake turbulence. The interaction of turbulence with both leading and trailing edges is important in this case. To solve this inflow problem, the inflow turbulence velocity spectrum is usually used as the input for the determination of the acoustic source on the blade surface. The broadband inflow noise from rotors was investigated by Amiet (1990) and Homicz (1974). Whilst the prediction procedure proposed here is also applicable to this inflow noise problem, it will not be discussed further in this thesis.

Self-noise is due to the interaction between the turbulence generated in the boundary layer on the blade surface and the trailing edge. It is the noise produced by the airfoil situated in a smooth, non-turbulent in-flow. The self-noise may be further divided into five categories based on its generating mechanism (Brooks, 1983), as shown in Fig.1.1.

Laminar-Boundary-Layer-Vortex-Shedding (LBL-VS) noise is due to vortex shedding in the presence of laminar boundary layers at low Reynolds number. The fluid dynamic process can be modelled in terms of Tollmien-Schlicting instability waves, which grow exponentially along the chord and radiate noise when scattered by the trailing edge (McAlpine et al. 1999). In the case of the airfoil, the discrete tonal frequency depends on the free stream velocity. For the case of a rotor, the variation of local-blade relative velocity is expected to result in a narrow band spectral hump in the radiation spectrum. In this thesis we assume that the Reynolds number is sufficiently large so that the LBL-VS noise can be neglected.

Trailing-Edge-Bluntness-Vortex-Shedding (TEB-VS) noise is due to vortex shedding in the presence of boundary layer turbulence at a blunt trailing edge. The narrow band spectral hump of this noise was first observed by Brooks and Hodgson (1981). Coherent vortex shedding gives rise to a fluctuating surface pressure differential, or lift, across the finite thickness edge, which produces noise. The vortex shedding frequencies correspond to Strouhal numbers based on trailing edge thickness of about 0.24. A sharp trailing edge is assumed in this thesis. TEB-VS noise is therefore neglected in this thesis.

Tip noise has been identified with the turbulence in the local separated flow associated with formation of the tip vortex. For non-zero angles of attack, the flow can separate near the trailing edge (TE) on the suction side of the airfoil to produce TE noise due to the shed turbulent vorticity. At very high angles of attack, the separated flow near the TE gives way to large-scale separation (deep stall) causing the airfoil to radiate low-frequency noise similar to that of bluff-body radiation. These two sources of tip vortex formation noise and turbulence separation noise are assumed here to be small compared to the self-noise radiation of interest in this thesis.

Both in-flow noise and self-noise show that the sound intensity varies as the fifth power of a related characteristic flow velocity (Amiet, 1975; Howe, 1978; Goldstein,1976) due to the effect of the edge scattering. However it is difficult to give the relative noise levels of all five self-noise generation mechanisms since these self-noise mechanisms usually coexist.

At high Reynolds number, turbulent boundary layers (TBL) develop over most of the airfoil surface. Noise is produced as this turbulent flow passes over the trailing edge. This is referred to as the Turbulence-Boundary-Layer-Trailing-Edge (TBL-TE) noise that will be addressed in this thesis. For the sake of conciseness, this noise mechanism will be referred as self-noise throughout this thesis.

This thesis describes a frequency domain method for predicting the broadband self-noise due to an open rotor or propeller. In this method, the rotor is assumed to operate with smooth incoming axial flow and with subsonic tip Mach number. The blade surface pressure spectrum due to boundary layer turbulence is used as the input to the prediction. A generalized formulation of the self-noise radiation from a rotor, which is valid in both near and far fields, has been obtained. A simpler formulation is also provided that is valid only in the far field.

1.2 Methods Currently Available for Self-noise Prediction

The prediction of rotor broadband self-noise proposed in this thesis comprises two separated stages. First the unsteady blade surface pressure distribution on the airfoil, or blade, surface is determined using the boundary layer spectrum combined with an analytic solution for the unsteady airfoil response function. The acoustic analogy (Goldstein, 1976) is then applied to relate the source distribution over the blade surface to the radiated noise.

This review focuses on three aspects involved in making self-noise prediction: First the spectrum of the pressure due to boundary layer turbulence incident on the trailing edge will be addressed in Section 1.2.1. This pressure spectrum will serve as the input to the self-noise prediction procedure. Second, the prediction of the airfoil surface pressure will be discussed in Section 1.2.2. Finally, the method for making rotor noise prediction will be summarized in Section 1.2.3.

1.2.1 Pressure Spectrum due to Boundary Layer Turbulence

For practical reasons, it is useful to take the airfoil surface pressure spectrum as the input quantity for making self-noise predictions. To devise a pressure spectrum model, various analytical relationships between the fluctuating wall pressure and the velocity field in the adjacent boundary layer have been proposed for boundary layer turbulence over an infinite flat-plate, or for inner pipe turbulence. The earliest works are due to Kraichnan (1956a, 1956b), Ffowcs Williams (1965), Corcos (1964), Mawardi (1955), Powell (1960), Phillips (1956), Chase (1987), Meecham & Tavis (1980) et al. The relationships between the wall pressure and the adjacent turbulent velocity can be determined by solving Lighthill's equation (see Section 2.3). The acoustic wave equation, or the Poisson equation if strictly uncompressible flow is assumed, is manipulated into an integral equation. In other words, the Lighthill's quadrupole source term is integrated over the turbulent region to give the turbulent pressure over an infinite flat-plate. The resulting expression is then subjected to various simplifying assumptions, which generally conform to existing experimental observations and intuitive reasoning.

Theoretical models of the frequency-wavenumber spectrum of the turbulent wall pressure generally assume the turbulence to be homogeneous, of low Mach number, and assume a flat, rigid wall with no mean pressure gradient. The steady growth of the boundary layer in the streamwise direction is usually ignored, and the mean flow velocity is taken to be parallel to the wall and dependent only on distance from the wall. Howe (1998) has summarized various spectral expressions for the frequency-wavenumber spectrum of the turbulent wall pressure. Chase (1987) has developed an empirical spectral formula with adjustable constants that can be fixed by comparison with experimental data. Corcos (1963) was the first to express the frequency-wavenumber spectrum as the product of separated frequency and wavenumber functions. It is more convenient to make use of experimental data to quantify the spectrum parameters when the separable form of frequency-wavenumber spectrum is used (Brooks and Hodgson, 1981). The Corcos' spectrum will therefore be adopted for self-noise prediction in this thesis.

Most models of boundary layer turbulent spectrum are valid only for low Mach number. This is because wall pressure fluctuations at high Mach number are generally accompanied by significant variation in temperature and density. Hence the properties of spectra at high Mach number are not well understood. Langanelli and Wolfe (1989) have given an approximation of the point wall pressure spectrum in high Mach number flow. The effect of Mach number on the wall pressure spectrum is beyond the scope of this thesis.

Effects of surface curvature and roughness on wall pressure spectra have been reviewed by Dowling (1992). These factors are of practical importance as adjustment of the flow to abrupt changes in wall roughness, and severe pressure gradients may lead to flow separation and hence noise generation. These effects will not be included in this thesis.

1.2.2 Prediction of Airfoil Surface Pressure and its Radiated Noise

Over the last three decades there have been numerous theoretical analyses undertaken of the unsteady response function for an airfoil undergoing unsteady motion or encountering a gust. Goldstein (1976) has summarized some of the classical closed-form solutions for both incompressible and compressible flows. Howe (1978) has presented a review of the literature on the theory of the generation of sound by the interaction of low Mach number turbulent flow with the edge of a semi-infinite rigid flat plate. For self-noise calculations involving trailing edge interaction, two distinct approaches have been developed to predict the surface pressure, and hence calculate its radiated noise. One approach solves the problem of a quadrupole source in the close vicinity of a rigid half-plane. Volume-quadrupole sources induce the surface dipole sources, which are the main sound producing sources. This method involves the calculation of these surface forces, followed by the calculation of the radiated noise (Hubbard, 1991) using a form of the acoustic analogy. This approach was adopted by Ffowcs Williams and Hall (1970) using a half-plane Green function. The effects of mean flow were ignored and hence the approach is only valid at low Mach number. Another important omission is that the half-plane Green function, used in the solution of Ffowcs Williams and Hall (1970), does not satisfy the Kutta condition at the trailing edge (Blake, 1986). However, as pointed out by Blake (1986), the incident vorticity interacts with the sharp trailing edge, creating a

velocity that becomes singular at the trailing edge. Vorticity is shed into the wake with exactly the strength and convection velocity to cancel the singularity created by the incident vorticity. Experimental evidence for this may be found in the flow visualization experiment of Yu and Tam (1978), who observed vortices shed in the wake of a one-sided wall jet flow in response to a primary upstream vortex convecting past the trailing edge. Howe (1978) subsequently extended this approach to include the effect of mean flow and the effect of imposing the trailing edge Kutta condition on the solution. The total, or stagnation, enthalpy is used as the fundamental acoustic variable and the quadrupole sources are expressed as a divergence of dipole sources of vorticity distribution. The final solution is obtained by employing the Wiener-Hopf technique. Recently an extension was made to predict sound produced by very low Mach number flow over the edge of an airfoil of finite thickness by the use of a compact Green function tailored to the trailing edge geometry (Howe, 1999). Both Ffowcs Williams & Hall (1970) and Howe (1978) predict that the scattered intensity increases in proportion to the fifth power of the mean velocity. The approaches mentioned above assume that the quadrupole strengths are known. However, this method presents the same fundamental difficulties associated with the prediction of jet noise from quadrupole distributions inferred from turbulence predictions. In general, the turbulence, and hence the distribution of the volume quadrupole sources, is not known to sufficient accuracy.

Another approach for the prediction of airfoil self-noise assumes that the surface pressure produced by convected turbulence is known (that is the incident pressure discussed in the last Section). The main objective in this case is to establish a relationship between the radiated sound and the surface pressure induced by the turbulence upstream of the trailing edge. Chase (1972) was one of the first to employ this method for making noise predictions. However the Kutta condition was not satisfied by this solution and mean flow effects were not included in his solution because the same half-plane Green function as used by Ffowcs Williams and Hall (1970) was employed. A solution that satisfies the Kutta condition was given by Chandiramani (1974), and subsequently used by Chase (1975). However Chandiramani solves the boundary value problem in such a way that only the scattered pressure is cancelled at the trailing edge. The total pressure in his solution does not fully satisfy the Kutta condition. A more general formulation, which includes a mean flow, was developed by Amiet

(1976a), although his solution is only valid for two dimensional flat plate airfoil geometries. His solution satisfies the linear Helmholtz equation and satisfies the Kutta condition and the condition of no-flow through the airfoil upstream of the trailing edge. The main advantage of Amiet's solution is that a closed-form relation between the scattered pressure and the incident pressure on the flat airfoil surface is clearly established. This simple closed-form solution will be found to be very useful for making rotor broadband noise predictions. Amiet's solution is restricted to normal incident harmonic plane wave gusts convected at the convective velocity. Howe (1999) gives the solution for skewed incident turbulent gusts, but without mean flow effects included. In this thesis, a general solution for skewed gusts with mean flow effects will be introduced following the method proposed by Amiet (1976b).

Solving for the airfoil surface pressures induced by incident turbulence impinging on the trailing edge usually results in an integral equation. For a semi-infinite flat plate airfoil, the integral equation can be solved using the Wiener-Hopf technique to obtain a closed-form solution for the surface pressures or pressure jump across the flat plat (Chandiramani, 1974; Howe, 1978, 1999). The method used by Amiet (1976a) is different in that the Schwartzschild solution (Schwartzschild, 1902) is applied in an iterative manner to give a series of solutions for the scattered surface pressure. In this case, the boundary conditions on both the leading and trailing edge can be satisfied when an infinite number of terms are taken. However, a good closed-form approximation can be obtained for a flat plate airfoil using only the first term and hence neglecting the leading edge contribution. For the general geometry of an airfoil, the integral equation may be solved using the Boundary Element Method (BEM). A review of the use of boundary integral equations in aerodynamics was presented by Morino (1993), with emphasis on unsteady flows (incompressible and compressible, potential and viscous). A time-domain BEM has been used by Gennaretti, Luceri and Morino (1997) to predict the pure tonal noise of a helicopter rotor. However, a frequency domain BEM is more desirable for airfoil noise prediction due to the excessive computation time involved in the time-domain method. A recent development for airfoil self-noise prediction is the Large Eddy Simulation (LES) of the incompressible Navier-Stokes equations (Oberai, Roknaldin and Hughes, 2002; Manoha, Delahay, Sagaut and Mary, 2001). LES is used to determine the acoustic sources on the airfoil surface and self-noise radiation is

predicted through the acoustic analogy. Numerical methods (BEM, LES) are attractive but the computation time required for making rotor broadband noise predictions is currently excessive. Therefore a closed-form solution for predicting the surface pressures will be proposed in this thesis for making rotor broadband noise predictions.

A complication in the prediction of rotor noise is the scattering of aerodynamic and acoustic pressure between adjacent blades. To incorporate the influence of adjacent blades, a cascade model, in which a row of airfoils is considered, can be formulated. Comparison of the single-airfoil Sears's function with the response function for a cascade version calculated by Whitehead (1962) shows that when the gap between adjacent blades is large compared with the upwash wavelength along the blade, the cascade effect is small and single-airfoil theory is a good approximation. Additional refinements to the theory have been made by Goldstein and Atassi (1976), who accounted for the effects of finite thickness and camber, and by Atassi and Akai (1979), who included the effects of high loading and finite angle of attack. The effects of scattering between adjacent blades are ignored in this thesis.

1.2.3 A Review of Rotor Noise Prediction Methods

The early history of research on rotating blade noise was reviewed by Morfey (1973) with emphasis on the fundamental aspects of aerodynamic sound generation by blades. Another review was undertaken by Cumpsty (1977) from the point of an engineer wanting to understand, reduce and predict noise from turbomachines. More recently, Brooks (1983) has summarized the research of helicopter rotor broadband noise. Extensive treatments of the theoretical acoustics of ducted fans and fans in the free field have been presented by Blake (1986) and Goldstein (1976).

The prediction of tonal noise from propellers was first made by Gutin (1936), who recognised the fundamental dipole character of airfoil radiation. In essence, his model predicts the far field sound produced by the thrust and torque distributed over the disk swept out by the propeller. Mean flow effects due to forward flight, 'thickness noise' generated by the volume displacement effects of the blades, and the volume distribution of quadrupole sources were not included in the model, however. Thickness effects were

first included in the propeller theory by Ernsthausen (1936), Demming (1938) and completed by Gutin himself in 1942. However, noise due to blade thickness is generally found to be unimportant until the tip speed approaches the speed of sound (Metzger, Magliozzi, Towle and Gray, 1969). Quadrupole source contributions were shown by Ffowcs Williams and Hawkings (1969a) to be important through the potential and turbulence velocity fields generated by multi-bladed high-speed fans. This quadrupole effect was investigated by Hanson and Fink (1979). They showed that for moderately subsonic, or fully supersonic, flow over thin blade sections, the quadrupole term is negligible, but the volume displacement source (thickness noise) and quadrupole source are of roughly equal importance at flow Mach numbers, relative to the blade, close to unity. Therefore, in this thesis, we are mainly concerned with dipole sources, which we assume to be the dominant sources for subsonic rotors. We further assume that the dominant radiation mechanism is by interaction of the turbulent boundary layer produced over the airfoil surface with the airfoil trailing edge. Furthermore, the effects due to blade-to-blade interaction are ignored.

Garrick and Watkins (1954) extended Gutin's analysis to account for the forward motion of the propeller. In Garrick and Watkins' formulation, the sound field is expressed in the frequency domain by integrating the source contribution over the projected disk of the propeller. A different approach was adopted by Van de Vooren and Zandbergen (1963) who calculated the sound field due to a source moving along a helicoidal path. This method gives a better representation of the physical source distribution, but it requires the solution of the retarded time equations. Lowson (1965) obtained a general expression for the sound field of a point force in arbitrary motion. His expression provided clear insight into the mechanism of sound generation due to the time-rate-of-change of the force distribution acting on the fluid, and the acceleration of the system in which the force is acting. An alternative approach is taken by Ffowcs Williams and Hawkings (1969b) who generalized Lighthill's acoustic analogy approach to include surfaces in arbitrary motion. Lowson's formulation and Ffowcs Williams and Hawkings' equations are quite general. However, both are time-domain formulations which involve the evaluation of convolution-type integrals. Farassat (1981) has developed a practical time-domain method for the calculation of noise due to rotating blades. The time-domain method is readily applied to arbitrary blade geometries but requires source strength time

histories to be known, as well as requiring calculations of retarded blade positions to be performed.

A transformation of the governing equation to the frequency domain eliminates the need for computing retarded blade locations and gives clearer insight into the influence on noise radiation of blade geometry. Hanson (1980, 1983) has proposed a frequency-domain formulation for propellers in flight via a helicoidal surface representation of the blades corresponding to the path followed by a point on the blade during flight. Hanson's integration is evaluated on the helicoidal surface of the blade mid-chord and hence the thin-blade approximation has to be made. However, as Peake and Crighton (1991) have pointed out, integration over the mean plane is inadequate when airfoil thickness is comparable with the Doppler-shifted wavelength. In particular, great care must be exercised when considering Mach radiation for which the effective Doppler frequency is infinite.

In the early stages of propeller noise research, integration of the source distribution was carried out over the propeller disk to reveal the basic characteristics of rotor noise radiation. The source distribution is therefore assumed to be concentrated on the projected-disc plane. The result is valid for the case when the axial dimension of the rotor is smaller than the acoustic wavelength. Far field assumptions are usually made in order to evaluate the integration in the blade-fixed coordinate reference frame. A combined analytical and numerical method has in recent years been applied to evaluate the integration over the disc-shaped source (Chapman, 1993; Carley, 1999). The method allows an efficient evaluation of the rotating sound fields. In the 1980s, Hanson (1980, 1983) and Farassat (1981) developed frequency-domain and time-domain formulations of propeller noise to allow the integration to be evaluated over more realistic blade surface geometries. However, their methods have not been extended to rotor broadband noise prediction. Time-domain methods are not appropriate for making broadband noise prediction because they requires random time history of source strength to be known. Hanson's frequency-domain method is too complicated to extend to broadband noise computations and, furthermore, it is only valid for thin airfoils. Due to the complexity of broadband noise calculations, empirical correlations between the radiated sound and operational parameters were developed by both Wright (1976) and Widnall (1969).

Ffowcs Williams and Hawkings (1969a) were the first to develop a formula relating the power spectral density of fluctuating forces on a rotating blade to the spectral description of the radiation field. Again the sources are regarded as concentrated at a point rotating in the projected-disc plane and the solution is only valid in the far field.

Frequency domain formulations have recently been extended to the non-axially symmetric sound field based on the unsteady ('once per revolution') loading experienced by the propeller blades when the propeller axis is at an angle of attack to the freestream (Mani, 1990; Hanson, 1995). An ideally uniform stream with the propeller axis coincident with the direction of the free stream is assumed in this paper because it is too complicated to include the effect of non-axially symmetric mean flow in the rotor broadband noise prediction.

1.3 Research Objectives

The purpose of this research is to develop a method in the frequency domain to predict broadband self-noise from rotors. The source model will first be applied to predict the broadband self-noise from a single airfoil in a uniform mean flow. The theory is then extended to multiple rotating blades. A general relationship between the radiated pressure spectrum and the unsteady blade surface pressure spectrum is derived. Parameter studies are performed to provide insight into the effects on rotor noise generation of rotor geometry, blade setting angles, angles of attack, blade number, and blade tip Mach numbers. The main objectives of this thesis are as follows:

(1) To investigate the relationship between the scattered pressure field from the trailing edge of an airfoil and the pressure in the turbulent boundary layer on airfoil surface incident on the trailing edge.

(2) To investigate the relationship between the radiated pressure spectrum and the surface pressure spectrum for the case of a single airfoil of realistic geometry.

(3) To investigate the characteristics of airfoil self-noise radiation, such as far-field directivity, the effects of airfoil geometry, and mean flow Mach number.

(4) To develop a validated theory of the broadband self-noise radiated by an un-ducted rotor, or propeller.

(5) To investigate the characteristics of rotor broadband self-noise, such as far-field directivity, radiation spectrum and investigate effects of rotor design parameters, such as blade setting angles, angles of attack, chord length, blade number, and blade tip Mach numbers.

1.4 Original Contributions

The main original contributions of this thesis are listed below:

1.4.1 Original Contributions to Airfoil Broadband Noise Prediction:

(1) An empirical model for the boundary layer wavenumber-frequency spectrum has been applied to make broadband self-noise prediction. This forms the basis for the engineering model of broadband rotor self-noise prediction presented later in this thesis.

(2) A general closed-form solution for the surface pressure on a flat plate due to an arbitrary time-harmonic single wavenumber component of boundary layer pressure incident upon the trailing edge has been derived. The important difference from previous solutions is that the effects of both Mach number and oblique-incidence turbulence are included in the solution.

(3) The closed-form flat-plate solution in (2) has been applied to a realistic airfoil geometry under the assumption of high reduced frequency and sharp trailing edge. Due to the local characteristics of the scattered pressure near the trailing edge, this flat plate model is expected to provide a good approximation to the surface pressure distribution for real airfoils.

(4) A frequency domain formulation has been developed for making airfoil self-noise predictions. The important difference from previous work is that it is valid for arbitrary airfoil geometries at small, but non-zero angles of attack. Moreover, the solution is valid in both near and far fields. It is shown to reduce to Amiet's analytic solution when the airfoil collapses to a flat plate with large span and the measurement point is taken to the far field.

(5) A numerical scheme for the evaluation of the integral formula required in (4) on an arbitrary airfoil surface has been presented. The method requires a closed-form source distribution of the scattered pressure on the airfoil surface. Numerical results show reasonable agreement with Brook empirical prediction scheme based on experimental data.

(6) Broadband noise directivity has been predicted for a flat-plate, NACA 0012 and NACA 0024 airfoils. The directivities are asymmetric due to the non-zero angle of attack. The results reveal that mean flow Mach number has an important influence on the magnitude and directivity of broadband self-noise. The directivity prediction due to a single harmonic component of turbulence for a flat plate airfoil shows excellent agreement with Amiet's analytic solution.

(7) Broadband self-noise predictions are made for both frozen and non-frozen boundary layer turbulence. Non-frozen turbulence is shown to generate higher noise radiation than frozen turbulence at high frequencies. However, the difference is generally less than 3 dB, suggesting that the frozen-gust assumption is a reasonable assumption for broadband noise predictions

1.4.2 Original Contributions to Rotor Broadband Noise Prediction:

(1) The single airfoil model for predicting airfoil surface pressure distribution has been extended to rotating blades using strip theory.

(2) A generalized frequency domain formulation has been developed for making rotor broadband noise predictions. It can be used for making broadband and tonal noise predictions, and is valid in both the near field and the far fields. The main difference

from previous work is that the source distribution is integrated over the real blade surface to provide greater accuracy. Previous formulae were integrated over the projected disk of the rotating blades only.

(3) The general formulation above has been validated by comparison with the analytic solution of the 3rd CAA benchmark problem.

(4) A simplified expression for making far-field self-noise predictions has been derived. This far-field frequency-domain formulation is computationally far more efficient than the general formulation in (2). It is shown to reduce to the classical Gutin solution of propeller tonal noise prediction when the steady surface pressure source is confined to the propeller-projected disc.

(5) The numerical method for making airfoil noise predictions is extended to rotating blades. The validation is performed from predictions of the measured broadband noise from an R212 propeller. Absolute sound pressure levels are generally within 10 dB of the measured data. Good agreement between the spectral shapes of the measured and predicted noise spectrum is obtained. The tonal noise predicted by the method also shows very good agreement with the R212 propeller experimental data.

(6) The broadband self-noise directivity is predicted to be significantly different from the pure-tone noise directivities. The main lobe of broadband self-noise directivity is in the direction of the propeller axis while the main lobe of the pure-tone noise directivity is normal to the propeller axis.

(7) Parameter studies on rotor self-noise prediction show that a propeller with large blade number and constant attack angle along the blade radius produces lower self-noise radiation compared with propellers with small blade number and non-constant attack angle. The predicted dependence of the broadband noise frequency spectrum is predicted to scale very closely with the fifth power of the blade tip Mach number.

1.5 Thesis Contents

This thesis is arranged as follows. Chapter II contains the general theory used in the development of the frequency domain formulation in subsequent chapters. The integral equation in the moving coordinate system is addressed, and the free-space Green function with mean flow effect has been derived for later use.

Chapter III provides a description of the turbulence spectra of the aerodynamic boundary-layer-turbulence pressure field incident upon the airfoil trailing edge. Measured point pressure spectra and boundary layer parameters (boundary layer thickness, turbulence integral length scales) are discussed. Chapter IV gives a detailed derivation of the closed-form solution of the surface pressure due to an incident pressure field impinging upon the trailing edge of a flat plate airfoil. A discussion of the application of thin airfoil theory to a realistic airfoil geometry is then presented. A transfer function relating the incident pressure to the airfoil surface pressure, which includes trailing edge scattering, is introduced in this chapter. Chapter III and Chapter IV together provide a description of the determination of the airfoil surface source distribution.

Chapter V presents the frequency domain formulation for making airfoil broadband noise predictions. Details are provided to show how it reduces to Amiet's analytic solution for flat plate airfoils. A numerical scheme is then introduced to implement the prediction of airfoil broadband self-noise. Chapter VI presents the validation results of the frequency domain formulation derived in Chapter V for making airfoil broadband self-noise predictions. The predicted results are compared with Amiet's analytic solution and the Brooks empirical prediction for a NACA 0012 airfoil. The effects of airfoil geometry and non-frozen boundary layer turbulence on broadband self-noise radiation are also presented.

Chapters VII to Chapter XI are concerned with the prediction of broadband self-noise radiation from an open rotor. A general frequency domain formulation is derived in Chapter VII and a simplified far-field approximation is presented in Chapter IX for rotor

broadband noise predictions. A mode transfer function between the radiated sound pressure and the unsteady blade surface pressure are introduced in these two formulations. These formulations provide insight into the mechanisms by which the unsteady surface pressure is shifted by the blade passing frequency to radiate sound with continuous pressure spectra. In Chapter VIII, the Category 2 benchmark problem of the 3th CAA Workshop (see Category 2—Rotor Noise, 1999) is used as a test case to provide a validation of the general frequency-domain formulation described in Chapter VII. In Chapter X, the far field frequency-domain formulation of rotor noise radiation is adapted to predict tonal noise. The predicted tone noise is compared against experimental data obtained by Trebble for a 1/5th scale model propeller (Trebble, 1987a). To further validate the far field formulation, the predicted self-noise radiation is compared against the broadband experimental data obtained by Trebble (1987b) in Chapter XI. Parameter studies are also presented in this Chapter, whereby the variation in self-noise is predicted against various blade setting angles, angle of attack, chord length, blade number, and blade tip Mach number. Finally, concluding remarks are put forward in Chapter XII.

Chapter II:

Fundamental Equations for the Prediction of Aerodynamic Noise

2.1 Introduction

The study of flow-generated acoustic noise due to rotating blades probably began with Gutin's (1936) theory of propeller noise. Yet, it was not until 1952, when Lighthill (1952,1954) introduced his acoustic analogy to deal with the problem of sound generated by unsteady flow that a general theory began to emerge. Lighthill's theory was subsequently extended by Curle (1955), and Ffowcs Williams and Hawking (1969b), to include the effects of solid boundaries. Ffowcs Williams and Hawkings' equation is quite general. It is a time-domain formulation that involves convolution-type integrals to be evaluated. However it was Goldstein (1976) who derived an integral formulation in which, not only the effects of solid boundaries, but also mean flow effects, are included. In this thesis Goldstein's formulation is used as the basis of frequency domain formulations for making broadband fan noise predictions.

In this chapter, two coordinate systems are introduced. The differential and integral equations, which form the basis of the broadband fan noise prediction in this thesis, will then be discussed. Finally, the free-space Green function with mean flow effects included will be derived for later use.

2.2 Coordinates and Coordinates Transformation

Two frames of reference are employed here for the prediction of airfoil, or propeller, noise, as shown in Fig.2.1. One is the stationary reference frame $\mathbf{y}'(y_1', y_2', y_3')$, which is an inertial system fixed to the earth, as shown in Fig.2.1b. Another is the moving coordinate system $\mathbf{y}(y_1, y_2, y_3)$, which moves with the constant forward flight velocity U of the rotor, as shown in Fig.2.1a. Note that in some literature, such as Goldstein (1976), the coordinate system $\mathbf{y}(y_1, y_2, y_3)$ is referred to as a stationary coordinate system in which the fluid medium moves with uniform velocity U.

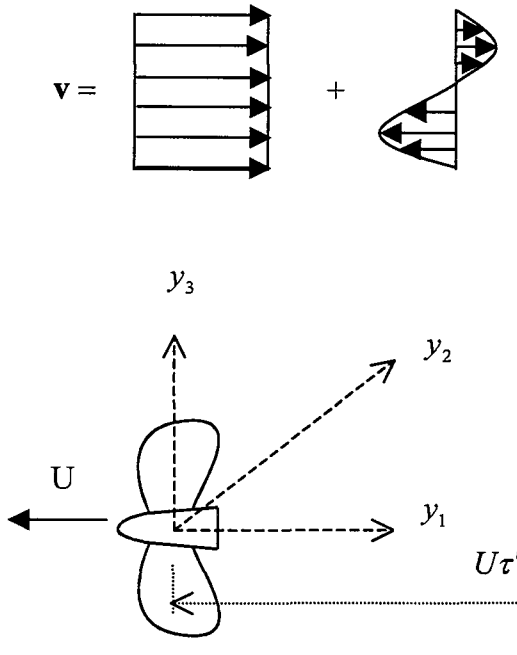

Figure 2.1a. Moving coordinates of reference $\mathbf{y}(y_1, y_2, y_3)$

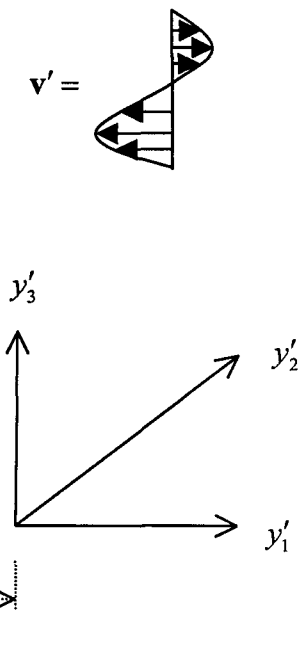

Figure 2.1b. Stationary coordinates of reference $\mathbf{y}'(y_1', y_2', y_3')$

The relationship between these two coordinate systems are given by

$$y_i = y_i' + \delta_{1i} U\tau' \tag{2.1a}$$

$$\tau = \tau' \tag{2.1b}$$

$$v_i = v_i' + \delta_{1i} U \tag{2.1c}$$

$$\frac{\partial}{\partial y_i} = \frac{\partial}{\partial y_i'} \tag{2.1d}$$

$$\frac{D}{D\tau} = \frac{\partial}{\partial \tau} + U\frac{\partial}{\partial y_1} = \frac{\partial}{\partial \tau'} \tag{2.1e}$$

where U is the velocity of the moving body in the y_1-direction, τ' and τ are times associated with the fixed coordinate system and the moving coordinates respectively, δ_{ij} is the Kronecker delta function, $\mathbf{v} = (v_1, v_2, v_3)$ is the total fluid velocity measured in the moving reference frame, and $\mathbf{v}' = (v_1', v_2', v_3')$ is the fluid velocity measured in the stationary coordinate system.

2.3 Governing Equations and their Equivalence

Under the assumption of an isentropic fluid, the fundamental system of differential equations governing the motion of an inviscid, compressible fluid takes the form of Euler's equations. Both Euler and Lighthill equations are invariant under the Galilean transformation of Eqs. (2.1). It can be shown that the equations in the block diagrams of Fig.2.2 are mutually equivalent. In these block diagrams, $\nabla' = \frac{\partial}{\partial y_i'}\mathbf{e}_i'$, $\nabla = \frac{\partial}{\partial y_i}\mathbf{e}_i$ are the vector operators in the fixed coordinate system and the moving coordinate system respectively, $\mathbf{e}_i'$, $\mathbf{e}_i$ are unit vectors in the y_i' and y_i direction, ρ is the density of the fluid, p is the pressure, and c_0 is the speed of sound in the steady background fluid. To obtain equations A3 from equation B2 in Fig. 2.2, one needs only to substitute Eq. (2.1e) into equation B2. To derive equation A2 from equation A3, Eqs. (2.1c), (2.1d) and (2.1e) are substituted into equation A3.

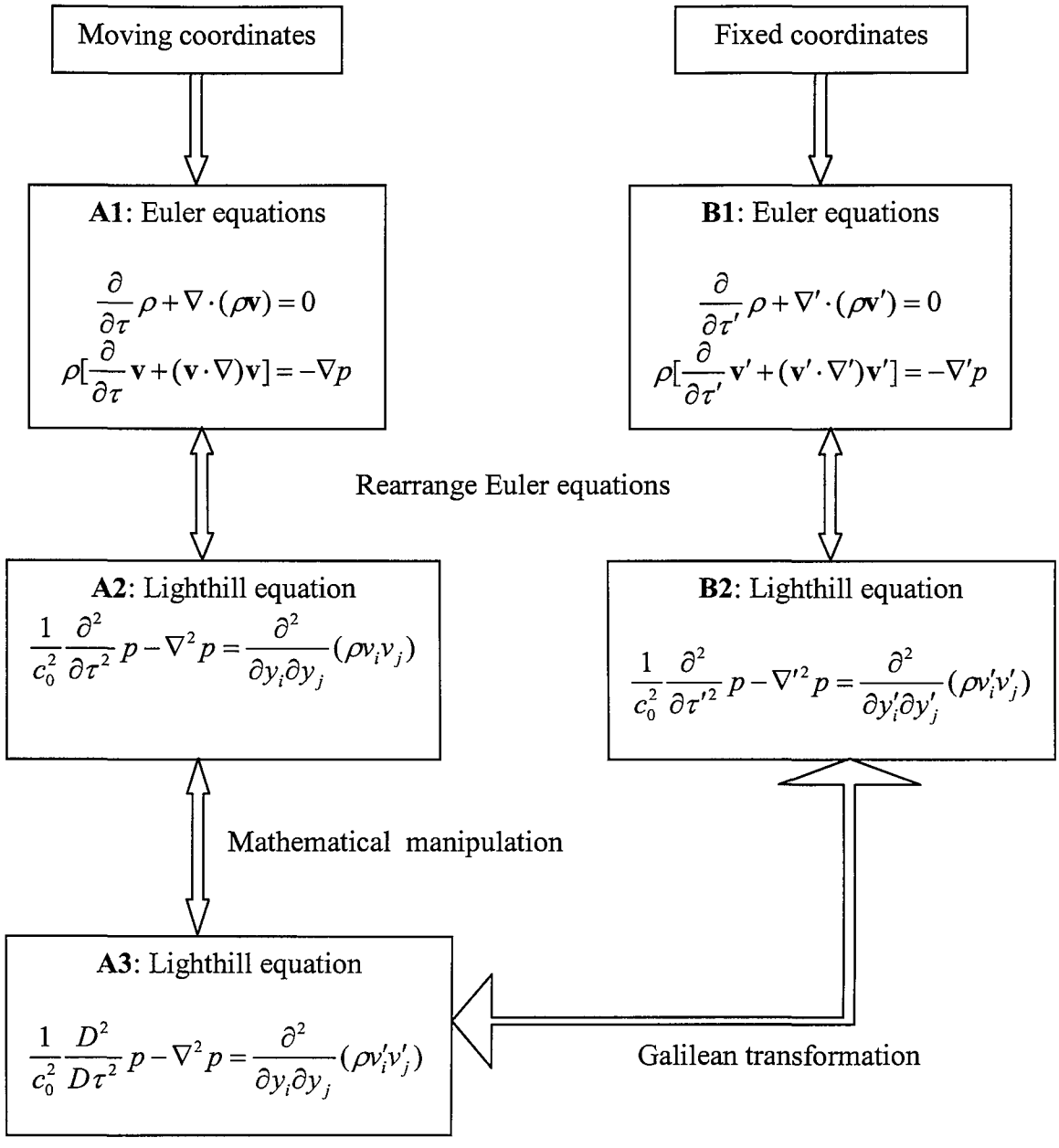

Figure 2.2. Equivalent equations in stationary and moving reference frames

Equation B2 is referred to as the stationary-medium wave equation while equation A3 is referred to as the moving-medium wave equation. The moving-medium wave equation will be used later in this thesis. This convected wave equation from equation A3 is rewritten below

$$\frac{1}{c_0^2}\frac{D^2}{D\tau^2}p-\nabla^2 p=\frac{\partial^2}{\partial y_i \partial y_j}(\rho v_i' v_j') \tag{2.2}$$

Note that Eq.(2.2), is expressed in the moving coordinate system, but the unsteady velocity is measured in the stationary frame of reference. It means that the acoustic waves propagate through a medium that is in a state of uniform motion relative to the observer. There are two advantages in the use of this equation: (i) The effect of mean flow is included in the Green function solution, and thus one does not need to consider this mean-flow effect again when dealing with the quadrupole sources, $\gamma(\mathbf{y},\tau)=\frac{\partial^2}{\partial y_i \partial y_j}(\rho v_i' v_j')$, (ii) Boundary surfaces are stationary relative to the moving reference of frame (i.e. airfoil-fixed reference frame) for computing airfoil noise, which allows a more convenient integration over the airfoil surface. In the case of rotor noise, further development of Eq.(2.2) will lead to an integration over a stationary boundary surface in the blade-fixed reference frame.

2.4 Integral Equations in the Moving Coordinate System

Consider a region $v(\tau)$ exterior to an impermeable closed surface $S(\tau)$, as shown schematically in Fig.2.3. Goldstein (1976) has derived a generalized integral equation (Goldstein 1976, Eq.(1.65)) which relates the acoustic pressure at an arbitrary field point **x** at time t to the distribution $\gamma(\mathbf{y},\tau)$ of quadrupole sources within v, and the distribution of the pressure $p(\mathbf{y},\tau)$ and its derivatives $\partial p(\mathbf{y},\tau)/\partial n$ on the boundary of v. In the moving frame of reference this generalized integral equation becomes

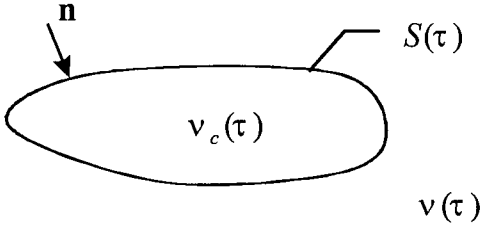

Figure 2.3. Fluid region $v(\tau)$ and its boundary $S(\tau)$

$$\int_{-T}^{T} d\tau \iint_{\substack{S(\tau)\\ \mathbf{x}\neq\mathbf{y}}} \left[G(\mathbf{x},t;\mathbf{y},\tau)\frac{\partial}{\partial n}p(\mathbf{y},\tau) - p(\mathbf{y},\tau)\frac{\partial}{\partial n}G(\mathbf{x},t;\mathbf{y},\tau) \right] dS(\mathbf{y})$$
$$+\frac{1}{c_0^2}\int_{-T}^{T} d\tau \iint_{\substack{S(\tau)\\ \mathbf{x}\neq\mathbf{y}}} V_n'(\mathbf{y}) \left[G(\mathbf{x},t;\mathbf{y},\tau)\frac{D}{D\tau}p(\mathbf{y},\tau) - p(\mathbf{y},\tau)\frac{D}{D\tau}G(\mathbf{x},t;\mathbf{y},\tau) \right] dS(\mathbf{y}) \qquad (2.3)$$
$$+\int_{-T}^{T} d\tau \iiint_{\substack{v(\tau)\\ \mathbf{x}\neq\mathbf{y}}} \gamma(\mathbf{y},\tau)G(\mathbf{x},t;\mathbf{y},\tau)d\mathbf{y} = \begin{cases} p(\mathbf{x},t) & \text{if } \mathbf{x} \text{ is in } v(\tau) \\ \frac{1}{2}p(\mathbf{x},t) & \text{if } \mathbf{x} \text{ is on } S(\tau) \\ 0 & \text{if } \mathbf{x} \text{ is outside of } v(\tau) \end{cases}$$

where $V_n' = V_n - n_1 U$ is the normal velocity of the boundary surface $S(\tau)$ observed in the stationary coordinate system, V_n is the normal velocity of the boundary surface observed in the moving coordinate system, $\mathbf{n}$ is the unit normal (drawn outward from $v(\tau)$), n_1 is the first component of $\mathbf{n}$, and T is some very large but finite interval of time. Here $p(\mathbf{y},\tau)$ and $p(\mathbf{x},t)$ are the acoustic pressures at the source point and the field point respectively which satisfy equation (2.2), and $G(\mathbf{x},t;\mathbf{y},\tau)$ is the Green function that satisfies

$$\begin{cases} \dfrac{1}{c_0^2}\dfrac{D^2}{D\tau^2}G - \nabla^2 G = \delta(\tau - t)\delta(\mathbf{y} - \mathbf{x}) \\ \lim\limits_{R_d\to\infty}\left|R_d G\right| < \infty \\ \lim\limits_{R_d\to\infty}\left[R_d\left(\dfrac{\partial G}{\partial R_d} - \dfrac{1}{c_0}\dfrac{\partial}{\partial \tau}G\right)\right] = 0 \quad or \quad \lim\limits_{R_d\to\infty}\left[R_d\left(\dfrac{\partial G}{\partial R_d} + \dfrac{1}{c_0}\dfrac{\partial}{\partial t}G\right)\right] = 0 \end{cases} \qquad (2.4)$$

In Eq.2.4 $R_d = |\mathbf{y} - \mathbf{x}|$ is the distance between the observation point $\mathbf{x}$ and the source point $\mathbf{y}$ in the moving coordinate system, δ is the Dirac delta function, and t is the time associated with the arrival of sound at the observation point.

Although the integral equation (2.3) refers to the moving reference frame of constant velocity, it is valid for arbitrary motion of the boundary surface. Another boundary integral formulation which allows the reference frame to have arbitrary motion can be

found in Gennaretti and Morino (1992). Gennaretti and Morino's integral equation is equivalent to the integral equation (2.3), but no non-linear terms related to $\gamma(\mathbf{y},\tau)$ are included.

Further mathematical manipulation of the integral equation (2.3) gives Goldstein's version of the acoustic analogy (Goldstein 1976, Eq.(4.10)), which is the fundamental equation governing the generation of aerodynamic sound in the presence of solid boundaries. It is in the form of the integral equation

$$\begin{aligned} p(\mathbf{x},t) = & \int_{-T}^{T} \iiint_{V(\tau)} \frac{\partial^2 G}{\partial y_i \partial y_j} T'_{ij}(\mathbf{y},\tau) d\mathbf{y} d\tau \\ & + \int_{-T}^{T} \iint_{S(\tau)} \frac{\partial G}{\partial y_i} f_i dS(\mathbf{y}) d\tau + \int_{-T}^{T} \iint_{S(\tau)} \rho_0 V'_n \frac{DG}{D\tau} dS(\mathbf{y}) d\tau \end{aligned} \tag{2.5}$$

where $f_i = -n_i(p-p_0) + n_j e_{ij}$ is the i^{th} component of the force per unit area exerted by the boundaries on the fluid, e_{ij} is the $(i,j)^{\text{th}}$ component of the viscous stress tensor, n_i is the i^{th} component of the unit inward normal $\mathbf{n}$ on the surface $S(\tau)$, p_0 is the pressure of the stationary background flow, ρ_0 is the density of the steady background flow, and $T'_{ij} = \rho v'_i v'_j + e_{ij}$ is Lighthill's stress tensor for isentropic flow.

Since the integral formulation of Eq. (2.5) is expressed in the moving reference frame, several important points are worthy of note. First, it involves a Green function for the wave equation with mean flow (determined by Eq. (2.4)) instead of a Green function for a stationary medium. Second, Lighthill's stress tensor is expressed in terms of the real velocity $v'_i = v_i - \delta_{1i} U$ measured in the fixed frame instead of the velocity v_i observed in the moving reference frame. Finally, the volume displacement term is expressed in terms of $V'_n = V_n - n_1 U$ and $D/D\tau$ rather than V_n and $\partial/\partial\tau$.

Equation (2.5) will serve as the starting point for the prediction of airfoil and rotor broadband self-noise presented in this thesis.

2.5 Green Function in the Moving Coordinate System

In the moving reference frame, the Green function $G(\mathbf{x},t;\mathbf{y},\tau)$ is a solution of the following equations

$$\begin{cases} \dfrac{1}{c_0^2}\dfrac{D^2}{D\tau^2}G-\nabla^2 G=\delta(\tau-t)\delta(\mathbf{y}-\mathbf{x}) \\ \lim\limits_{R\to\infty}|RG|<\infty \\ \lim\limits_{R\to\infty}[(\dfrac{\partial}{\partial R}-\dfrac{1}{\beta^2 c_0}\dfrac{\partial}{\partial\tau})(RG)]=0 \end{cases} \tag{2.6}$$

where $R=\sqrt{(y_1-x_1)^2+\beta^2(y_2-x_2)^2+\beta^2(y_3-x_3)^2}$, $\beta^2=1-M^2$, $M=U/c_0$ is the Mach number of the mean flow (airfoil velocity or axial rotor speed). One should note that when the partial derivative with respect to R is taken in the last equation of Eq.(2.6), the quantity R is assumed to be an independent variable although it is dependent on the variables $\mathbf{x}$ and $\mathbf{y}$. The third expression of Eq.(2.6) is a statement of Sommerfeld radiation condition and is equivalent to the last equation of Eq. (2.4). However, the last equation of Eq.(2.6) is easier to verify in analytical studies.

Expansion of the first expression of Eq. (2.6) gives

$$(1-M^2)\frac{\partial^2 G}{\partial y_1^2}+\frac{\partial^2 G}{\partial y_2^2}+\frac{\partial^2 G}{\partial y_3^2}-2\frac{M}{c_0}\frac{\partial^2 G}{\partial y_1\partial\tau}-\frac{1}{c_0^2}\frac{\partial^2 G}{\partial\tau^2}=-\delta(\tau-t)\delta(\mathbf{y}-\mathbf{x}) \tag{2.7}$$

Equation (2.7) may be reduced to an equivalent no-flow problem by making the Lorentz transformations:

$$\begin{cases} Y_1 = y_1 \\ Y_2 = \beta y_2 \\ Y_3 = \beta y_3 \\ T = \beta^2 c_0 \tau + M y_1 \end{cases} \tag{2.8}$$

which simplifies Eq.(2.7) to

$$\begin{aligned} &\frac{\partial^2 G}{\partial Y_1^2} + \frac{\partial^2 G}{\partial Y_2^2} + \frac{\partial^2 G}{\partial Y_3^2} - \frac{\partial^2 G}{\partial T^2} \\ &= -\frac{1}{\beta^2}\delta\left(\frac{1}{\beta^2 c_0}(T - MY_1) - t\right)\delta(Y_1 - x_1)\delta\left(\frac{1}{\beta}Y_2 - x_2\right)\delta\left(\frac{1}{\beta}Y_3 - x_3\right) \end{aligned} \tag{2.9}$$

It may be verified that the general solution to Eq.(2.9) is of the form

$$G = \frac{1}{R} f(T \pm R) \tag{2.10}$$

where $R = \sqrt{(Y_1 - X_1)^2 + (Y_2 - X_2)^2 + (Y_3 - X_3)^2}$ is the distance between two points in the transformed coordinate system, and f denotes an arbitrary function of its argument. In order to determine the arbitrary function f, let v_0 be taken to be a sphere of fixed radius R_0 centred about the point $\mathbf{y} = \mathbf{x}$ and $d\Omega$ denotes an element of solid angle (so that $dS = R_0^2 d\Omega$). Integration of Eq. (2.9) with the aid of the Gauss divergence theorem shows that

$$\begin{aligned} &R_0^2 \int_{4\pi} \left[\frac{\partial}{\partial R}\left(\frac{1}{R} f(T \pm R)\right)\right]_{R=R_0} d\Omega - \int_{4\pi}\int_0^{R_0} \frac{1}{R}\frac{\partial^2}{\partial T^2} f(T \pm R) R^2 dR d\Omega \\ &= -\frac{1}{\beta^2}\iiint_{v_0} \delta\left[\frac{1}{\beta^2 c_0}(T - MY_1) - t\right]\delta(Y_1 - x_1)\delta\left(\frac{1}{\beta}Y_2 - x_2\right)\delta\left(\frac{1}{\beta}Y_3 - x_3\right) dY_1 dY_2 dY_3 \end{aligned} \tag{2.11}$$

Integration of Eq. (2.11) by parts leads to

$$f(T)=\frac{1}{4\pi}\delta[\frac{1}{\beta^2 c_0}(T-Mx_1)-t] \quad . \tag{2.12}$$

In terms of the original variables, the unique Green function solution expressed in the moving coordinate system is derived by making use of Sommerfeld's radiation condition of Eqs.(2.6)

$$G(\mathbf{x},t;\mathbf{y},\tau)=\frac{1}{4\pi R}\delta[\tau+\frac{1}{\beta^2 c_0}(R+M(y_1-x_1))-t] \quad . \tag{2.13}$$

We shall make use of the Green function in the frequency domain, which takes the form of

$$\overline{G}(\mathbf{x},\mathbf{y},\omega)=\int_{-\infty}^{\infty}G(\mathbf{x},t;\mathbf{y},\tau)e^{i\omega(t-\tau)}dt=\frac{1}{4\pi R}e^{i\mu E} \tag{2.14}$$

where ω is the angular frequency, $E=R+M(y_1-x_1)$, $\mu=\kappa/\beta^2$, and $\kappa=\omega/c_0$ is the acoustic wave number. A similar Green function to that in Eq. (2.14) was given by Garrick and Watkins (1954).

Chapter III

Characteristics of Boundary Layer Turbulence

3.1 Introduction

For making airfoil or rotor self-noise predictions we shall show in Chapter IV that it is convenient to use as input data the surface boundary layer pressures measured well away from the trailing edge. These pressure data could be obtained by measurements or from CFD predictions. We define the unsteady pressure developed beneath the turbulent boundary layer on an infinite surface (i.e. with trailing edge absent) as the incident pressure p_i, and the pressure subsequently scattered from the trailing edge as the scattered pressure p_s. The scattered pressure may be obtained from p_i by imposing the Kutta condition at the airfoil trailing edge, such that the incident and scattered pressure exactly cancels at the trailing edge. These two pressures add to form the total airfoil surface pressure p_t with trailing edge present,

$$p_t = p_i + p_s \tag{3.1}$$

Once the relationship between p_i and p_s is known, the problem of broadband self-noise prediction is therefore completely determined from the incident pressure spectrum. Brooks and Hodgson (1981), for example, argue that the scattered pressure is only significant at distances less than about one hydrodynamic wavelength from the trailing edge. This agrees with the conclusion by Ffowcs Williams and Hall (1970) who state

that if the eddies are far from the trailing edge ($(k_s|\eta_s|)^{1/2} >> 1$) then sound amplification by the trailing edge is negligible. We assume in this thesis that the measured pressure used in the model (see Eq. (3.2)) is the pressure incident upon the trailing edge provided that the measurement point is sufficiently far from the trailing edge. This is the same assumption made implicitly by Amiet (1976a).

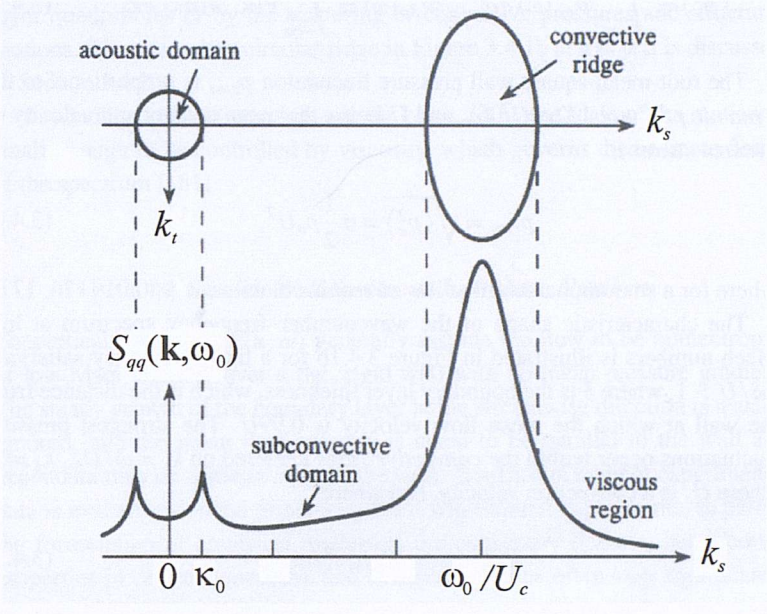

Figure 3.1. Characteristic of the wall pressure spectrum, see Howe (1998)

Figure 3.1 illustrates qualitatively the general characteristic of the wall-pressure spectrum $S_{qq}(\mathbf{k},\omega_0)$ at a fixed frequency satisfying $\omega_0\delta/U_0 >> 1$ versus streamwise wavenumber, where δ is the boundary layer thickness, U_0 is the airfoil velocity or mean-flow velocity, ω_0 is the source angular frequency (see, for example, Howe (1998)). It shows two main peaks. The largest peak occurs in the 'convective regime', where the turbulent eddies convect at speeds slower than the speed of sound, c_0. Most of the energy convects at, or close to, the characteristic eddy convection velocity, U_c. Turbulent energy in this region is said to be in the convective ridge. The second peak is in the vicinity of the acoustic wavenumber κ_0 where k, the modulus of the vector $\mathbf{k} = (k_s, k_t)$, is centred on $\kappa_0 = \omega_0/c_0$. The range $k < |\kappa_0|$ corresponds to the 'acoustic domain'. Here, the phase velocity of the eddies is supersonic; and the wall pressure fluctuations are acoustic in nature produced directly by boundary layer quadrupoles or by the scattering of convective pressures. The phase velocity, ω_0/k, of the eddies in the convective domain is subsonic. Here, the pressure fluctuation decays rapidly with distance from the wall and does not radiate efficiently to the far field. However, the pressures in the convective domain can generate sound when

they interact with discontinuities such as the airfoil trailing edge. The level of the pressure spectrum in the convective peak is typically some 40dB larger than in the acoustic domain (Crighton etc. (1992)). In this thesis we assume that the spectrum of the incident pressure lies in the convective regime. The turbulent energy in the acoustic domain will not be included.

In addition to the rectangular coordinate system $\mathbf{y} = (y_1, y_2, y_3)$ employed in this thesis, it will be shown to be useful to formulate the airfoil surface pressure in the curvilinear coordinates system, $\boldsymbol{\eta} = (\eta_s, \eta_t)$, attached to the airfoil, as shown in Fig. 3.2. Here $\eta_s = \eta_s(\mathbf{y})$ is the streamwise coordinate of the pressure or suction side, originating at the trailing edge, and $\eta_t = \eta_t(\mathbf{y})$ is the spanwise coordinate originating at the mid-span along the suction-side or pressure-side trailing edges. Correspondingly, we define k_s as the wavenumber in the η_s-direction and k_t as the wavenumber in the η_t-direction. For a flat plate airfoil, $(\eta_s, \eta_t) = (y_1, y_2)$ and $(k_s, k_t) = (k_1, k_2)$.

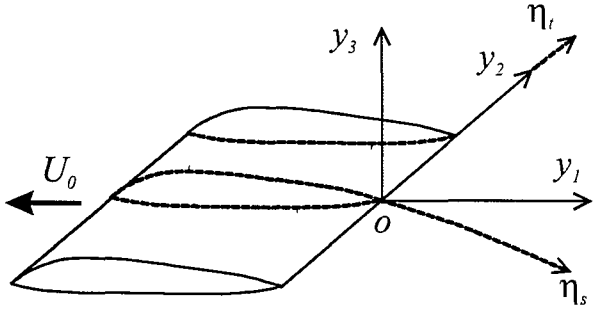

Figure 3.2. Curvilinear coordinates $\boldsymbol{\eta} = (\eta_s, \eta_t)$ and rectangular coordinates $\mathbf{y}(y_1, y_2, y_3)$

In this chapter, the frequency-wavenumber spectra of the boundary layer pressure incident upon the trailing edge will be modelled using the Corcos (1963) theory for the wavenumber spectrum of a fully developed turbulent boundary layer over a flat plate, combined with measured frequency spectra on an airfoil surface. The turbulence wall-pressure frequency-wavenumber spectrum over an infinite flat-plate airfoil will be investigated in Section 3.2. This flat plate spectrum model will then be extended to the application of realistic airfoil geometry in Section 3.3. A simplified frozen spectrum of turbulence wall pressure is discussed in section 3.4. Finally, the Brooks semi-empirical

expression for predicting the boundary layer thickness is described in section 3.5, which is subsequently used as the input to the frequency spectrum model.

3.2 Turbulence Wall-pressure Spectrum of an Infinite Flat-plate Airfoil

As an approximation to the turbulent boundary layer above an airfoil, the turbulent boundary-layer above a smooth, rigid plane without mean pressure gradient is considered in this Section, as shown schematically in Fig.3.3. The unsteady wall

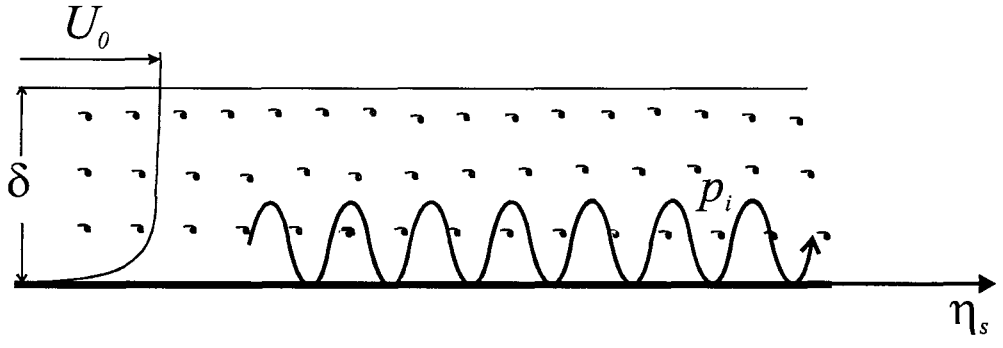

Figure 3.3. Boundary layer turbulence over a flat plate

pressure, $p_i(\mathbf{y},\tau)$, of the turbulence incident upon the trailing edge can be written in terms of its wavenumber-frequency components $\hat{p}_i(\mathbf{k},\omega_0)$ (Chase (1980)),

$$p_i(\mathbf{y},\tau) = \int_{-\infty}^{\infty}\int_{-\infty}^{\infty}\int_{-\infty}^{\infty}\hat{p}_i(\mathbf{k},\omega_0)e^{i(k_s\eta_s+k_t\eta_t-\omega_0\tau)}dk_s dk_t d\omega_0 \tag{3.2}$$

where $\mathbf{k}=(k_s,k_t)$. The Fourier components $\hat{p}_i(\mathbf{k},\omega_0)$ can be determined from $p_i(\mathbf{y},\tau)$ by the inverse relation

$$\hat{p}_i(\mathbf{k},\omega_0) = \frac{1}{(2\pi)^3}\int_{-\infty}^{\infty}\int_{-\infty}^{\infty}\int_{-\infty}^{\infty}p_i(\mathbf{y},\tau)e^{-i(k_s\eta_s+k_t\eta_t-\omega_0\tau)}d\eta_s d\eta_t d\tau \tag{3.3}$$

For broadband problems, it is useful to work with pressure wavenumber-frequency spectral densities. For simplicity, we assume here that the turbulent pressure field is spatially homogeneous and stationary with respect to time, i.e. the space-time correlations of the boundary layer pressure field are dependent only on the separation distance and temporal interval. Under this assumption, the wall-pressure frequency-wavenumber spectral density $S_{qq}(k_s,k_t,\omega_0)$ is related to the Fourier components of wall pressure $\hat{p}_i(\mathbf{k},\omega_0)$ by

$$E[\hat{p}_i^*(k_s,k_t,\omega_0)\hat{p}_i(k_s',k_t',\omega_0')] = \delta(k_s'-k_s)\delta(k_t'-k_t)\delta(\omega_0'-\omega_0)S_{qq}(k_s,k_t,\omega_0) \tag{3.4}$$

where $S_{qq}(k_s,k_t,\omega_0)$ is the wavenumber-frequency spectral density of the turbulence wall pressure, the superscript " * " denotes complex conjugation, $E[\cdots]$ denotes the expected value and δ is the Dirac delta function.

The wavenumber-frequency spectral density S_{qq} is obtained by Fourier transforming to the space-time correlation of the boundary layer pressure. Under the assumption of homogeneous and stationary boundary layer turbulence, the Fourier transform of the cross-correlation of the surface pressure is defined by,

$$\overline{R}_{qq}(\xi,\omega_0) = \int_{-\infty}^{\infty}\langle p_i(\mathbf{y},\tau)p_i(\mathbf{y}+\xi,\tau+t)\rangle e^{i\omega_0 t}dt \tag{3.5}$$

where the brackets $\langle\cdots\rangle$ denote an ensemble average, $\xi=(\xi_1,\xi_2)$ is the separation distance between two points on the airfoil surface, ξ_1 is streamwise separation distance and ξ_2 spanwise separation distance and the overbar denotes complex amplitude of an oscillation quantity in the frequency domain. The wall-pressure spectrum in the convective region has been studied by Corcos (1963), and is discussed in detail in a review article by Willmarth (1975). Corcos assumes that a stationary and homogeneous pressure field is developed in the fully turbulent boundary layer over the flat plate, whereby the statistical properties of the pressure field change very little in the streamwise direction over a length comparable either to a transducer size or to a typical

turbulence scale. For a fully developed turbulent boundary layer flow in the absence of mean-pressure gradients, Corcos assumes the following separable form for $\overline{R}_{qq}(\xi,\omega_0)$

$$\overline{R}_{qq}(\xi,\omega_0) = S_0(\omega_0)A(\omega_0\xi_1/U_c)B(\omega_0\xi_2/U_c)e^{i\omega_0\xi_1/U_c} \tag{3.6}$$

where $S_0(\omega_0)$ is the wall point pressure frequency spectrum, A and B are non-dimensional functions determined from experimental data. The cross-power spectral density may be obtained by the spatial Fourier transform of Eq. (3.6) to give

$$S_{qq}(\mathbf{k},\omega_0) = S_0(\omega_0)\left(\frac{U_c}{\omega_0}\right)^2 \hat{A}(1-\frac{k_sU_c}{\omega_0})\hat{B}(\frac{k_tU_c}{\omega_0}) \tag{3.7}$$

where $\hat{A}$ and $\hat{B}$ are the Fourier transforms of A and B,

$$\hat{A}(\alpha) = \frac{1}{2\pi}\int_{-\infty}^{\infty} A(\beta)e^{i\alpha\beta}d\beta \quad \text{and} \quad \hat{B}(\alpha) = \frac{1}{2\pi}\int_{-\infty}^{\infty} B(\beta)e^{i\alpha\beta}d\beta \tag{3.8}$$

Blake (1986, equation (8.49)) fits algebraic expressions to the functions A and B, and shows that the Corcos model provides a good estimate to the cross-spectral density of the surface pressure fluctuations in the vicinity of the convective peak, where most of the turbulent energy is contained.

Brooks and Hodgson (1981) have investigated the statistical character of the hydrodynamic pressure field in the region that is far enough upstream of the trailing edge for edge scattering to be unimportant. Brooks and Hodgson (1981) show that the functions A and B given by

$$A(\beta) = e^{-\varsigma_1|\beta|}, \qquad B(\beta) = e^{-\varsigma_2|\beta|} \tag{3.9}$$

provide a good fit to their experimental data, where ς_1 and ς_2 are adjustable coefficients. From experiment,

$$\varsigma_1 = 0.11, \quad \varsigma_2 = 0.6 \tag{3.10}$$

Substituting Eqs. (3.9) into Eqs. (3.7) and (3.8), one obtains the Brook version of Corcos's spectrum, of the form

$$S_{qq}(\mathbf{k}, \omega_0) = S_0(\omega_0) S_1(k_s) S_2(k_t) \tag{3.11}$$

where

$$S_1(k_s) = \frac{l_1}{\pi}\left[\frac{1}{1 + l_1^2(\omega_0 / U_c - k_s)^2}\right] \tag{3.12}$$

$$S_2(k_t) = \frac{l_2}{\pi}\left[\frac{1}{1 + l_2^2 k_t^2}\right] \tag{3.13}$$

The integral scales l_1 and l_2 in the streamwise and spanwise directions are defined by (Brooks and Hodgson,1981)

$$l_1 = \frac{\int_0^\infty \xi_1 A(\omega_0 \xi_1 / U_c) d\xi_1}{\int_0^\infty A(\omega_0 \xi_1 / U_c) d\xi_1}, \qquad l_2 = \frac{\int_0^\infty \xi_2 B(\omega_0 \xi_2 / U_c) d\xi_2}{\int_0^\infty B(\omega_0 \xi_2 / U_c) d\xi_2} \tag{3.14), (3.15}$$

If the convection speed U_c is assumed to be constant, substituting Eq.(3.9) into Eqs. (3.14) and (3.15) gives

$$l_1 = U_c / \varsigma_1 \omega_0 \quad , \qquad l_2 = U_c / \varsigma_2 \omega_0 \tag{3.16}$$

A point pressure spectrum $S_0(\omega_0)$ based on data collated by Chase (1980) for an infinite flat plate can be found in the book by Howe (1998). In non-dimensional form, it is given by

$$\tilde{S}_0(\tilde{\omega}_0) = \frac{6.1409\times10^{-6}\tilde{\omega}_0^2}{(\tilde{\omega}_0^2 + 0.0144)^{1.5}} \tag{3.17}$$

where $\tilde{S}_0(\tilde{\omega}_0) = S_0(\omega_0)(U_0/\delta^*)/(0.5\rho_0 U_0^2)^2$, $\tilde{\omega}_0$ is the non-dimensional frequency defined by $\tilde{\omega}_0 = \omega_0\delta^*/U_0$ (Strouhal number with respect to δ^*), and δ^* is the displacement thickness of the turbulent boundary layer.

An alternative expression (presented by Amiet, 1976) for the surface pressure spectrum can be obtained by curve fitting the data of Willmarth and Roos (1965) for a flat plate. The result is

$$\tilde{S}_0(\tilde{\omega}_0) = \frac{2\times10^{-5}}{(1+\tilde{\omega}_0 + 0.217\tilde{\omega}_0^0 + 0.00562\tilde{\omega}_0^4)}, \qquad 0.1 < \tilde{\omega}_0 < 20 \tag{3.18}$$

3.3 Turbulence Wall-pressure Spectrum on a Realistic Airfoil

Figure 3.4 shows schematically boundary layer turbulence over one side of an airfoil. Due to the curvature of the airfoil surface and the non-zero angle of attack, the features

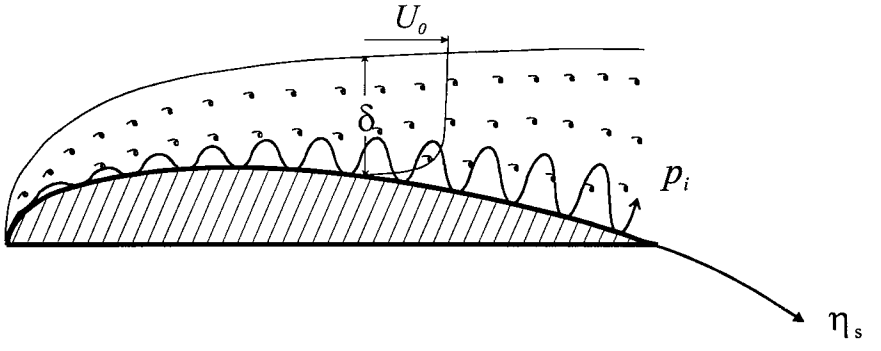

Figure 3.4. Boundary layer turbulence over an airfoil

of the turbulence over the airfoil differ from those over a flat plate in three important respects: (1) boundary layer thickness varies along the streamwise direction; (2) local

incoming velocity U_0 is non-uniform due to potential flow effects; (3) there is a pressure gradient in the streamwise direction within the boundary layer. We assume here that the boundary layer thickness, the incoming velocity and the pressure gradient change very little over a small facet of the airfoil surface so that the Corcos pressure spectrum remains locally valid. We further assume that an airfoil with the same local inflow velocity $U_0(\mathbf{y})$, and boundary layer thickness $\delta(\mathbf{y})$ (as shown in Fig. 3.4) develops the same pressure spectrum as a flat plate under the same conditions. Corcos' model of pressure spectrum will therefore be extended to a realistic airfoil by applying it locally to a small region on the airfoil surface, which is small compared with an acoustic and hydrodynamic wavelength.

From Eq.(3.2), a single time-harmonic component of the incident surface pressure field can be written as

$$p_i(\mathbf{y},\tau) = \overline{p}_i(\mathbf{y},\omega_0)e^{-i\omega_0\tau} \tag{3.19}$$

where $\overline{p}_i(\mathbf{y},\omega_0) = \hat{p}_i(\mathbf{k},\omega_0)e^{i(k_s\eta_s+k_t\eta_t)}$. However, as pointed out by Amiet (1978), use of this expression to represent the boundary layer pressure suggests that the pressure field appears suddenly at the airfoil leading edge, which is non-physical. A better model would be one in which the pressure gradually increased from zero at the leading edge, to reach its maximum value at the trailing edge, and which was identically zero further downstream. Accordingly, Amiet (1978) introduces the exponential decay function f_p of Eq. (3.20), which multiplies the right hand side of Eq. (3.19) to give the desired behaviour,

$$f_p(\mathbf{y},\mathbf{k},\omega_0) = e^{-\varepsilon|k_s\eta_s|} \tag{3.20}$$

where ε is a decay factor, which Amiet chooses arbitrarily. Here, we choose another function f_p in a manner that is consistent with the surface pressure spectra predictions made locally on the airfoil surface, which has the desired behaviour indicated above. Equations (3.17) and (3.18) suggest that the wall pressure spectrum is a function of position $\mathbf{y}$ on the blade surface due to boundary layer growth. We therefore introduce the following position-dependent function for the wall pressure spectrum, defined by

$$f_p(\mathbf{y},\mathbf{k},\omega_0)=\sqrt{\frac{S_{qq}(\mathbf{y},\mathbf{k},\omega_0)}{S_{qq}(\mathbf{y}_0,\mathbf{k},\omega_0)}} \tag{3.21}$$

where $\mathbf{y}_0$ is an arbitrary reference point which we shall take at the trailing edge. A single spectral component of the incident surface pressure field of Eq.(3.19) can therefore be written as

$$p_i(\mathbf{y},\tau)=f_p(\mathbf{y},\mathbf{k},\omega_0)\overline{p}_i(\mathbf{y}_0,\omega_0)e^{-i\omega_0\tau}=f_p(\mathbf{y},\mathbf{k},\omega_0)\hat{p}_i(\mathbf{k},\omega_0)e^{i(k_s\eta_s+k_t\eta_t-\omega_0\tau)} \tag{3.22}$$

where we denote $\hat{p}_i(\mathbf{y}_0,\mathbf{k},\omega_0)=\hat{p}_i(\mathbf{k},\omega_0)$, and the pressure spectrum $S_{qq}(k_s,k_t,\omega_0)$ in Eq. (3.11) will be referred to as the pressure spectrum at the reference point $\mathbf{y}_0$, which is taken at the trailing edge $\mathbf{y}_0=(0,0)$.

Strictly speaking, the Fourier amplitude, $\hat{p}_i(\mathbf{k},\omega_0)$, cannot be a function of position $\mathbf{y}$ since $p_i(\mathbf{y},\tau)$ and $\hat{p}_i(\mathbf{k},\omega_0)$ are equivalent Fourier transform representations. However, all the surface pressure spectra obtained up to now are functions of the displacement thickness δ^* which depends on position $\mathbf{y}$. Thus, although Eq. (3.22) may not be mathematically rigorous, it provides a useful engineering approximation.

Equations (3.17) and (3.18) were derived using data for a flat plate at zero angle of incidence. They may therefore be inaccurate for an actual airfoil at non-zero angle of attack. By curve fitting the experimental data of both Yu & Joshi (1979) and Brooks & Hodgson (1980) measured on an airfoil, Chou and George (1984) present an empirical expression for $\widetilde{S}_0(\widetilde{\omega}_0)$ covering two frequency ranges. For $\widetilde{\omega}_0<0.06$,

$$\widetilde{S}_0(\widetilde{\omega}_0)=\frac{1.732\times10^{-3}\widetilde{\omega}_0}{(1-5.489\widetilde{\omega}_0+36.74\widetilde{\omega}_0^2+0.1505\widetilde{\omega}_0^5)} \tag{3.23}$$

and for $0.06\le\widetilde{\omega}_0\le20$

$$\widetilde{S}_0(\widetilde{\omega}_0) = \frac{1.4216\times10^{-3}\,\widetilde{\omega}_0}{(0.3261+4.1837\widetilde{\omega}_0+22.818\widetilde{\omega}_0^2+0.0013\widetilde{\omega}_0^3+0.0028\widetilde{\omega}_0^5)} \tag{3.24}$$

Figure 3.5 is a plot of $\widetilde{S}_0(\widetilde{\omega}_0)$ versus $\widetilde{\omega}_0$ for a flat plate (Eqs. (3.17) and (3.18)) and for a NACA 0012 airfoil (Eqs. (3.23) and (3.24)). Note that for $\widetilde{\omega}_0 > 0.1$, the airfoil results are typically 10dB higher in level than those for a zero pressure gradient fully developed turbulence boundary layer over a flat plate, and more than 15dB at $\widetilde{\omega}_0$ below 0.1. This difference is caused by the change of boundary layer thickness due to the effect of airfoil geometry. The frequency of the spectral peak is at about $\widetilde{\omega}_0 = 0.1$. Figure 3.6 is a plot of Corcos dimensionless wavenumber spectrum, $S_1(k_s)S_2(k_t)/\delta^{*2}$, versus dimensionless streamwise wavenumber $k_s U_c/\omega_0$ and dimensionless spanwise wavenumber $k_t c_0/\omega_0$, at an airfoil trailing edge of chord $c = 0.252$ m, Mach number $M_0 = 0.4$, non-dimensional frequency $\widetilde{\omega}_0 = 0.2$ and a convective velocity coefficient $c_u = 0.65$. Consistent with Fig. 2.1, the pressure spectrum peaks at the convective wavenumber of $k_s = \omega_0/U_c$.

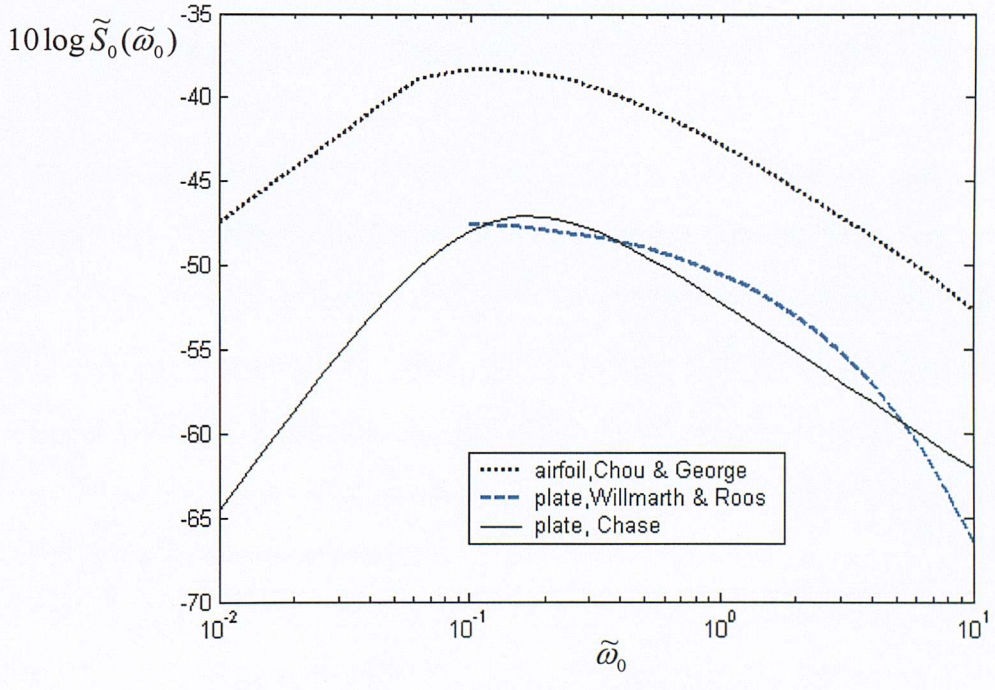

Figure 3.5. Comparison of wall pressure frequency spectra

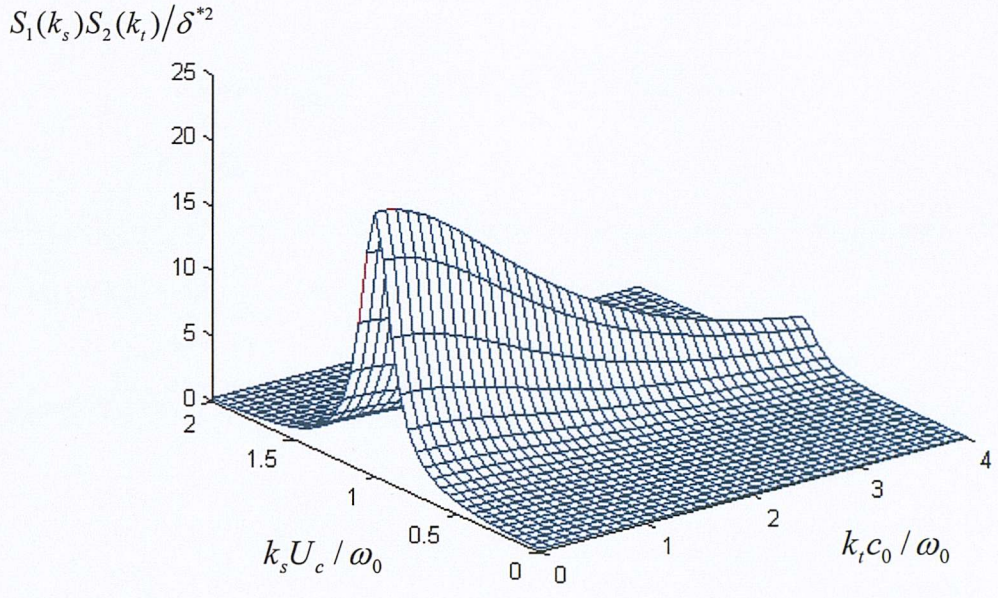

Figure 3.6. Corcos dimensionless wavenumber spectrum, $S_1(k_s)S_2(k_t)/\delta^{*2}$ **, from Eqs.(3.12) and (3.13), at an airfoil trailing edge of chord** $c = 0.252$ **m,** $M_0 = 0.4$**,** $\tilde{\omega}_0 = 0.2$**,** $c_u = 0.65$

3.4 Frozen Spectrum of Turbulence Wall Pressure

A substantial simplification of the boundary layer turbulence description may be obtained by making the assumption of a frozen pressure spectrum. Here, turbulence is assumed to be frozen and convected as a frozen pattern at the convection velocity U_c. In a coordinate system $\eta_s' = \eta_s - U_c\tau$, which moves with the convective velocity of the flow, the surface pressure can be written as $p_i(y') = p_i(\eta_s', \eta_t)$. In the airfoil-fixed coordinate system, the wall pressure $p_i(\mathbf{y}, \tau)$ for frozen turbulence, written in terms of its wavenumber components, is

$$p_i(\mathbf{y}, \tau) = \int_{-\infty}^{\infty}\int_{-\infty}^{\infty} \hat{p}_i(\mathbf{k}) e^{i[k_s(\eta_s - U_c\tau) + k_t\eta_t]} dk_s dk_t \tag{3.25}$$

The Fourier components $\hat{p}_i(\mathbf{k})$ can be determined from $p_i(\mathbf{y}')$ by the inverse relation

$$\hat{p}_i(\mathbf{k}) = \frac{1}{(2\pi)^2} \int_{-R_\infty}^{R_\infty} \int_{-R_\infty}^{R_\infty} p_i(\mathbf{y}') e^{-i(k_s \eta_s' + k_t \eta_t)} d\eta_s' d\eta_t \tag{3.26}$$

where R_∞ is a large but finite distance to ensure that the integration is convergent if $p_i(\mathbf{y}')$ does not go to zero as $\mathbf{y}'$ goes to infinity.

For spatially homogeneous turbulence, it can be shown that (Amiet, 1975)

$$E[\hat{p}_i^*(k_s, k_t)\hat{p}_i(k_s, k_t')] = \frac{R_\infty}{\pi} \delta(k_t' - k_t)\hat{S}_{qq}(k_s, k_t) \tag{3.27}$$

which is equivalent to assuming uncorrelated wavenumber components. The frozen spectrum $\hat{S}_{qq}(k_s, k_t)$ is related to the non-frozen spectrum of Eq.(3.11) by

$$\hat{S}_{qq}(k_s, k_t) = \int_{-\infty}^{\infty} S_{qq}(k_s, k_t, \omega_0) d\omega_0 \tag{3.28}$$

From Eq. (3.12), one has

$$\int_{-\infty}^{\infty} S_1(k_s) dk_s = 1 \tag{3.29}$$

For frozen turbulence, $l_1 \to \infty$, which in Eq.(3.12), leads to $S_1(k_s) \to \infty$ as $k_s \to \omega_0 / U_c$. These properties suggest that for frozen turbulence $S_1(k_s)$ can be approximated by a delta function

$$S_1(k_s) \to \delta(k_s - \omega_0 / U_c), \qquad \text{as } l_1 \to \infty \tag{3.30}$$

Substituting Eqs. (3.11) and (3.30) into Eq. (3.28), the frozen wall pressure spectrum may be written as

$$\hat{S}_{qq}(k_s, k_t) = U_c S_0(k_s U_c) S_2(k_t) \tag{3.31}$$

A similar result has been obtained by Amiet (1975) by following similar reasoning.

3.5 Calculation of Boundary Layer Thickness

Equations (3.17), (3.18), (3.23) and (3.24) suggest that the wall pressure spectrum may be characterized by the boundary layer thickness. For a flat plate, the boundary layer displacement thickness, δ^*, for fully developed turbulence can be approximated by (Eckert and Drake J_R., 1959)

$$\delta^* / \eta_e \approx 0.047 R_e^{-1/5} \tag{3.32}$$

where R_e is the Reynolds number based on the arc length distance, η_e, from the leading edge.

Brooks, Pope and Marcolini (1989) have measured the boundary layer thickness for a NACA0012 airfoil section with chords ranging between 3.54cm to 30.48cm, with a range of Mach numbers between 0.115 to 0.213, and an angle of attack between 0° to 20°. Based on this data, the following empirical expressions for the untripped (natural transition) boundary layers were obtained for the boundary layer displacement thickness δ^* versus distance η_e at zero angle of attack

$$\delta_0^* / \eta_e = 10^{[3.0187 - 1.5397 \log R_e + 0.1059 (\log R_e)^2]} \tag{3.33}$$

The effect of attack angle α on the boundary layer turbulence for the pressure and suction sides, compared with that at $\alpha = 0$, was found to vary as

$$\delta_p^*/\delta_0^* = 10^{[-0.0432\alpha+0.00113\alpha^2]} \tag{3.34}$$

on the pressure side, and by

$$\frac{\delta_s^*}{\delta_0^*} = \begin{cases} 10^{0.0679\alpha} & 0° \le \alpha \le 7.5° \\ 0.0162(10^{0.3066\alpha}) & 7.5° < \alpha \le 12.5° \\ 52.42(10^{0.0258\alpha}) & 12.5° < \alpha \le 25° \end{cases} \tag{3.35}$$

on the suction side, where the zero subscripts indicate zero angle of attack, and the angle of attack α is measured in degrees. The subscript "p" expresses the boundary thickness for the pressure side while "s" is for the suction side. Figure 3.7 shows a comparison between the boundary layer displacement thickness expression of Eq.(3.32) and the Brooks expression of Eq.(3.33) for the case of zero angle of attack. It can be seen from Fig.3.7 that the airfoil produces a larger boundary layer displacement thickness compared with that on a flat plate. However, the difference reduces as Reynolds number increases.

Figure 3.8 shows the ratio of the boundary displacement thickness, δ^*/δ_0^*, versus angle of attack. The boundary layer displacement thickness, and hence the pressure spectrum on the airfoil suction side, varies significantly with angle of attack. Smaller variation is observed on the pressure side. In accordance with Eqs.(3.11), (3.23) and (3.24), therefore, most of the energy is anticipated to originate from the suction side.

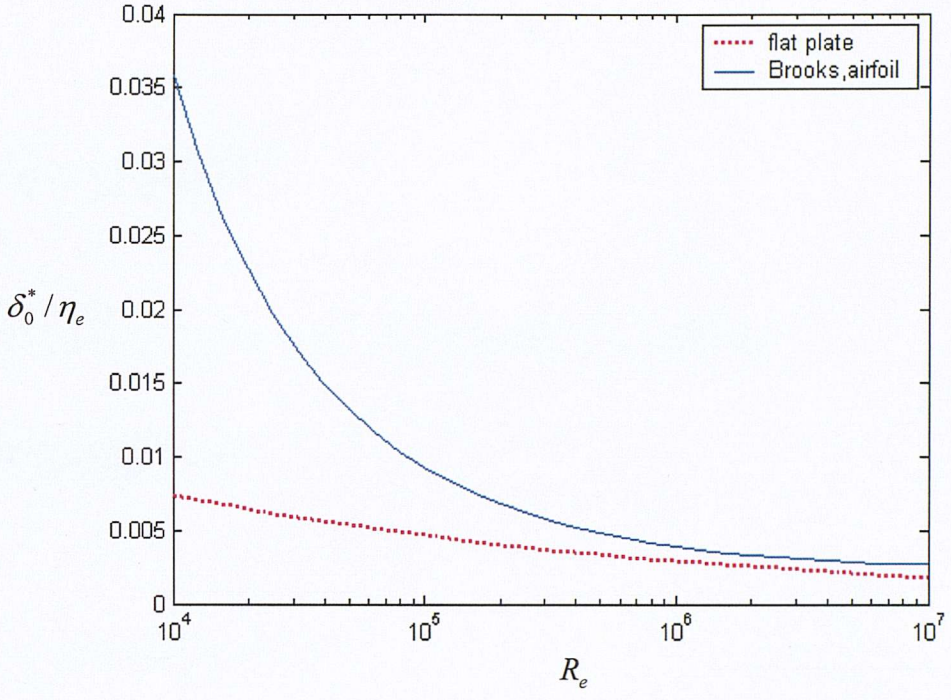

Figure 3.7. Comparison of boundary layer displacement thickness between the flat plate expression of Eq. (3.32) and the Brooks' expression of Eq. (3.33) for the case of zero angle of attack

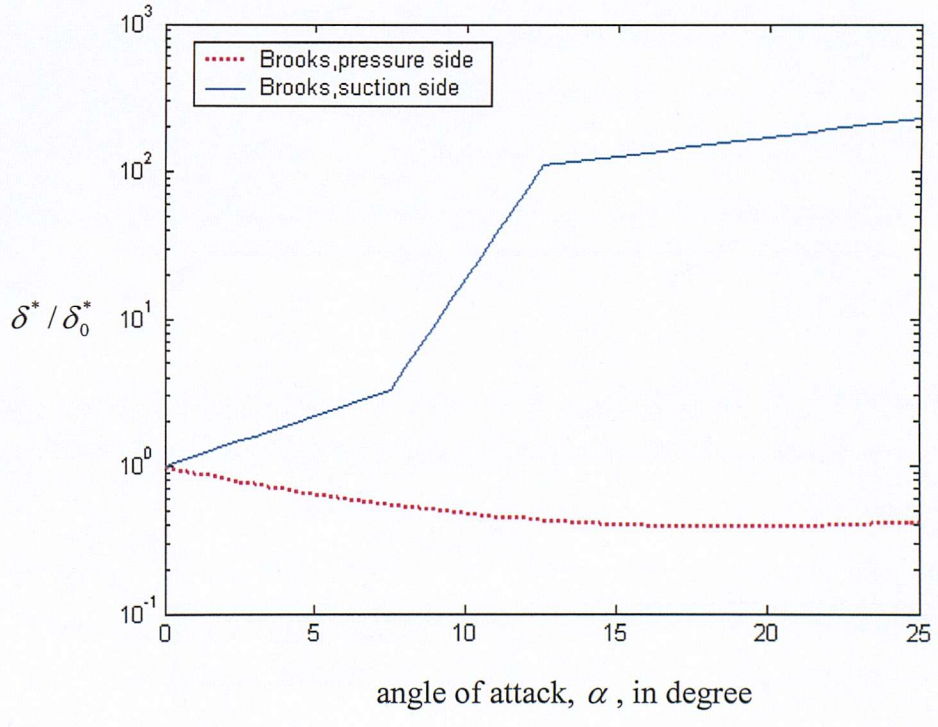

Figure 3.8. Ratio of boundary layer displacement thickness versus angle of attack

Chapter IV

Prediction of Airfoil Surface Pressures

4.1 Introduction

In the last Chapter the characteristics of the pressure field p_i incident upon the trailing edge were discussed. In this Chapter we are mainly concerned with predicting the scattered pressure p_s from p_i. The calculation of p_s for airfoils of arbitrary geometry is, in general, very difficult. All the analytical results obtained so far make the assumption that the fluctuating velocity is small compared with the steady velocity (Goldstein (1976)), primarily because the problem can then be linearized. This assumption implies that $|\mathbf{u}| << U$, where $\mathbf{u}$ is unsteady velocity and U is the mean flow velocity.

The boundary value problem for the scattered pressure p_s is required to satisfy the linear Helmholtz equation, the Kutta condition, and the condition of no-flow on the airfoil surface. At high-reduced frequency (high ratio of chord to hydrodynamic wavelength) the interaction between the leading edge and the trailing edge is weak so that the leading edge contribution to self-noise may be neglected. For the purpose of calculating the surface pressure induced by the convecting boundary layer pressure p_i, the airfoil is therefore assumed to be semi-infinite with a trailing edge but no leading edge. Roger (2002) has demonstrated that this is a good assumption at reduced

frequencies greater than about unity. Under this assumption, it is possible to derive a closed-form analytic solution for the surface pressure transfer function, which relates the total surface pressure $p_t = p_i + p_s$ to the boundary layer surface pressure p_i incident upon the trailing edge.

In Section 4.2, a closed-form solution will be derived for the surface pressure on a semi-infinite flat plate airfoil due to a single frequency-wavenumber component of boundary layer pressure incident upon the trailing edge. In Section 4.3 the flat plate solution will then be applied to a realistic airfoil under the assumption of high-reduced frequency and sharp trailing edge. The result will finally be generalised to boundary layer turbulence for an airfoil with arbitrary angle of attack.

4.2 Surface Pressure Predictions from Thin Airfoil Theory

In Section 3.2, we defined an incident pressure field $p_i = \overline{p}_i e^{-i\omega_0 \tau}$ over an infinite flat plate without trailing edge. In this Section, we are mainly concerned with the scattered pressure $p_s = \overline{p}_s e^{-i\omega_0 \tau}$ due to the incident pressure p_i impinging upon the trailing edge. As shown schematically in Fig. 4.1, a harmonic incident pressure component,

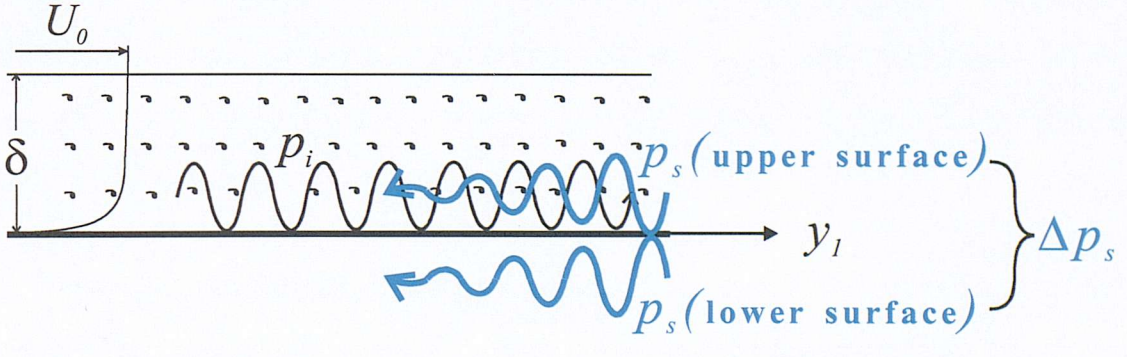

Figure 4.1. Boundary turbulence over a semi-infinite flat plate with trailing edge

$\overline{p}_i(\mathbf{y}, \omega_0) = \hat{p}_i(\mathbf{k}, \omega_0) e^{i(k_1 y_1 + k_2 y_2)}$, is taken as the input, and a scattered pressure $\overline{p}_s$ is

developed at the trailing edge on the upper surface and the lower surface with half value of the pressure jump $\Delta\overline{p}_s = \overline{p}_s(\text{upper surface}) - \overline{p}_s(\text{lower surface})$ (Howe, 1999; Amiet, 1976a). A solution for this scattered pressure jump $\Delta p_s = \Delta\overline{p}_s e^{-i\omega_0\tau}$ across the flat plate is sought here. The analytic solution derived by Amiet (1976b) for the unsteady surface pressure jump Δp_s over a flat-plate airfoil in a two-dimensional compressible flow will be extended to the general case of a skewed gust (i.e. $k_2 \neq 0$). This analytical solution may be expressed in terms of a transfer function H_s relating Δp_s and p_i.

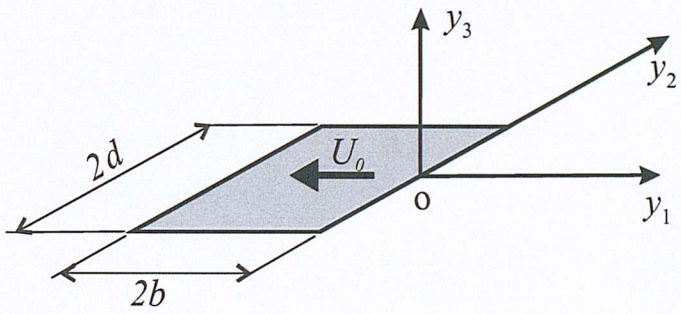

Figure 4.2. Coordinate system for a flat-plate airfoil

Consider a rectangular flat plate of chord $2b$ and span $2d$, located at $\{-2b \le y_1 \le 0\}$, $\{-d \le y_2 \le d\}$, moving with velocity U_0 in the negative y_1 direction, as shown in Fig. 4.2. We assume that the chord $2b$ and the span $2d$ are large compared to the hydrodynamic wavelength so that the flat plate airfoil may be assumed to be semi-infinite with a trailing edge but no leading edge. Moreover, scattering by the ends of the airfoil is ignored. For a two-dimensional harmonic component of incoming turbulence convecting along the flat plate surface $y_3 = 0$ with velocity U_c and with wavenumber component (k_1, k_2), the fluctuating velocity u_3 normal to the flat plate surface is of the form

$$u_3(\mathbf{y},\tau) = \hat{u}_3 e^{i(k_1 y_1 + k_2 y_2 - \omega_0\tau)} = \overline{u}_3(y_1, y_2, \omega_0) e^{-i\omega_0\tau} \tag{4.0}$$

Note that u_3 is the virtual velocity that would be produced by the turbulent boundary layer if the airfoil surface were absent. It is related to the velocity potential $\Phi_I = \phi_I e^{-i\omega_0\tau}$ by

$$\frac{\partial \Phi_I}{\partial y_3} = u_3, \qquad \frac{\partial \phi_I}{\partial y_3} = \overline{u}_3 \tag{4.1a), (4.1b}$$

We now consider the total velocity potential Φ_t that results following the interaction of Φ_I with the trailing edge and the field induced by the presence of the rigid airfoil surface. The velocity potential Φ_t must satisfy the wave equation

$$\left(\nabla^2 - \frac{1}{c_0^2}\frac{D_0^2}{D\tau^2}\right)\Phi_t(\mathbf{y},\tau) = 0 \tag{4.2a}$$

where $D_0/D\tau = \partial/\partial\tau + U_0\,\partial/\partial y_1$, together with the boundary condition of zero-normal velocity on the flat plate surface

$$\frac{\partial}{\partial y_3}\Phi_t(y_1, y_2, 0, \tau) = 0 \quad , \qquad -2b < y_1 \le 0 \tag{4.2b}$$

The total velocity potential Φ_t must also satisfy the Kutta condition, which specifies zero pressure jump at the trailing edge and downstream of the trailing edge in the wake

$$D_0\Phi_t/D\tau = 0 \quad , \qquad y_1 \ge 0,\ y_3 = 0 \tag{4.2c}$$

The velocity potential Φ_t may be decomposed into the sum of the incident field Φ_I and the contribution Φ due to trailing edge interaction and the effect of the airfoil surface,

$$\Phi_t = \Phi_I + \Phi \tag{4.3}$$

Substituting Eq.(4.3) into Eq.(4.2) gives the following equation for Φ

$$\left(\nabla^2 - \frac{1}{c_0^2}\frac{D_0^2}{D\tau^2}\right)\Phi(\mathbf{y},\tau) = 0 \tag{4.4a}$$

$$\frac{\partial}{\partial y_3}\Phi(y_1,y_2,0,\tau) = -u_3(y_1,y_2,0,\tau) \quad , \qquad -2b < y_1 \le 0 \tag{4.4b}$$

$$D_0\Phi/D\tau = -D_0\Phi_I/D\tau \quad , \qquad y_1 \ge 0 \tag{4.4c}$$

Again a harmonic time dependence is assumed of the form $\Phi(\mathbf{y},\tau) = \phi(\mathbf{y},\omega_0)e^{-i\omega_0\tau}$. Introducing a coordinate transformation identical to Eqs. (2.8)

$$\begin{cases} Y_1 = y_1 \\ Y_2 = \beta_0 y_2 \\ Y_3 = \beta_0 y_3 \\ T = \omega_0\tau + M_0\mu_0 y_1 \end{cases} \tag{4.5}$$

where $\beta_0^2 = 1 - M_0^2$, $M_0 = U_0/c_0$, Eq.(4.4a) becomes

$$\left(\frac{\partial^2}{\partial Y_1^2} + \frac{\partial^2}{\partial Y_2^2} + \frac{\partial^2}{\partial Y_3^2} + \mu_0^2\right)\psi(\mathbf{Y}) = 0 \tag{4.6a}$$

where $\mathbf{Y} = (Y_1,Y_2,Y_3)$, $\psi(\mathbf{Y},\omega_0) = \phi(\mathbf{Y},\omega_0)e^{iM_0\mu_0 Y_1}$, $\mu_0 = M_0\kappa_1/\beta_0^2 = \kappa_0/\beta_0^2$, $\kappa_0 = \omega_0/c_0$ and $\kappa_1 = \omega_0/U_0$. Correspondingly, the boundary conditions of (4.4b) and (4.4c) become

$$\frac{\partial}{\partial Y_3}\psi(Y_1,Y_2,0,\omega_0) = -\frac{1}{\beta_0}\,\bar{u}_3(Y_1,Y_2,\omega_0)e^{iM_0\mu_0 Y_1}, \qquad -2b < Y_1 \le 0 \tag{4.6b}$$

and

$$(-i\kappa_1/\beta_0 + \partial/\partial Y_1)\psi(Y_1,Y_2,0,\omega_0) = -(-i\kappa_1/\beta_0 + \partial/\partial Y_1)\psi_I(Y_1,Y_2,0,\omega_0) \quad , \qquad Y_1 \ge 0 \tag{4.6c}$$

where $\psi_I(\mathbf{Y},\omega_0) = \phi_I(\mathbf{Y},\omega_0)e^{iM_0\mu_0 Y_1}$. For a harmonic velocity component incident upon the trailing edge of the form,

$$\overline{u}_3(y_1,y_2,\omega_0) = \hat{u}_3(\mathbf{k},\omega_0)e^{i(k_1y_1+k_2y_2)} \tag{4.7}$$

with velocity potential,

$$\psi_I(\mathbf{Y},\omega_0) = \varphi_I(Y_1,Y_3,\omega_0)e^{ik_2Y_2/\beta_0} \tag{4.8}$$

a solution is sought by separation of variables in the form of

$$\psi(\mathbf{Y},\omega_0) = \varphi(Y_1,Y_3,\omega_0)e^{ik_2Y_2/\beta_0} \tag{4.9}$$

Substituting Eq.(4.9) into Eq. (4.6), reduces Eqs. (4.6) to the boundary value problem formulated by Amiet (1976b) for a two-dimensional airfoil, but now extended to non-zero k_2 - values. The velocity potential φ is now required to satisfy

$$\left(\frac{\partial^2}{\partial Y_1^2}+\frac{\partial^2}{\partial Y_3^2}+K^2\right)\varphi(Y_1,Y_3,\omega_0) = 0 \tag{4.10a}$$

where $K = \sqrt{\mu_0^2-(k_2/\beta_0)^2}$, with boundary conditions

$$\frac{\partial}{\partial Y_3}\varphi(Y_1,0,\omega_0) = -\frac{1}{\beta_0}\hat{u}_3 e^{ik_1Y_1}e^{iM_0\mu_0Y_1}, \qquad -2b < Y_1 \le 0 \tag{4.10b}$$

$$(-i\kappa_1/\beta_0+\partial/\partial Y_1)\varphi(Y_1,0,\omega_0) = -(-i\kappa_1/\beta_0+\partial/\partial Y_1)\varphi_I(Y_1,0,\omega_0), \qquad Y_1 \ge 0 \tag{4.10c}$$

Following, for example, Amiet (1976b), Eqs. (4.10) are solved with the aid of the Schwartzchild solution. In order to use this solution, the velocity potential φ is further

decomposed into two parts: One is the velocity potential $\varphi^{(0)}$ reflected by an infinite plate boundary with no trailing edge present, which satisfies

$$\left(\frac{\partial^2}{\partial Y_1^2}+\frac{\partial^2}{\partial Y_3^2}+K^2\right)\varphi^{(0)}(Y_1,Y_3,\omega_0)=0 \tag{4.11a}$$

$$\frac{\partial}{\partial Y_3}\varphi^{(0)}(Y_1,0,\omega_0)=-\frac{1}{\beta_0}\hat{u}_3 e^{ik_1Y_1}e^{iM_0\mu_0Y_1}, \qquad -\infty<Y_1\le\infty \tag{4.11b}$$

The other is the velocity potential $\varphi^{(1)}$ that accounts for the interaction by the trailing edge, which satisfies,

$$\left(\frac{\partial^2}{\partial Y_1^2}+\frac{\partial^2}{\partial Y_3^2}+K^2\right)\varphi^{(1)}(Y_1,Y_3,\omega_0)=0 \tag{4.12a}$$

$$\frac{\partial}{\partial Y_3}\varphi^{(1)}(Y_1,0,\omega_0)=0, \qquad Y_1<0 \tag{4.12b}$$

$$(-i\kappa_1/\beta_0+\partial/\partial Y_1)\varphi^{(1)}(Y_1,0,\omega_0)=-(-i\kappa_1/\beta_0+\partial/\partial Y_1)\left[\varphi_I(Y_1,0,\omega_0)+\varphi^{(0)}(Y_1,0,\omega_0)\right], \qquad Y_1\ge 0 \tag{4.12c}$$

For an airfoil with large chord $2b$ compared to hydrodynamic wavelength, the contribution from the leading-edge is negligible, the sum of these velocity potentials,

$$\varphi=\varphi^{(0)}+\varphi^{(1)} \tag{4.13}$$

provides a good approximation to the solution of equations (4.10).

The solution of equations (4.11) for $\phi^{(0)}$ can be found, from a superposition of two-dimensional sources, of form (Amiet, 1976b)

$$\phi^{(0)}(y_1, y_2, y_3, \omega_0) = \frac{i}{2\beta_0} e^{ik_2 y_2} \int_{-\infty}^{\infty} e^{-i\mu_0 M_0 (y_1 - \xi)} H_0^{(1)} \{K\sqrt{(y_1 - \xi)^2 + \beta^2 y_3^2}\} \hat{u}_3 e^{ik_1 \xi} d\xi \qquad (4.14)$$

where $H_0^{(1)}$ is the zero-order Hankel function of the first kind (note that Amiet use $H_0^{(2)}$ due to the assumption of the time dependence $e^{i\omega_0 \tau}$, while we use $e^{-i\omega_0 \tau}$). Equation (4.14) is the zero-order velocity potential expressed in the coordinate system **y**. Note that we have made the variable substitution $\phi^{(0)} = \varphi^{(0)} e^{-iM_0 \mu_0 y_1} e^{ik_2 y_2}$. Evaluating the integral in equation (4.14) on the plate surface, $y_3 = 0$, gives

$$\phi^{(0)}(y_1, y_2, 0, \omega_0) = A_\phi \hat{u}_3 e^{i(k_1 y_1 + k_2 y_2)} \qquad (4.15)$$

where $A_\phi = 1/\left(\beta_0 \sqrt{(\mu_0 M_0 + k_1)^2 - K^2}\right)$. Since the pressure is related to the velocity potential by

$$\overline{p}(\mathbf{y}, \omega_0) e^{-i\omega_0 \tau} = -\rho_0 (D_0 \Phi / D\tau) \qquad (4.16)$$

the surface pressure corresponding to the zero-order velocity potential $\phi^{(0)}$ of Eq.(4.15) is

$$\overline{p}^{(0)}(y_1, y_2, 0, \omega_0) = i\rho_0 U_0 (\kappa_1 - k_1) \phi^{(0)}(y_1, y_2, 0, \omega_0) \qquad (4.17)$$

Similarly, the surface pressure related to the 'virtual' velocity potential ϕ_I of Eq.(4.1b) is

$$\overline{p}_I(y_1, y_2, 0, \omega_0) = -\rho_0 (-i\omega_0 + U_0 \frac{\partial}{\partial y_1}) \phi_I(y_1, y_2, 0, \omega_0) \qquad (4.18)$$

It can be seen that the surface pressure

$$\overline{p}_i = \overline{p}_I + \overline{p}^{(0)} \qquad (4.19)$$

satisfies the condition of no-flow through the airfoil surface but does not satisfy the Kutta condition of Eq. (4.12). The surface pressure of Eq. (4.19) is the incident surface pressure p_i discussed in Chapter II. To satisfy both the no-flow, and the Kutta conditions, a trailing-edge correction is needed that satisfies equations (4.12). Substituting the zero-order solution (4.15) and φ_I into Eqn (4.12c), and making use of the Schwartschild solution (see Schwartschild, 1902; Landahl, 1961), the solution of Eqs.(4.12) in terms of pressure is given by Amiet (1976b, Eqs. (7a) and (7b)) as

$$\Delta\overline{p}_s(y_1,y_2,0,\omega_0) = -\frac{1}{\pi}\int_0^{\infty}\left(\frac{-y_1}{\xi}\right)^{1/2} e^{i(K+\mu_0 M_0)(-y_1+\xi)}\,\overline{p}_i(\xi,y_2,0,\omega_0)\frac{1}{-y_1+\xi}\,d\xi \tag{4.20}$$

Note that Amiet uses $e^{-i(K+\mu_0 M_0)(-y_1+\xi)}$ due to the assumption of the time dependence $e^{i\omega_0\tau}$, while we use $e^{-i\omega_0\tau}$. Substituting Eqs. (4.17) and (4.18) into Eq. (4.20) and carrying out the ξ-integration, one obtains the trailing-edge corrected pressure jump as

$$\Delta\overline{p}_s(y_1,y_2,0,\omega_0) = H_s(\mathbf{y},\mathbf{k},\omega_0)\,\overline{p}_i(y_1,y_2,0,\omega_0) \tag{4.21}$$

where H_s is the transfer function that relates the scattered pressure jump $\Delta\overline{p}_s$ to the pressure $\overline{p}_i$ incident upon the trailing edge

$$H_s(\mathbf{y},\mathbf{k},\omega_0) = erf\left(\sqrt{i(K+\mu_0 M_0+k_1)y_1}\right)-1 \tag{4.22}$$

Note that Eq.(4.22) is valid for all k_2- values. For $k_2^2/\beta_0^2 \le \mu_0^2$, which corresponds to wave components whose phase velocity along the trailing edge exceeds the speed of sound, the transfer function of Eq.(4.22) becomes

$$H_s(\mathbf{y},\mathbf{k},\omega_0) = erf\left(\sqrt{i(K+\mu_0 M_0 + k_1)y_1}\right) - 1$$

$$= (1-i)E\left[-(K+\mu_0 M_0 + k_1)y_1\right] - 1 \quad , \text{ for } k_2^2/\beta_0^2 \le \mu_0^2 \tag{4.23}$$

$$= (1+i)E^*\left[(K+\mu_0 M_0 + k_1)y_1\right] - 1$$

where $E^*(\xi)$ is the complex conjugate of $E(\xi)$, $E(\xi)$ is the Fresnel integral and $erf(\xi)$ is the error function, defined by

$$E(\xi) = \int_0^{\xi} \frac{e^{iu}}{\sqrt{2\pi u}} du, \qquad erf(\xi) = \frac{2}{\sqrt{\pi}} \int_0^{\xi} e^{-u^2} du \tag{4.24a), (4.24b}$$

They are related by $(1-i)E(\xi) = erf(\sqrt{-i\xi})$. The pressure $\overline{p}_i + \Delta\overline{p}_s$ now satisfies both the no-flow and the Kutta condition. When μ_0 and k_1 are set to be negative (note that Amiet use $e^{i\omega\tau}$) and k_2 is equal to zero, equation (4.23) is consistent with the solution formulated by Amiet (1976a). When $M_0 = 0$, equation (4.22) reduces to the solution given by Howe (1999).

Equation (4.22) shows that the transfer function H_s is completely defined by the non-dimensional distance $\kappa_c y_1$, streamwise wavenumber k_1/κ_c, spanwise wavenumber $k_2\beta_0/\kappa_0$, and Mach number M_0. Here $\kappa_c = \omega_0/U_c$ is the streamwise wavenumber related to the convection velocity. Figures (4.3) to (4.5) are plots of H_s against these parameters. For the calculations of following Figs (4.3) to (4.5), the parameters are taken as $M_0 = 0.4373$, $U_c = c_u U_0$, $c_u = 0.65$, $k_1/\kappa_c = 1$, and frequency $f = 500$ Hz.

Figure 4.3 shows the modulus of the transfer function $|H_s|$ versus spanwise wavenumber $k_2\beta_0/\kappa_0$ for the various distances of $\kappa_c y_1 = -0.5, -1.0, -1.5$ from the trailing edge. It can be seen from Fig.4.3 that the main contribution to the scattered pressure jump comes from Fourier components of turbulence which travel with

supersonic phase speed, i.e. $k_2\beta_0/\kappa_0 \le 1$. However the contribution from turbulence component travelling with subsonic phase speed, i.e. $k_2\beta_0/\kappa_0 > 1$, is not negligible.

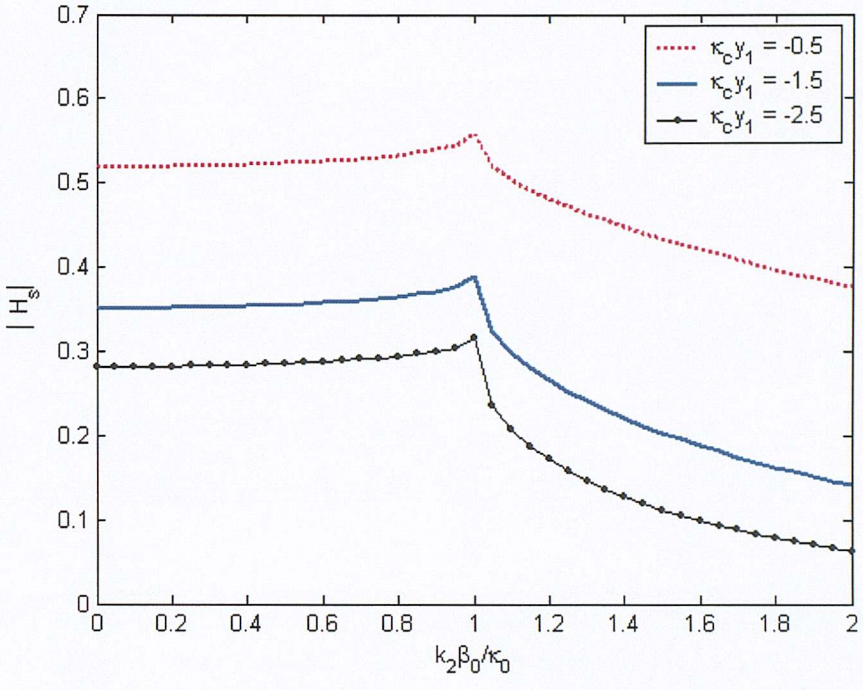

Figure 4.3. Modulus of the scattering transfer function $|H_s|$ versus non-dimensional spanwise wavenumber $k_2\beta_0/\kappa_0$ for various distances $\kappa_c y_1$ from the trailing edge.

Figure 4.4 and 4.5 show, respectively, the modulus and phase angle (in degrees) of the transfer function H_s versus dimensionless distance, $\kappa_c|y_1|$, from the trailing edge for various normalized spanwise wavenumber $k_2\beta_0/\kappa_0 = 0.0, 1.0, 2.0$. Figure 4.4 shows that the modulus of H_s decays rapidly with distance from the trailing edge. This finding suggests that the scattered pressure jump is only significant close to the trailing edge, which agrees with the finding of Brooks and Hodgson (1981). Figure 4.5 suggests that the rate of change of phase in H_s with difference from the trailing edge is more rapid than that of the incident pressure. In addition, the 180° phase angle change of H_s at the trailing edge suggests that the incident pressure is exactly cancelled by the scattered pressure jump in accordance with the Kutta condition.

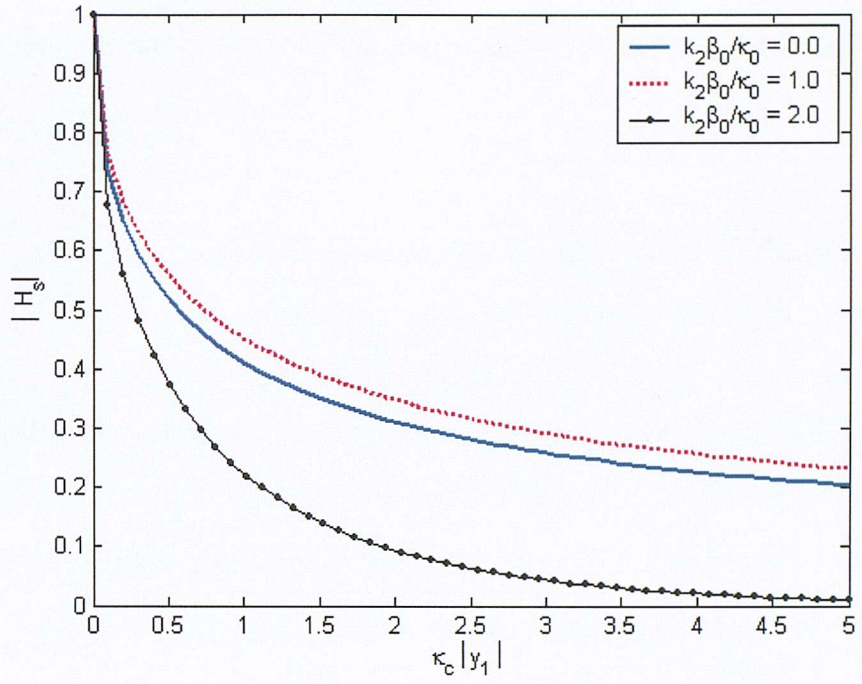

Figure 4.4. Modulus of the transfer function H_s versus dimensionless distance $\kappa_c|y_1|$ for various normalized spanwise wavenumber $k_2\beta_0/\kappa_0$.

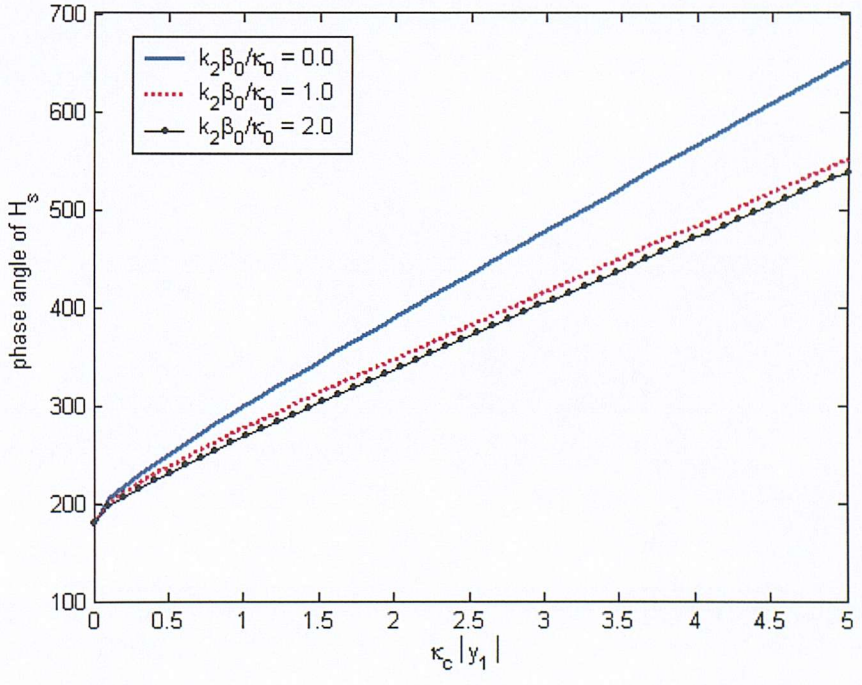

Figure 4.5. Phase angle of the transfer function H_s versus dimensionless distance $\kappa_c|y_1|$ for various normalized spanwise wavenumber $k_2\beta_0/\kappa_0$.

4.3 Application of Thin Airfoil Theory to Realistic Airfoils

In the last Section, a closed-form solution was derived for the scattered pressure jump Δp_s due to a single Fourier component of the incident pressure p_i impinging upon the trailing edge of a flat plate airfoil. In this section, the flat plate theory described above will be adapted in an approximate way to real airfoil geometries. The input quantity here is the incident pressure, $p_i(\mathbf{y},\tau) = f_p(\mathbf{y},\mathbf{k},\omega_0)\overline{p}_i(\mathbf{y},\omega_0)e^{-i\omega_0\tau}$, described by Eq. (3.22). We wish to calculate the total pressure $p_t = p_i + p_s$, where again p_s denotes the scattered pressure due to the incident pressure p_i impinging upon the airfoil trailing edge. The purpose here is to derive a transfer function H_p between p_t and p_i on both sides of the airfoil. The relation between the above quantities is shown schematically in Fig. 4.6. In general, turbulence develops on both the suction side and the pressure side. For simplicity, turbulence on one side of the airfoil is considered here. However, the formulation provided below can be applied to turbulence on both sides of the airfoil and the results then added.

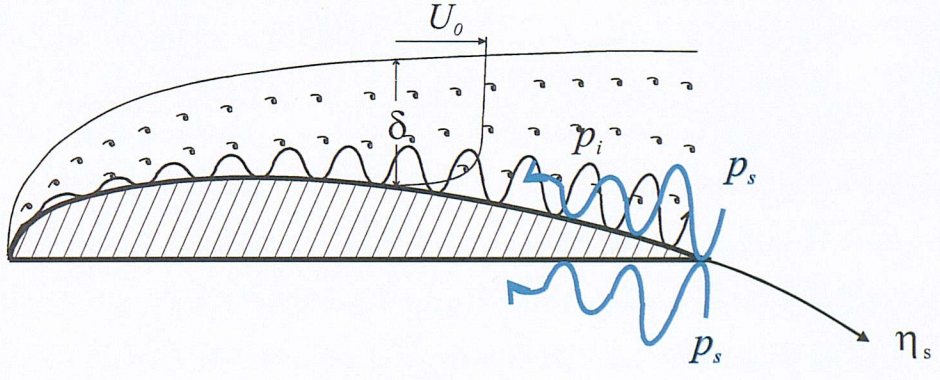

Figure 4.6. Boundary layer turbulence and its related surface pressure over an airfoil

We define a reduced frequency as

$$\sigma_1 = k_s b \tag{4.25}$$

where $b = c/2$ is the airfoil semi-chord, and k_s is the streamwise wavenumber defined in Chapter III. The reduced frequency may be interpreted as a non-dimensional frequency that is proportional to the ratio of semi-chord to hydrodynamic wavelength in the boundary layer. For a frozen gust, $k_s = \kappa_c = \omega_0 / U_c$, where $U_c = c_u U_0$ is the convection velocity and c_u is convective velocity coefficient typically in the range $c_u = 0.65 \sim 0.8$. The product $M\sigma_1 = \kappa_0 b / c_u$ is proportional to the ratio of semi-chord to acoustic wavelength. In this thesis we indicate the reduced frequency by $\sigma_1 = \kappa_c b$.

Equation (4.22) relates to the scattered pressure jump produced over the surface of a flat plate airfoil. For more realistic airfoil geometries, numerical methods, such as the boundary element method, may be used to obtain more accurate solutions. However, the computation time required in the calculation of H_s at each frequency and wavenumber in the broadband problem, which involves a spectrum of wavenumbers and frequencies, is currently excessive. Therefore, we make the assumption of high-reduced frequency $\sigma_1 = \kappa_c b$, which allows the use of the closed form solution of Eq.(4.22). When the reduced frequency σ_1 is high, the hydrodynamic wavelength of turbulence is much smaller than the semi-chord so that the leading edge correction due to the backward scattered pressure jump impinging on the leading edge is comparatively small (Roger, 2002). On the other hand, since the scattered pressure jump is only significant close to the trailing edge (Brooks and Hodgson, 1981; Ffowcs Williams and Hall, 1970), we further assume that no boundary layer separation occurs and that the trailing edge is sufficiently "sharp" for flat plate theory to apply. The effect of the airfoil geometry on the aerodynamic response function H_s is therefore ignored. The airfoil response function in this case can therefore be treated as a flat plate with chord equal to the arc length of the actual airfoil, which differs on the pressure and suction sides. However, the effects of airfoil geometry on sound radiation, taking into account retarded time effects, are included in the formulation by integrating over the actual blade surface.

The scattered pressure described by Eqs. (4.21) and (4.22) refers to pressure jump across the flat plate (Amiet,1976a); Howe,1999). Experimental verification of these results has been obtained by Brooks and Hodgson (1981). Howe (1999) has shown from a low Mach number approximation to the trailing edge problem that each side of the airfoil develops a scattered pressure with half value of the pressure jump. To apply equations (4.21) and (4.22) to a realistic airfoil, the variables y_1, y_2, k_1, k_2 are replaced by η_s, η_t, k_s, k_t defined in Section 3.1 (to be consistent with the notation of the following Chapters, the first argument of p_s is still denoted by $\mathbf{y}$ instead of $\boldsymbol{\eta}$ due to the coordinate transformation $\eta_s = \eta_s(\mathbf{y})$, $\eta_t = \eta_t(\mathbf{y})$). With these variable substitutions and noting the relation of equation (3.19), the scattered pressure $\overline{p}_s$ takes half value of the pressure jump of Eq. (4.21) of the form

$$\overline{p}_s(\mathbf{y},\omega_0) = \begin{cases} \frac{1}{2} H_s(\mathbf{y},\mathbf{k},\omega_0)\, \hat{p}_i(\mathbf{k},\omega_0) e^{i(k_s\eta_s + k_t\eta_t)}, & \mathbf{y} \text{ on turbulence side} \\ -\frac{1}{2} H_s(\mathbf{y},\mathbf{k},\omega_0)\, \hat{p}_i(\mathbf{k},\omega_0) e^{i(k_s\eta_s + k_t\eta_t)}, & \mathbf{y} \text{ not on turbulence side} \end{cases} \tag{4.26}$$

where H_s is now given by

$$H_s(\mathbf{y},\mathbf{k},\omega_0) = erf\left(\sqrt{i(K + \mu_0 M_0 + k_s)\eta_s}\right) - 1 \tag{4.27}$$

where now $K = \sqrt{\mu_0^2 - (k_t/\beta_0)^2}$ and η_s replaces y_1 in Eq.(4.22). Note that the pressure amplitude $\hat{p}_i$ in Eq. (4.26) must be taken as the incident pressure at the trailing edge $\eta_s = 0$, since $\hat{p}_i$ varies along the streamwise direction for the reason given in Section 3.3. Note also that the scattered pressure jump cancels with the incident pressure p_i at the trailing edge owing to the imposition on the solution of the Kutta condition.

In Chapter III, we showed that it was necessary to include the position-dependent function $f_p(\mathbf{y},\mathbf{k},\omega)$ in the definition of the incident pressure p_i according to Eq. (3.22). Multiplying both sides of equations (4.26) by a time factor $e^{-i\omega_0\tau}$, noting that only one

sided turbulence has been considered, and noting that $p_s(\mathbf{y},\tau) = \overline{p}_s(\mathbf{y},\omega_0)e^{-i\omega_0\tau}$, the total pressure p_t distributed over the surface of a real airfoil due to interaction with the trailing edge by a single frequency, single wavenumber, surface pressure component, $p_i(\mathbf{y},\tau) = \overline{p}_i(\mathbf{y},\omega_0)e^{-i\omega_0\tau}$, may be approximated by

$$p_t(\mathbf{y},\tau) = p_i(\mathbf{y},\tau) + p_s(\mathbf{y},\tau) = H_q(\mathbf{y},\mathbf{k},\omega_0)\hat{p}_i(\mathbf{k},\omega_0)e^{i(k_s\eta_s + k_t\eta_t - \omega_0\tau)} \tag{4.28}$$

where H_q is the transfer function between the surface pressure at any point on the airfoil surface $\boldsymbol{\eta} = (\eta_s,\eta_t)$ and the incident pressure at the reference point y_0 along the trailing edge, of the form

$$H_q(\mathbf{y},\mathbf{k},\omega_0) = \begin{cases} f_p(\mathbf{y},\mathbf{k},\omega_0) + \frac{1}{2}H_s(\mathbf{y},\mathbf{k},\omega_0), & \mathbf{y} \text{ is on the turbulence side} \\ -\frac{1}{2}H_s(\mathbf{y},\mathbf{k},\omega_0), & \mathbf{y} \text{ is not on the turbulence side} \end{cases} \tag{4.29}$$

For the general case of a turbulent pressure field incident upon the trailing edge, which involves a continuum of all wavenumber and frequency components, equation (4.28) generalises to

$$p_t(\mathbf{y},\tau) = \int_{-\infty}^{\infty}\int_{-\infty}^{\infty}\int_{-\infty}^{\infty} H_q(\mathbf{y},k_s,k_t,\omega_0)\hat{p}_i(k_s,k_t,\omega_0)e^{i(k_s\eta_s + k_t\eta_t - \omega_0\tau)}dk_s dk_t d\omega_0 \tag{4.30}$$

where $\hat{p}_i(\mathbf{k},\omega_0)$ is given by Eq.(3.3) and is related to the boundary layer turbulence spectrum of Eq. (3.4).

Equation (4.30) gives the Fourier component amplitude of surface pressure $\hat{p}_t(\mathbf{y},\mathbf{k},\omega_0)$ as

$$\hat{p}_t(\mathbf{y},\mathbf{k},\omega_0) = H_q(\mathbf{y},\mathbf{k},\omega_0)\hat{p}_i(\mathbf{k},\omega_0) \tag{4.31}$$

where the argument **y** arises due to the presence of position-dependent function $f_p(\mathbf{y},\mathbf{k},\omega_0)$. If the incident pressure field $\hat{p}_i(\mathbf{k},\omega_0)$ is spatially homogeneous and time-stationary, then so must the pressure field $\hat{p}_t(\mathbf{y},\mathbf{k},\omega_0)$. Analogous to Eq. (3.4), the Fourier components of surface pressure $\hat{p}_t(\mathbf{y},\mathbf{k},\omega_0)$ are related to the spectrum S_{QQ} of total surface pressure by

$$E[\hat{p}_t^*(k_s,k_t,\omega_0)\hat{p}_t(k_s',k_t',\omega_0')] = \delta(k_s'-k_s)\delta(k_t'-k_t)\delta(\omega_0'-\omega_0)S_{QQ}(k_s,k_t,\omega_0') \tag{4.32}$$

The surface pressure spectrum S_{QQ}, which includes the airfoil response, can therefore be calculated from

$$S_{QQ}(\mathbf{y},\mathbf{k},\omega_0) = \left|H_q(\mathbf{y},\mathbf{k},\omega_0)\right|^2 S_{qq}(\mathbf{k},\omega_0) \tag{4.33}$$

Like the transfer function H_s for the scattered pressure jump, the transfer function H_q depends on the dimensionless distance $\kappa_c\eta_s$, the normalized streamwise wavenumber k_s/κ_c, normalized spanwise wavenumber $k_t\beta_0/\kappa_0$, and the Mach number M_0. Figures 4.7 to 4.11 are plots of $\left|H_q\right|^2$ against these parameters evaluated on the turbulence side of the airfoil, since on the non-turbulence side H_q is identical to H_s except for a constant difference of 1/2. Amiet's exponential decay function of Eq. (3.20) was used for the calculation of f_p in Figures 4.7 to 4.11. Common parameters used in these calculations are $M_0 = 0.4373$, $c_u = 0.65$, $\varepsilon = 0.03$, and frequency $f = 500$ Hz. For the calculations of Figs (4.7) to (4.9), $k_1/\kappa_c = 1$ is also assumed.

The modulus squared transfer function $\left|H_q\right|^2$ is plotted in Fig. 4.7 against dimensionless spanwise wavenumber $k_t\beta_0/\kappa_0$ at distances of $\kappa_c\eta_s = -0.5, -1.0, -1.5, -2.0, -2.5$. The main contribution to $\left|H_q\right|^2$ comes from turbulence components travelling along the trailing edge with supersonic phase speed, i.e. $k_t\beta_0/\kappa_0 \le 1$. However the contribution

from turbulence components travelling with subsonic phase speed, i.e. $k_t\beta_0/\kappa_0 > 1$, cannot be neglected in the evaluation of the surface pressure.

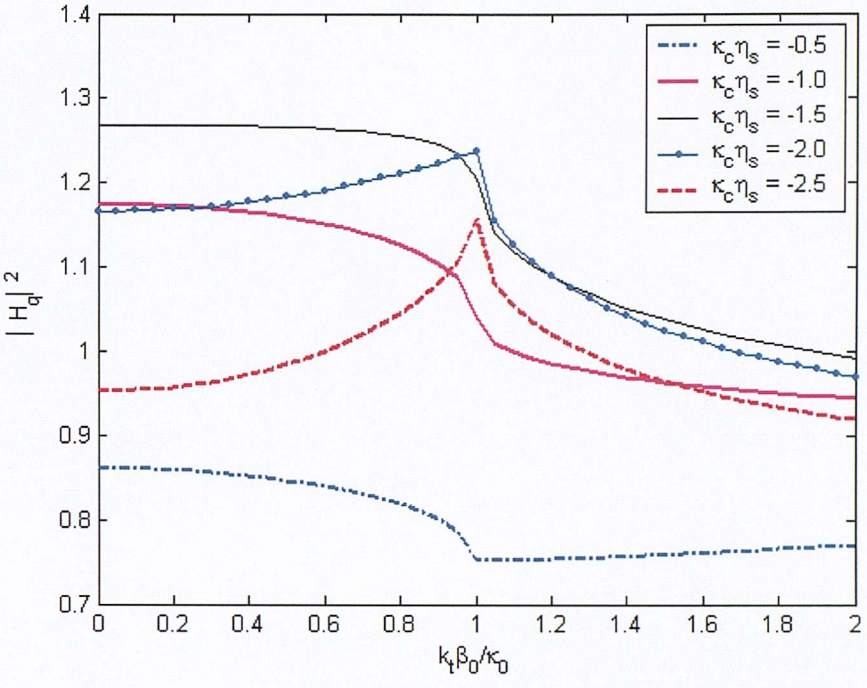

Figure 4.7. Modulus squared transfer function H_q plotted against dimensionless spanwise wavenumber $k_t\beta/\kappa_0$ at various distances, $\kappa_c\eta_s$, from the trailing edge

Figure 4.8 shows the modulus squared transfer function $|H_q|^2$ plotted against dimensionless distance $\kappa_c|\eta_s|$ from the trailing edge for various spanwise wavenumber $k_t\beta_0/\kappa_0 = 0.0, 1.0, 2.0$. In the supersonic phase speed domain, $k_t\beta_0/\kappa_0 \le 1$, the function $|H_q|^2$ oscillates with distance $\kappa_c|\eta_s|$, while for $k_t\beta_0/\kappa_0 > 1$, it does not. However in both domains the amplitude of $|H_q|^2$ decays with distance from the trailing edge for $\kappa_c|\eta_s| > 2$.

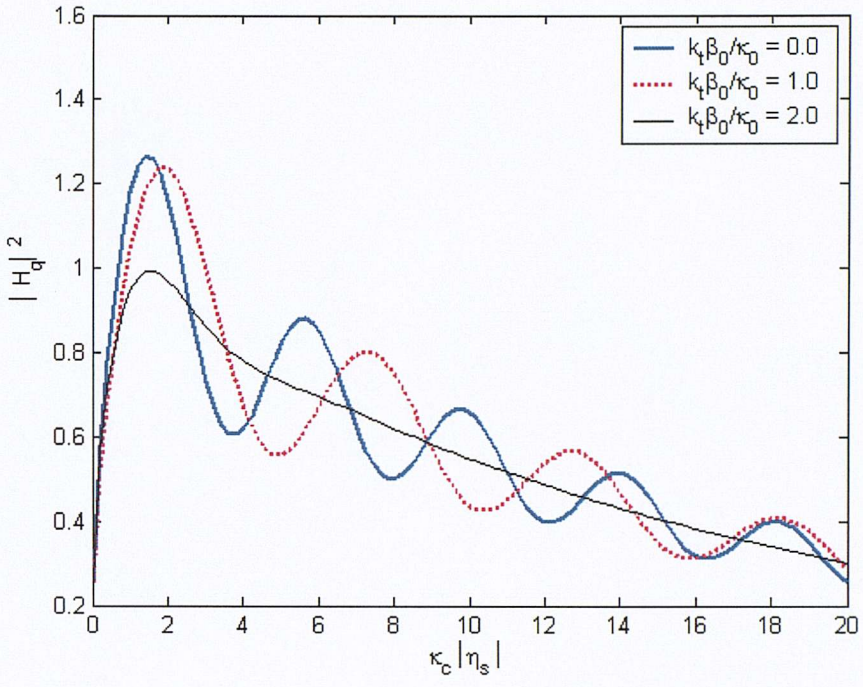

Figure 4.8. Modulus squared transfer function $|H_q|^2$ plotted against dimensionless distance, $\kappa_c|\eta_s|$, from the trailing edge for various spanwise wavenumber $k_t\beta_0/\kappa_0$.

Figure 4.9 is a plot of the modulus squared transfer function $|H_q|^2$ against dimensionless distance $\kappa_c|\eta_s|$ from the trailing edge for the various streamwise wavenumbers $k_s/\kappa_c = 0.6, 1.0, 2.0$. It is shown that the transfer function for small-streamwise-wavenumber component fluctuates more slowly than large-streamwise-wavenumber components of turbulence. This means that small wavenumber components will make a larger contribution to the noise radiation than large wavenumber components when an integration of the source pressure over airfoil surface is performed to give the total radiated noise. The reason for this is that the large wavenumber component corresponds to small wavelength turbulence therefore the source contribution to the noise radiation is weak due to the cancellation effects.

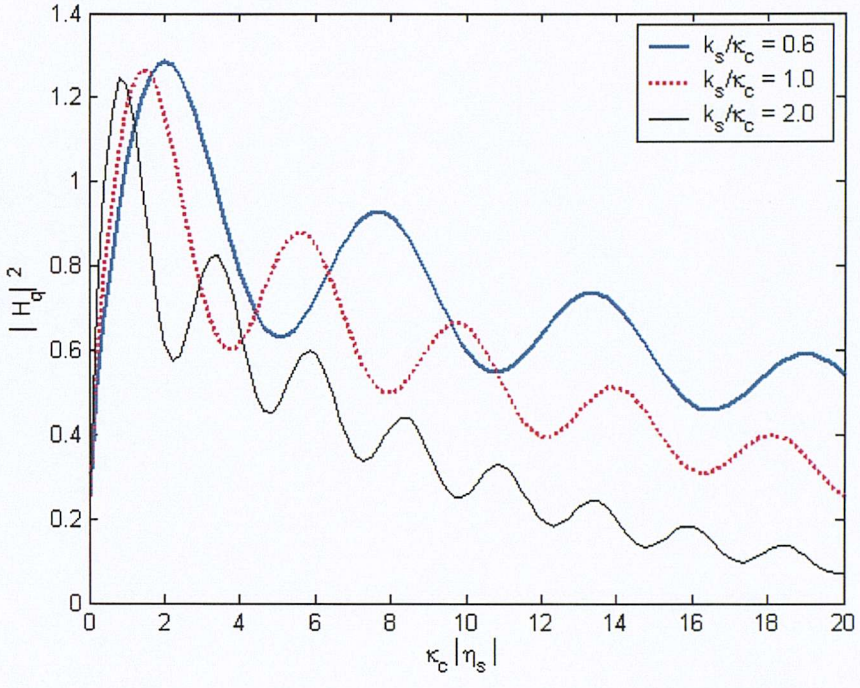

Figure 4.9. Modulus squared transfer function $|H_q|^2$ plotted against dimensionless distance, $\kappa_c|\eta_s|$, from the trailing edge for various streamwise wavenumber k_s/κ_c.

Figure 4.10 shows the function $|H_q|^2$ versus dimensionless streamwise wavenumber k_s/κ_c for various spanwise wavenumbers $k_t\beta_0/\kappa_0 = 0.0, 1.0, 2.0$ at distances $\kappa_c\eta_s = -0.5$ respectively. Figure 4.11 is the same plot as Fig. 4.10 but evaluated at the distance $\kappa_c\eta_s = -2.5$. The figures suggest that the fluctuation of the transfer function with respect to streamwise wavenumber k_s/κ_c is slower at measurement positions close to the trailing edge. However the main peak in Fig. 4.11 is located at the convective wavenumber κ_c. When this main peak coincides with the peak of the incident pressure spectrum (see Fig. 3.6), which also peaks at κ_c, the surface pressure spectrum S_{QQ} will be greatly amplified. Fortunately, this coincidence does not occur at all points on the airfoil surface.

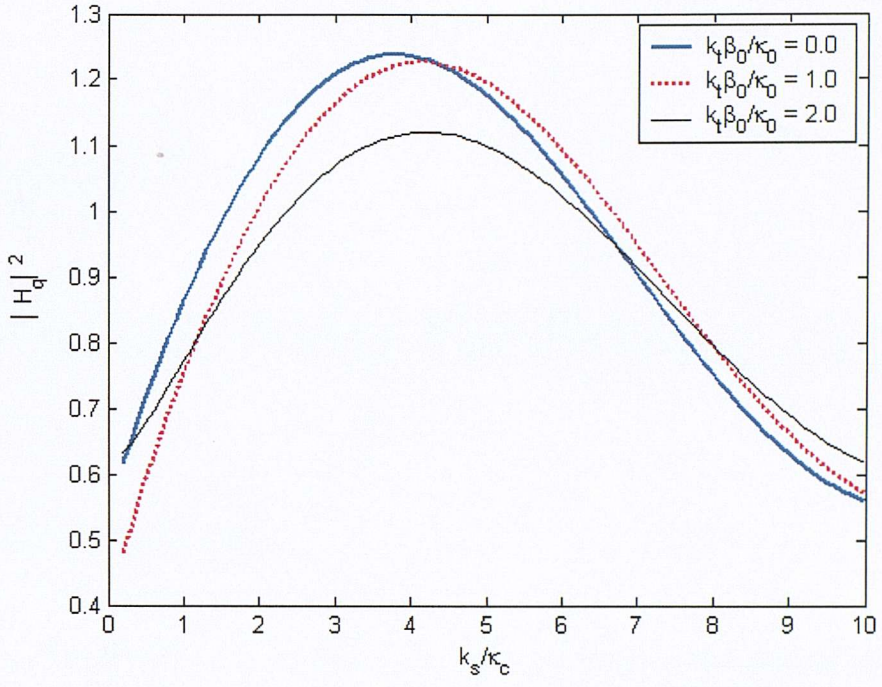

Figure 4.10. Modulus squared transfer function $|H_q|^2$ against dimensionless streamwise wavenumber k_s/κ_c for various spanwise wavenumbers $k_t\beta_0/\kappa_0$ at a distance of $\kappa_c\eta_s = -0.5$.

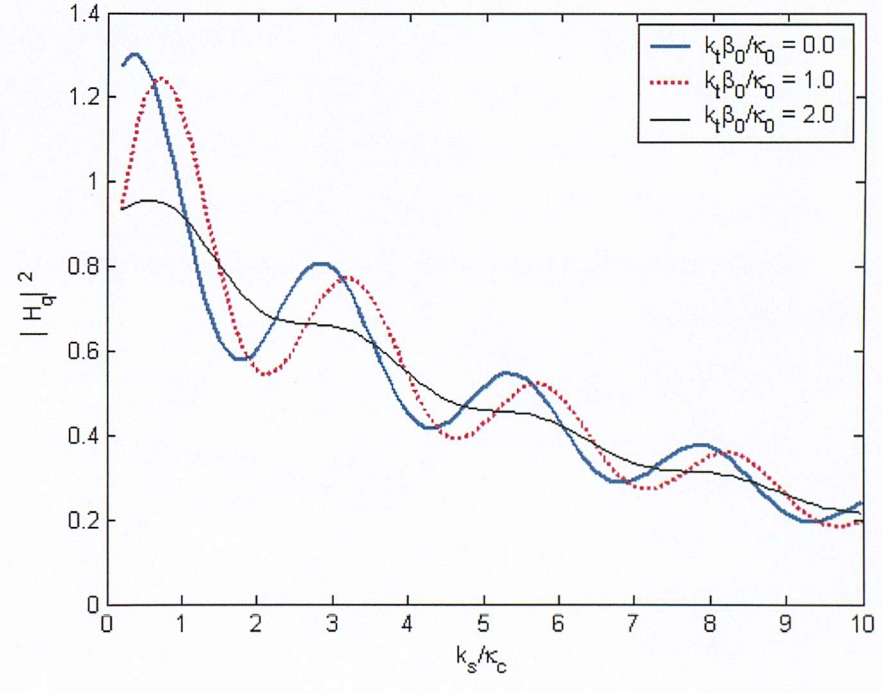

Figure 4.11. Modulus squared transfer function $|H_q|^2$ against dimensionless streamwise wavenumber k_s/κ_c for various spanwise wavenumbers $k_t\beta_0/\kappa_0$ at a distance of $\kappa_c\eta_s = -2.5$.

Chapter V

Airfoil Self Noise Prediction: Theory

5.1 Introduction

In the last two Chapters, the spectral characteristics of the airfoil surface pressure due to boundary layer turbulence were discussed. This Chapter uses these results to deduce a theory of self-noise radiation by a single airfoil. The radiated sound pressure at any field point **x** can be predicted by using Eq. (2.5) from the knowledge of the surface pressure $p_t(\mathbf{y},\tau)$ at the source point **y** on the airfoil surface, as shown schematically in Fig. 5.1. Airfoil broadband noise has been investigated in both the time domain and the frequency domain. Casper and Farassat's (2002) approach is a time domain method while Amiet (1976a) solves the problem in the frequency domain. Both are restricted to flat plate airfoils. The frequency method presented here is more general than previous formulations since no far-field and large span flat-plate assumptions are made. Approximations are introduced that enable the thin airfoil theory discussed in Chapter IV to be extended to realistic airfoil geometries of small camber and small angle of attack.

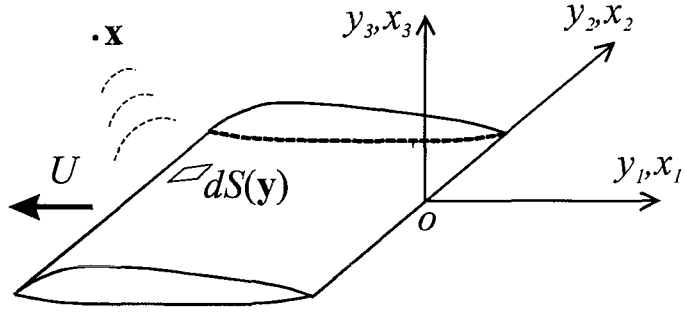

Figure 5.1. A pressure source on the element area, $dS(\mathbf{y})$, of airfoil surface radiates noise received at observation point $\mathbf{x}(x_1,x_2,x_3)$

In Sections 5.2 and 5.3 of this Chapter, a frequency domain

formulation will be developed for making airfoil self-noise predictions under the assumptions that the leading edge effect can be neglected and that the trailing edge is sharp, as described in the last Chapter. The formula can be used to investigate the effects on self-noise radiation of airfoil geometry and angle of attack, providing that the incident pressure spectrum is known and that thickness, camber and angle of attack are not too great. In Section 5.4, the formulation of self-noise radiation is shown to reduce to Amiet's analytic solution (Amiet, 1976a) when appropriate simplifying assumptions are made. A numerical scheme for the evaluation of the integral formulation on an arbitrary airfoil surface will be presented in Section 5.5.

5.2 Frequency Domain Formulation for Airfoil Sound Radiation

Neglecting viscous stresses, the i'th component of force acting on the fluid per unit area by the airfoil is given by

$$f_i(\mathbf{y},\tau) = -n_i p_t(\mathbf{y},\tau) \tag{5.1}$$

where p_t is the unsteady pressure disturbance on the airfoil surface described in Chapter IV, and n_i is i^{th} component of the unit inward normal $\mathbf{n}$ on the airfoil surface S. Volume-quadrupole sources generated by shear stresses in the boundary layer are assumed to be negligible compared with the dipole sources on the airfoil surface, although the proposed method has no difficulty in dealing with this quadrupole term in principle. For a rigid airfoil, the third term of the right side of equation (2.5) represents a steady pressure, which does not radiate sound. In this case, equation (2.5) reduces to

$$p(\mathbf{x},t) = -\int_T^T \iint_S p_t(\mathbf{y},\tau) n_i \frac{\partial}{\partial y_i} G(\mathbf{x},t;\mathbf{y},\tau) dS(\mathbf{y}) d\tau \tag{5.2}$$

Equation (5.2) is essentially a convolution of the space-time dependent surface-pressure fluctuation $p_t(\mathbf{y},\tau)$ with the spatial-temporal impulse response function $G(\mathbf{x},t;\mathbf{y},\tau)$.

Note that the velocity U, as shown in Fig. 5.1, which appears in the Green function $G(\mathbf{x},t;\mathbf{y},\tau)$ is the airfoil velocity rather than the rotor shaft velocity shown in Fig. 2.1a. For an infinite flat-plate airfoil, both U and U_0 are airfoil velocities but the subscript '0' indicates the corresponding quantity related to the source on the airfoil surface, for example, the Mach number M_0, β_0, and the frequency ω_0 (note that source frequency and observer frequency differ in the case of a rotor). In general, U_0 is used to indicate the local mean flow velocity at the interface of the boundary layer, as shown in Fig.3.4. In this case U_0 equals U plus the local potential velocity due to airfoil thickness and boundary layer displacement thickness. The effect of this local mean flow on the airfoil surface pressure is taken into account through the position-dependent function of Eq. (3.21) and eventually through the incident surface pressure spectrum S_{qq} of Eq. (3.11). For simplicity, it is assumed in this thesis that the airfoil does not disturb the background flow, which is assumed to be constant and uniform, $U = U_0$.

Fourier transforming Eq. (5.2) with respect to time t gives the acoustic pressure at a single frequency due to the unsteady loading on the airfoil surface

$$\begin{aligned}\overline{p}(\mathbf{x},\omega) &= \frac{1}{2\pi}\int_{-\infty}^{\infty} p(\mathbf{x},t)e^{i\omega t}dt \\ &= \frac{1}{2\pi}\int_{-T}^{T}\iint_{S}[-n_i p_t(\mathbf{y},\tau)]\frac{\partial}{\partial y_i}\overline{G}(\mathbf{x},\mathbf{y},\omega)dS(\mathbf{y})e^{i\omega\tau}d\tau\end{aligned} \tag{5.3}$$

Equation (5.3) may be written more compactly as

$$\overline{p}(\mathbf{x},\omega) = \frac{1}{2\pi}\int_{-T}^{T}\iint_{S} p_t(\mathbf{y},\tau)I(\mathbf{x},\mathbf{y},\omega)dS(\mathbf{y})e^{i\omega\tau}d\tau \tag{5.4}$$

where $I(\mathbf{x},\mathbf{y},\omega)$ is a form of radiation Green function given by

$$I(\mathbf{x},\mathbf{y},\omega) = -n_i(\mathbf{y})\frac{\partial}{\partial y_i}\overline{G}(\mathbf{x},\mathbf{y},\omega) \tag{5.5}$$

From Chapter II, $\overline{G}(\mathbf{x},\mathbf{y},\omega)$ is given by Eq. (2.14). For subscript $i=1$, the derivative of Green function $\overline{G}$ in Eq. (2.14) is given by

$$\frac{\partial}{\partial y_1}\overline{G}(\mathbf{x},\mathbf{y},\omega)=[-\frac{y_1-x_1}{R^2}+i\mu(\frac{y_1-x_1}{R}+M)]\overline{G}(\mathbf{x},\mathbf{y},\omega) \tag{5.6}$$

while for subscript $i=2,3$,

$$\frac{\partial}{\partial y_i}\overline{G}(\mathbf{x},\mathbf{y},\omega)=[-\frac{\beta^2}{R}+i\kappa]\frac{y_i-x_i}{R}\overline{G}(\mathbf{x},\mathbf{y},\omega) \tag{5.7}$$

where $\mu=\kappa/\beta^2$, $\kappa=\omega/c_0$, $\beta^2=1-M^2$, $M=U/c_0$ as defined in Chapter II.

5.3 General Formulation for Turbulent Inputs

The time-harmonic analysis performed in the previous Section is now applied to one-sided turbulent boundary layer pressures on an airfoil. Substituting equation (4.30) into equation (5.4) gives

$$\begin{aligned}\overline{p}(\mathbf{x},\omega)=&\iint_S\int_{-\infty}^{\infty}\int_{-\infty}^{\infty}\int_{-\infty}^{\infty}H_q(\mathbf{y},k_s,k_t,\omega_0)\hat{p}_i(k_s,k_t,\omega_0)I(\mathbf{x},\mathbf{y},\omega)\\&\times e^{i(k_s\eta_s+k_t\eta_t)}\frac{1}{2\pi}\int_{-T}^{T}e^{-i(\omega_0-\omega)\tau}d\tau dk_s dk_t d\omega_0 dS(\mathbf{y})\end{aligned} \tag{5.8}$$

Using the identity,

$$\delta(\omega_0-\omega)=\frac{1}{2\pi}\int_{-T}^{T}e^{-i(\omega_0-\omega)\tau}d\tau \tag{5.9}$$

and carrying out the integration with respect to ω_0, the expression for the radiated pressure becomes

$$\overline{p}(\mathbf{x},\omega) = \iint_S \int_{-\infty}^{\infty}\int_{-\infty}^{\infty} H_q(\mathbf{y},k_s,k_t,\omega)\hat{p}_i(k_s,k_t,\omega)I(\mathbf{x},\mathbf{y},\omega)e^{i(k_s\eta_s+k_t\eta_t)}dk_s dk_t dS(\mathbf{y}) \tag{5.10}$$

Equation (5.10) may be written more compactly as

$$\overline{p}(\mathbf{x},\omega) = \int_{-\infty}^{\infty}\int_{-\infty}^{\infty} H_p(\mathbf{x},k_s,k_t,\omega)\hat{p}_i(k_s,k_t,\omega)dk_s dk_t \tag{5.11}$$

where H_p is a radiation transfer function relating the radiated pressure at $\mathbf{x}$ to each wavenumber component (k_s, k_t) of pressure on the airfoil surface. From equations (5.10) and (5.11), it takes the form

$$H_p(\mathbf{x},k_s,k_t,\omega) = \iint_S H_q(\mathbf{y},k_s,k_t,\omega)e^{i(k_s\eta_s+k_t\eta_t)}I(\mathbf{x},\mathbf{y},\omega)dS(\mathbf{y}) \tag{5.12}$$

The power spectral density of the pressure at position $\mathbf{x}$ is given by

$$S_{pp}(\mathbf{x},\omega')\delta(\omega'-\omega) = E\left[\overline{p}^*(\mathbf{x},\omega')\overline{p}(\mathbf{x},\omega)\right] \tag{5.13}$$

Substituting equation (5.11) into equation (5.13) and making use of equation (3.4) for homogenous turbulence, the pressure spectrum at any field point $\mathbf{x}$ is of the form

$$S_{pp}(\mathbf{x},\omega) = \int_{-\infty}^{\infty}\int_{-\infty}^{\infty}\left|H_p(\mathbf{x},k_s,k_t,\omega)\right|^2 S_{qq}(k_s,k_t,\omega)dk_s dk_t \tag{5.14}$$

Using Eqs. (3.11) and (3.30) and performing the integration with respect to k_s, equation (5.14) for a frozen turbulent boundary layer reduces to

$$S_{pp}(\mathbf{x},\omega)=\frac{1}{U_c}\int_{-\infty}^{\infty}\left|H_p(\mathbf{x},\omega/U_c,k_t,\omega)\right|^2\hat{S}_{qq}(\omega/U_c,k_t)dk_t \tag{5.15}$$

Since the effect of attack angle is incorporated into the formulation through the incident pressure spectra and the position-dependent function $f_p(\mathbf{y},\mathbf{k},\omega)$ of Eq. (3.21), equations (5.14) and (5.15) are valid, not only for flat plates with zero angle of attack, but also for an airfoil of arbitrary geometry with non-zero attack angle.

5.4 Consistency with Amiet's Solution

In a classic paper, Amiet (1976a) has obtained an analytic solution for the self-noise radiated by a large-span, flat plate airfoil with frozen turbulence convecting past the trailing edge. We now demonstrate the consistency of the present formulation with Amiet's solution. For far-field positions $|\mathbf{x}|>>|\mathbf{y}|$, the flow-corrected distance R appearing in Eqs. (5.5) to (5.7) can be approximated by

$$\begin{aligned} R&=\sqrt{(y_1-x_1)^2+\beta^2(y_2-x_2)^2+\beta^2(y_3-x_3)^2}\\ &\approx R_s-(x_1y_1+\beta^2x_2y_2)/R_s \end{aligned} \tag{5.16}$$

where

$$R_s=\sqrt{x_1^2+\beta^2(x_2^2+x_3^2)} \tag{5.17}$$

For large R, equation (5.7) approximates to

$$\frac{\partial}{\partial y_3}\overline{G}(\mathbf{x},\mathbf{y},\omega)\approx -i\kappa\frac{x_3}{R_s}\frac{1}{4\pi R_s}e^{i\mu[R+M(y_1-x_1)]} \tag{5.18}$$

Substituting equation (5.16) into (5.18), one has

$$\frac{\partial}{\partial y_3}\overline{G}(\mathbf{x},\mathbf{y},\omega) \approx -\frac{i\kappa x_3}{4\pi R_s^2} e^{i\mu(R_s - Mx_1)} e^{i\mu y_1 (M - x_1/R_s)} e^{-i\kappa x_2 y_2 / R_s} \tag{5.19}$$

Substituting equation (5.19) into (5.12), and integrating over the surface of the flat plate airfoil with span $2d$, and noting that for a flat plate, $\eta_s = y_1$, $\eta_t = y_2$, $k_s = k_1$ and $k_t = k_2$, the transfer function H_p of equation (5.12) becomes

$$H_p(\mathbf{x},k_1,k_2,\omega) = -\frac{i\kappa d b x_3}{2\pi R_s^2} e^{i\mu(R_s - Mx_1)} L(\mathbf{x},k_1,k_2,\omega) \frac{\sin[(k_2 - \kappa x_2/R_s)d]}{(k_2 - \kappa x_2/R_s)d} \tag{5.20}$$

where

$$L(\mathbf{x},k_1,k_2,\omega) = \int_{-2}^{0} H_q(\mathbf{y},k_1,k_2,\omega) e^{ik_1 b\xi} e^{i\mu b\xi (M - x_1/R_s)} d\xi \tag{5.21}$$

and $\mathbf{y} = (b\xi, 0, 0)$. Substituting equations (4.29) and (3.20) into Eq.(5.21), the integration of Eq.(5.21) can be performed analytically. The result for L can be expressed as the sum of the contribution L_I due to the incident boundary layer pressure, and the contribution L_s due to the scattered pressure

$$L(\mathbf{x},k_1,k_2,\omega) = L_I(\mathbf{x},k_1,\omega) + L_S(\mathbf{x},k_1,k_2,\omega) \tag{5.22}$$

The incident part L_I is of the form

$$L_I(\mathbf{x},k_1,\omega) = \frac{1}{\varepsilon b|k_1| + iK_s}\left[1 - e^{-2(\varepsilon b|k_1| + iK_s)}\right] \tag{5.23}$$

and the scattered part of the form

$$L_S(\mathbf{x},k_1,k_2,\omega) = \frac{1}{iK_s}\left[\sqrt{a_b/k_b}\, erf\left(\sqrt{-i2k_b}\right) - e^{-i2K_s} erf\left(\sqrt{-i2a_b}\right) + e^{-i2K_s} - 1\right] \tag{5.24}$$

where $K_s = b[k_1 + \mu(M - x_1 / R_s)]$, $a_b = b(K + \mu M + k_1)$, $k_b = b(K + \mu x_1 / R_s)$, and $K = \sqrt{\mu^2 - (k_2/\beta)^2}$ as defined in Section 4.2. For $k_2^2 / \beta_0^2 \le \mu_0^2$, which corresponds to wave components whose phase velocity is supersonic along the trailing edge, equation (5.24) is more usefully written in the form

$$L_S(\mathbf{x}, k_1, k_2, \omega) = \frac{1}{iK_s}\left\{(1+i)\left[\sqrt{a_b/k_b}E^*(-2k_b) - e^{-i2K_s}E^*(-2a_b)\right] + e^{-i2K_s} - 1\right\} \tag{5.25}$$

where E^* is defined in Chapter IV. Neglecting 'end effects', the far-field pressure spectrum S_{pp} can be obtained by substituting equation (5.20) into (5.15). The result is

$$S_{pp}(\mathbf{x}, \omega) = \frac{1}{U_c}\left[\frac{\kappa b x_3}{2\pi R_s^2}\right]^2 \pi d \int_{-\infty}^{\infty} \frac{\sin^2\left[(k_2 - \kappa x_2 / R_s)d\right]}{(k_2 - \kappa x_2 / R_s)^2 \pi d} \left|L(\mathbf{x}, k_1, k_2, \omega)\right|^2 \hat{S}_{qq}(k_1, k_2) dk_2 \tag{5.26}$$

where for frozen turbulence, $k_1 = \omega / U_c$. Equation (5.26) is identical to that obtained by Amiet (1975b, Eq. (15)) except that here the input quantity is the surface pressure spectrum rather than velocity spectrum (note that Amiet's paper (1975b) is for inflow noise and Amiet's paper (1976a) is for self-noise).

Assuming that the airfoil span is large, $k_2 d >> 1$, Amiet (1975b) makes use of the delta function property

$$\lim_{d\to\infty} \frac{\sin^2\left[(k_2 - \kappa x_2 / R_s)d\right]}{(k_2 - \kappa x_2 / R_s)^2 \pi d} = \delta(k_2 - \kappa x_2 / R_s) \tag{5.27}$$

Equation (5.26) then reduces to

$$S_{pp}(\mathbf{x}, \omega) = \frac{1}{U_c}\left[\frac{\kappa b x_3}{2\pi R_s^2}\right]^2 \pi d \left|L(\mathbf{x}, k_1, k_2', \omega)\right|^2 \hat{S}_{qq}(k_1, k_2') \tag{5.28}$$

where $k_2' = \kappa x_2 / R_s$. A commonly used approximation (Amiet 1975b, 1976a) is that,

$$\hat{S}_{qq}(k_1,0) = \tfrac{1}{\pi} l_y U_c S_0(\omega) \tag{5.29}$$

where $l_y \approx 2.1U_c/\omega$ is the spanwise correlation length (Amiet ,1976a). Equation (5.28) suggests that only the $k_2 = 0$ pressure component contributes to the radiated pressure spectrum for an observer at the mid span point $x_2 = 0$. Substituting equation (5.29) into (5.28), and putting $k_2' = 0$, and $f_p(\mathbf{y},\mathbf{k},\omega) = e^{-\varepsilon|k_1 y_1|}$ in accordance with Amiet (1976b), a simplified analytic solution is obtained for observers at the mid-span of the form

$$S_{pp}(\mathbf{x},\omega) = \left[\frac{\kappa b x_3}{2\pi R_s^2}\right]^2 l_y d \left|L(\mathbf{x},k_1,0,\omega)\right|^2 S_0(\omega) \tag{5.30}$$

Note that Amiet's result is recovered when the parameters μ and k_1 appearing in Eqs. (5.22) to (5.24) are replaced by $-\mu$ and $-k_1$ respectively due to the assumption of the time dependence $e^{i\omega_0 \tau}$ used by Amiet (1976a). The reduction of the general result of equation (5.15) to the classic solution due to Amiet of Eq.(5.30) provides some verification of the present approach.

Note that by making the assumption that only the $k_2 = 0$ pressure component contributes to the radiated pressure spectrum at $x_2 = 0$,

$$\lim_{k_2 \to 0} \frac{\sin[(k_2 - \kappa x_2 / R_s)d]}{(k_2 - \kappa x_2 / R_s)} = \lim_{k_2 \to 0} \frac{\sin(k_2 d)}{k_2} = d \tag{5.31}$$

from which the transfer function $\left|H_p\right|^2$ related to equation (5.20) may be expressed as

$$\left|H_p(\mathbf{x},k_1,0,\omega)\right|^2 = \left[\frac{\kappa b x_3}{2\pi R_s^2}\right]^2 d^2 \left|L(\mathbf{x},k_1,0,\omega)\right|^2 \tag{5.32}$$

Thus $|H_p|^2$ is predicted to vary as d^2. This is because for a single wave component with $k_2 = 0$, the surface pressure is coherent along the span so that $l_y = d$. Equation (5.30) can then be rewritten as

$$S_{pp}(\mathbf{x},\omega) = |H_p(\mathbf{x},\omega/U_c,0,\omega)|^2 S_0(\omega) \tag{5.33}$$

Here H_p is the radiation transfer function, defined by Eq. (5.32), valid only for large-span flat-plate airfoils.

5.5 Numerical Scheme for the Evaluation of the Transfer Function H_p

As shown above, once the spectrum S_{qq} of the pressure field incident upon the trailing edge is known, computation of the radiated broadband field reduces to a calculation of the transfer function H_p. For a flat plate airfoil, an approximate analytic solution is available for the far-field radiated pressure as described in the previous section. For airfoils of arbitrary geometries, a numerical scheme is now presented for performing this calculation based on the fact that the hydrodynamic wavelength of the boundary layer turbulence is usually smaller than the acoustic wavelength. Integration of Eq. (5.12) is then split into two parts: one is related to the acoustic term, the other is related to the hydrodynamic term. The benefit of this

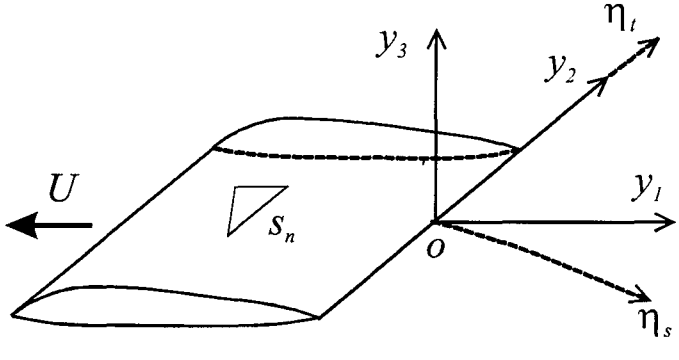

Figure 5.2. A triangular elements S_n on the airfoil surface

separation is that it allows the hydrodynamic term to be integrated analytically over a small element facet of airfoil surface thereby improving the efficiency of the computation.

In order to carry out the numerical calculation of Eq. (5.12) for arbitrary airfoil geometries, the airfoil surface is discretized into finite triangular elements as shown schematically in Fig.5.2. Suppose that, at a single frequency, each element n $(n=1,2,3,\cdots,N_{ef})$ is small compared with the acoustic wavelength so that the position-dependent function $f_p(\mathbf{y},\mathbf{k},\omega)$ and the function $I(\mathbf{x},\mathbf{y},\omega)$ at this element, defined by Eqs. (5.5) and (5.12), can be taken to be constant within that element. Under this assumption, the numerical expression of equation (5.12) becomes

$$H_p(\mathbf{x},k_s,k_t,\omega)=\sum_{n=1}^{N_{ef}}\{I_n(\mathbf{x},\mathbf{y}_n,\omega)I_n^H(\mathbf{y}_n,k_s,k_t,\omega)\} \tag{5.34}$$

where N_{ef} is the total number of elements, the superscript H in equation (5.34) refers to the 'Hydrodynamic' term. The acoustic term (see Eqs. (5.5) and (5.12)) is given by

$$I_n(\mathbf{x},\mathbf{y}_n,\omega)=N_n^i(\mathbf{y}_n)\frac{\partial}{\partial y_i}\overline{G}(\mathbf{x},\mathbf{y}_n,\omega) \tag{5.35}$$

where $N_n^i=-n_i$ is the unit outward normal vector of element n and $\mathbf{y}_n$ is the coordinates of the centre of element n. From Eqs. (5.12) and (5.34), the term I_n^H associated with the hydrodynamic pressure contribution is defined by an integral over the facet of element n

$$I_n^H(\mathbf{y}_n,k_s,k_t,\omega_0)=\iint_{S_n}H_q(\mathbf{y},k_s,k_t,\omega_0)e^{i(k_s\eta_s+k_t\eta_t)}dS(\mathbf{y}) \tag{5.36}$$

where $\omega_0=\omega$ in this Chapter, and S_n is the area of the n^{th} element facet on the airfoil surface. From Eqs.(3.11), (3.23) to (3.24), and Eq.(3.21), it can be seen that the position-

dependent function $f_p(\mathbf{y},\mathbf{k},\omega)$ mainly depends on the boundary layer thickness. It is reasonable to assume that $f_p(\mathbf{y},\mathbf{k},\omega)$ is a slowly varying function compared to variations in the hydrodynamic surface pressure. When the element S_n is sufficiently small compared to the airfoil chord, $f_p(\mathbf{y},\mathbf{k},\omega)$ can be taken out of the surface integration. In order to perform the integration analytically, we substitute Eqs. (4.27) and (4.29) into Eq.(5.36), and split the result into two parts:

$$I_n^H(\mathbf{y}_n,k_s,k_t,\omega_0)=$$

$$\begin{cases} \frac{1}{2}I_n^{H_e}(k_s,k_t,\omega_0)+[f_p(\mathbf{y}_n,k_s,k_t,\omega_0)-\frac{1}{2}]I_n^{H_f}(k_s,k_t), & \mathbf{y}_n \text{ on turbulence side} \\ -\frac{1}{2}[I_n^{H_e}(k_s,k_t,\omega_0)-I_n^{H_f}(k_s,k_t)], & \mathbf{y}_n \text{ not on turbulence side} \end{cases} \tag{5.37}$$

The terms $I_n^{H_e}$ and $I_n^{H_f}$ are defined as

$$I_n^{H_e}(k_s,k_t,\omega_0)=\iint_{S_n} erf(\sqrt{a\eta_s})e^{i(k_s\eta_s+k_t\eta_t)}d\eta_s d\eta_t \tag{5.38}$$

$$I_n^{H_f}(k_s,k_t)=\iint_{S_n} e^{i(k_s\eta_s+k_t\eta_t)}d\eta_s d\eta_t \tag{5.39}$$

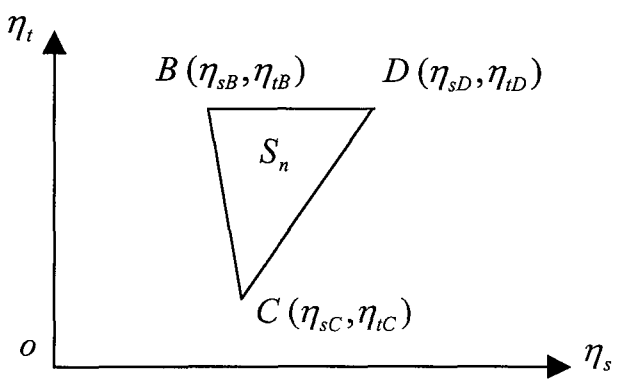

Figure 5.3 A triangle element S_n with apexes BCD

where $a=i(K+\mu_0 M+k_s)$.

Figure 5.3 depicts a triangular element S_n on the airfoil surface in curvilinear coordinates $\boldsymbol{\eta}=(\eta_s,\eta_t)$ described in Section 3.1. The apexes of the triangle are $B(\eta_{sB},\eta_{tB})$, $C(\eta_{sC},\eta_{tC})$, and

$D(\eta_{sD},\eta_{tD})$. The triangular element S_n is meshed with one edge parallel to the η_s axis (for the case of Fig. 5.2, $\eta_{tD}=\eta_{tB}$) as shown in Fig. 5.3. The equation of any edge of the triangle, for example line *CD*, may be written as

$$\eta_s^{CD} = p^{CD}\eta_t^{CD} + q^{CD} \tag{5.40}$$

where the constants p^{CD} and q^{CD} can be determined by the coordinates of points $C(\eta_{sC},\eta_{tC})$ and $D(\eta_{sD},\eta_{tD})$ on the line *CD*,

$$p^{CD} = (\eta_{sD}-\eta_{sC})/(\eta_{tD}-\eta_{tC}) \tag{5.41}$$

$$q^{CD} = -p^{CD}\eta_{tC} + \eta_{sC} \tag{5.42}$$

For the line *CB*, equations (5.40) to (5.42) are still valid with the superscript *CD* replaced by *CB*, and the subscript *D* replaced by *B*.

With the above notation, the integration of Eq. (5.38) can be performed analytically to give

$$\begin{aligned} I_n^{H_e}(k_s,k_t,\omega_0) = {} & F_e(a,p^{CB},q^{CB},\eta_{tD},k_s,k_t,\omega_0) - F_e(a,p^{CB},q^{CB},\eta_{tC},k_s,k_t,\omega_0) \\ & - F_e(a,p^{CD},q^{CD},\eta_{tD},k_s,k_t,\omega_0) + F_e(a,p^{CD},q^{CD},\eta_{tC},k_s,k_t,\omega_0) \end{aligned} \tag{5.43}$$

When $p \neq 0$ and $k_t \neq 0$, the function F_e is defined as

$$F_e(a,p,q,\eta_t,k_s,k_t,\omega_0) = \frac{1}{ipk_s} e^{-ik_t'q}\left[I_e(a,k_{st},\eta_s) - \sqrt{\frac{a}{k_a}} I_e(k_a,k_g',\eta_s) \right] \tag{5.44}$$

where

$$I_e(a,k_s,\eta_s)=\frac{1}{ik_s}\left[erf(\sqrt{a\eta_s})e^{ik_s\eta_s}-\sqrt{\frac{a}{k_a}}erf(\sqrt{k_a\eta_s})\right] \tag{5.45}$$

and

$$\eta_s = p\eta_t + q \tag{5.46}$$

$$k_a = a - ik_s, \quad k_t' = k_t / p, \quad k_{st} = k_s + k_t' \tag{5.47}$$

For $p=0$ and $k_t \neq 0$, the function F_e is defined as

$$F_e(a,p,q,\eta_t,k_s,k_t,\omega_0)=\frac{1}{ik_t}e^{ik_t\eta_t}I_e(a,k_s,\eta_s) \tag{5.48}$$

For $p\neq 0$ and $k_t=0$, the function F_e is

$$F_e(a,p,q,\eta_t,k_s,k_t,\omega_0)=\frac{1}{ipk_s}\left[I_e(a,k_s,\eta_s)-\sqrt{\frac{a}{k_a}}I_2(k_a,\eta_s)\right] \tag{5.49}$$

where

$$I_2(k_a,\eta_s)=\left(\eta_s-\frac{1}{2k_a}\right)erf\left(\sqrt{k_a\eta_s}\right)+\frac{1}{\sqrt{\pi k_a}}\sqrt{\eta_s}e^{-k_a\eta_s} \tag{5.50}$$

Finally, for $p=0$ and $k_t=0$,

$$F_e(a,p,q,\eta_t,k_s,k_t,\omega_0)=\eta_t I_e(a,k_s,\eta_s) \tag{5.51}$$

Analogous to equation (5.43), the integration of Eq. (5.39) can be expressed as

$$I_n^{H_f}(k_s,k_t) = \left[F_f(p^{CB},q^{CB},\eta_{tD},k_s,k_t) - F_f(p^{CB},q^{CB},\eta_{tC},k_s,k_t)\right. \\ \left. - F_f(p^{CD},q^{CD},\eta_{tD},k_s,k_t) + F_f(p^{CD},q^{CD},\eta_{tC},k_s,k_t)\right] \tag{5.52}$$

The function F_f is defined as

$$F_f(p,q,\eta_t,k_s,k_t) = -\frac{1}{k_s(k_s p + k_t)} e^{i[k_s(p\eta_t+q)+k_t\eta_t]}, \quad p \neq 0,\ k_s \neq 0 \text{ and } k_t \neq 0 \tag{5.53}$$

$$F_f(p,q,\eta_t,k_s,k_t) = -\frac{1}{k_s k_t} e^{i[k_s q + k_t\eta_t]}, \quad p = 0,\ k_s \neq 0 \text{ and } k_t \neq 0 \tag{5.54}$$

and

$$F_f(p,q,\eta_t,k_s,k_t) = -i\frac{\eta_t}{k_s} e^{ik_s q}, \quad p = 0,\ k_s \neq 0 \text{ and } k_t = 0 \tag{5.55}$$

Example calculations using this theory are presented in the next chapter.

Chapter VI

Airfoil Self Noise Prediction: Numerical Results

6.1 Introduction

In this Chapter, the frequency domain formulations of Eqs. (5.14), (5.15) and (5.33) will be applied to predict the self-noise radiated from a flat plate and a NACA 0012 and NACA 0024 airfoil. An investigation will be made of the radiation due to both a single Fourier (wavenumber) component of incident surface pressure, and broadband incident boundary layer turbulence comprising a continuum of wavenumbers.

For a single Fourier component of boundary layer pressure incident upon the trailing edge, the radiated pressure field can be characterized by the modulus squared transfer function $|H_p|^2$ defined by equations (5.12) and (5.32). The transfer function H_p relates the radiated pressure, at any observation point, to the amplitude of a single frequency-wavenumber component of pressure on the airfoil surface. Here we define a directivity function of the radiated sound field due to a single frequency-wavenumber component of pressure, which is related to the transfer function H_p, by

$$D_H(R_d, \Psi, \theta, \mathbf{k}, \omega) = \left|H_p(\mathbf{x}, \mathbf{k}, \omega)\right|^2 \tag{6.1}$$

where $\mathbf{x} = (R_d \sin\theta\cos\Psi, R_d \cos\theta, R_d \sin\theta\sin\Psi)$ is the observer coordinates, and where (R_d, Ψ, θ) is a spherical coordinate system, as shown in Fig.6.1. Here R_d is the observer distance from the origin, located at the mid-span point along the trailing edge, Ψ is the polar angle measured from the x_1 - axis in the mid-span plane, and θ is the azimuthal angle measured from x_2 axis.

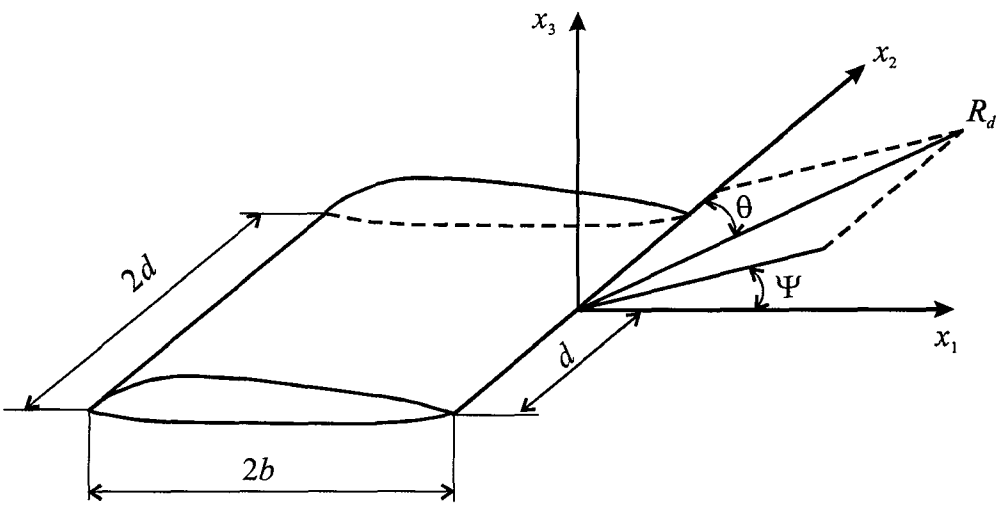

Figure 6.1. Spherical coordinate system (R_d, Ψ, θ) and rectangular coordinate system $\mathbf{x}(x_1, x_2, x_3)$

For broadband noise, the sound pressure level (SPL) is defined as the spectral density of mean square pressure in a $1Hz$ bandwidth, in decibels relative to $p_{ref} = 2\times10^{-5}\ Pa$

$$L_p(\mathbf{x}, f) = 10\log_{10}\frac{4\pi S_{pp}(\mathbf{x}, \omega)}{p_{ref}^2} \tag{6.2}$$

where $f = \omega/2\pi$ is the frequency in Hertz, and the factor 4π is included to convert from a double sided spectrum to a single sided ($0 < \omega < \infty$) spectrum, and from radian frequency to Hertz.

The directivity of the radiated sound field in decibel for broadband noise is defined here as

$$D(\Psi,\theta,f) = 10\log_{10}\left[R_d{}^2 \frac{4\pi S_{pp}(\mathbf{x},\omega)}{p_{ref}^2} \right] \qquad (6.3)$$
$$= L_p(\mathbf{x},f) + 20\log_{10} R_d$$

In Section 6.3, the noise from two NACA airfoils will be investigated. The results will then be compared with the empirical predictions based on the experimental data by Brooks etc. (1989). We first focus on predicting the noise radiated by a flat plate airfoil in Section 6.2. The results will be compared with the analytic solution of Amiet (1976a).

The use of Eqs.(5.14), (5.15) and (5.33) to compute the spectrum of radiated pressure spectrum S_{pp} assumes that the boundary layer turbulence on the airfoil suction side and pressure side are statistically independent. The spectra of radiated pressure due to the turbulence on each side are calculated separately and then added incoherently to obtain the total pressure spectrum at any observation point. The contribution to the radiated pressure due to the turbulence on each side of the airfoil is obtained by integrating the transfer functions of Eq. (5.12) over both the suction side and the pressure side. This procedure is described by Eq. (5.37).

6.2 Self-noise Radiation From a Flat Plate Airfoil

The flat plate airfoil used for this prediction has a chord length of $2b = 1.0\,\text{m}$ and a span of $2d = 4.0\,\text{m}$, typical of a small aircraft wing. It moves in the $-y_1$ direction with Mach number M. For the purpose of comparison with the analytic solution, this dimension is chosen to comply with Amiet's assumption of large span. For consistency with Amiet, the convective velocity coefficient of $c_u = 0.8$ is used. Figure 6.2 shows the mesh of the flat plate airfoil used for the numerical calculation at frequencies less then 3000Hz. The element dimension must be 10 times less than acoustic wavelength so that the transfer function of Eq.(5.12) can be expressed in the separable form of Eq.(5.34). Finer meshes are needed for calculation at higher frequencies. For a mesh that is valid for frequencies up to $f = 3000\,\text{Hz}$, the element size is chosen such that $l_e \le c_0/(10f) = 11.5\,\text{mm}$. Below

3kHz, 60552 triangle elements and 30712 nodes are used to represent the $1.0m \times 4.0m$ flat plate airfoil, as shown below in Fig. 6.2.

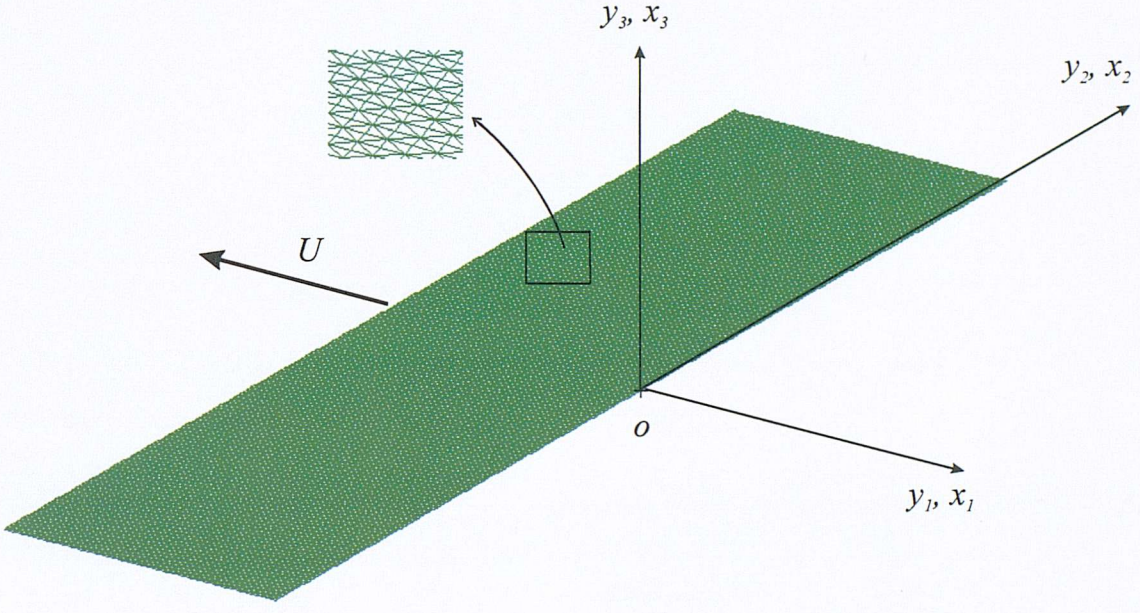

Figure 6.2. Mesh of flat plate airfoil for numerical calculation of self-noise radiation

6.2.1 Comparison of Numerical Results With Amiet's Analytic Solution for Modulus Squared Transfer Function $|H_p|^2$ in the Mid-span Plane due to Single Frozen, Normally Incident Gust Components

By way of verification of the numerical scheme presented in Chapter V, numerical predictions of the self-noise radiation due to a flat plate airfoil are compared with the analytic solution of Amiet (1976a). For consistency with the assumptions made by Amiet, i.e. flat plate airfoil, large span and far field observer in the mid-span plane $x_2 = 0$, the parameters used for the calculations here are $R_d = 150.0$ m, $x_2 = 0$ ($\theta = \pi/2$), a decay factor of $\varepsilon = 0.3$ for the incident field, $k_1 = \kappa_c$ for a frozen incident gust convecting at the free stream velocity, $k_2 = 0$ for a normally incident gust. A Mach number of $M = 0.3$ is assumed.

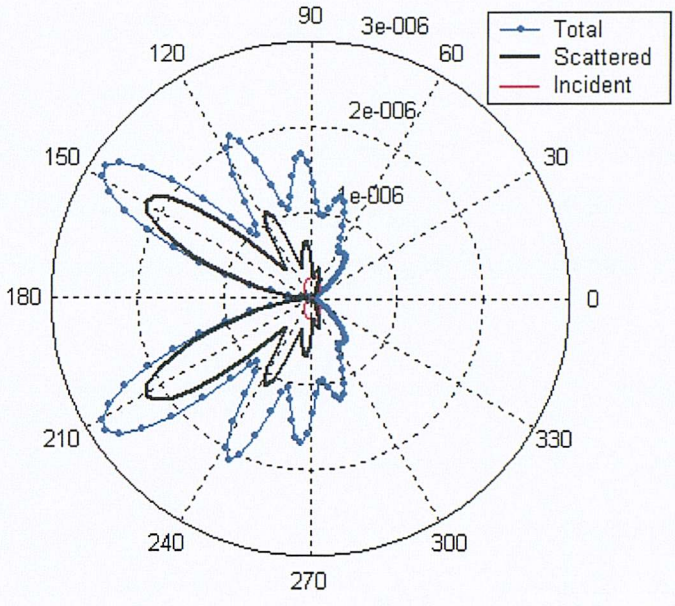

Figure 6.3a. Directivity function, D_H, calculated from Amiet's analytic solution for a flat plate airfoil, $\theta = 90°$, $M = 0.3$, $\sigma_1 = 30.5$

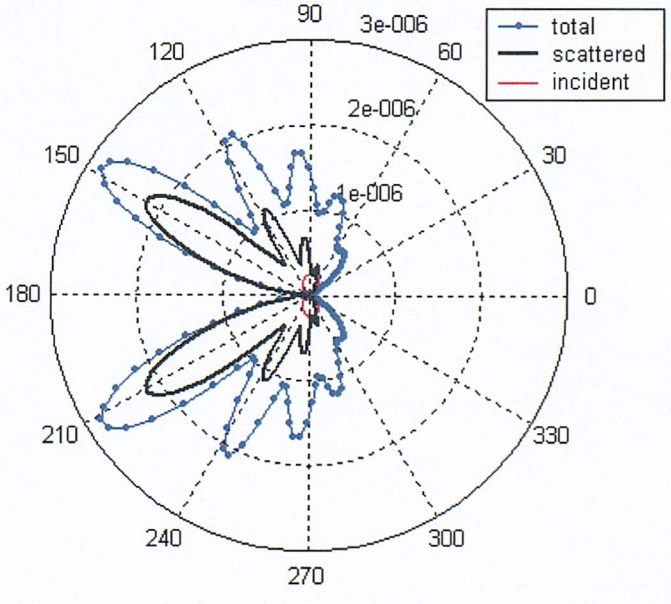

Figure 6.3b. Directivity function, D_H, calculated by the numerical method for a flat plate airfoil, $\theta = 90°$, $M = 0.3$, $\sigma_1 = 30.5$

Figure 6.3a shows the directivity function $D_H(R_d, \Psi, \pi/2, k_1, 0, \omega)$ calculated from Amiet's solution (equation (5.32)) at a reduced frequency of $\sigma_1 = 30.5$ ($f = 800$ Hz). The radiation integral L in equation (5.32) for the incident, scattered and the total pressure fields are calculated from equations (5.23), (5.25) and (5.22) respectively. Figure 6.3b is the corresponding directivity function D_H calculated by the numerical method of Eq. (5.34). The numerical and analytical solutions are in very close agreement.

The variation of $|H_p|^2$, defined in Eqs.(5.12) and (5.32), with reduced frequency $\sigma_1 = \kappa_c b$ is plotted in Figs. 6.4. The observation point is taken at $\mathbf{x} = (0.0, 0.0, 150.0)$ m. Figure 6.4a is obtained using Amiet's solution (equation (5.32)) and Figure 6.4b obtained by the numerical method given by Eqs. (5.12) and (5.34). Again, excellent agreement is obtained over the entire frequency range.

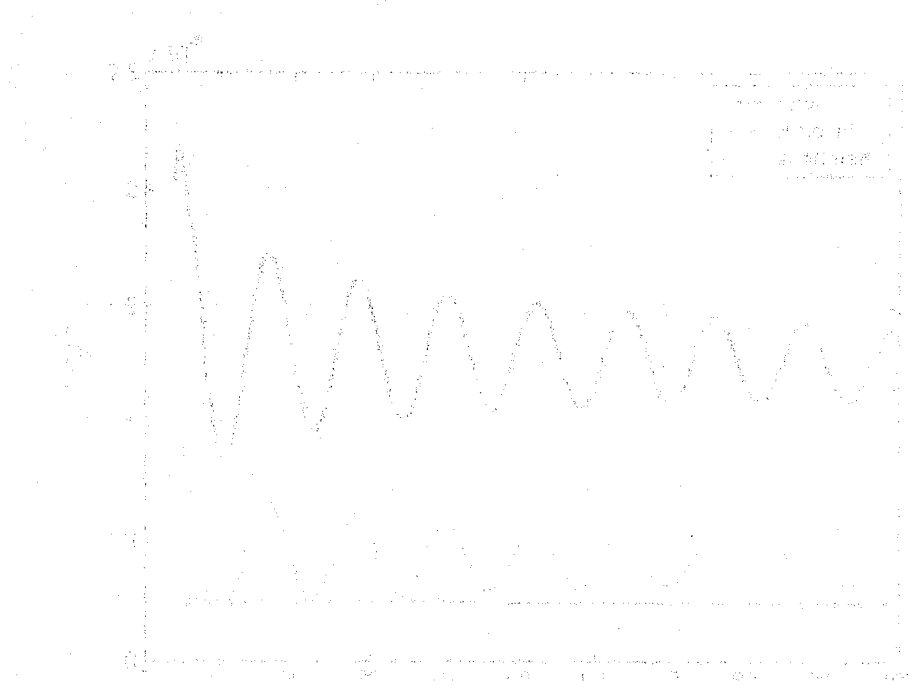

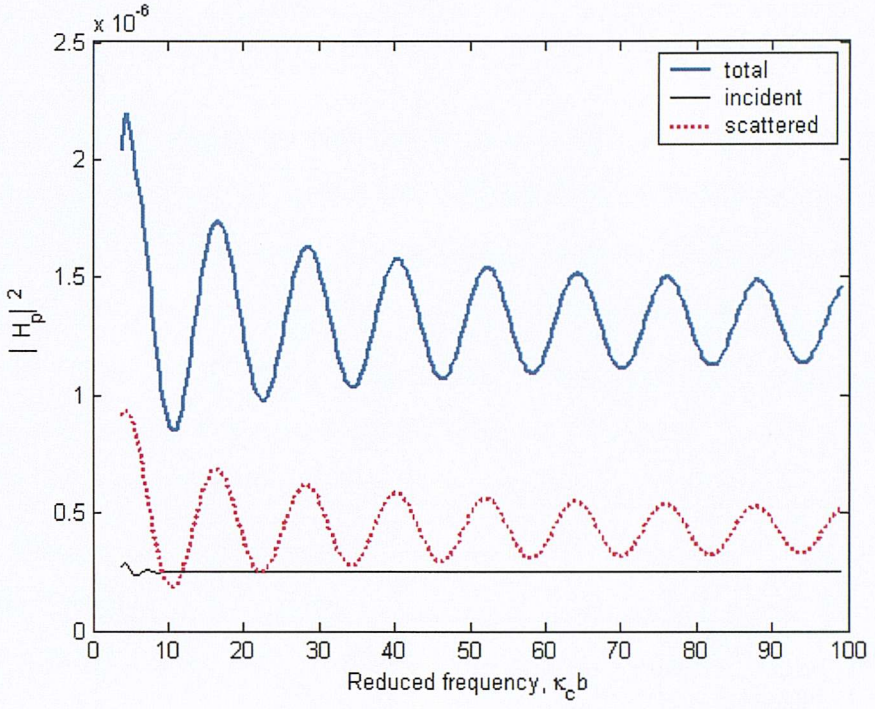

Figure 6.4a. Modulus squared transfer function $|H_p|^2$ versus σ_1 calculated by Amiet's analytic method for a flat plate airfoil, $R_d = 150.0$ m, $\varepsilon = 0.3$, $M = 0.3$

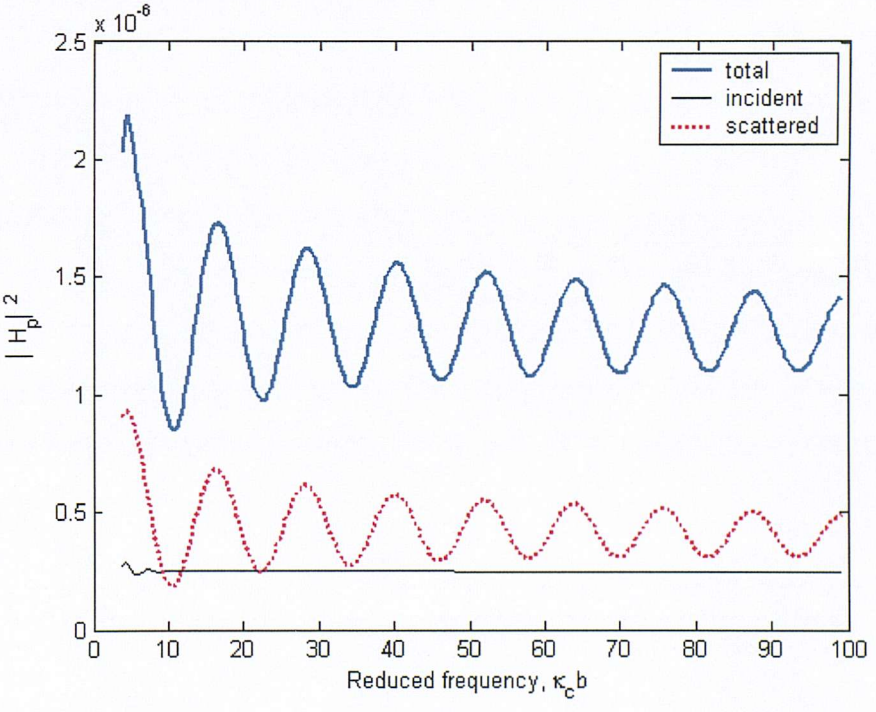

Figure 6.4b. Modulus squared transfer function $|H_p|^2$ versus σ_1 calculated by the numerical method for a flat plate airfoil, $R_d = 150.0$ m, $\varepsilon = 0.3$, $M = 0.3$

6.2.2. Comparison of Numerical Results With Amiet's Solution for Self-noise Radiation in the Mid-span Plane due to Frozen Boundary Layer Turbulence

Figure 6.5 shows a comparison between the broadband self-noise spectrum predicted using Amiet's solution of Eq. (5.33) and the numerical solution of Eq. (5.15) for an observer at $\mathbf{x} = (0.0, 0.0, 150.0)$ m. The correlation length is taken as $l_y = 2.1U_c / \omega$ for consistency with Amiet (1976a). The combined Chase and Corcos spectrum of Eqs. (3.17) and (3.31) is used to represent the incident boundary layer turbulence frequency-wavenumber spectrum. Figure 6.5 shows that at low frequencies, $f < 800Hz$, the numerical result is only about 1 dB greater than that predicted from the analytic solution. At higher frequencies, agreement is less than 0.5 dB. In the intermediate frequency range, agreement is even better. The main reason for the difference between predictions is because the numerical result includes integration over spanwise wavenumber k_2, while Amiet's solution makes the approximation that only $k_2 = 0$ contributes to the radiation in the mid-span plane. Figure 6.5 suggests that Amiet's solution is a reasonable approximation for flat plate airfoils with span large compared to the acoustic wavelength for far field observers in the mid-span plane. The validity of Amiet's approximation is investigated further in Section 6.2.3.

Note that for the purpose of computational expediency, the numerical result presented in Fig.6.5 only includes integration over a k_2 range of $0 \le k_2 \le \kappa / 3$. The error in the pressure predictions incurred by this approximation was found to be negligible (see Fig. 6.29). The average computation time per frequency per observation point on a 1.2GHz PC for the broadband noise predictions presented here for the $1\text{m} \times 4\text{m}$ flat plate airfoil is 8.5 minute. For larger airfoils, more elements are needed to meet the sampling criterion, which will therefore take a longer time, particularly for broadband noise calculations.

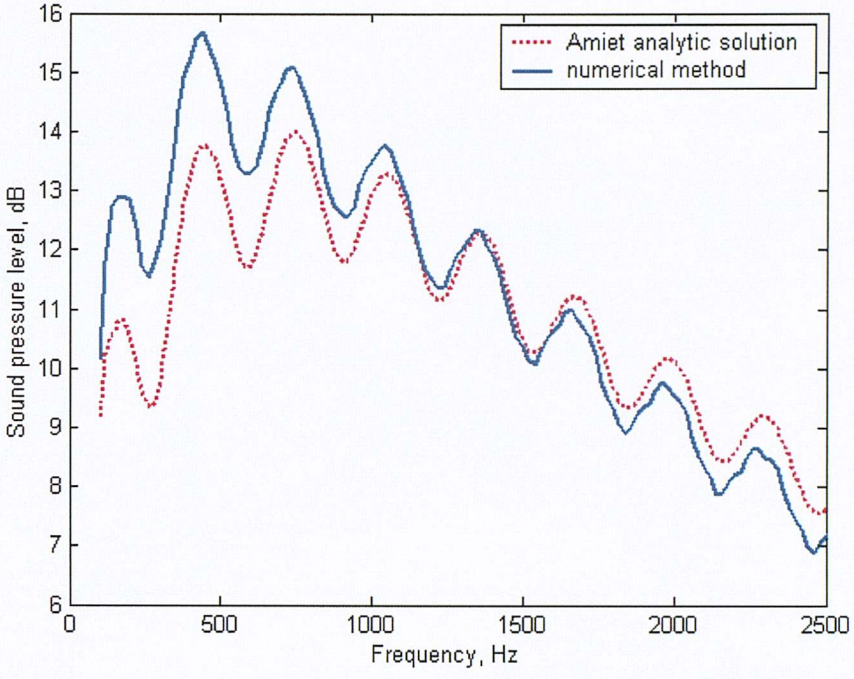

Figure 6.5. Comparison of broadband self-noise prediction for a flat plate airfoil, decay factor $\varepsilon = 0.3$, Mach number $M = 0.3$

6.2.3 Variation of $|H_p|^2$ With Observer Position for Frozen, Normally Incident Gusts

In Section 6.2.1, self-noise predictions are restricted to observer positions in the far field mid-span plane. In this Section, the computation parameters are kept the same as in Section 6.2.1 but with the constraint on observer position relaxed.

Figure 6.6 shows the directivity function $D_H(R_d, \Psi, \pi/4, k_1, 0, \omega)$ calculated from the numerical method of equation (5.34) at a reduced frequency of $\sigma_1 = 30.5$ ($f = 800$ Hz). The parameters are the same as in Fig. 6.3b but with an azimuthal angle θ equal to 45° rather than 90° as in Fig. 6.3b. Figure 6.6 indicates that for Fourier components of surface pressure normally incident upon the trailing edge ($k_2 = 0$) almost no noise is radiated at observer positions away from the mid-span plane. This is the same conclusion drawn by Amiet (1976a). Figure 6.7 shows the azimuthal directivity function $D_H(R_d, \pi/2, \theta, k_1, 0, \omega)$ for a polar angle of $\Psi = 90°$. Again it suggests that noise due to

normal incident wavenumber components is only radiated in the direction of the mid-span plane ($\theta = \pm 90°$).

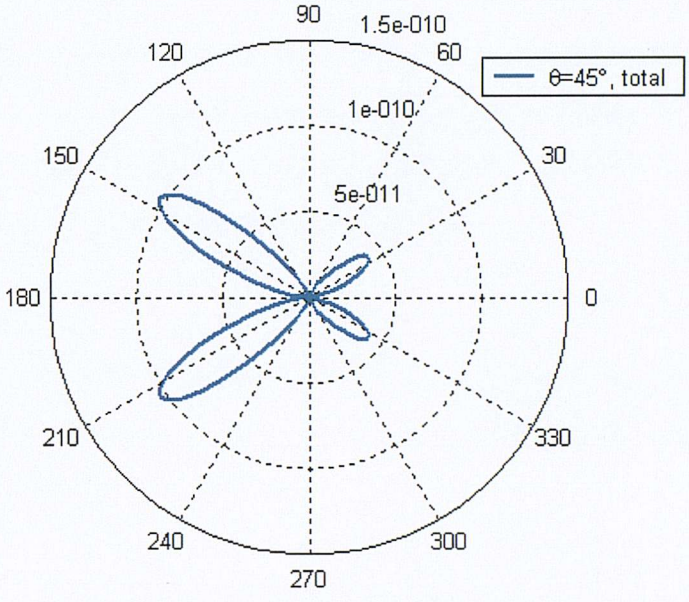

Figure 6.6. Polar directivity function (in Ψ – direction) calculated by numerical method for a flat plate airfoil, for $\theta = 45°, M = 0.3, \sigma_1 = 30.5$

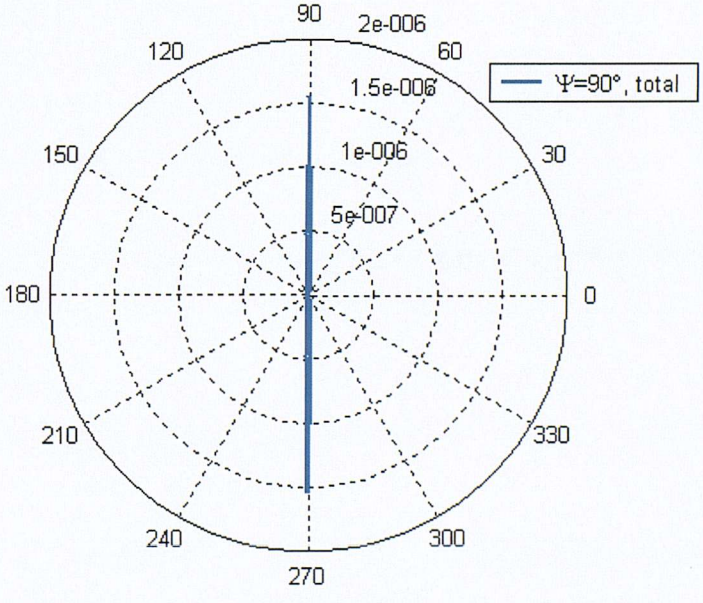

Figure 6.7. Azimuthal directivity function (in θ – direction) calculated by the numerical method for a flat plate airfoil, for $\Psi = 90°, M = 0.3, \sigma_1 = 30.5$

Figures 6.8 shows the same calculation as plotted in Figs. 6.4 but with the observer distance reduced to $R_d = 50.0$ m, i.e. $\mathbf{x} = (0.0, 0.0, 50.0)$ m. The dash line in Fig. 6.8 shows the variation of $|H_p|^2$ versus reduced frequency calculated using Amiet's solution, the solid line shows the corresponding variation calculated using the numerical method. The difference between the two solutions is now significantly larger. It is due to the break down of the geometric far-field assumption made in the Amiet solution. No such restriction is placed on the numerical scheme proposed here.

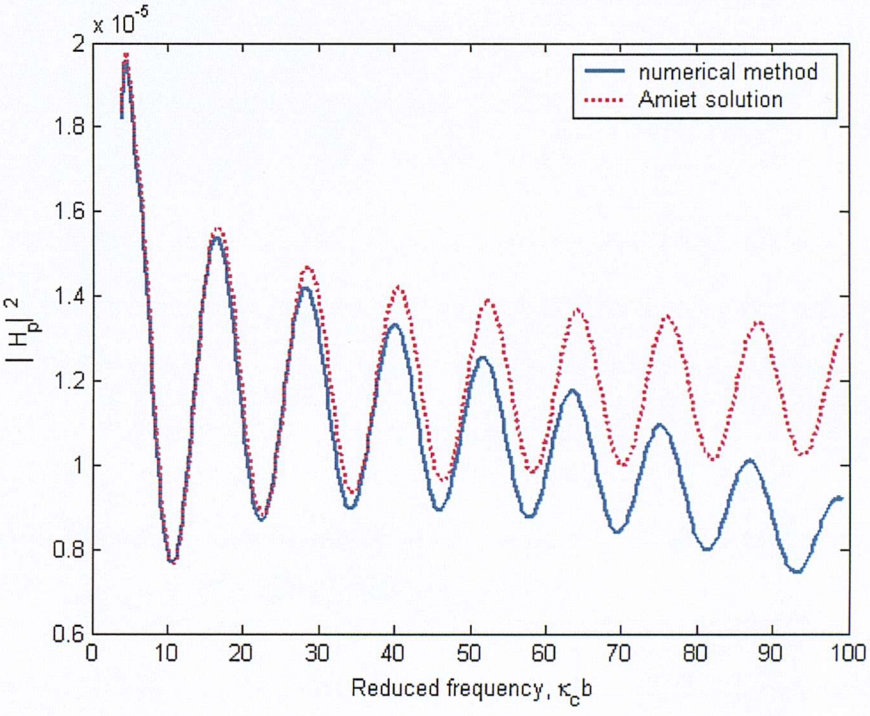

Figure 6.8. Comparison of the modulus squared transfer function $|H_p|^2$ for a flat plate airfoil, for $R_d = 50.0$ m, $\varepsilon = 0.3$, $M = 0.3$

6.2.4 Effects of Decay Factor on Self-noise Prediction

A decay factor of $\varepsilon = 0.3$ is assumed for the incident pressure field in all calculations presented in Sections 6.2.1 to 6.2.3. This section examines the sensitivity of the self-noise prediction to this parameter. Figure 6.9 shows the modulus squared transfer function $|H_p|^2$ plotted against reduced frequency σ_1. All the parameters are chosen to

be the same as in Fig.6.4b, but with a decay factor reduced to $\varepsilon = 0.03$ from $\varepsilon = 0.3$. At

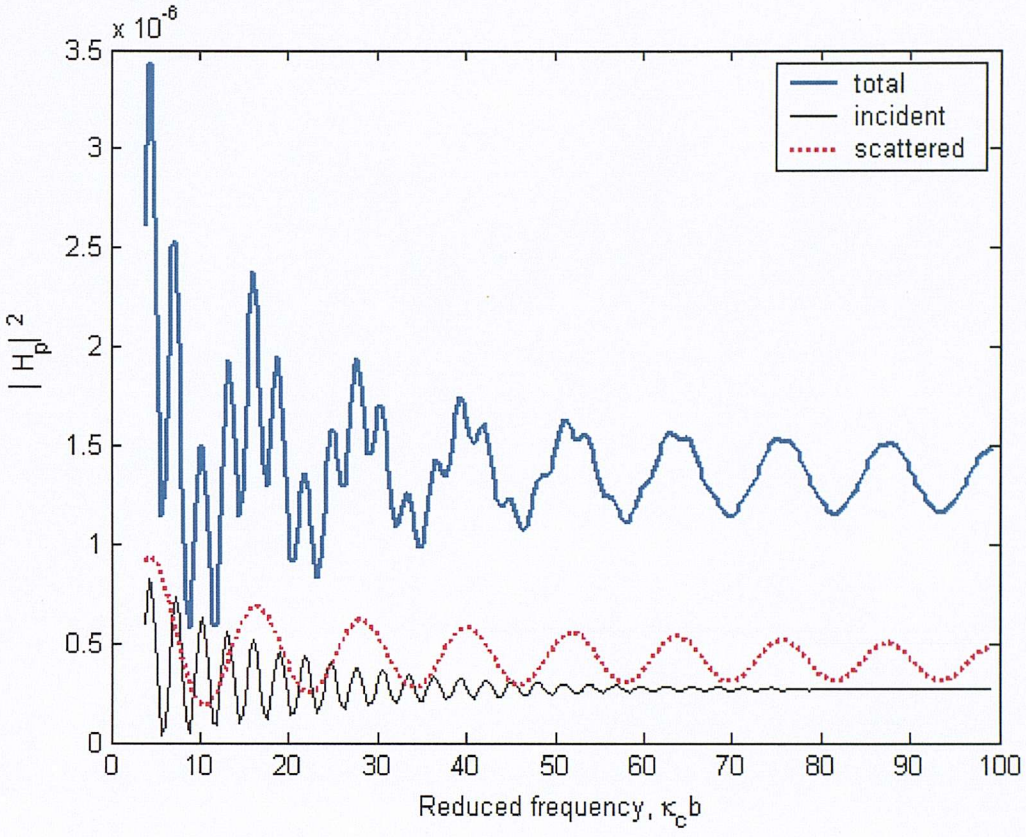

Figure 6.9. Modulus squared transfer function $|H_p|^2$ calculated by the numerical method for a flat plate airfoil, for $\varepsilon = 0.03$

small values of ε and σ_1, fluctuations in the 'incident part' of $|H_p|^2$ (thin solid line) indicates that Amiet's choice of exponential function f_p does not decay quickly enough to avoid physically unrealistic behaviour in which the turbulence appears suddenly at the leading edge. Figure 6.10 shows again $|H_p|^2$ plotted against reduced frequency σ_1, but with the position-dependent function f_p calculated from Eq. (3.21) to perform the calculation. In this case the function f_p depends on the boundary layer thickness through the boundary layer pressure spectra of Eqs. (3.17), (3.18), (3.23) and (3.24). Figure 6.10 shows that it gives the correct behaviour over whole reduced frequency range inasmuch as $|H_p|^2$ due to the incident pressure is now very nearly frequency-independent.

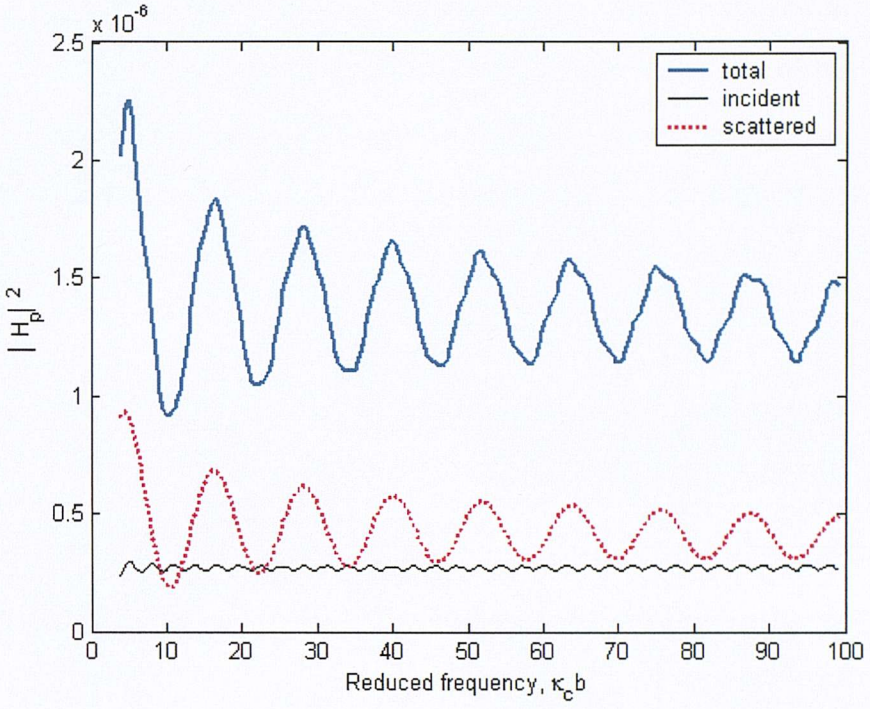

Figure 6.10. Modulus Squared Transfer function $|H_p|^2$ calculated by the numerical method for a flat plate airfoil, with f_p calculated from Eq. (3.21)

Figure 6.11 is a plot of sound pressure level versus frequency computed using the numerical method. The solid line shows the result with the position-dependent function f_p calculated by Eqs. (3.21) and the dash line gives the result with the function f_p computed using the exponential function of Eqs. (3.20). All other parameters in the computation are the same as in Fig.6.5. Figure 6.11 suggests that the prediction of the total radiated noise is not sensitive to the choice of position-dependent function f_p provided that the decay factor ε is not too small. This is because the contribution from the incident pressure to the total radiated noise is small compared with that from the scattered pressure.

From the above analysis, it can be seen that the behaviour of the predicted radiation using Amiet's exponential decay function f_p of Eq. (3.20) depends on both frequency and the choice of decay factor ε. To simulate the correct behaviour of the turbulence at the leading edge, a frequency-dependent factor ε must be determined beforehand.

However, there is a difficulty in choosing this arbitrary frequency-dependent factor ε to give the required behaviour of leading edge turbulence. On the other hand, the position-dependent function f_p of Eq. (3.21) provides the correct behaviour of the leading edge turbulence without the use of an arbitrary function. We therefore use the position-dependent function f_p of Eq. (3.21) for the remainder of the computations presented in this thesis except in Section 6.2.7.

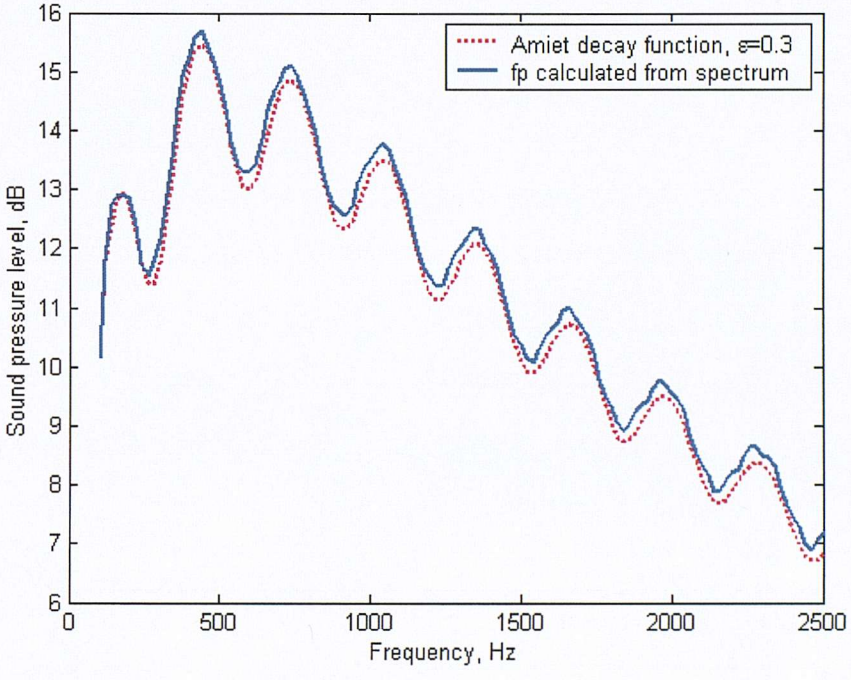

Figure 6.11. Comparison of the choice of position-dependent function for making broadband self-noise prediction of a flat plate, decay factor $\varepsilon = 0.3$ for Amiet position-dependent function f_p

6.2.5 Variation of $|H_p|^2$ to Frozen Oblique Gust Components for Observers in the Mid-span Plane

The results presented in Sections 6.2.1 to 6.2.4 are concerned with incident gusts that impinge on the trailing edge at normal incidence ($k_2 = 0$) and which convect at the convection velocity. We now consider the radiation at positions in the mid-span plane

for the more general case of a skewed gust ($k_2 \neq 0$). Figure 6.12 shows $|H_p|^2$ plotted against the reduced frequency σ_1 based on the same calculation parameters as in Figure 6.4b but for dimensionless spanwise wave numbers of $k_2/\kappa = 0.0, 0.5, 1.5$. Here we assume $k_1 = \kappa_c$ corresponding to a frozen incident gust convecting at the convection velocity. Figure 6.12 shows that the contribution to self-noise radiation from skewed gusts is generally much smaller than that for the normally incident gusts at this mid-span position.

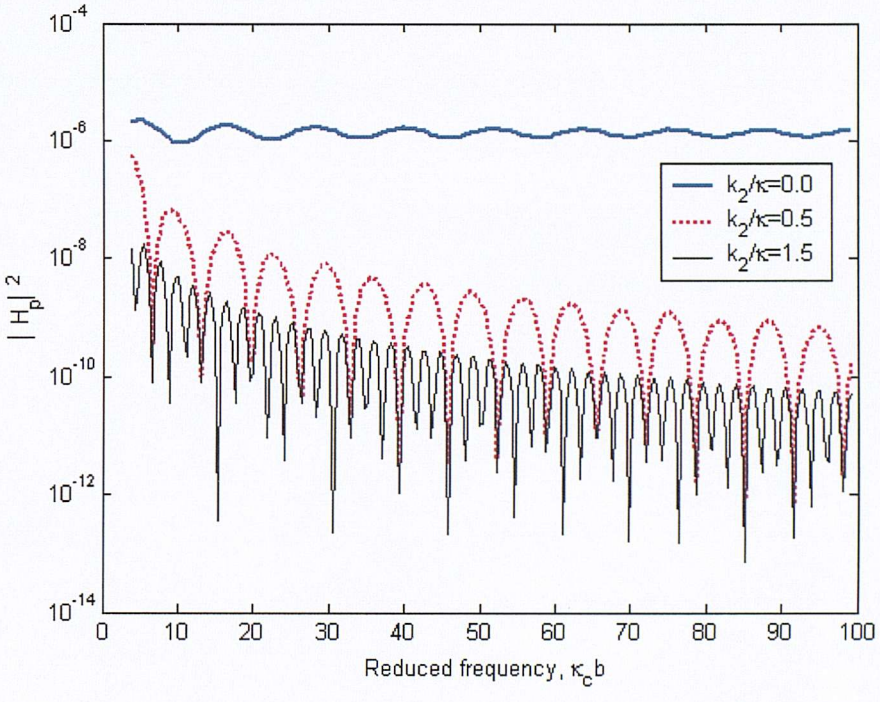

Figure 6.12. Modulus squared transfer function $|H_p|^2$ versus σ_1, calculated by numerical method for a flat plate airfoil, f_p calculated from Eq. (3.21), $k_1 = \kappa_c$, for different values of k_2/κ

6.2.6. Variation of $|H_p|^2$ due to Non-Frozen, Normally Incident Gusts

In all the figures presented above, the boundary layer turbulence impinging on the airfoil trailing edge has been assumed to be frozen ($k_1 = \kappa_c$). In order to assess the variation of

$|H_p|^2$ with variation in streamwise gust wavenumber $k_1 \neq \kappa_c$, i.e., with gust components convecting at velocities other than the convection velocity, we plot in Fig. 6.13 the modulus squared transfer function $|H_p|^2$ versus reduced frequency σ_1 for various streamwise wave numbers $k_1 b = 10, 30, 50, 70$. Other parameters used in the calculation are the same as those in Fig. 6.4b. It can be seen that $|H_p|^2$ generally increases as $k_1 b$ decreases and κ_c increases. Thus, at any given frequency, low k_1 (large wavelength) components in the k_1-spectrum of non-frozen boundary layer turbulence, radiate more efficiently than those of high streamwise wavenumber (small wavelength) components. This is principally due to the high degree of cancellation that occurs for streamwise components of wavelengths much smaller than a chord.

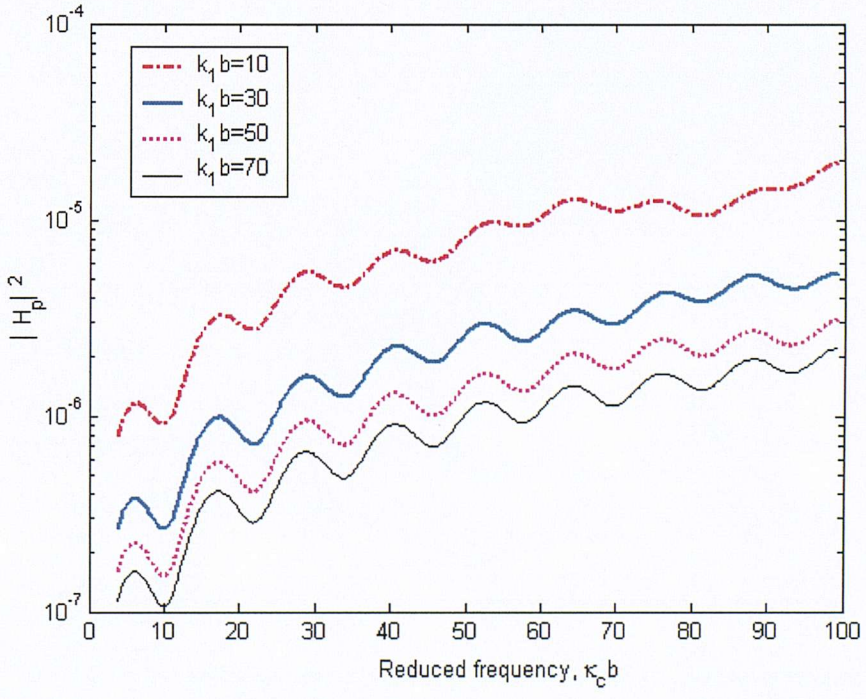

Figure 6.13. Modulus squared transfer function $|H_p|^2$ versus σ_1, calculated by numerical method for a flat plate airfoil, f_p calculated from Eq. (3.21), $k_2 = 0$, for different values of $k_1 b$

6.2.7 Effects of Mean Flow Velocity on the Directivity Function

All the results presented in Sections 6.2.1 to 6.2.6 are calculated at a Mach number of $M = 0.3$. Figure 6.14 shows the directivity function $D_H(R_d, \psi, \pi/2, k_1, 0, \omega)$ calculated from Amiet's solution (equation (5.32)) based on the same parameters as in Fig. 6.3a but at a significantly higher Mach number of $M = 0.8$. To ensure that there is no significant contribution from the leading edge, a large decay factor of $\varepsilon = 0.3$ is used for the calculation. By comparing Fig. 6.3a with Fig.6.14, it can be seen that at this higher Mach number the main radiation lobe moves from the forward flight direction to the aft flight direction, and that the contribution from the incident pressure now dominates that due to the scattered component.

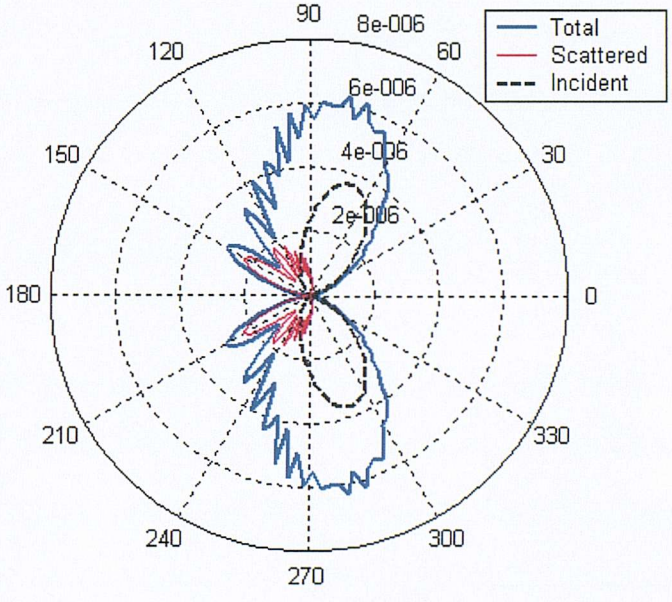

Figure 6.14. Polar directivity function (in Ψ – direction) calculated using Amiet's analytic solution for a flat plate airfoil with $\theta = 90°$ and $M = 0.8$

To understand this dependence of Mach number on directivity we separate the transfer function H_p, expressed by equations (5.32), (5.22), (5.23) and (5.24), into the product of three factors:

$$|H_p| \propto L_0 \frac{1}{K_s R_s} \frac{|x_3|}{R_s} \tag{6.4}$$

The first factor is the radiation integral L of Eq.(5.22) but without the factor $1/K_s$. From Eqs. (5.22) to (5.24), it can be written as the sum of two parts:

$$L_0(\mathbf{x}, k_1, 0, \omega) = L_{I0}(\mathbf{x}, k_1, 0, \omega) + L_{S0}(\mathbf{x}, k_1, 0, \omega) = K_s L(\mathbf{x}, k_1, 0, \omega) \tag{6.5}$$

where L_{I0} is the contribution to the noise radiation from the incident pressure of the form

$$L_{I0}(\mathbf{x}, k_1, \omega) = \frac{K_s}{\varepsilon b|k_1| + iK_s}\left[1 - e^{-2(\varepsilon b|k_1| + iK_s)}\right] \tag{6.6}$$

and L_{S0} is the contribution from the scattered pressure, given by

$$L_{S0}(\mathbf{x}, k_1, k_2, \omega) = \frac{1}{i}\left[\sqrt{a_b/k_b}\, erf\left(\sqrt{-i2k_b}\right) - e^{-i2K_s} erf\left(\sqrt{-i2a_b}\right) + e^{-i2K_s} - 1\right] \tag{6.7}$$

This first term may be regarded as a source directivity factor since it relates to the pressure distribution over the airfoil surface. The directivity of the functions $|L_{I0}|$, $|L_0|$, and $|L_{S0}|$, at Mach numbers of $M = 0.3$ and $M = 0.8$ are shown in Figures 6.15a and 6.16a, respectively. The other parameters used in the calculation are as for Figs. 6.3a and 6.14. Figures 6.15b and 6.16b are amplified versions of Figures 6.15a and 6.16a to allow a clearer view. It can be seen that the mean flow velocity has no influence on the contribution from the incident pressure L_{I0}, but shifts the lobes of the scattered pressure towards the forward flight direction at higher Mach number.

The second part of the solution is the directivity associated with the factor $1/(K_s R_s)$. This term may be regarded as a geometric spreading factor and is plotted in Fig. 6.17 for

Mach numbers of $M = 0.3$ and $M = 0.8$. It can be seen that the directivity lobe for $M = 0.8$ is significantly larger in the aft flight direction than that for $M = 0.3$.

The third part of the transfer function $|H_p|$ of Eq. (5.32) is the factor $|x_3|/R_s$, and may be interpreted as dipole directivity factor, as shown in the plot of this function in Fig. 6.18. It indicates that the main radiation lobes associated with this term are always normal to the flat plate airfoil; the only effect of the Mach number being to alter the magnitude of the main lobes.

The combination of the last two factors, $|x_3|/(K_s R_s^2)$, accounts for the propagation to the far field. The directivity of this function is plotted in Figure 6.19 at Mach numbers of $M = 0.3$ and $M = 0.8$. Figure (6.19) shows that the main lobes are significantly larger in the aft flight direction at $M = 0.8$ than at $M = 0.3$. Figure. 6.16b suggests that $L_{I0} > L_{S0}$ in the aft flight direction and Fig. 6.19 indicates there is a large amplification in the same direction in the case of $M = 0.8$. It is therefore not surprising that the combined results of Figs. 6.16b and 6.19 account for a large noise radiation in Fig. 6.14 in the aft flight direction due to the incident pressure component. The results in Figs. 6.17 and 6.18 suggest that the mean-flow-corrected non-dimensional distance $K_s R_s$ are the main reasons for the shift in the main radiation lobe in D_H, and not changes in the source directivity.

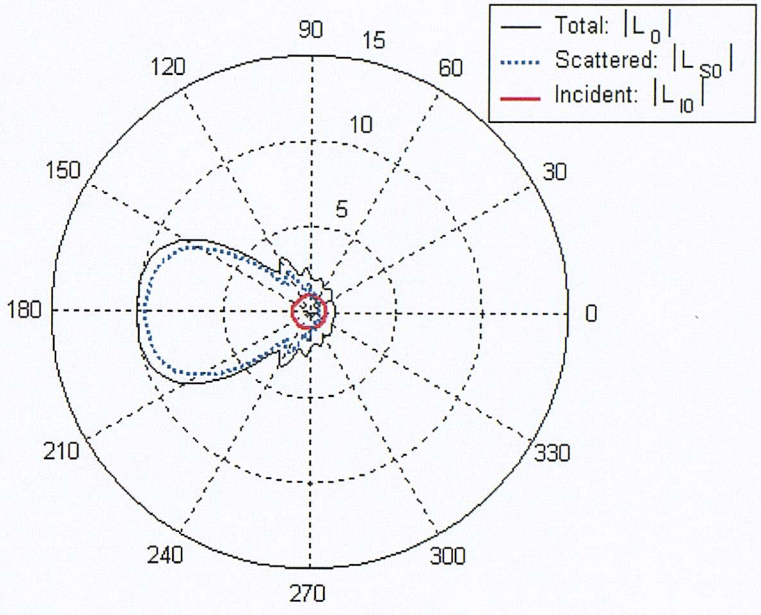

Figure 6.15a. Directivity of $|L_0|$, $|L_{S0}|$, $|L_{I0}|$ at Mach number $M = 0.3$

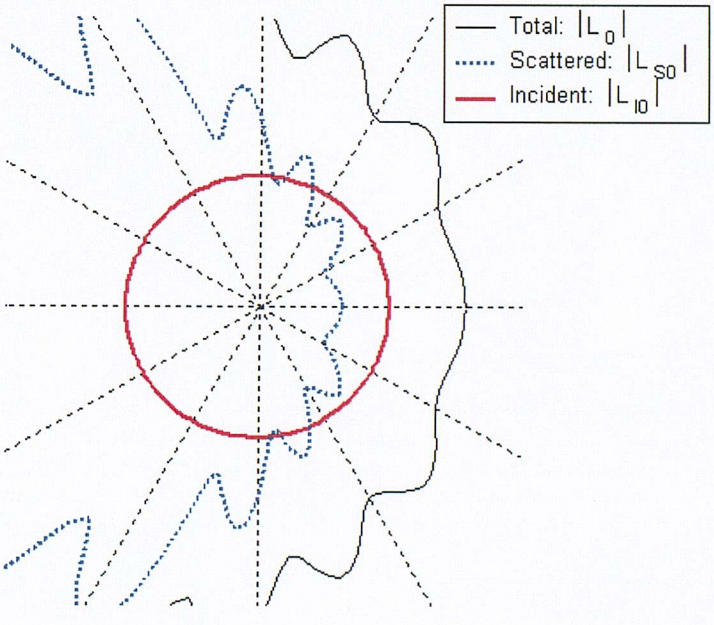

Figure 6.15b. Directivity of $|L_0|$, $|L_{S0}|$, $|L_{I0}|$ at Mach number $M = 0.3$, enlargement of Fig. 6.15a

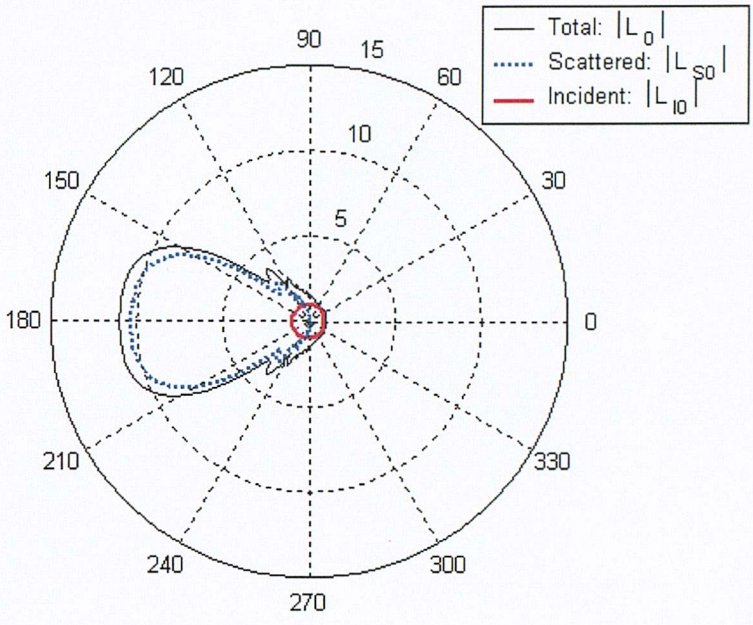

Figure 6.16a. Directivity of $|L_0|$, $|L_{S0}|$, $|L_{I0}|$ at Mach number $M = 0.8$

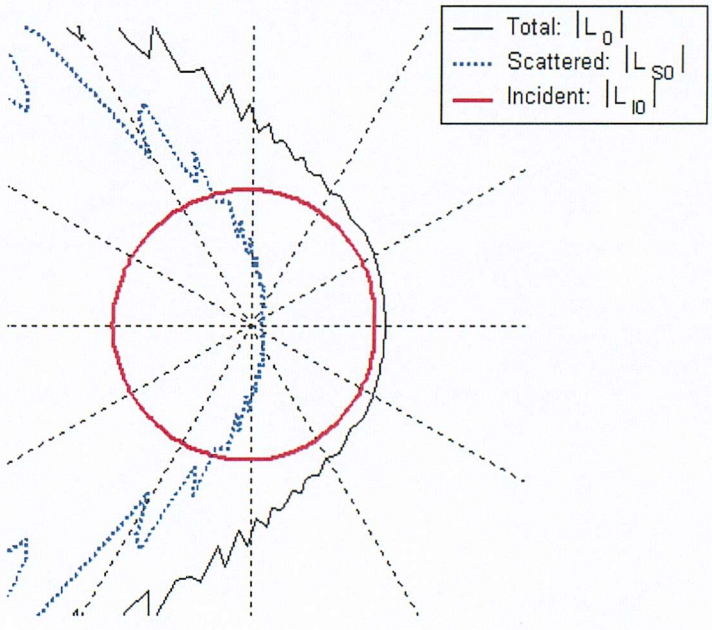

Figure 6.16b. Directivity of $|L_0|$, $|L_{S0}|$, $|L_{I0}|$ at Mach number $M = 0.8$, enlargement of Fig. 6.16a

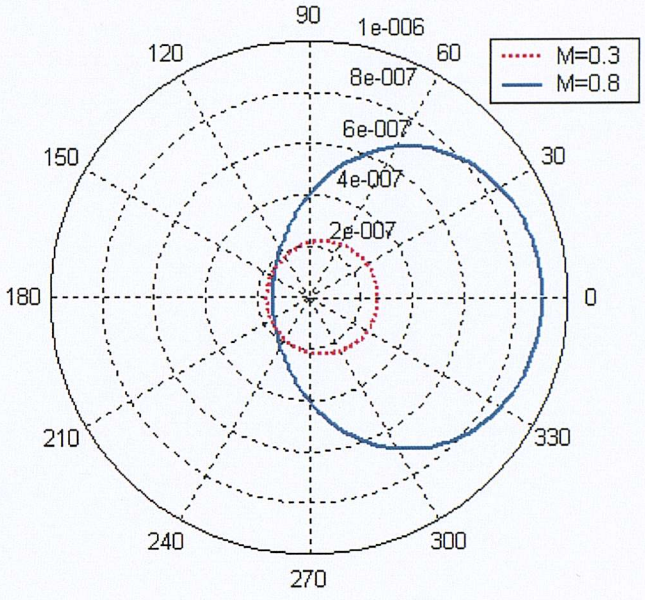

Figure 6.17. Directivity of geometric spreading factor $1/(K_s R_s)$

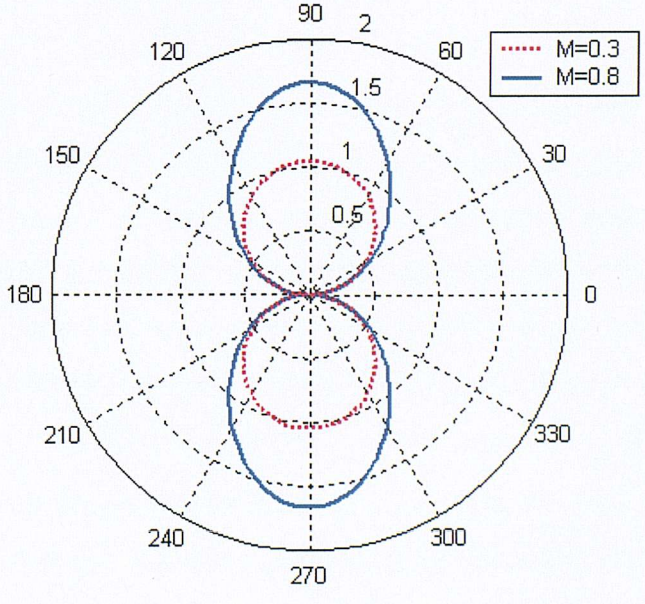

Figure 6.18. Directivity of factor $|x_3|/R_s$

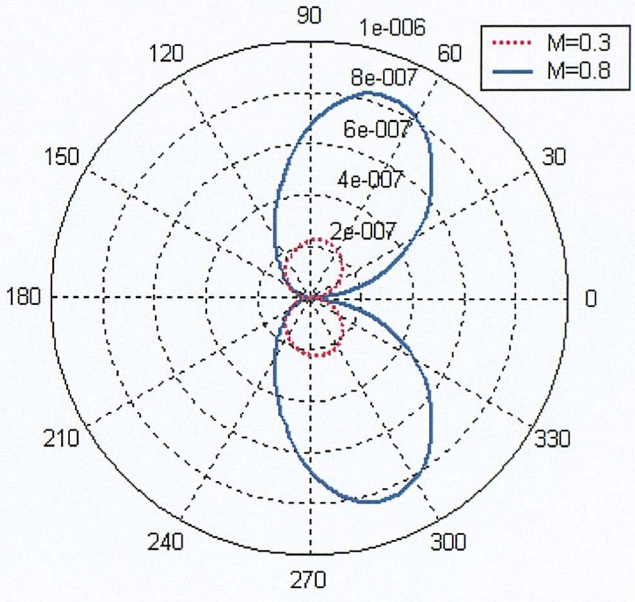

Figure 6.19. Directivity of the combined factor $|x_3|/(R_s^2 K_s)$

6.3 Self-noise Radiation From a NACA 0012 Airfoil

In this section, we investigate the self-noise radiation from the general family of NACA airfoils. Airfoil self-noise predictions using the numerical method given in Section 5.5 of the last Chapter are compared with the empirical predictions due to Brooks et al. (Brooks, Pope and Marcolini, 1989), which are based on experimental data from a NACA 0012 airfoil. The numerical method will be applied to predict the self-noise radiation from one of the NACA 0012 airfoils investigated by Brooks with 0.3048m chord length, a span of 0.4752m, and which moves in the $-y_1$ direction with Mach number $M = 0.208$ at an attack angle of $\alpha = 4°$. A convective velocity coefficient of $c_u = 0.8$ is used. Figure 6.20 shows the suction-side mesh of the NACA 0012 airfoil used for numerical calculation. The element dimension depends on the frequency requirement for self-noise prediction. If the element size l_e is required to be 10 times less than acoustic wavelength for a mesh that is valid up to $f = 3000$ Hz, the element

length should be less than $c_0/(10f) = 0.0115\,\text{m}$. Thus we use a mesh comprising 5952 triangle elements and 3038 nodes for the $0.3048m \times 0.4752m$ NACA 0012 airfoil. In

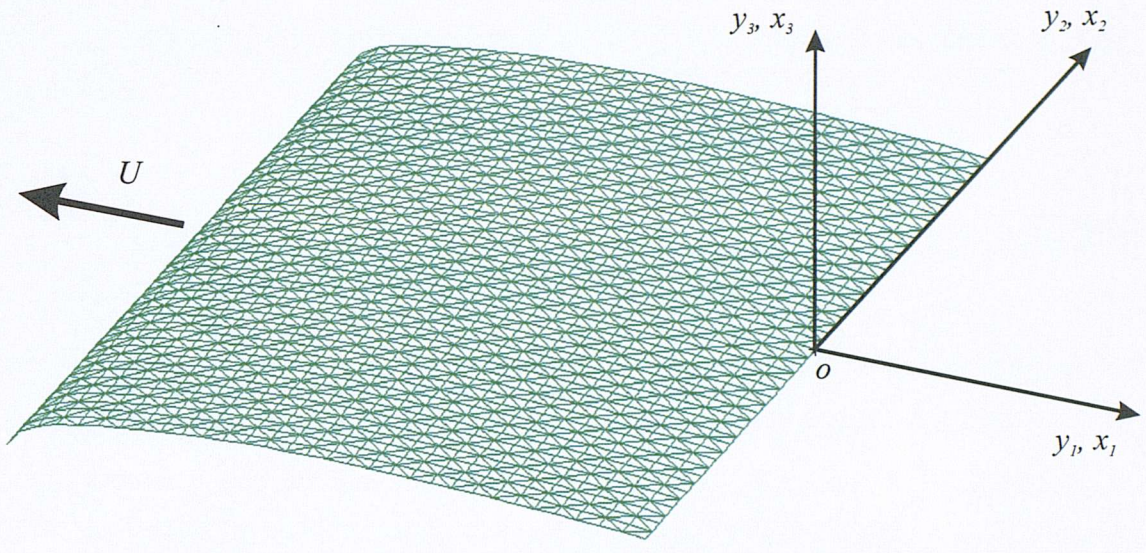

Figure 6.20. Suction side mesh of the NACA 0012 airfoil for numerical calculation, $c = 2b = 0.3048$ m, $2d = 0.4752$ m

order to investigate the effects of airfoil geometry, the NACA 0012 prediction are compared with prediction from a flat plate and a NACA 0024 airfoil. For the purpose of comparison, meshes of a flat plate airfoil and a NACA 0024 airfoil with the same chord and span length as the NACA 0012 airfoil were also created.

In this Section, the numerical method described by equation (5.34) will be used to predict the self-noise radiation. Amiet's solution is restricted to flat plate airfoils and, strictly speaking, is therefore unsuitable for this airfoil geometry. The use of Eqs. (5.38) and (5.39) for the numerical calculation of

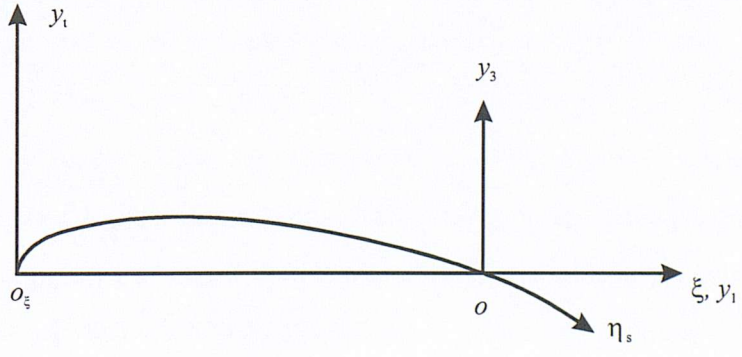

Figure 6.21. Airfoil coordinates

self-noise radiation requires the streamwise coordinate η_s of the airfoil profile to be determined. Figure 6.21 shows the coordinate system (ξ, y_t) used to express the airfoil profile, where ξ is the abscissa normalized on chord and y_t is the ordinate of the airfoil thickness distribution, also normalised on the chord. The streamwise coordinate η_s may be obtained from

$$\eta_s = c\int_1^{1-|y_1|/c} \sqrt{1+(dy_t/d\xi)^2}\, d\xi \tag{6.8}$$

where $c = 2b$ is airfoil chord length. For a NACA 0012 airfoil, the thickness distribution (see Abbott & Von Doenhoff, 1959) is given by

$$y_t = 0.6(0.2969\sqrt{\xi} - 0.126\xi - 0.3516\xi^2 + 0.2843\xi^3 - 0.1015\xi^4) \tag{6.9}$$

where $0 \le \xi \le 1$. The derivative of y_t required by Eq.(6.8) is

$$dy_t / d\xi = 0.6(0.14845/\sqrt{\xi} - 0.126 - 0.7032\xi + 0.8529\xi^2 - 0.406\xi^3) \tag{6.10}$$

The integration of (6.8) is performed numerically.

For the flat plate calculations presented in Section 6.2, all computations were carried out for zero angle of attack. It was therefore only necessary to perform the integration of Eq. (5.12) on one side of the flat plate airfoil since, by symmetry arguments, the total radiated noise is twice that for a (hypothetical) one-sided flat plate airfoil (Amiet, 1976a). However, for an airfoil of arbitrary geometry with non-zero angle of attack, the boundary layer turbulence on the airfoil pressure and suction sides differ and are statistically independent. In this case, the surface integrations appearing in Eqs. (5.12), (5.14) and (5.15) for the radiated pressure spectra must be performed on each side of the airfoil surface and the pressure spectral density due to each side added incoherently to give the total noise radiation. This is the method adopted in the rest of the thesis.

The combined Chase and Corcos spectrum described in Chapter II will be adopted for the prediction throughout this section. The position-dependent function f_p is calculated from the spectrum of Eq.(3.21).

6.3.1 Relative Contribution to Airfoil Self-Noise Radiation from Oblique Gust Components

In Section 6.2.5, the variation of $|H_p|^2$ with k_2 was investigated for single gust compoents on a flat plate airfoil. In this section, we investigate the relative contribution to self-noise radiation from the different k_2 components in a turbulent boundary layer comprising all k_2 components simultaneously. Figures 6.22 and 6.23 present a plot of the dimensionless integrands, $|H_p|^2 \hat{S}_{qq} / U_c (0.5\rho_0 \delta^*)^2 U^3$, in Eq. (5.15) against spanwise wavenumber $k_t \beta / \kappa_0$ (solid line). This complicated expression plotted against k_t specifies the relative contribution to airfoil self-noise radiation from the different k_t components (recall that k_t is the transverse wavenumber components in the curvilinear coordinate system attached to the airfoil). The calculations are made at the mid-span observation point $\mathbf{x} = (0.0, 0.0, 1.22)$ m, with $U = 71.3$ m/s at reduced frequencies of $\sigma_1 = 5.0, 20.1, 35.3, 50.4$ ($f = 300$ Hz, 1200Hz, 2100Hz, 3000Hz). Other parameters used are $c_u = 0.8$ and $\alpha = 4°$. Also shown for comparison (dashed curve) is the function $F(k_2)$ of Eq. (6.11) below, which is the factor appearing in the Amiet solution of Eqs. (5.26) and (5.27) for describing the variation of self-noise radiation with k_2 due to a flat plate airfoil,

$$F(k_2) = A \frac{\sin^2[(k_2 - \kappa x_2 / R_s)d]}{(k_2 - \kappa x_2 / R_s)^2 \pi d} \tag{6.11}$$

where A is a constant chosen arbitrarily to allow straightforward comparison with the numerical result. It can be seen that Eq. (6.11) provides a reasonable fit the k_t-dependence of the integrand in Eq. (5.15). Amiet makes the further approximation that Eq. (6.11) tends to a delta function at high $k_2 d$, suggesting that in this limit, only the

single k_2- component, $k_2 = \kappa x_2 / R_s$, makes a significant contribution to the far field radiation.

This behaviour is corroborated in figure 6.23. It shows that, at high frequency, the main contribution to broadband self-noise radiation for mid-span observers $x_2 = 0$ comes from the Fourier components of pressure arriving at the trailing edge close to normal incidence, $k_2 = 0$. This is due to the lack of cancellation in spanwise direction when a turbulent component arrives at the trailing edge in the normally incident direction. At low frequencies, as shown in Fig. 6.22, a broader spectrum of k_2-components can be seen to be making a significant contribution to the radiated pressure, including subsonic wave components for which $k_t \beta / \kappa_0 > 1$.

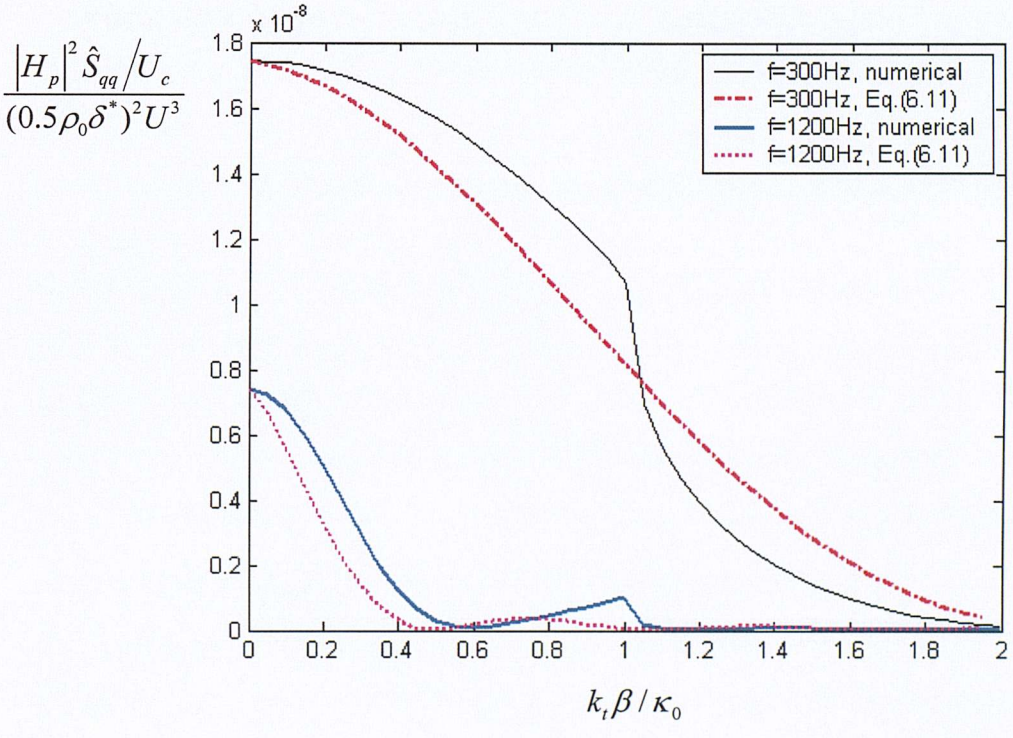

Figure 6.22. Non-dimensional integrand of Eq. (5.15) versus spanwise wavenumber $k_t \beta / \kappa_0$ for frozen incident turbulence, suction side, f = 300Hz, 1200Hz

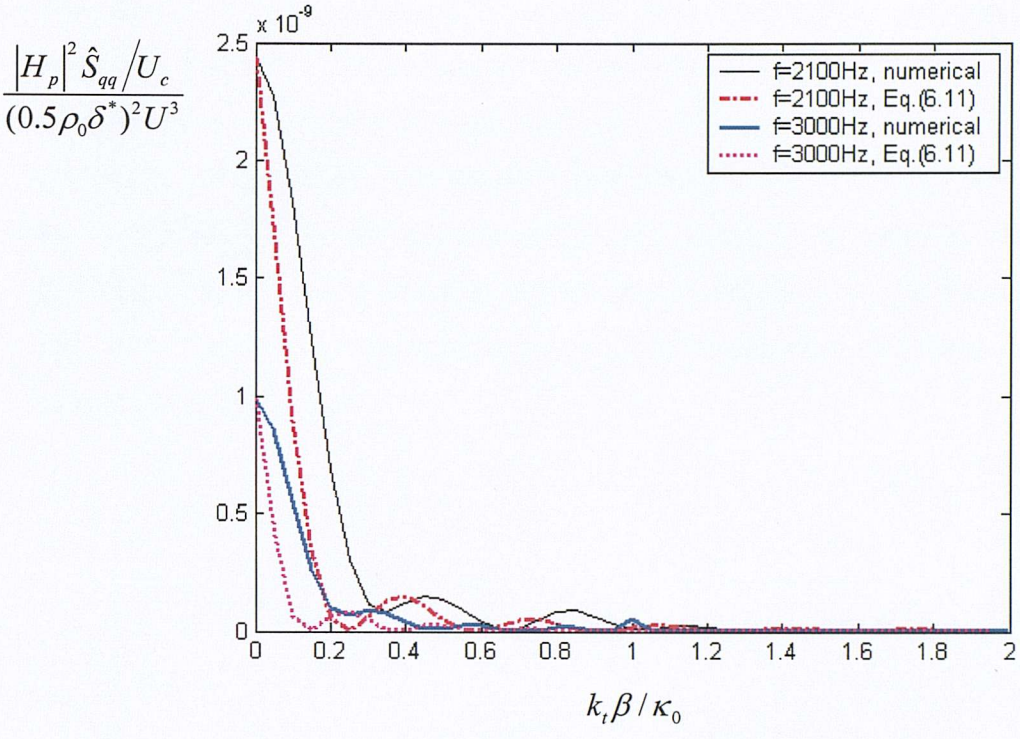

Figure 6.23. Non-dimensional integrand of Eq. (5.15) versus span wise wave number $k_t\beta/\kappa_0$ for frozen incident turbulence, suction side, $f = 2100$ Hz, 3000Hz

6.3.2 Broadband Self-Noise Directivity and the Effect of Airfoil Geometry

In this section, we investigate broadband self-noise directivity and the effect of airfoil geometry on self-noise radiation. Figures 6.24, 6.25, and 6.26 present the polar directivities of broadband self-noise, $D(\Psi, \pi/2, \omega)$, evaluated in the mid-span plane, for a flat plate, and a NACA 0012 and a NACA 0024 airfoil. The parameters used for the calculation are $R_d = 10.0$ m, $k_s = \kappa_c$, $\theta = \pi/2$, $c_u = 0.8$, and an attack angle of $\alpha = 4°$. Other parameters used in Fig. 6.24 are the frequency $f = 1042.8$ Hz ($\sigma_1 = 12.13$) and the Mach number $M = 0.3$. Figure 6.25 has the same Mach number as Fig. 6.24 but with a higher frequency of $f = 2780.8$ Hz ($\sigma_1 = 32.35$). Figure 6.27 has the same frequency as Fig. 6.24 but at a higher Mach number of $M = 0.8$. In these three figures the directivities for the NACA 0024 airfoil, the NACA 0012 airfoil, and the flat plate are represented by the dark solid line, the dotted line and the solid line, respectively. All airfoil geometries have the same chord of $c = 0.3048$ m and span of $2d = 0.4752$ m.

The directivity patterns exhibit asymmetric behaviour due to the non-zero angle of attack. In contrast with the single wavenumber directivity function of Fig.6.3, the broadband directivity function vary very slowly with polar angle. Airfoil geometry does not appear to appreciably alter the directivity pattern relative to a flat plate airfoil but it does significantly alter the sound pressure level in the airfoil chord direction, $\Psi = 0, \pi$, this effect being most pronounced at high Mach number. This effect of flow speed on directivity has been investigated in Section 6.2.7 for a single harmonic component of boundary layer pressure.

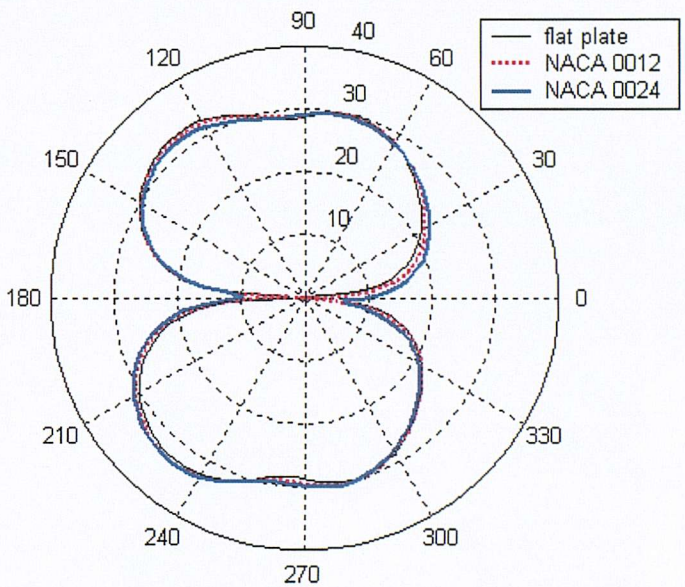

Figure 6.24. Polar directivity (in Ψ -direction), $D(\Psi, \pi/2, \omega)$ -13.0dB, of broadband noise for frozen incident turbulence, $\sigma_1 = 12.13$, $M = 0.3$

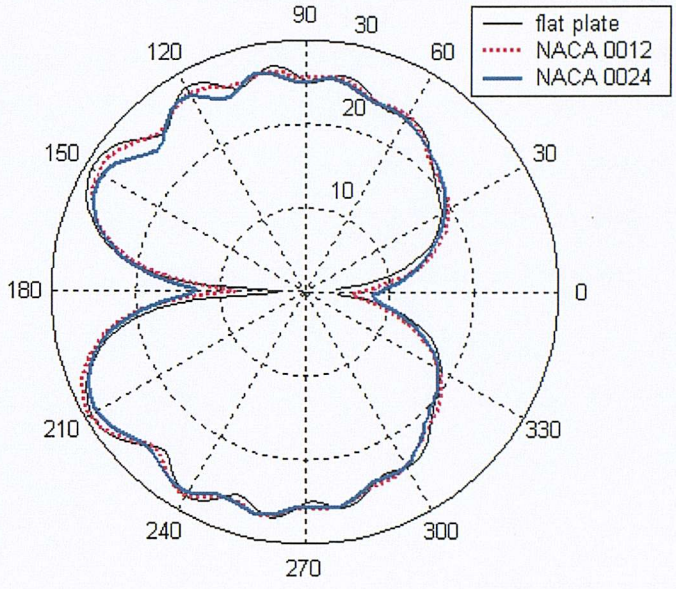

Figure 6.25. Polar directivity (in Ψ-direction), $D(\Psi,\pi/2,\omega)$ -13.0dB, of broadband noise for frozen incident turbulence, $\sigma_1 = 32.35$, $M = 0.3$

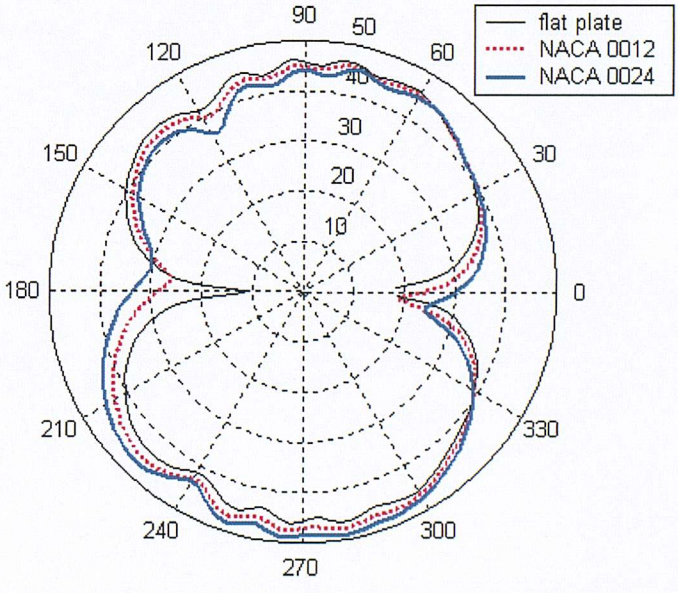

Figure 6.26. Polar directivity (in Ψ-direction), $D(\Psi,\pi/2,\omega)$ -13.0dB, of broadband noise for frozen incident turbulence, $\sigma_1 = 4.549, M = 0.8$

Figures 6.24 to 6.26 show the self-noise polar directivities, $D(\Psi,\pi/2,\omega)$ in the mid-span plane. We are now concerned with the directivity pattern at an arbitrary position away from mid-span plane ($\theta \neq \pi/2$). Figure 6.27 shows a comparison between the directivity patterns evaluated in the $\theta=\pi/2$ plane (mid-span plane) and the $\theta=\pi/4$ plane (non mid-span plane) for a NACA 0012 airfoil. It can be seen that the broadband directivity pattern does not alter significantly from the $\theta=\pi/4$ plane to the $\theta=\pi/2$ plane. Figure 6.28 shows the self-noise azimuthal directivity, $D(\pi/2,\theta,\omega)$, in the $\Psi=\pi/2$ plane for a NACA 0012 airfoil. Figure 6.28 suggests that the self-noise is about 20 dB lower in the spanwise direction ($\theta=0$) than in the normal spanwise direction ($\theta=\pi/2$). The computation parameters used to calculate Figs 6.27 and 6.28 are the same as for Fig. 6.24.

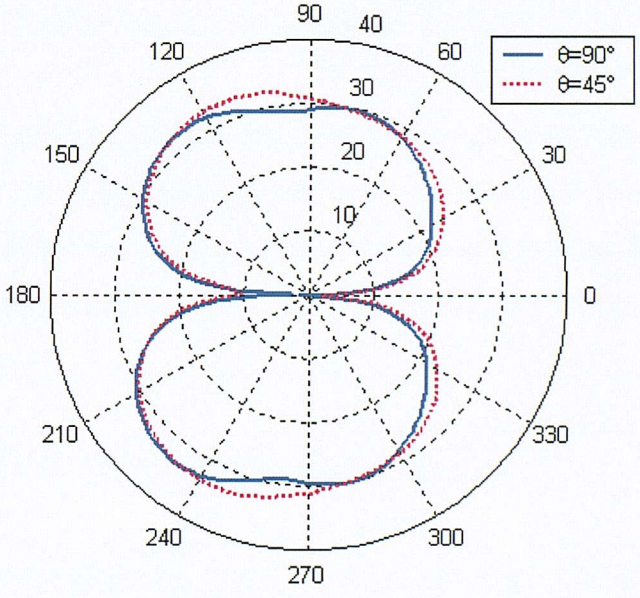

Figure 6.27. Polar directivity, $D(\Psi,\pi/2,\omega)$ -13.0dB, of broadband self-noise (in Ψ -direction) for frozen incident turbulence, $\sigma_1=12.13$, $M=0.3$

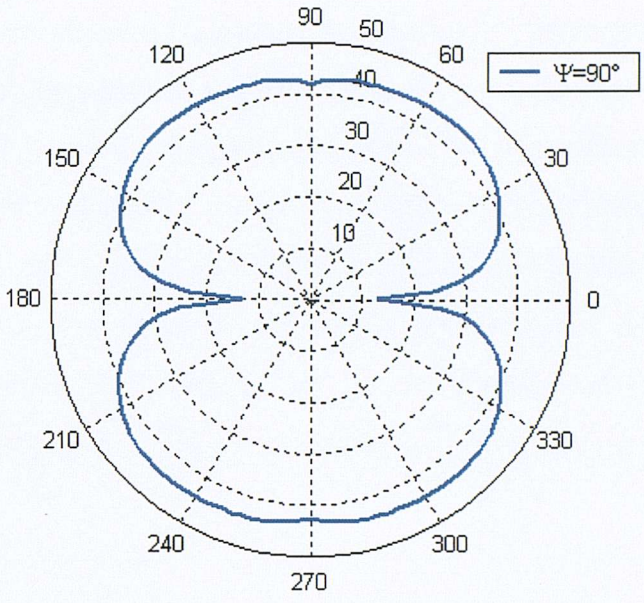

Figure 6.28. Azimuthal directivity, $D(\pi/2,\theta,\omega)$, of broadband self-noise (in θ-direction) for frozen incident turbulence, $\sigma_1 = 12.13$, $M = 0.3$

6.3.3 Broadband Self-noise Spectral Predictions

In this section, the broadband self-noise prediction obtained using the numerical scheme presented in this thesis is compared with the empirical prediction scheme proposed by Brooks. The effect of airfoil geometry on the broadband self-noise spectrum will then be discussed. The effect of airfoil geometry on directivity has previously been discussed in Section 6.3.2.

6.3.3.1 Validation of Airfoil Self-noise Prediction Scheme

By way of validation of the proposed prediction method, Figure 6.29 shows comparisons between the numerical predictions of broadband self-noise with that predicted using the empirical prediction scheme due to Brooks. The Brooks scheme is based on a regression analysis of extensive experimental data of the self-noise radiation from a NACA 0012 airfoil over a broad range of flow speeds, angles of attack and chord lengths (Brooks, Pope and Marcolini, 1989). The sound pressure level (SPL) is defined in equation (6.2). The prediction is made for a NACA 0012 airfoil with a chord length of 0.3048m and a

span of 0.4752m, moving in the $-y_1$ direction with Mach number $M = 0.208$. The observation point is at $\mathbf{x} = (0.0, 0.0, 1.22)$ m, to be consistent with the experimental set up of Brooks. In Fig. 6.29, the solid line is the result calculated from the Brooks prediction scheme. The dark solid line is the numerical prediction assuming frozen boundary layer turbulence integrated over the full k_t range (with upper limit of integration chosen to ensure convergence of the pressure prediction), while the dashed line is the numerical result integrated within the range of supersonic wavenumber components only, $0 \le k_t \le \kappa$. The dotted solid line in Fig. 6.29 is the broadband noise prediction for non-frozen boundary layer turbulence integrated over the k_t range of $0 \le k_t \le \kappa$ as calculated

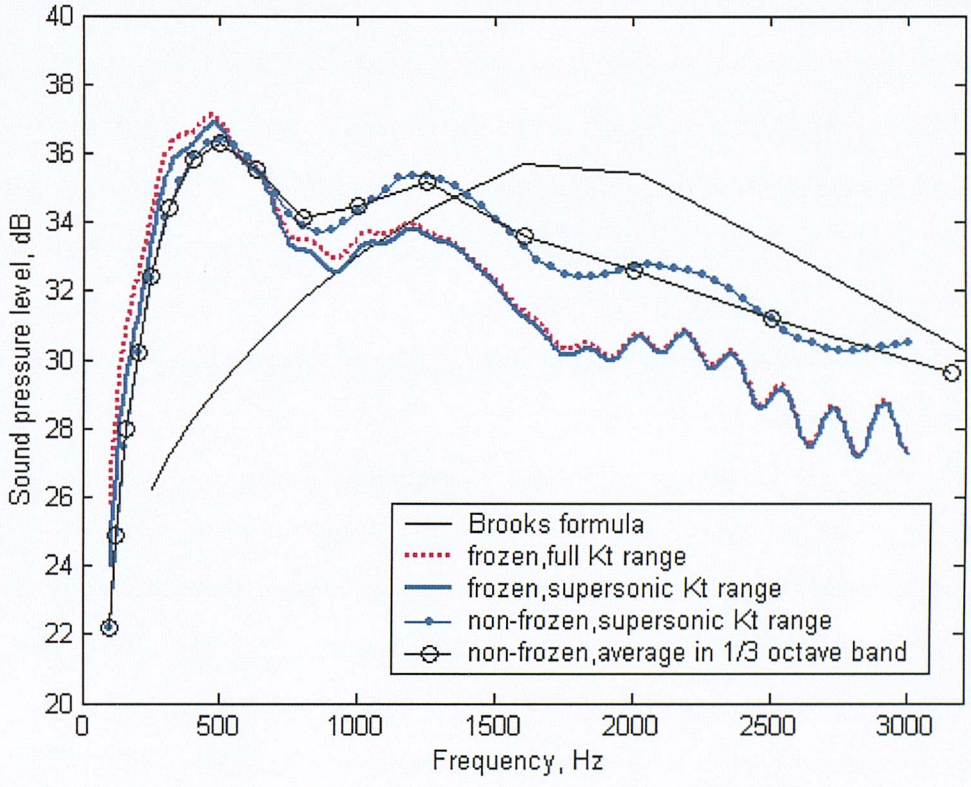

Figure. 6.29. Comparison of broadband self-noise with Brooks empirical prediction

from Eq. (5.14). The numerical predictions are shown to be within 6dB of the Brooks prediction. Note that the Brooks prediction scheme applies to 1/3 octave bands only and cannot capture the details in the spectrum. The solid line with circles shows the spectral density averaged in 1/3 octave bands for non-frozen boundary layer turbulence integrated over the supersonic k_t range. At the high frequencies this matches the Brooks

data slightly better. Figure 6.29 shows that the contributions from subsonic k_t components become increasingly small as frequency increases. It also suggests that the frozen turbulence assumption gives a better approximation at low frequency than at high frequency. The difference in the self-noise prediction between the frozen and non-frozen gust assumptions is about 2 dB at high frequency. Thus, the frozen-turbulence assumption appears to be a reasonable assumption for making airfoil self-noise predictions.

The computation time for numerical prediction presented here is 4.5 minutes per frequency per observation point for frozen incident turbulence over full k_t- integration range while for a k_t- integration range of $0 \le k_t \le \kappa$, the computation takes only 2.2 minutes per frequency per observation point on a 1.2 GHz PC. However, for non- frozen turbulence, which involves performing an additional integration over k_s, the computation takes 240.9 minutes per frequency per observation point for a supersonic k_t- range integration of $0 \le k_t \le \kappa$ in a 1.2 GHz PC.

6.3.3.2 Effect on Airfoil Self-Noise Radiation due to Airfoil Geometry

Figures 6.30 to 6.32 show broadband self-noise prediction for the three airfoil geometries of, NACA 0024, NACA 0012 and a flat plate airfoil. Figure 6.30 is the self-noise prediction at observation point $\mathbf{x} = (0.0, 0.0, 1.22)$ m (at $\Psi = 90°$) for a Mach number of $M = 0.208$, Figure 6.31 is for the same set of parameters as in Fig. 6.30 but with Mach number of $M = 0.8$, Figure 6.32 is the prediction at $\mathbf{x} = (-1.178, 0.0, -0.316)$ m (at $\Psi = 195°$) for a Mach number of $M = 0.8$. These figures suggest that at high Mach number, airfoil geometry may significantly influence the radiation, particularly in the forward flight direction, as indicated in Fig. 6.26.

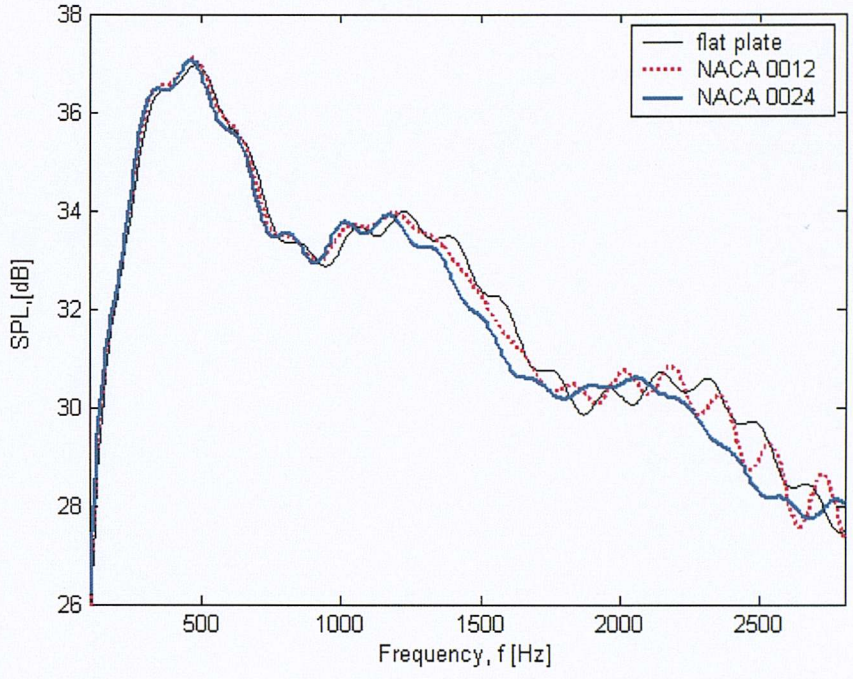

Figure 6.30. Comparison of broadband self-noise for different airfoil geometries, at observation point $\mathbf{x} = (0.0, 0.0, 1.22)$ m, $M = 0.208$

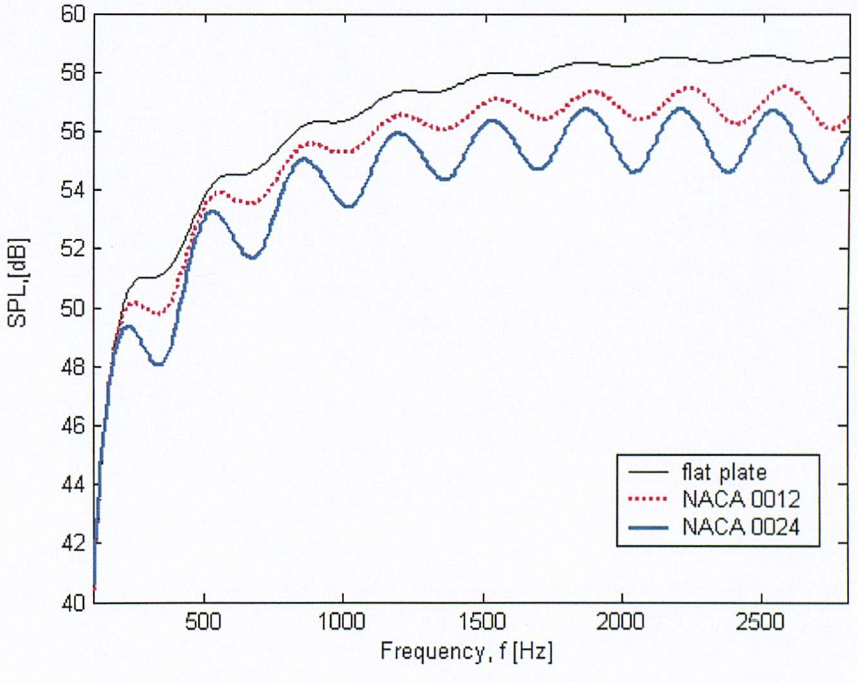

Figure 6.31. Comparison of broadband self-noise for different airfoil geometries, at observation point $\mathbf{x} = (0.0, 0.0, 1.22)$ m, $M = 0.8$

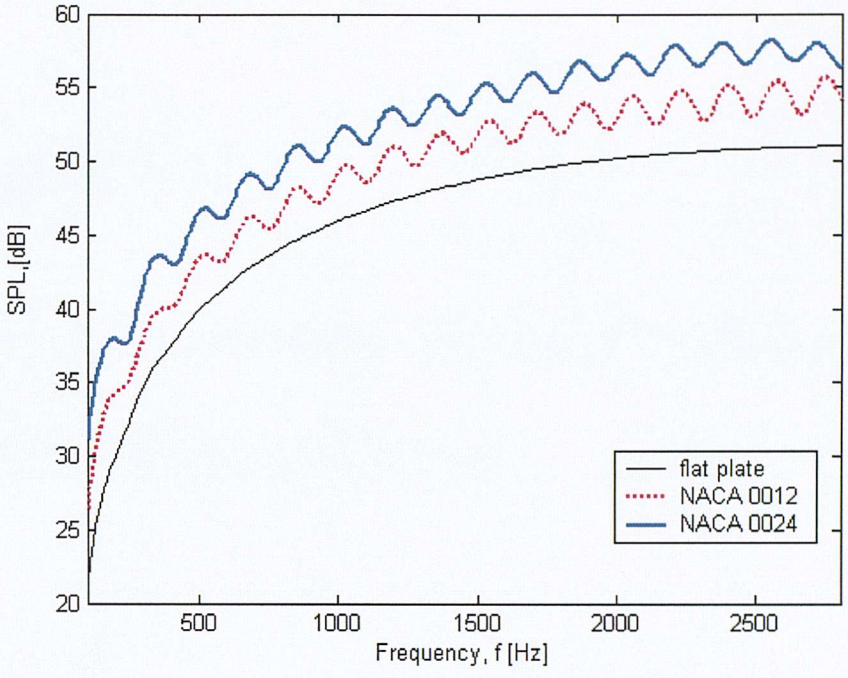

Figure 6.32. Comparison of broadband self-noise for different airfoil geometry, at observation point $\mathbf{x} = (-1.178, 0.0, -0.316)\,\mathbf{m}$, $M = 0.8$

Chapter VII

Rotor Broadband Noise Prediction: General Formulation

7.1 Introduction

This Chapter describes a frequency domain approach for the prediction of broadband noise radiated from a rotor or propeller in free field. The formula obtained can also be used to calculate the tonal noise when the surface pressure is taken as a steady force distribution due to the lift and drag forces over the rotating blades. The approach has particular application to fan broadband self-noise. This generalized formulation allows for the integration of the steady and unsteady forces over the real blade surfaces and hence no thin airfoil approximation is made, as has been done in previous studies(Hanson,1983). The relationship between the spectrum of unsteady surface pressure and the radiated far-field spectrum is clearly established. The unsteady blade loading, which constitutes the aerodynamic sound sources, can be estimated by combining single-airfoil theory discussed in Chapter IV, the representation of the turbulence wavenumber spectrum proposed by Corcos (1963), and the measured boundary layer frequency spectrum and boundary thickness measurements made by Brooks, Pope and Marcolini (1989). The application of unsteady airfoil theory to predict the self-noise due to a rotor blade requires an assumption that the boundary layer turbulence at a particular spanwise position is the same as that on an airfoil of infinite span with prismatic cross section at the same mean free-stream velocity and angle of attack. This is similar to the strip theory used for an airfoil (for example, Goldstein, 1976).

7.2 Co-ordinate Systems

The analysis presented here is formulated in a moving reference frame (aircraft-fixed coordinates), which moves with constant velocity $\mathbf{U} = (U,0,0)$ as shown in Fig.7.1. In the moving reference frame, the coordinates of the observation point and source point in

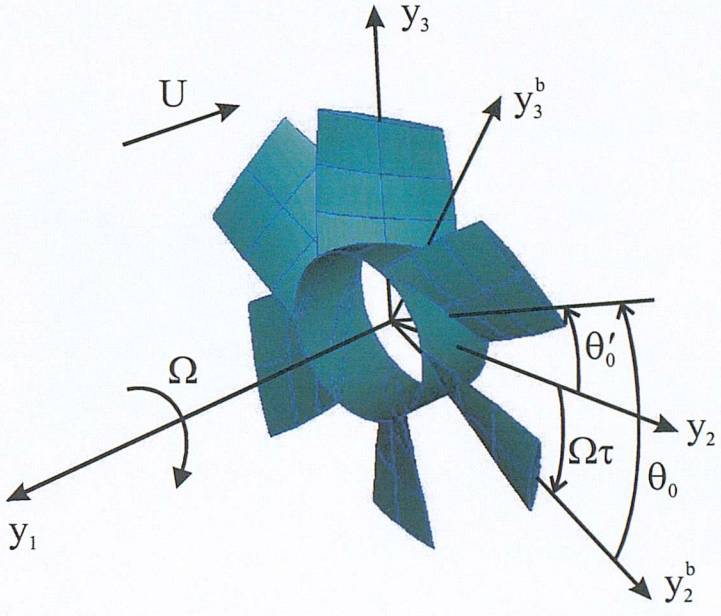

Figure 7.1. Relation between the moving coordinate system $\mathbf{y} = (y_1, r_0, \theta_0')$ and the blade-fixed coordinate system $\mathbf{y}^b = (y_1, r_0, \theta_0)$

a cylindrical coordinate system are denoted by $\mathbf{x} = (x_1, r, \theta')$ and $\mathbf{y} = (y_1, r_0, \theta_0')$, respectively. The relationships between the rectangular coordinate system and the cylindrical coordinate systems are:

$$x_1 = x_1,\ x_2 = r\cos\theta', x_3 = r\sin\theta' \tag{7.1}$$

$$y_1 = y_1,\ y_2 = r_0\cos\theta_0', y_3 = r_0\sin\theta_0' \tag{7.2}$$

In the blade-fixed coordinates, the observation point and the source point are respectively denoted by $\mathbf{x}^b = (x_1, r, \theta)$ and $\mathbf{y}^b = (y_1, r_0, \theta_0)$. The transformations between the moving coordinate system and the blade-fixed coordinate system are:

$$\mathbf{x}(x_1, r, \theta') = \mathbf{x}^b(x_1, r, \theta - \Omega\tau) \tag{7.3}$$

$$\mathbf{y}(y_1, r_0, \theta_0') = \mathbf{y}^b(y_1, r_0, \theta_0 - \Omega\tau) \tag{7.4}$$

where τ is the time associated with the emission of sound, and Ω is the angular velocity of the blade rotating in the opposite direction of θ_0', as shown in Fig.7.1.

In addition to the rectangular coordinate system $\mathbf{y} = (y_1, y_2, y_3)$ employed in this thesis, we also make use of the curvilinear coordinate system $\boldsymbol{\eta} = (\eta_s, \eta_t)$ to express the surface pressure distribution, as shown in Fig. 7.2. Here $\eta_s = \eta_s(\mathbf{y}^b)$ is the streamwise arc length with the origin located at the trailing edge and $\eta_t = \eta_t(\mathbf{y}^b)$ is the spanwise arc length normal to η_s upon the suction-side or pressure-side surface. Correspondingly, we use k_s and k_t to denote the streamwise wavenumber and the spanwise wavenumber, respectively.

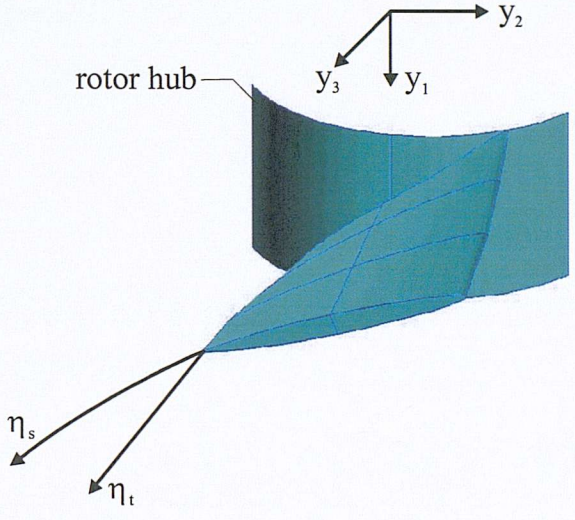

Figure 7.2. Blade curvilinear coordinate system (η_s, η_t) and associated wavenumber (k_s, k_t)

If we use a cylinder of radius r_0 cut through the propeller blade with cylinder axis parallel to the propeller axis, the blade section profile will closely fit onto the cylinder surface. Unwrapping the cylinder surface onto a flat plane forms a right-angled triangle as

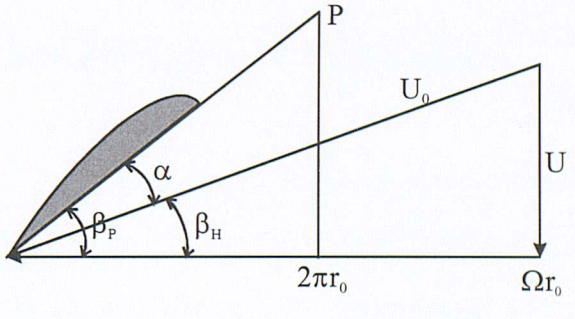

Figure 7.3. Geometric pitch triangle and hydrodynamic velocity triangle (the arrow shows the direction of fluid velocity) , pitch angle β_P, hydrodynamic angle β_H and attack angle α

shown in Fig. 7.3. The adjacent side of the triangle is the circumference $2\pi r_0$ of the cylinder circular end. The opposite side is the advanced distance (pitch distance), P, of a point along the helicoidal chord line when the point rotates with a full circular angle. The hypotenuse forms part of the blade section chord line as shown in Fig. 7.3. The angle formed between the adjacent side and the hypotenuse is referred to as the geometric pitch angle β_P.

Figure 7.3 also shows the velocity triangle formed from the propeller forward flight velocity U, the blade section rotational velocity Ωr_0, and the resultant inflow velocity U_0, given by

$$U_0 = \sqrt{U^2 + (\Omega r_0)^2} \tag{7.5}$$

From this velocity triangle, shown in Fig. 7.3, the relative inflow angle β_H can be obtained by

$$\beta_H = \tan^{-1}\left(U / \Omega r_0\right) \tag{7.6}$$

Finally, the attack angle of the blade section is given by

$$\alpha = \beta_P - \beta_H \tag{7.7}$$

7.3 Unsteady Blade Surface Pressure Estimation

We assume that the blade section develops the same surface pressure distribution as an isolated airfoil with the same local inflow velocity U_0, the same angle of attack α, and the same sectional geometry. Here the local incoming velocity U_0 at the blade section of radius r_0 is used instead of the airfoil incoming velocity U. Under this assumption, the pressure, $p_t(\mathbf{y}^b, \tau)$, of Eq. (4.30) on the blade surface can be written in terms of an integral over wavenumber-frequency components $\hat{p}_i(k_s, k_t, \omega_0)$ of the incident surface pressure of the form

$$p_t(\mathbf{y}^b,\tau)=\int_{-\infty}^{\infty}\int_{-\infty}^{\infty}\int_{-\infty}^{\infty}H_q(\mathbf{y}^b,k_s,k_t,\omega_0)\hat{p}_i(k_s,k_t,\omega_0)e^{i(k_s\eta_s+k_t\eta_t-\omega_0\tau)}dk_s dk_t d\omega_0 \tag{7.8}$$

where ω_0 is the source angular frequency measured in the blade fixed coordinate system.

The turbulence wall pressure $p_t(\mathbf{y},\tau)$ is measured in the blade fixed coordinate system, which we now denote by $p_t(\mathbf{y}^b,\tau)$. The surface pressure varies along the chord direction of the blade-section airfoil. This variation is accommodated in the position-dependent function, which we now indicate by $f_p(\mathbf{y}^b,\mathbf{k},\omega_0)$. Note that $f_p(\mathbf{y}^b,\mathbf{k},\omega_0)$ varies in the streamwise direction as well as the blade spanwise direction because the incoming velocity U_0 and the angle of attack α vary along the rotor radius r_0. For an airfoil of uniform profile, $f_p(\mathbf{y},\mathbf{k},\omega_0)=1$ along the airfoil trailing edge. However, for a rotating blade, $f_p(\mathbf{y}^b,\mathbf{k},\omega_0)\neq 1$ along the blade trailing edge. To allow for this situation, equation (4.29) must be reformulated as

$$H_q(\mathbf{y}^b,\mathbf{k},\omega_0)=\begin{cases} f_p(\mathbf{y}^b,\mathbf{k},\omega_0)+\frac{1}{2}f_p(\mathbf{y}^b_{TE},\mathbf{k},\omega_0)H_s(\mathbf{y}^b,\mathbf{k},\omega_0), & \mathbf{y}^b \text{ on the turbulence side} \\ -\frac{1}{2}f_p(\mathbf{y}^b_{TE},\mathbf{k},\omega_0)H_s(\mathbf{y}^b,\mathbf{k},\omega_0), & \mathbf{y}^b \text{ not on the turbulence side} \end{cases} \tag{7.9}$$

where $\mathbf{y}^b_{TE}$ takes coordinate value of $\mathbf{y}^b$ at the trailing edge, in the coordinate system of (η_s,η_t), $\mathbf{y}^b_{TE}=(0,\eta_t)$. Note that the quantities M_0, β_0, μ_0, K in Eq. (7.9) take their local blade section values at radius r_0.

When the transfer function H_s of Eq. (4.27), which is valid for a single airfoil, is applied to a multi-bladed rotor, an inherent assumption is made that the blade surface pressure due to the scattering of sound by adjacent blades can be neglected. However, if the incident surface pressure spectrum is measured on a rotating blade surface with

adjacent blades present (Carley and Fitzpatrick, 2000), the scattering effects of adjacent blades will have been included in the incident pressure spectrum. On the other hand, we shall emphasize that the effects of multiblade geometry on sound radiation are always included in the later derived formulation by integrating over all the blade surface.

7.4 Important Identities for the Derivation of the Frequency-domain Formulation

In this section, mathematical identities will be presented to assist further derivation of the frequency-domain theory developed in the next section for making rotor self-noise prediction.

As described in Section 1.2.3, volume-displacement sources due to the blade thickness and quadrupole sources outside the blade surface are only important at high relative flow speeds close to the sound speed. We shall therefore confine our attention to the sound radiation due to the unsteady blade forces exerted by the blade surface on the adjacent fluid, caused by turbulence interaction with the airfoil and its trailing edge. Thus, we are concerned only with the second term of Eq.(2.5), which we now denote by

$$p(\mathbf{x},t) = \int_{-T}^{T} \iint_{S(\tau)} \frac{\partial G}{\partial y_j} f_j \, dS(\mathbf{y}) d\tau \tag{7.10}$$

The difficulty arises in the evaluation of Eq. (7.10) because the emission time τ is implicitly included within its integrand. In order to avoid this difficulty, the following key steps will be employed to reformulate the governing equations in the frequency domain. Equation (7.10) is expressed in the moving, aircraft-fixed coordinate system. The cylindrical coordinate system described by Eqs.(7.1) and (7.2) will be employed for convenience. It is natural to express the observation point $\mathbf{x} = (x_1, r, \theta')$ in the moving reference frame, while the source point $\mathbf{y}^b = (y_1, r_0, \theta_0)$ is expressed in the blade-fixed coordinate system, thereby allowing simple integration of the source distribution over the blade surface, as required by Eq. (7.10). The coordinate transform (7.4) will

therefore be applied to Eq. (7.10), but the coordinate transform (7.3), which is related to the observation point, will not. With the above considerations, the mean-flow corrected distance R in the Green function of Eq.(2.13), in which the observation point $\mathbf{x}=(x_1,r,\theta')$ is expressed in the moving coordinate system and the source point $\mathbf{y}^b=(y_1,r_0,\theta_0)$ expressed in the blade-fixed coordinates, becomes

$$R=\sqrt{(y_1-x_1)^2+\beta^2[r^2+r_0^2-2rr_0\cos(\theta_0-\Omega\tau-\theta')]} \tag{7.11}$$

Note that only the source-time variable τ appears inside the expression for R, and not the observation time t. Fourier transformation of Eq. (7.10) with respect to t using the Green function of Eq.(2.13) can therefore be carried out explicitly to give

$$\frac{e^{i\mu R}}{R}=\frac{e^{i\mu\sqrt{X^2+R_0^2}}}{\sqrt{X^2+R_0^2}} \tag{7.12}$$

where $X=y_1-x_1$, $R_0=\beta\sqrt{r^2+r_0^2-2rr_0\cos(\theta_0-\Omega\tau-\theta')}$, and $\mu=\kappa/\beta^2$ defined after Eq.(2.14). Equation (7.12) can be rewritten as an integral over a separable function of X and R_0 by using the identity (Gradshteyn and Ryzhik (1965))

$$\frac{e^{i\mu\sqrt{X^2+R_0^2}}}{\sqrt{X^2+R_0^2}}=\frac{i}{2}\int_{-\infty}^{\infty}e^{ik_0X}H_0^{(1)}(R_0\sqrt{\mu^2-k_0^2})dk_0 \tag{7.13}$$

where $H_0^{(1)}$ is the zero order Hankel function of the first kind. In what follows we shall also make use of the identity:

$$H_0^{(1)}(K_0\sqrt{r^2+r_0^2-2rr_0\cos(\theta_0-\Omega\tau-\theta')})=\sum_{m=-\infty}^{\infty}J_m(K_0r_<)H_m^{(1)}(K_0r_>)e^{im(\theta_0-\Omega\tau-\theta')} \tag{7.14}$$

where

$$K_0 = \beta\sqrt{\mu^2 - k_0^2}\,, \qquad r_< = \min\{r, r_0\}, \qquad r_> = \max\{r, r_0\} \qquad (7.15,7.16,7.17)$$

and J_m denotes the m^{th} order Bessel function of the first kind. The useful aspect of Eq.(7.14) is that τ now only appears in a complex exponential term, which allows the integration of Eq. (7.10) with respect to τ to be readily performed.

7.5 Radiation Transfer Function and Pressure Spectrum

Consider a rotor comprising N_b blades. Substituting the Green function of Eq.(2.13) into Eq. (7.10) for the radiated pressure due to a single blade surface S_i gives

$$p(\mathbf{x},t) = \int_{-T}^{T}\iint_{S_i} f_j(\mathbf{y},\tau)\frac{\partial}{\partial y_j}\left[\frac{1}{4\pi R}\delta[\tau + \frac{1}{\beta^2 c_0}(R + M(y_1 - x_1)) - t]\right]dS(\mathbf{y})d\tau \qquad (7.18)$$

Fourier transforming Eq. (7.18) with respect to t gives the acoustic pressure due to a single blade as

$$\begin{aligned}\overline{p}(\mathbf{x},\omega) &= \frac{1}{2\pi}\int_{-\infty}^{\infty} p(\mathbf{x},t)e^{i\omega t}dt \\ &= \frac{1}{4\pi}\frac{1}{2\pi}\int_{-T}^{T}\iint_{S_i} f_j(\mathbf{y},\tau)e^{i\omega\tau}\frac{\partial}{\partial y_j}\left[\frac{1}{R}e^{i\mu R}e^{i\mu M(y_1 - x_1)}\right]dS(\mathbf{y})d\tau\end{aligned} \qquad (7.19)$$

Substituting Eqs. (7.12) to (7.14) into Eq. (7.19), and noting that on a blade surface $y_1 = S_i(r_0,\theta_0)$ and hence $dS(\mathbf{y}) = \sqrt{1 + (\partial y_1/\partial r_0)^2 + (\partial y_1/r_0\partial\theta_0)^2}\, r_0 d\theta_0 dr_0$, leads to

$$\overline{p}(\mathbf{x},\omega)=\frac{i}{8\pi}\frac{1}{2\pi}\int_T^T\iint_{S_i}f_j(\mathbf{y}^b,\tau)e^{i\omega\tau}\sqrt{1+\left(\frac{\partial y_1}{\partial r_0}\right)^2+\left(\frac{1}{r_0}\frac{\partial y_1}{\partial \theta_0}\right)^2}$$

$$\times\frac{\partial}{\partial y_j^b}\left[\sum_{m=-\infty}^{\infty}e^{im(\theta_0-\Omega\tau)}\int_{-\infty}^{\infty}g^m(\mathbf{x},r_0,k_0,\omega)e^{i(k_0+\mu M)y_1}dk_0\right]r_0d\theta_0dr_0d\tau \tag{7.20}$$

where $g^m(\mathbf{x},r_0,k_0,\omega)$ is defined as

$$g^m(\mathbf{x},r_0,k_0,\omega)=e^{-i(k_0+\mu M)x_1}J_m(K_0r_<)H_m^{(1)}(K_0r_>)e^{-im\theta'} \tag{7.21}$$

The blade loading f_j in Eq.(7.20) is related to the surface pressure by

$$\mathbf{f}(\mathbf{y}^b,\tau)=-\mathbf{n}\,p_s(\mathbf{y}^b,\tau) \tag{7.22}$$

where $\mathbf{n}=\{n_1,n_r,n_\theta\}$ is the unit normal vector pointing inwards from the blade surface. Substituting Eq. (7.8) and Eq. (7.22) into Eq. (7.20) allows $\overline{p}(\mathbf{x},\omega)$ to be expressed in the form,

$$\overline{p}(\mathbf{x},\omega)=\int_{-\infty}^{\infty}\int_{-\infty}^{\infty}\hat{p}(\mathbf{x},k_s,k_t,\omega)dk_sdk_t \tag{7.23}$$

where $\hat{p}(\mathbf{x},k_s,k_t,\omega)$ is the contribution to the radiated pressure from each wavenumber component of boundary layer pressure at frequency ω. Each of these components can be related to the Fourier components of the incident surface pressure via a transfer function $H_p(\mathbf{x},k_s,k_t,\omega,\omega_0)$ defined by

$$\hat{p}(\mathbf{x},k_s,k_t,\omega)=\int_{-\infty}^{\infty}H_p(\mathbf{x},k_s,k_t,\omega,\omega_0)\hat{p}_i(k_s,k_t,\omega_0)d\omega_0 \tag{7.24}$$

From Eqs. (7.20), (7.23) and (7.24), H_p is given by

$$H_p(\mathbf{x},k_s,k_t,\omega,\omega_0)=\frac{-i}{8\pi}\sum_{m=-\infty}^{\infty}\left\{\iint_{S_i}H_q(\mathbf{y}^b,k_s,k_t,\omega_0)e^{i(k_s\eta_s+k_t\eta_t)}\sqrt{1+\left(\frac{\partial y_1}{\partial r_0}\right)^2+\left(\frac{1}{r_0}\frac{\partial y_1}{\partial \theta_0}\right)^2}\,n_j(\mathbf{y}^b)\right.$$
$$\left.\times\frac{\partial}{\partial y_j^b}\left[e^{im\theta_0}\int_{-\infty}^{\infty}g^m(\mathbf{x},r_0,k_0,\omega)e^{i(k_0+\mu M)y_1}dk_0\right]\delta(\omega_0-\omega+m\Omega)\right\}r_0d\theta_0dr_0 \tag{7.25}$$

where we have used the identity

$$\delta(\omega_0-\omega+m\Omega)=\frac{1}{2\pi}\int_{-T}^{T}e^{-i(\omega_0-\omega+m\Omega)\tau}d\tau \tag{7.26}$$

Equation (7.25) only requires integration over a single blade surface S_i. In order to include the effect of all N_b blades, we denote the θ_0-dependent terms in Eq. (7.25) by

$$F_j(\mathbf{y}^b,k_0,k_s,k_t,\omega,\omega_0)=n_j(\mathbf{y}^b)H_q(\mathbf{y}^b,k_s,k_t,\omega_0)e^{i(k_s\eta_s+k_t\eta_t)}$$
$$\times e^{i(k_0+\mu M)y_1}\sqrt{1+(\partial y_1/\partial r_0)^2+(\partial y_1/r_0\partial\theta_0)^2} \tag{7.27}$$

which for a single blade lies within the finite range of blade angles $-\theta_a\le\theta_0\le\theta_a$ as shown in Fig.7.4.

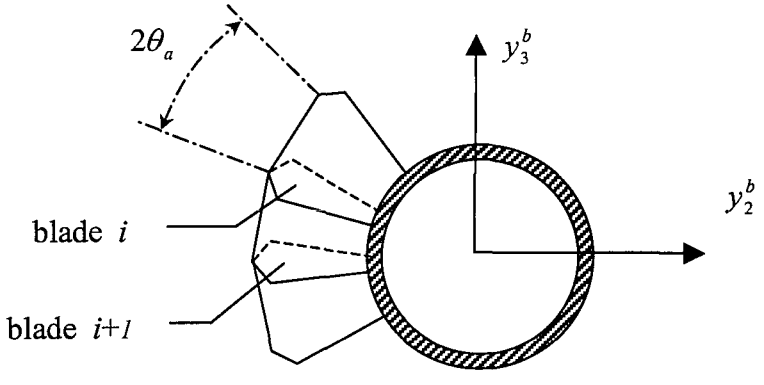

Figure 7.4 Definition of blade angle

It will be shown to be useful to express F_j as a Fourier series expansion in the form of

$$F_j(\mathbf{y}^b,k_0,k_s,k_t,\omega,\omega_0)=\sum_{l=-\infty}^{\infty}\hat{F}_j^l(r_0,k_0,k_s,k_t,\omega,\omega_0)\,e^{i(\pi/\theta_a)l\theta_0} \tag{7.28}$$

with Fourier coefficients $\hat{F}_j^l$ given by

$$\hat{F}_j^l(r_0,k_0,k_s,k_t,\omega,\omega_0)=\frac{1}{2\theta_a}\int_{-\theta_a}^{\theta_a}F_j(\mathbf{y}^b,k_0,k_s,k_t,\omega,\omega_0)e^{-i(\pi/\theta_a)l\theta_0}d\theta_0 \tag{7.29}$$

Substituting Eq. (7.28) into Eq. (7.25), and summing over N_b blades, H_p becomes

$$\begin{aligned}H_p(\mathbf{x},k_s,k_t,\omega,\omega_0)=\frac{-i}{8\pi}\sum_{l=-\infty}^{\infty}\sum_{m=-\infty}^{\infty}\int_{r_d}^{r_t}r_0\,\delta(\omega_0-\omega+m\Omega)\,B_{lm}\int_{-\theta_a}^{\theta_a}e^{i\mu_{lm}\theta_0}\,d\theta_0\\ \times\int_{-\infty}^{\infty}\Big[i(k_0+\mu M)\hat{F}_1^l(r_0,k_0,k_s,k_t,\omega,\omega_0)+\hat{F}_2^l(r_0,k_0,k_s,k_t,\omega,\omega_0)\frac{\partial}{\partial r_0}\\ +\frac{im}{r_0}\hat{F}_3^l(r_0,k_0,k_s,k_t,\omega,\omega_0)\Big]g^m(\mathbf{x},r_0,k_0,\omega)dk_0dr_0\end{aligned} \tag{7.30}$$

where r_d and r_t are the radii of the blade root and blade tip, and $\mu_{lm}=(\pi/\theta_a)l+m$. The term B_{lm} is the blade-number amplifying factor, defined by

$$B_{lm}=1+e^{i\mu_{lm}\theta_c}+e^{i2\mu_{lm}\theta_c}+\cdots+e^{i(N_b-1)\mu_{lm}\theta_c}=\frac{1-e^{iN_b\mu_{lm}\theta_c}}{1-e^{i\mu_{lm}\theta_c}} \tag{7.31}$$

where $\theta_c=2\theta_a$ is the blade angle defined in Fig.7.4, and $\mu_{lm}=(\pi/\theta_a)l+m$. For overlapping blades the surface integral of Eq. (7.30) should include the overlapped blades and both sides of each blade surface.

The integration of $e^{i\mu_{lm}\theta_0}$ with respect to θ_0 in Eq. (7.30) gives $I_\theta = (2/\mu_{lm})\sin(\mu_{lm}\pi/N_b)$ so that $|B_{lm}I_\theta| = 2\pi|\sin(\mu_{lm}\pi)/(\mu_{lm}\pi)|$. Since $N_b = \pi/\theta_a$ and $\mu_{lm} = N_b l + m$ must both take integer values, it can be seen that $|B_{lm}I_\theta| \neq 0$ only for $\mu_{lm} = 0$, and is zero for all other μ_{lm} values. Thus, $m = -N_b l$, ($l = 0,1,2,\cdots$), and so $I_\theta B_{lm} = 2\pi$. Equation (7.30) therefore reduces to

$$H_p(\mathbf{x},k_s,k_t,\omega,\omega_0) = \sum_{l=-\infty}^{\infty} H_l(\mathbf{x},k_s,k_t,\omega,\omega_0)\delta(\omega_0 - \omega + m\Omega) \tag{7.32}$$

where the transfer function H_l due to the l^{th} Fourier series component is given by

$$H_l(\mathbf{x},k_s,k_t,\omega,\omega_0) = \frac{-i}{4}\int_{r_d}^{r_t} r_0 \int_{-\infty}^{\infty}\Big[i(k_0+\mu M)\hat{F}_1^l(r_0,k_0,k_s,k_t,\omega,\omega_0) + \hat{F}_2^l(r_0,k_0,k_s,k_t,\omega,\omega_0)\frac{\partial}{\partial r_0} + \frac{im}{r_0}\hat{F}_3^l(r_0,k_0,k_s,k_t,\omega,\omega_0)\Big] g^m(\mathbf{x},r_0,k_0,\omega)\,dk_0 dr_0 \tag{7.33}$$

where $m = -N_b l$. It can be seen that the term H_l can be interpreted as the transfer function between the radiated acoustic pressure at the observation point and the harmonic pressure component on the blade surface of frequency ω_0 and wavenumbers k_s, k_t. The Fourier coefficients $\hat{F}_j^l$ serve as weighting factor in the transfer function of Eq.(7.33). Substituting Eqs. (7.27) and (7.29) into Eq. (7.33), the transfer function H_l can be reformulated as

$$H_l(\mathbf{x},k_s,k_t,\omega,\omega_0) = \frac{-iN_b}{4\pi}\iint_{S_i}\int_{-\infty}^{\infty}\Big[\big(i(k_0+\mu M)n_1 + n_r(\partial/\partial r_0) + n_\theta(im/r_0)\big) \times e^{i(k_0+\mu M)y_1} g^m(\mathbf{x},r_0,k_0,\omega)\Big]dk_0 \cdot H_q(\mathbf{y}^b,k_s,k_t,\omega_0)e^{i(k_s\eta_s+k_t\eta_t)}dS(\mathbf{y}^b) \tag{7.34}$$

Note that the relation $dS(\mathbf{y}^b) = dS(\mathbf{y})$ is used in the derivation of Eq. (7.34) since the area element is invariant under the coordinate transformation of Eq. (7.4). Equation (7.34) shows that the transfer function H_l is an integration over a rotor blade surface, and the integrand involves the normal vector of blade geometry, the pressure source on the blade surface, and a form of Green function for rotating sources.

Substituting Eq. (7.32) into Eqs. (7.23), (7.24) and performing the integration with respect to ω_0, the expression for the radiated pressure is of the form

$$\overline{p}(\mathbf{x},\omega) = \sum_{l=-\infty}^{\infty} \int_{-\infty}^{\infty}\int_{-\infty}^{\infty} H_l(\mathbf{x},k_s,k_t,\omega,\omega+N_b l\Omega)\hat{p}_s(k_s,k_t,\omega+N_b l\Omega)dk_s dk_t \tag{7.35}$$

Equations (7.34) and (7.35) show that the pressure received at frequency ω is due to the blade surface pressure at the frequencies, $\omega_0 = \omega + N_b l\Omega$, which corresponds to frequencies shifted by the blade passing frequencies, $\omega_b = N_b l\Omega$, where l takes all integer values. For broadband excitation, the radiated pressure $\overline{p}$ may be regarded as a random process which is most suitably expressed as a power spectral density, defined by

$$S_{pp}(\mathbf{x},\omega')\delta(\omega'-\omega) = E\left[\overline{p}^*(\mathbf{x},\omega')\overline{p}(\mathbf{x},\omega)\right] \tag{7.36}$$

Inserting Eq. (7.35) into Eq. (7.36), making use of the statistical orthogonal relationship of Eq. (3.4), and integrating the result with respect to ω', gives the final result for the power spectrum of the radiated pressure as

$$S_{pp}(\mathbf{x},\omega) = \sum_{l=-\infty}^{\infty} \int_{-\infty}^{\infty}\int_{-\infty}^{\infty} \left|H_l(\mathbf{x},k_s,k_t,\omega,\omega+N_b l\Omega)\right|^2 S_{qq}(k_s,k_t,\omega+N_b l\Omega)dk_s dk_t \tag{7.37}$$

Equation (7.36) reveals that the source spectrum evaluated in the blade-fixed reference frame $S_{qq}(k_s,k_t,\omega_0)$ appears shifted in frequency by multiples of the blade passing frequency in the moving frame, $S_{qq}(k_s,k_t,\omega+N_b l\Omega)$.

For frozen turbulence, substituting Eqs. (3.11) and (3.30) into Eq. (7.37) and integrating the result with respect to k_s gives the radiated pressure spectrum in the form

$$S_{pp}(\mathbf{x},\omega)=\frac{1}{U_c}\sum_{l=-\infty}^{\infty}\int_{-\infty}^{\infty}\left|H_l(\mathbf{x},k_s,k_t,\omega,\omega+N_b l\Omega)\right|^2\hat{S}_{qq}(k_s,k_t)dk_t \tag{7.38}$$

where $k_s=(\omega+N_b l\Omega)/U_c$, $U_c=c_u U_0=c_u\sqrt{U^2+(0.7\Omega r_t)^2}$. Note that for the position-dependent function f_p, a reference point should preferably be taken at the trailing edge at 0.7 of the rotor disk radius.

Chapter VIII

Rotor Broadband Noise Prediction: Benchmark Problem

8.1 Introduction

In this Chapter, the Category 2 benchmark problem of the 3rd CAA Workshop (see Category 2—Rotor Noise, 1999) is used as a test case to provide verification of the frequency-domain formulation for propeller noise described in Chapter VII. The Category 2 benchmark problem is concerned with the tonal noise generated by a hypothetical rotor, which is represented by a rotating body force distribution specified over a volume. The body force distribution is chosen so that its radiation has an analytic solution which can be used for the purpose of comparison. Two equivalent formulations will be presented for numerical computation. Mean flow effects on the directivity of the radiated sound are also discussed in this chapter, which are not accounted for in the benchmark analytic solution.

8.2 Description of the Benchmark Problem

The Category 2 benchmark problem relates to the sound field generated by an open rotor. The rotor is represented by a rotating body force distribution (see Category 2—Rotor Noise, 1999). In our notation, this steady body force distribution is prescribed by

$$\bar{\gamma}(\mathbf{y}) = -\frac{\partial \overline{B}_j}{\partial y_j} = \begin{cases} (138.6y_1 - iN_b)e^{-69.3y_1^2} J_{N_b}(\lambda_{N_b} r_0) e^{iN_b\theta_0'}, & r_0/d \le 1 \\ 0, & r_0/d > 1 \end{cases} \tag{8.1}$$

where $N_b = 8$ is the blade number, $J_{N_b}(Z)$ is the Bessel function of order N_b, $\lambda_{N_b} = 9.64742$, d is the blade span and $B_j(\mathbf{y},\tau) = \overline{B}_j(\mathbf{y})e^{i\omega_0\tau}$ is a steady body force component in the j - coordinate direction described in the Category 2 benchmark problem, and $\omega_0 = N_b\Omega$ is the source frequency. Equation (8.1) may be rewritten in the form

$$\gamma(\mathbf{y},\tau) = \bar{\gamma}(\mathbf{y})e^{i\omega_0\tau} = \hat{\gamma}(y_1, r_0)e^{iN_b(\theta_0' + \Omega\tau)} \tag{8.2}$$

where $\hat{\gamma}(y_1, r_0)$ is the steady body force distribution $\bar{\gamma}(\mathbf{y})$ without the θ_0'-dependent term $e^{iN_b\theta_0'}$. Note that Eqs. (8.1) and (8.2) are expressed in the moving reference system $\mathbf{y} = (y_1, r_0, \theta_0')$ (airplane-fixed coordinate system) rather than the blade-fixed coordinate system $\mathbf{y}^b = (y_1, r_0, \theta_0)$.

Substituting Eq. (8.2) into Eq. (2.3) and neglecting terms related to the boundary surface, the integral of Eq.(2.3) becomes

$$p(\mathbf{x},t) = \int_{-T}^{T} \iiint_{V(\tau)} \hat{\gamma}(y_1, r_0)e^{iN_b\theta_0'} e^{i\omega_0\tau} G(\mathbf{x},t;\mathbf{y},\tau)\,d\mathbf{y}\,d\tau \tag{8.3}$$

Now substituting the Green function of Eq. (2.13) into Eq. (8.3), the radiated sound pressure due to the rotating body force distribution is given by

$$p(\mathbf{x},t) = \int_{-T}^{T} \iiint_{V(\tau)} \hat{\gamma}(y_1, r_0)e^{iN_b\theta_0'} e^{i\omega_0\tau} \frac{1}{4\pi R} \delta\left[\tau + \frac{1}{\beta^2 c_0}\left(R + M(y_1 - x_1)\right) - t\right] d\mathbf{y}\,d\tau \tag{8.4}$$

Fourier transforming Eq. (8.4) with respect to t gives the frequency domain solution in the form

$$\begin{aligned}\overline{p}(\mathbf{x},\omega) &= \frac{1}{2\pi}\int_{-\infty}^{\infty} p(\mathbf{x},t)e^{i\omega t}dt \\ &= \frac{1}{4\pi}\frac{1}{2\pi}\int_{-T}^{T}\iiint_{\nu(\tau)}\hat{\gamma}(y_1,r_0)e^{iN_b\theta_0'}e^{i(\omega+\omega_0)\tau}\frac{1}{R}e^{i\mu E}d\mathbf{y}d\tau\end{aligned} \tag{8.5}$$

where $E = R + M(y_1 - x_1)$, $\mu = \kappa/\beta^2$, $\kappa = \omega/c_0$, ω is the observation frequency, and R is the mean-flow corrected distance given by

$$R = \sqrt{(y_1 - x_1)^2 + \beta^2[r^2 + r_0^2 - 2rr_0\cos(\theta_0' - \theta')]} \tag{8.6}$$

in which both observation point $\mathbf{x} = (x_1, r, \theta')$ and source point $\mathbf{y} = (y_1, r_0, \theta_0')$ are expressed in the moving reference frame (airplane-fixed coordinate system). The main difference here from the last Chapter (see Section 7.5) is that the source coordinate y_1 is independent of the source time τ in Eq. (8.5). In the last chapter, $y_1 = S_i(r_0, \theta_0) = S_i(r_0, \theta_0' + \Omega\tau)$ is a function of τ in the moving reference frame because the integration of Eq. (7.19) has to be carried out over the two-dimensional blade surface. Since the distance R in Eq. (8.5) is independent of the source time τ, the integration of Eq. (8.5) with respect to τ can be performed to give

$$\overline{p}(\mathbf{x},\omega) = \frac{1}{4\pi}\iiint_{\nu(\tau)}\hat{\gamma}(y_1,r_0)e^{iN_b\theta_0'}\frac{1}{R}e^{i\mu E}d\mathbf{y}\,\delta(\omega+\omega_0) \tag{8.7}$$

Fourier transformation of Eq. (8.7) with respect to ω give the radiated acoustic pressure in the time domain as

$$p(\mathbf{x},t) = \frac{1}{4\pi}\iiint_{\nu(\tau)}\hat{\gamma}(y_1,r_0)e^{iN_b\theta_0'}\frac{1}{R}e^{i\mu E}d\mathbf{y}\,e^{iN_b\Omega t} \tag{8.8}$$

Equation (8.8) suggests that the radiated noise from a rotating body force distribution may be obtained by integrating the source distribution over the source volume in the moving reference frame rather than the blade-fixed coordinate system. This concise form of Eq. (8.8) with the integration expressed in the moving reference frame is computationally more efficient than the expression presented below with the integration expressed in the blade-fixed coordinate system. However, it is more natural to perform the integration in the blade-fixed coordinate system while the observer remains in the moving reference frame. Furthermore, for the purpose of verifying the formulations derived in the last chapter, we now derive an alternative frequency domain formulation with the integration expressed in the blade-fixed coordinate system.

Substituting the coordinate transformation of Eq. (7.4) into Eq.(8.5), the radiated pressure in the frequency domain is given by

$$\overline{p}(\mathbf{x},\omega)=\frac{1}{4\pi}\frac{1}{2\pi}\int_{T}^{T}\iiint_{V(\tau)}\hat{\gamma}(y_1,r_0)e^{iN_b\theta_0}e^{i\omega\tau}\frac{1}{R}e^{i\mu R}e^{i\mu M(y_1-x_1)}d\mathbf{y}d\tau \tag{8.9}$$

where the mean-flow corrected distance now becomes

$$R=\sqrt{(y_1-x_1)^2+\beta^2[r^2+r_0^2-2rr_0\cos(\theta_0-\Omega\tau-\theta')]} \tag{8.10}$$

in which source point $\mathbf{y}^b=(y_1,r_0,\theta_0)$ is expressed in the blade- fixed coordinate system. Now substituting Eqs. (7.13) and (7.14) into Eq. (8.9), the radiated pressure is obtained in the τ -variable separated form as

$$\begin{aligned}\overline{p}(\mathbf{x},\omega)=&\frac{i}{8\pi}\sum_{l=-\infty}^{\infty}\iint_{S_l^{yr}}\hat{\gamma}(y_1,r_0)\int_0^{2\pi}e^{i(m+N_b)\theta_0}d\theta_0\int_{-T}^{T}e^{i(\omega-m\Omega)\tau}d\tau\\&\times\left[\int_{-\infty}^{\infty}e^{i(k_0+\mu M)y_1}g^m(\mathbf{x},r_0,k_0,\omega)dk_0\right]r_0dy_1dr_0\end{aligned} \tag{8.11}$$

where S_i^{yr} is the projected area of the rotating volume around the blade in the $y_1 - r$ plane, g^m is defined by Eq. (7.21). Integrating Eq. (8.11) with respect to τ and noting that

$$\int_0^{2\pi} e^{i(m+N_b)\theta_0} d\theta_0 = \begin{cases} 2\pi , & m = -N_b \\ 0 , & m \neq -N_b \end{cases} \tag{8.12}$$

gives

$$\overline{p}(\mathbf{x},\omega) = \frac{i}{4} \iint_{S_i^{yr}} \hat{\gamma}(y_1, r_0) \left[\int_{-\infty}^{\infty} e^{i(k_0+\mu M)y_1} g^m(\mathbf{x}, r_0, k_0, \omega) dk_0 \right] r_0 dy_1 dr_0 \, \delta(\omega + N_b\Omega) \tag{8.13}$$

In the time domain, equation (8.13) becomes

$$p(\mathbf{x},t) = \frac{i}{4} \iint_{S_i^{yr}} \hat{\gamma}(y_1, r_0) \left[\int_{-\infty}^{\infty} e^{i(k_0+\mu M)y_1} g^m(\mathbf{x}, r_0, k_0, \omega) dk_0 \right] r_0 dy_1 dr_0 \, e^{iN_b\Omega t} \tag{8.14}$$

where $\omega = -N_b\Omega$, Numerical calculations show Eqs. (8.8) and (8.14) give identical results but Eq. (8.8) is much more efficient for numerical computation than Eq. (8.14). This is because the k_0-integration involved in Eq. (8.14) is slow to converge especially in the case of the singularity arising in the Hankel function appearing in g^m. The consistency of Eqs.(8.8) and (8.14) indicate that an approximation may exist for the radiated pressure expressed in the non-rotating reference frame under some conditions, such as if the y_1 coordinate is approximately independent of the θ_0 coordinate.

8.3 Numerical Results

The frequency domain method (FDM) of Eq. (8.14) is compared with the analytical solutions of Tam (1999). Figures 8.1 and 8.3 show comparisons of the rotor noise

directivities at two different tip speed Mach number, $\widetilde{\Omega} = \Omega d / c_0$. The definition of directivity for the Category 2 problem is

$$D(\Psi) = 10\log_{10}\left[\frac{1}{p_{ref}^2}\lim_{\widetilde{R}_d \to \infty} \widetilde{R}_d{}^2 \overline{p^2}(\widetilde{R}_d, \Psi, \theta', t)\right] \tag{8.15}$$

where $\widetilde{R}_d = R_d / d$ is the non-dimensional distance, $R_d = \sqrt{x_1^2 + r^2}$, Ψ is the polar angle measured from the x_1 - axis, and the overbar denotes time averaging. For numerical calculations, we take $\widetilde{R}_d = 10$ and $\theta' = 0$. It can be seen from Figs.8.1 and 8.3 that the agreement between the FDM solution and the analytical solution is excellent, with no discernable difference being observed between them. This agreement provides verification of the frequency domain formulation presented in the last chapter.

Tam's analytical solution (1999) is only valid for noise radiation without mean flow. However, mean flow effects on radiated sound are included in the frequency-domain formulation of Eq. (8.14). Figures 8.2 and 8.4 show the directivity of rotor noise for different forward flight Mach numbers, $M = U / c_0$, for the two tip speed Mach numbers of $\widetilde{\Omega} = 0.85$ and $\widetilde{\Omega} = 1.15$ respectively. It can be seen that the directivities change significantly, not only with the forward flight speed, but also with tip speed.

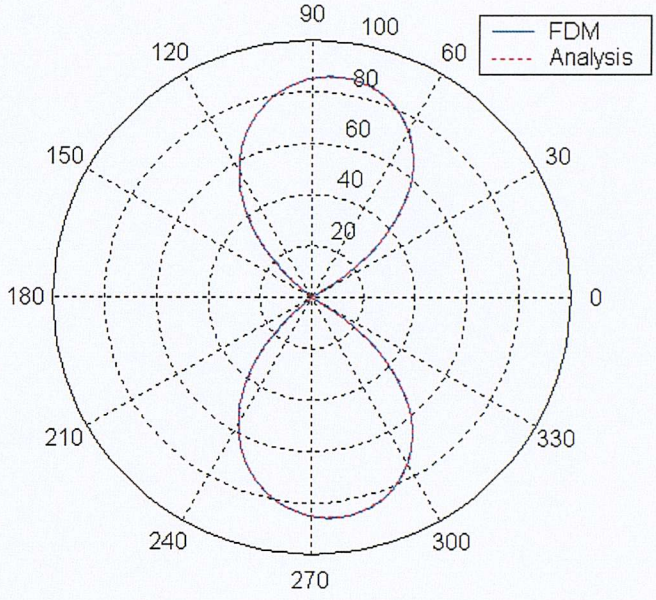

Figure 8.1 Directivity of body-force rotor noise, FDM result compared with analytical solution, M=0.0, $\widetilde{\Omega} = 0.85$

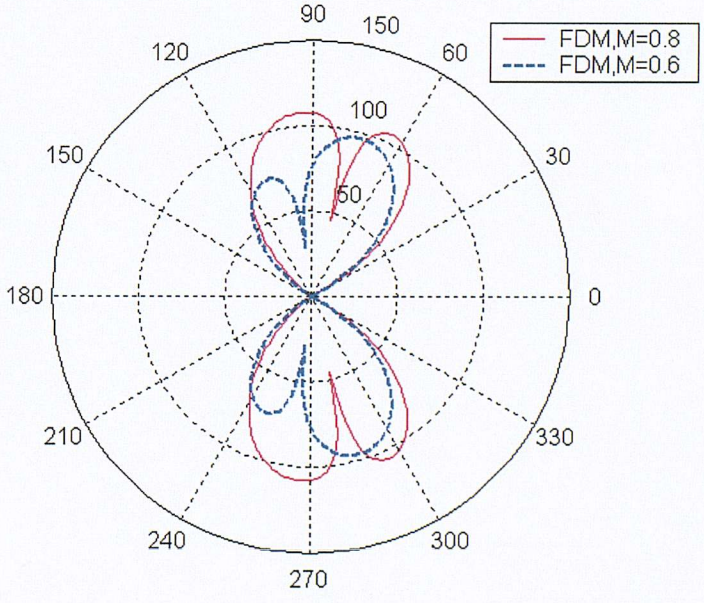

Figure 8.2 Directivity of body-force rotor noise for two forward flight Mach numbers of 0.6 and 0.8 at rotational speed $\widetilde{\Omega} = 0.85$

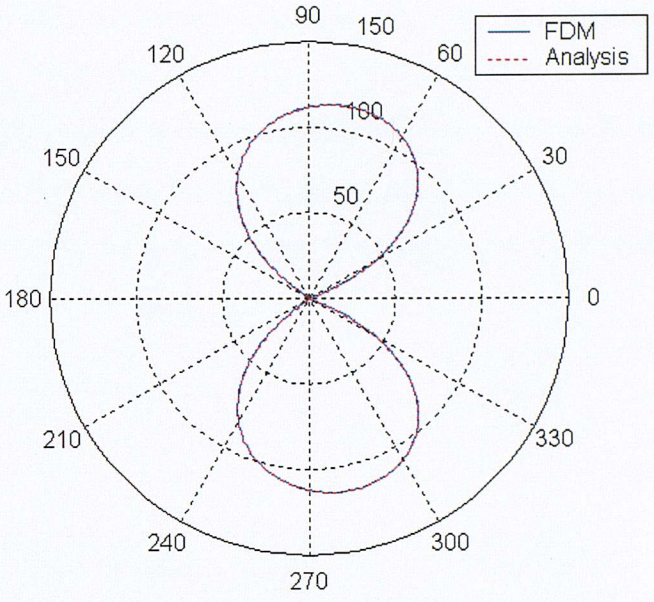

Figure 8.3 Directivity of body-force rotor noise, FDM result compared with analytical solution, M=0.0, $\widetilde{\Omega} = 1.15$

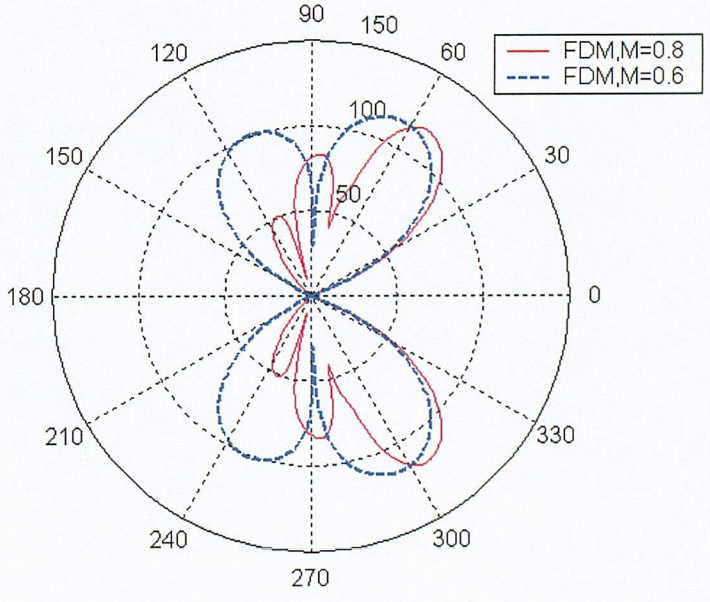

Figure 8.4 Directivity of body-force rotor noise for two forward flight Mach numbers of 0.6 and 0.8 at rotational speed $\widetilde{\Omega} = 1.15$

Figure 8.5 shows the field-point mesh for the contour plot of sound pressure level (SPL) shown in Figs (8.6) to (8.9). The rotor is located within the blank area of the "+" sign. The dimensions of the mesh are $16d$ in the x- direction and $10d$ in the y- direction. Figures 8.6 to 8.9 are the sound pressure level in dB for different forward flight Mach numbers of M=0.0, 0.4, 0.6, 0.8 at the tip speed Mach number of $\widetilde{\Omega} = 0.85$. The SPL in dB is represented by the colour at the corresponding grid point. The flight direction is opposite to the x-axis indicated in the figures.

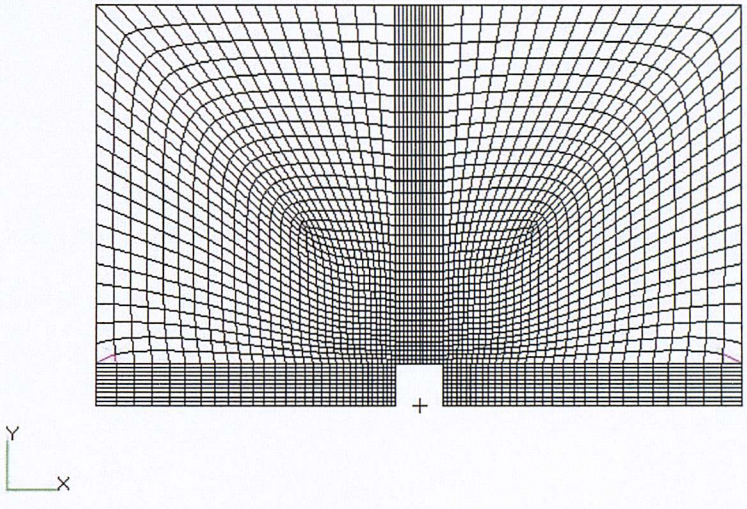

Figure 8.5 Mesh for SPL map, rotor located at the blank area of the "+" sign

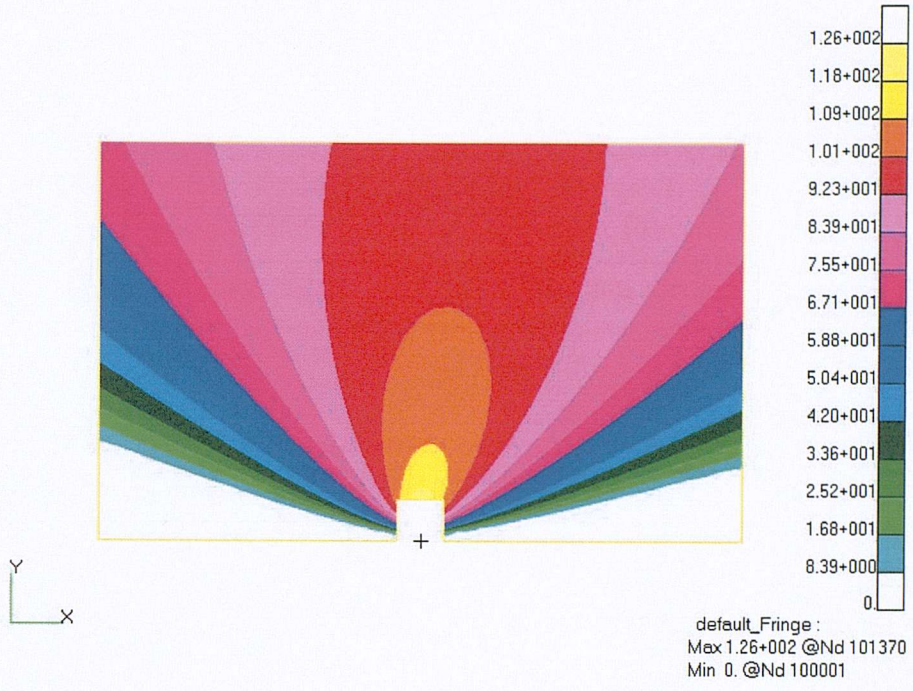

Figure 8.6 Map of sound pressure level (dB), M=0.0, $\widetilde{\Omega} = 0.85$

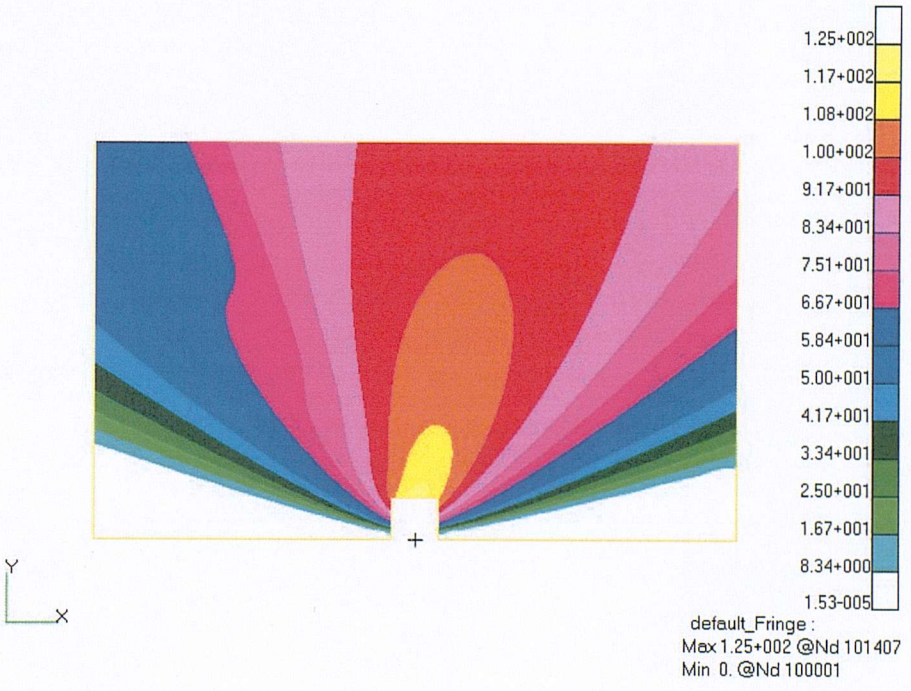

Figure 8.7 Map of sound pressure level (dB), M=0.4, $\widetilde{\Omega} = 0.85$

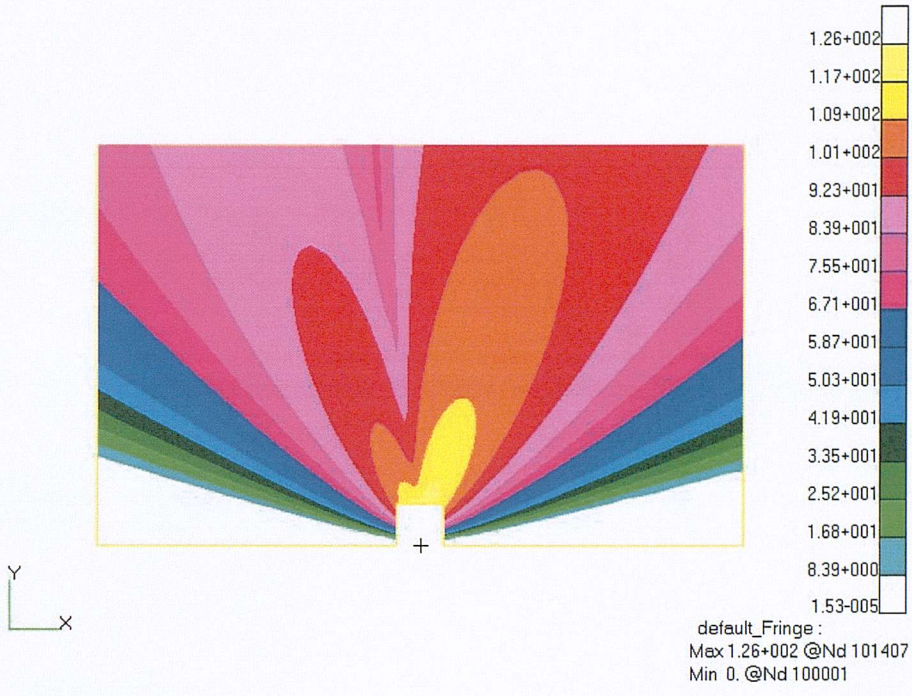

Figure 8.8 Map of sound pressure level (dB), M=0.6, $\widetilde{\Omega} = 0.85$

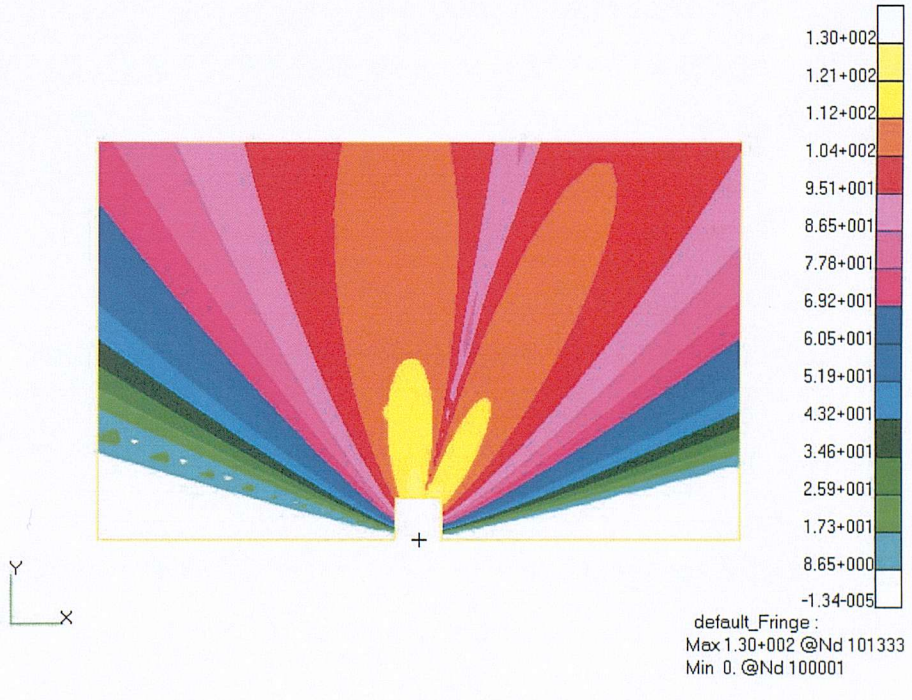

Figure 8.9 Map of sound pressure level (dB), M=0.8, $\widetilde{\Omega} = 0.85$

Chapter IX

Rotor Broadband Noise Prediction: Far-field Approximation

9.1 Introduction

In Chapter VII, a general frequency-domain formulation of broadband self-noise radiation from a free field rotor is developed that is valid both in the near field and in the far field. We now consider approximations to this result, which whilst only being valid in the far field, has the advantage of being simpler to compute. The results derived in this Chapter for far field radiation are shown to reduce to the classical solution due to Gutin (1936) for tonal noise when the flight speed is set to zero and the source integral is confined to the projected disk of the rotating blades.

9.2 Far Field Approximation for the Prediction of Rotor Broadband Self-noise

The starting point for the derivation of the far field approximation is Eq. (7.19). Here we rewrite it as

$$\overline{p}(\mathbf{x},\omega)=\frac{1}{2\pi}\int_{-T}^{T}\iint_{S_i} f_j(\mathbf{y},\tau)e^{i\omega\tau}\frac{\partial}{\partial y_j}\overline{G}(\mathbf{x},\mathbf{y})dS(\mathbf{y})d\tau \tag{9.1}$$

When $j=1$, the derivative of Green function $\overline{G}$ in Eq. (9.1) is given by

$$\frac{\partial}{\partial y_1}\overline{G}(\mathbf{x},\mathbf{y})=[-\frac{y_1-x_1}{R^2}+i\mu(\frac{y_1-x_1}{R}+M)]\overline{G}(\mathbf{x},\mathbf{y}) \tag{9.2}$$

while for $j=2,3$,

$$\frac{\partial}{\partial r_0}\overline{G}(\mathbf{x},\mathbf{y})=-\frac{\beta^2}{R}(\frac{1}{R}-i\mu)[r_0-r\cos(\theta_0'-\theta')]\overline{G}(\mathbf{x},\mathbf{y}) \tag{9.3}$$

$$\frac{\partial}{\partial \theta_0'}\overline{G}(\mathbf{x},\mathbf{y})=-\frac{\beta^2}{R}(\frac{1}{R}-i\mu)\, rr_0\sin(\theta_0'-\theta')\overline{G}(\mathbf{x},\mathbf{y}) \tag{9.4}$$

We now make the far field approximations that r_0, $y_1 << R_s$, where $R_s=\sqrt{x_1^2+\beta^2 r^2}$ is the flow corrected distance from the origin of the source to the observation point, as

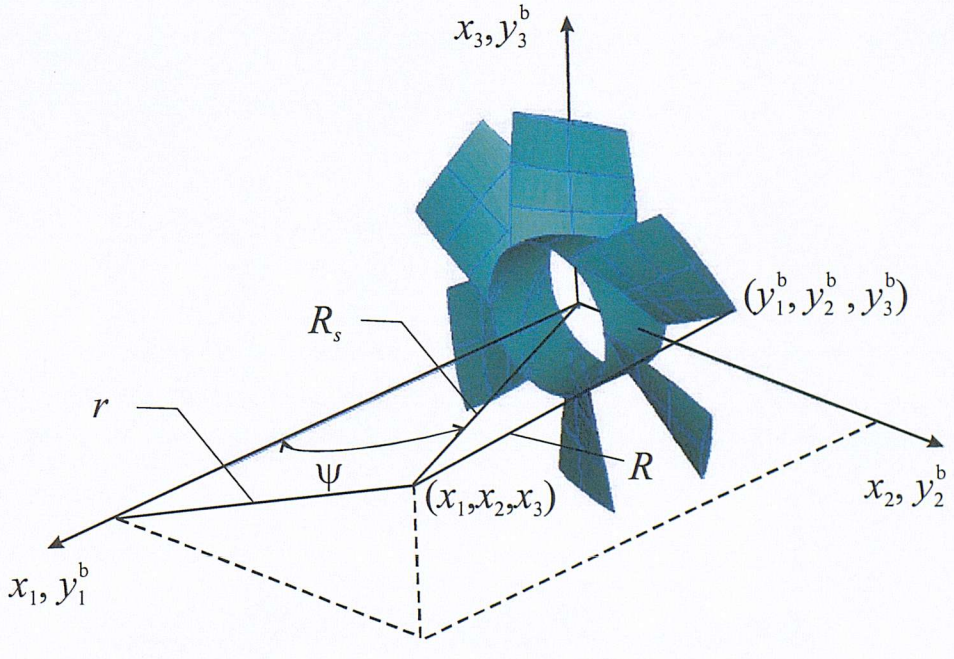

Figure 9.1. Relationship between distances R, R_s and polar angle ψ. Note that the distances R, R_s shown in the figure are for $\beta=1$

shown in Fig.9.1.

Expanding the expression for R of Eq. (7.11), and ignoring terms of second order give

$$R \approx R_s - [y_1 \cos\psi + \beta^2 r_0 \sin\psi \cos(\theta_0' - \theta')] \tag{9.5}$$

where $\cos\psi = x_1 / R_s$ and $\sin\psi = r / R_s$. Substituting Eqs. (9.2) to (9.5) into Eq. (9.1) and ignoring the second order terms in Eqs. (9.2) ~ (9.4), one obtains

$$\begin{aligned}\overline{p}(\mathbf{x},\omega) = \frac{-i\mu}{8\pi^2}\frac{e^{i\mu R_s}}{R_s}\int_{-T}^{T}\iint_{S_i}\{&- f_T(y,\tau)[(y_1 - x_1)/R_s + M] \\ &+ f_R(y,\tau)\beta^2[-r_0/R_s + \sin\psi\cos(\theta_0' - \theta')] - f_D(y,\tau)\beta^2 \sin\psi \sin(\theta_0' - \theta')\} \\ &\times e^{i\omega\tau} e^{i\mu M(y_1 - x_1)} e^{-i\mu[y_1\cos\psi + \beta^2 r_0 \sin\psi\cos(\theta_0' - \theta')]} dS(\mathbf{y}) d\tau\end{aligned} \tag{9.6}$$

where f_T, f_R and f_D denote the forces per unit area exerted by the rotor blades in the y_1, r_0, θ_0 directions, respectively. Here, the usual far field approximation is made whereby $1/R$ is replaced by $1/R_s$ but the phase factors are retained. The forces in Eq. (9.6) are related to the blade surface pressures of Eq. (7.8) by

$$\begin{Bmatrix} f_T \\ f_R \\ f_D \end{Bmatrix} = -\begin{Bmatrix} n_1 \\ n_r \\ n_\theta \end{Bmatrix} p_t(\mathbf{y}^b, \tau) \tag{9.7}$$

Inserting Eqs. (7.8) and (9.7) into Eq. (9.6) gives an expression for the radiated pressure in the form

$$\overline{p}(\mathbf{x},\omega) = \int_{-\infty}^{\infty}\int_{-\infty}^{\infty}\int_{-\infty}^{\infty} H_p(\mathbf{x}, k_s, k_t, \omega, \omega_0)\hat{p}_i(k_s, k_t, \omega_0)\, d\omega_0 dk_s dk_t \tag{9.8}$$

with the transfer function H_p given by

$$H_p(\mathbf{x},k_s,k_t,\omega,\omega_0)=\frac{i\mu}{8\pi^2}\frac{e^{i\mu R_s}}{R_s}\int_T^T\iint_{S_i}\{-n_1[(y_1-x_1)/R_s+M]$$

$$+n_r\beta^2[-r_0/R_s+\sin\psi\cos(\theta_0'-\theta')]-n_\theta\beta^2\sin\psi\sin(\theta_0'-\theta')\} \tag{9.9}$$

$$\times H_q(\mathbf{y}^b,k_s,k_t,\omega_0)e^{i(k_s\eta_s+k_t\eta_t)}e^{-i(\omega_0-\omega)\tau}e^{i\mu M(y_1-x_1)}e^{-i\mu[y_1\cos\psi+\beta^2 r_0\sin\psi\cos(\theta_0'-\theta')]}dS(\mathbf{y})d\tau$$

where $\mu=\kappa/\beta^2$ as defined in Chapter II. The expression above for H_p can be written in a form more suitable for computation by noting the generating function (Gradshteyn and Ryzhik, 1965; Goldstein, 1976)

$$e^{-iZ\cos\theta}=\sum_{m=-\infty}^{\infty}J_m(Z)e^{-im(\theta+\pi/2)} \tag{9.10}$$

for the Bessel function $J_m(Z)$ of the first kind, together with the following generating functions for the derivatives of Eq. (9.10) with respective to θ and Z:

$$\sin\theta e^{-iZ\cos\theta}=-\frac{1}{Z}\sum_{m=-\infty}^{\infty}mJ_m(Z)e^{-im(\theta+\pi/2)} \tag{9.11}$$

$$\cos\theta e^{-iZ\cos\theta}=\frac{-1}{i}\sum_{m=-\infty}^{\infty}\left[\frac{m}{Z}J_m(Z)-J_{m+1}(Z)\right]e^{-im(\theta+\pi/2)} \tag{9.12}$$

Substituting these identities into Eq. (9.9) and performing the integration with respect to τ gives

$$H_p(\mathbf{x},k_s,k_t,\omega,\omega_0)=\frac{i}{4\pi}\iint_{S_i}\sum_{m=-\infty}^{\infty}\mu\frac{e^{i\mu R_s}}{R_s}e^{-i\mu M x_1}e^{i\mu(M-\cos\psi)y_1}\left\{-n_1\left[\frac{y_1-x_1}{R_s}+M\right]\right.$$

$$\left.+n_r\beta^2\left[-r_0/R_s+i\sin\psi\left(\frac{m}{Z}-\frac{J_{m+1}(Z)}{J_m(Z)}\right)\right]+n_\theta\beta^2\frac{m}{\kappa r_0}\right\}J_m(Z)e^{-im(\theta_0-\theta'+\frac{\pi}{2})}$$

$$H_q(\mathbf{y}^b,k_s,k_t,\omega_0)e^{i(k_s\eta_s+k_t\eta_t)}\sqrt{1+\left(\frac{\partial y_1}{\partial r_0}\right)^2+\left(\frac{1}{r_0}\frac{\partial y_1}{\partial\theta_0}\right)^2}\,r_0dr_0d\theta_0\delta(\omega_0-\omega-m\Omega) \tag{9.13}$$

where $Z=\kappa r_0\sin\psi$. Analogous to the steps leading to Eq. (7.27) and Eq. (7.33), we denote the θ_0-dependent terms in the integrand of Eq. (9.13) by

$$F_j(\mathbf{y}^b,k_s,k_t,\omega,\omega_0)=\left\{\begin{matrix}n_1[(y_1-x_1)/R_s+M]\\ n_r\\ n_\theta\end{matrix}\right\}H_q(\mathbf{y}^b,k_s,k_t,\omega_0)$$

$$\times e^{i(k_s\eta_s+k_t\eta_t)}e^{i\mu(M-\cos\psi)y_1}\sqrt{1+\left(\frac{\partial y_1}{\partial r_0}\right)^2+\left(\frac{1}{r_0}\frac{\partial y_1}{\partial\theta_0}\right)^2} \tag{9.14}$$

and expand $F_j(\mathbf{y}^b,k_s,k_t,\omega,\omega_0)$ as a Fourier series in the form of

$$F_j(\mathbf{y}^b,k_s,k_t,\omega,\omega_0)=\sum_{l=-\infty}^{\infty}\hat{F}_j^l(r_0,k_s,k_t,\omega,\omega_0)e^{i(\pi/\theta_a)l\theta_0} \tag{9.15}$$

with Fourier coefficients $\hat{F}_j^l$ given by

$$\hat{F}_j^l(r_0,k_s,k_t,\omega,\omega_0)=\frac{1}{2\theta_a}\int_{-\theta_a}^{\theta_a}F_j(\mathbf{y}^b,k_s,k_t,\omega,\omega_0)e^{-i(\pi/\theta_a)l\theta_0}d\theta_0 \tag{9.16}$$

Substituting Eq. (9.15) into Eq. (9.13), and summing over N_b blades, the transfer function H_p becomes

$$H_p(\mathbf{x},k_s,k_t,\omega,\omega_0)=\frac{\mu i}{4\pi}e^{i\mu(R_s-Mx_1)}e^{im(\theta'-\frac{\pi}{2})}\sum_{l=-\infty}^{\infty}\sum_{m=-\infty}^{\infty}\int_{r_d}^{r_t}B_{lm}I_\theta\delta(\omega_0-\omega-m\Omega)$$
$$\times\left\{-\hat{F}_1^l(r_0,k_s,k_t,\omega,\omega_0)+\hat{F}_2^l(r_0,,k_s,k_t,\omega,\omega_0)\left[-\frac{r_0}{R_s}\right.\right.$$
$$\left.\left.+i\sin\psi\left(\frac{m}{Z}-\frac{J_{m+1}(Z)}{J_m(Z)}\right)\right]+\hat{F}_3^l(r_0,k_s,k_t,\omega,\omega_0)\beta^2\frac{m}{\kappa r_0}\right\}r_0dr_0 \tag{9.17}$$

where r_d and r_t are the radii of the blade root and blade tip. The term B_{lm} is the blade-number amplifying factor defined by Eq. (7.31). The θ_0-dependent integration I_θ is defined by

$$I_\theta=\int_{-\theta_a}^{\theta_a}e^{i\mu_{lm}\theta_0}d\theta_0 \tag{9.18}$$

where $\mu_{lm}=(\pi/\theta_a)l-m$. Following the same analysis as in Section 7.5, one has

$$B_{lm}I_\theta=\begin{cases}2\pi & , \quad m=N_bl\\ 0 & , \quad m\neq N_bl\end{cases} \tag{9.19}$$

Substituting Eq. (9.19) into Eq. (9.17), the transfer function H_p reduces to

$$H_p(\mathbf{x},k_s,k_t,\omega,\omega_0)=\sum_{l=-\infty}^{\infty}H_l(\mathbf{x},k_s,k_t,\omega,\omega_0)\delta(\omega_0-\omega-m\Omega) \tag{9.20}$$

with the 'mode' transfer function H_l given by

$$H_l(\mathbf{x},k_s,k_t,\omega,\omega_0)=\frac{i\mu}{2R_s}e^{i\mu(R_s-Mx_1)}e^{im(\theta'-\frac{\pi}{2})}\int_{r_d}^{r_t}\Big\{-\hat{F}_1^l(r_0,k_s,k_t,\omega,\omega_0)$$
$$+\hat{F}_2^l(r_0,k_s,k_t,\omega,\omega_0)\beta^2\left[-r_0/R_s+i\sin\psi\left(\frac{m}{Z}-\frac{J_{m+1}(Z)}{J_m(Z)}\right)\right] \tag{9.21}$$
$$+\hat{F}_3^l(r_0,k_s,k_t,\omega,\omega_0)\beta^2\, m/(\kappa r_0)\Big\}J_m(Z)\,r_0dr_0$$

where $m=N_bl$ rather than $m=-N_bl$ as described in Section 7.5.

Substituting Eq. (9.21) into Eqs. (9.20) and (9.8), and performing the integration with respect to ω_0, the expression for the radiated pressure may be written in the form

$$\overline{p}(\mathbf{x},\omega)=\sum_{l=-\infty}^{\infty}\int_{-\infty}^{\infty}\int_{-\infty}^{\infty}H_l(\mathbf{x},k_s,k_t,\omega,\omega+N_bl\Omega)\hat{p}_s(k_s,k_t,\omega+N_bl\Omega)dk_sdk_t \tag{9.22}$$

Following the same steps leading to Eq. (7.37), the power spectrum of the far field pressure is given by

$$S_{pp}(\mathbf{x},\omega)=\sum_{l=-\infty}^{\infty}\int_{-\infty}^{\infty}\int_{-\infty}^{\infty}\left|H_l(\mathbf{x},k_s,k_t,\omega,\omega+N_bl\Omega)\right|^2 S_{qq}(k_s,k_t,\omega+N_bl\Omega)dk_sdk_t \tag{9.23}$$

The corresponding expression for frozen turbulence is obtained by substituting Eqs. (3.11) and (3.30) into Eq. (9.23) and integrating the result with respect to k_s. The radiated pressure spectrum of Eq. (9.23) reduces to

$$S_{pp}(\mathbf{x},\omega)=\sum_{l=-\infty}^{\infty}\int_{-\infty}^{\infty}\left|H_l(\mathbf{x},k_s,k_t,\omega,\omega+N_bl\Omega)\right|^2 S_0(|k_s|U_c)S_2(k_t)dk_t \tag{9.24}$$

where $k_s=(\omega+N_bl\Omega)/U_c$, $U_c=c_uU_0=c_u\sqrt{U^2+(0.7\Omega r_t)^2}$. Note that the reference point for the position-dependent function f_p is taken at the trailing edge at 0.7 of the rotor disk radius.

Equations (9.23) and (9.24) are computationally more efficient than Eqs (7.37) and (7.38) since the mode transfer function H_l of Eq. (9.21) differs from Eq. (7.33) in two important respects: (i) the integration with respect to k_0 is eliminated; (ii) equation (9.21) only involves the Bessel function of the first kind and hence the singularity involved in Eq. (7.21) is removed.

9.3 Numerical Scheme for the Evaluation of the Mode Transfer Function H_l

To predict rotor broadband self-noise radiation using equations (9.23) and (9.24), the main difficulty arises from the calculation of the mode transfer function H_l. The numerical scheme proposed here is based on the fact that, as presented in Section 5.5, the hydrodynamic wavelength of boundary layer turbulence is usually smaller than the acoustic wavelength. This fact is used to split the integration required in Eq. (9.21) into three parts: one is the term independent of the blade surface coordinates and can therefore be taken out from the integrand; another is related to the acoustic term, and the third is the hydrodynamic term. The acoustic term can be taken out from the integration over the small element facet to allow the remaining term (the hydrodynamic term) in the integration to be performed analytically, thereby speeding up the computation time.

Substituting Eq. (9.14) into Eq. (9.16), one obtains the source Fourier coefficients as

$$\hat{F}_j^l(\mathbf{y}^b,k_s,k_t,\omega,\omega_0)=\frac{1}{2\theta_a}\int_{-\theta_a}^{\theta_a}\begin{Bmatrix} n_1\left[(y_1-x_1)/R_s+M\right] \\ n_r \\ n_\theta \end{Bmatrix} H_q(\mathbf{y}^b,k_s,k_t,\omega_0) \tag{9.25}$$

$$\times e^{i(k_s\eta_s+k_t\eta_t)}e^{i\mu(M-\cos\psi)y_1}\sqrt{1+\left(\frac{\partial y_1}{\partial r_0}\right)^2+\left(\frac{1}{r_0}\frac{\partial y_1}{\partial \theta_0}\right)^2}\,e^{-iN_bl\theta_0}d\theta_0$$

Substituting Eq. (9.25) into Eq. (9.21) gives the mode transfer function as

$$H_l(\mathbf{x},k_s,k_t,\omega,\omega_0)=\frac{i\mu N_b}{4\pi R_s}e^{i\mu(R_s-Mx_1)}e^{im(\theta'-\frac{\pi}{2})}\iint_{S_i}\left\{-n_1\left[\frac{y_1-x_1}{R_s}+M\right]\right.$$
$$\left.-n_r\beta^2\left[r_0/R_s-i\sin\psi\left(\frac{m}{Z}-\frac{J_{m+1}(Z)}{J_m(Z)}\right)\right]+n_\theta\frac{\beta^2 m}{\kappa r_0}\right\}H_q(\mathbf{y}^b,k_s,k_t,\omega_0) \tag{9.26}$$
$$\times e^{i(k_s\eta_s+k_t\eta_t)}e^{i\mu(M-\cos\psi)y_1}e^{-iN_b l\theta_0}J_m(Z)\,dS(\mathbf{y}^b)$$

Using a procedure similar to that followed in Section 5.5, the blade surface is discretized into finite triangular elements. Under the assumption that the acoustic wavelength is much larger than the element scale, the numerical expression of equation (9.26) approximates to

$$H_l(\mathbf{x},k_s,k_t,\omega,\omega_0)=I(\mathbf{x},\omega)\sum_{n=1}^{N_{ef}}\{I_n(\mathbf{x},\mathbf{y}_n^b,\omega)I_n^H(\mathbf{y}_n^b,k_s,k_t,\omega_0)\} \tag{9.27}$$

where $I(\mathbf{x},\omega)$ is the term related to the observation coordinates and is independent of the blade surface geometry

$$I(\mathbf{x},\omega)=\frac{i\mu N_b}{4\pi R_s}e^{i\mu(R_s-Mx_1)}e^{im(\theta'-\frac{\pi}{2})} \tag{9.28}$$

Note that the integrand of Eq. (9.26) may be split into two parts. One varies with the acoustic wavelength, which may be called the influence coefficient of source strength I_n. Another is related to the hydrodynamic wavelength, which is called the source strength I_n^H. The influence coefficient of source strength I_n is defined by

$$I_n(\mathbf{x},\mathbf{y}_n^b,\omega)=\left\{-n_1^n\left[\frac{y_1^n-x_1}{R_s^n}+M\right]-n_r^n\beta^2\left[\frac{r_0^n}{R_s^n}-i\sin\psi\left(\frac{m}{Z^n}-\frac{J_{m+1}(Z^n)}{J_m(Z^n)}\right)\right]\right.$$
$$\left.+n_\theta^n\beta^2\frac{m}{\kappa r_0^n}\right\}e^{i\mu(M-\cos\psi)y_1^n}J_m(Z^n) \tag{9.29}$$

where $\mathbf{n}=\{n_1^n,n_r^n,n_\theta^n\}$ is the unit inward normal vector of element n, $Z^n=\kappa r_0^n\sin\psi$ and $\mathbf{y}_n^b=\{y_1^n,r_0^n,\theta_0^n\}$ is the coordinates of the centre of the element n. Once the centre coordinates of element n is known, equation (9.29) can be calculated easily. Combining Eqs. (9.26) and (9.27), the source strength I_n^H is defined as an integral on the surface of element n given by

$$I_n^H(y_n^b,k_s,k_t,\omega_0)=\iint_{S_n}H_q(\mathbf{y}^b,k_s,k_t,\omega_0)e^{i(k_s\eta_s+k_t\eta_t)}e^{-iN_blB_0}\,dS(\mathbf{y}^b) \tag{9.30}$$

where S_n is the surface area of the n^{th} element facet on the blade surface. Equation (9.30) differs from equation (5.36) by the additional term $e^{-iN_blB_0}$. This term cannot be included in Eq.(9.29) since it cannot be assumed to be constant within the element for large $m=N_bl$. If the source has a component that matches with the mode modulating pattern of $e^{-iN_blB_0}$, the source contribution will be amplified.

Two methods were attempted in the evaluation of the integral in Eq. (9.30). One is a purely numerical method which is computationally slow. The other is an analytic method for which a linear relation between η_s and θ_0 has to be established. This relationship is described below. If we use a cylinder of radius r_0 cut through the propeller blade with cylinder axis parallel to the propeller axis, the blade section profile will closely fit on the cylinder surface. Unwrapping the cylinder surface onto a flat plane forms a blade section profile as shown in Fig. 9.2. In Fig. 9.2, x_u and y_u represent, respectively, the abscissa and ordinate of a typical point of the upper surface of the airfoil section, and C is the centre of an element on the blade surface. The coordinate y_1

of the section upper or lower line is a function of $r_0\theta_0$ as shown in Fig. 9.2. The streamwise curvilinear coordinate η_s can be calculated from

$$\eta_s = \eta_c + \int_{\theta_c}^{\theta_0} \sqrt{1+\left(\frac{1}{r_0}\frac{\partial y_1}{\partial \theta_0}\right)^2}\, r_0 d\theta_0 \tag{9.31}$$

where θ_0 is the azimuthal angle of the cylindrical coordinates, θ_c and η_c are respectively the azimuthal angle θ_0 and streamwise curvilinear coordinate η_s at the

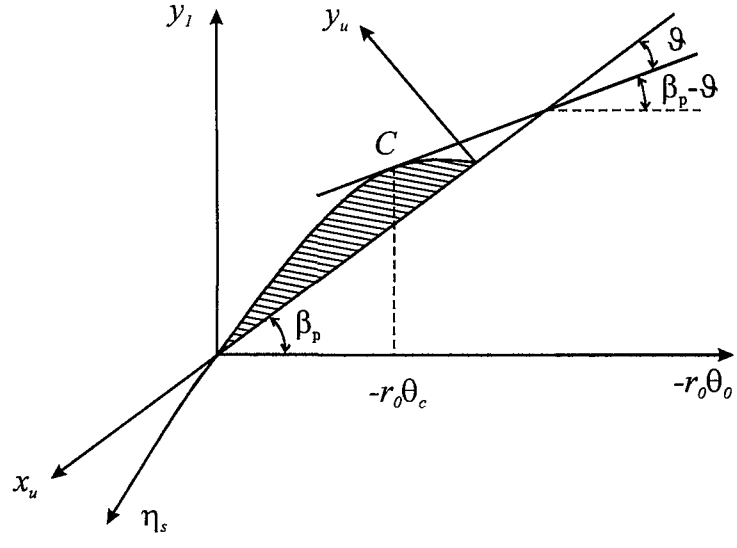

Figure 9.2 Relationship between curvilinear coordinates η_s, circumferential length $r_0\theta_0$, rectangle coordinate y_1 and blade section pitch angle β_p on a flatten plane of cylinder surface at radius r_0. θ_0 is the azimuthal angle of the cylindrical coordinates and θ_c is the angle at element centre. (x_u, y_u) is rectangle coordinates for airfoil profile

element centre *C*. In general, the relation between η_s and θ_0 is complicated. However, if the element size is small, the arc length within elements can be replaced by a straight line to connect the points. Following this approximation, we have

$$\frac{1}{r_0}\frac{\partial y_1}{\partial \theta_0} = -\tan(\beta_p - \vartheta) \tag{9.32}$$

where β_p is the blade section pitch angle, which is a known value once the blade geometry is determined, and ϑ is the tangent angle, which may be calculated from $\vartheta = \tan^{-1}(dy_u/dx_u)$ of the airfoil profile. Under this approximation, a linear relation between η_s and θ_0 is obtained by substituting Eq. (9.32) into Eq. (9.31)

$$\theta_0 = \theta_c + \frac{\cos(\beta_p - \vartheta)}{r_0}(\eta_s - \eta_c) \tag{9.33}$$

Substituting Eq. (9.33) into Eq. (9.30) gives the following expression for the source strength coefficient I_n^H

$$I_n^H(\mathbf{y}_n^b, k_s, k_t, \omega_0) = e^{-im(\theta_c - \eta_c\cos(\beta_p-\vartheta)/r_0)} \iint_{S_n} H_q(\mathbf{y}^b, k_s, k_t, \omega_0) e^{i(k_{sm}\eta_s + k_t\eta_t)}\, dS(\mathbf{y}^b) \tag{9.34}$$

where $k_{sm} = k_s - m\cos(\beta_p - \vartheta)/r_0$. Substituting Eq. (7.9) into Eq. (9.34) and performing the integration of Eq. (9.34) gives the analytic integration scheme in the form of Eq. (9.35). For $\mathbf{y}_n^b$ on the turbulence side

$$\begin{aligned} I_n^H(\mathbf{y}_n^b, k_s, k_t, \omega_0) = e^{-im(\theta_c - \eta_c\cos(\beta_p-\vartheta)/r_0)} \Big\{ & \tfrac{1}{2} f_p(\mathbf{y}_{TE}^b, \mathbf{k}, \omega_0) I_n^{H_e}(k_{sm}, k_t, \omega_0) \\ & + \left[f_p(\mathbf{y}_n^b, \mathbf{k}, \omega_0) - \tfrac{1}{2} f_p(\mathbf{y}_{TE}^b, \mathbf{k}, \omega_0) \right] I_n^{H_f}(k_{sm}, k_t) \Big\} \end{aligned} \tag{9.35a}$$

For $\mathbf{y}_n^b$ not on the turbulence side

$$\begin{aligned} I_n^H(\mathbf{y}_n^b, k_s, k_t, \omega_0) = -\frac{1}{2} e^{-im(\theta_c - \eta_c\cos(\beta_p-\vartheta)/r_0)} \Big\{ & f_p(\mathbf{y}_{TE}^b, \mathbf{k}, \omega_0) I_n^{H_e}(k_{sm}, k_t, \omega_0) \\ & - f_p(\mathbf{y}_{TE}^b, \mathbf{k}, \omega_0) I_n^{H_f}(k_{sm}, k_t) \Big\} \end{aligned} \tag{9.35b}$$

where $a = i(K + \mu_0 M_0 + k_{sm})$. The terms $I_n^{H_e}(k_{sm}, k_t, \omega_0)$ and $I_n^{H_f}(k_{sm}, k_t)$ can be calculated using Eqs. (5.38) and (5.39), whose arguments are now a function of the element-centre position.

Appendix 9.A Reduction of the Far-field Expression to Gutin's Solution

This appendix demonstrates the consistency of the formulation of propeller noise with the classical solution due to Gutin (1936). Gutin's solution was concerned with the tonal noise due to steady blade surface pressures, which forms the mean thrust and drag forces acting on the blade. When the pressure exerted by the blade surface is steady, the forces per unit area exerted by the blade in Eq. (9.7) can be rewritten as

$$\begin{Bmatrix} \bar{f}_T \\ \bar{f}_R \\ \bar{f}_D \end{Bmatrix} = -\begin{Bmatrix} n_1 \\ n_r \\ n_\theta \end{Bmatrix} \bar{p}_t(\mathbf{y}^b) \tag{9.A.1}$$

where $\bar{p}_t(\mathbf{y}^b)$ is now the steady pressure on the blade surface. Substituting Eq. (9.A.1) into Eq. (9.6) to replace the unsteady forces f_T, f_R and f_D, the radiated pressure in a form analogous to Eq.(9.8) without integrating over frequency and wavenumber components is given by

$$\bar{p}(\mathbf{x},\omega) = h_p(\mathbf{x},\omega) \tag{9.A.2}$$

where the function h_p is defined as

$$\begin{aligned} h_p(\mathbf{x},\omega) = {} & \frac{i\mu}{8\pi^2}\frac{e^{i\mu R_s}}{R_s}\int_T \iint_{S_i}\{-n_1[(y_1-x_1)/R_s + M] \\ & + n_r\beta^2[-r_0/R_s + \sin\psi\cos(\theta_0'-\theta')] - n_\theta\beta^2\sin\psi\sin(\theta_0'-\theta')\} \\ & \times \bar{p}_t(\mathbf{y}^b)e^{i\omega\tau}e^{i\mu M(y_1-x_1)}e^{-i\mu[y_1\cos\psi+\beta^2 r_0\sin\psi\cos(\theta_0'-\theta')]}dS(\mathbf{y})d\tau \end{aligned} \tag{9.A.3}$$

Note that, unlike the transfer function H_p, the function h_p has dimensions of pressure $\bar{p}$. This is due to the oscillating part, $H_q e^{i(k_s\eta_s+k_t\eta_t)}$, of the unsteady pressure in Eq. (9.9) being replaced by the steady pressure $\bar{p}_t(\mathbf{y}^b)$ in Eq. (9.A.3). Following the same derivation procedure leading to Eqs. (9.20) and (9.26), the far field pressure of the radiated tonal noise is of the form,

$$\bar{p}(\mathbf{x},\omega)=\sum_{l=-\infty}^{\infty}h_l(\mathbf{x},\omega)\delta(\omega+m\Omega) \tag{9.A.4}$$

with the mode function h_l given by

$$\begin{aligned} h_l(\mathbf{x},\omega)=\frac{i\mu N_b}{4\pi R_s}e^{i\mu(R_s-Mx_1)}e^{im(\theta'-\frac{\pi}{2})}\iint_{S_i}\Bigg\{&-n_1\left[\frac{y_1-x_1}{R_s}+M\right]\\ &-n_r\beta^2\left[r_0/R_s-i\sin\psi\left(\frac{m}{Z}-\frac{J_{m+1}(Z)}{J_m(Z)}\right)\right]+n_\theta\frac{\beta^2 m}{\kappa r_0}\Bigg\}\\ &\times\bar{p}_t(\mathbf{y}^b)e^{i\mu(M-\cos\psi)y_1}e^{-iN_b l\theta_0}J_m(Z)\,dS(\mathbf{y}^b)\end{aligned} \tag{9.A.5}$$

where $m=N_b l$.

Consider the case in which the forward flight speed U and the force in the radial direction $\bar{f}_R$ are set to zero, and the integration is confined to the projected disk of the rotating plane, therefore $y_1(r_0,\theta_0)=0$ and $dS(\mathbf{y}^b)=r_0 d\theta_0 dr_0$. Substituting the following parameters

$$M=0,\ \beta=1,\ \mu=\kappa=N_b l\Omega/c_0 \tag{9.A.6}$$

into Eq. (9.A.5), one obtains

$$h_l(\mathbf{x},\omega) = \frac{i\kappa N_b}{4\pi R_s} e^{i\kappa R_s} e^{iN_b l(\theta'-\frac{\pi}{2})} \iint_{S_i} \left[\bar{f}_T(r_0,\theta_0)\cos\psi - \bar{f}_D(r_0,\theta_0)\frac{c_0}{\Omega r_0} \right] e^{-iN_b l\theta_0} J_m(\kappa r_0 \sin\psi)\, r_0 d\theta_0 dr_0 \tag{9.A.7}$$

Equation (9.A.7) is identical to the classical Gutin's solution presented by Goldstein (1976, Eqn (3.115)) for the same case except for a sign difference in the exponential term $e^{-iN_b l\theta_0}$. This sign difference gives no difference to the radiated pressure amplitude. Gutin's result has been substantiated by experiment. The reduction of Eq (9.22) to this classical result provides verification of the proposed formulation.

Chapter X

Rotor Broadband Noise Prediction: Far-field Tone Noise

10.1 Introduction

In this Chapter, the frequency-domain formulation of rotor noise radiation will be adapted to predict tonal noise. In this case, the source is a steady pressure distribution on the blade surface. Since the steady pressures can be easily determined from wing section theory and measured airfoil lift curves, this tonal noise prediction provides an alternative method of validating the frequency-domain formulation derived in the last Chapter. The predicted tone noise will be compared against experimental data obtained by Trebble for a $1/5^{th}$ scale model propeller (Trebble,1987a).

10.2 Experimental Arrangement and Geometric Parameters of R212 Model Propeller

The experimental results for tonal noise radiation used to validate the theory are reported by Trebble (1987a). The noise measurements of the four-bladed Dowty Rotol R212 propeller (NACA 16 sections) are made at $1/5^{th}$ scale in the RAE (Royal Aircraft Establishment) 1.5 metre acoustic tunnel. The propeller was mounted on the propeller test rig, which is capable of drive-speeds up to 10000 rev/min, as shown in Fig.10.1.

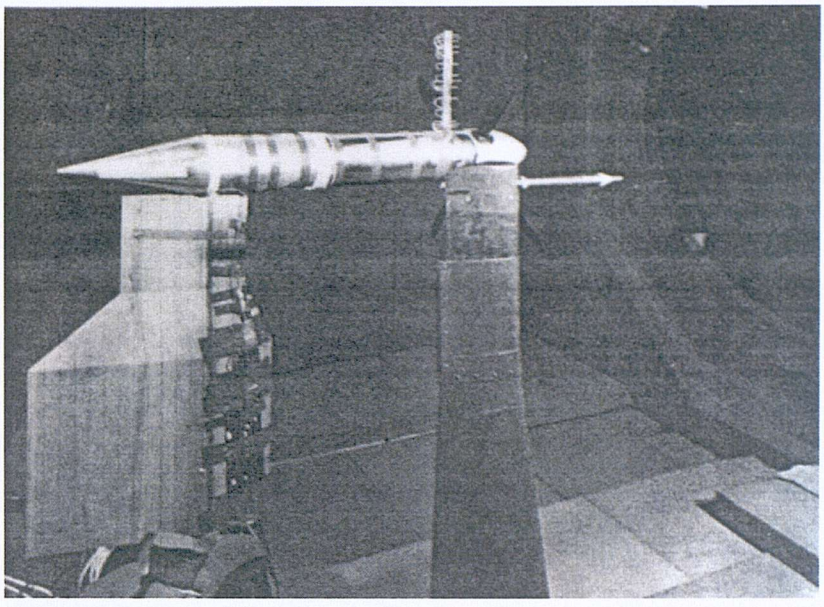

Figure 10.1 Test arrangement for R212 propeller, figure from Trebble (1987a)

blade radius station $2r_0 / D$	chord c [mm]	thickness ratio t / c	camber C_{li}	Twist angle β_T [degree]
0.2	40.1	0.2399	0.325	31.0
0.25	45.0	0.224	0.463	25.5
0.3	48.5	0.181	0.535	21.2
0.45	52.6	0.121	0.590	11.0
0.6	52.6	0.087	0.575	3.4
0.7	50.3	0.072	0.550	0.0
0.8	45.3	0.063	0.520	-2.7
0.9	36.3	0.061	0.468	-4.7
0.95	30.2	0.059	0.473	-5.6
0.975	26.7	0.059	0.468	-6.0
1.0	22.6	0.059	0.468	-6.4

Table 10.1 Geometric parameters of the R212 propeller

The main geometric parameters of the model propeller are listed in Table 10.1. The diameter of the $1/5^{th}$ scale model propeller is $D = 0.73\,\text{m}$. In Table 10.1, $2r_0 / D$ is the blade section radius station (radius ratio); t / c is the blade section thickness ratio relative

to the section chord c; β_T is the blade twist angle relative to that at the 0.70 radius station which is the standard position for setting the blade angle; and the camber C_{li} is used to express the design lift coefficient (ideal lift coefficient) for the blade section.

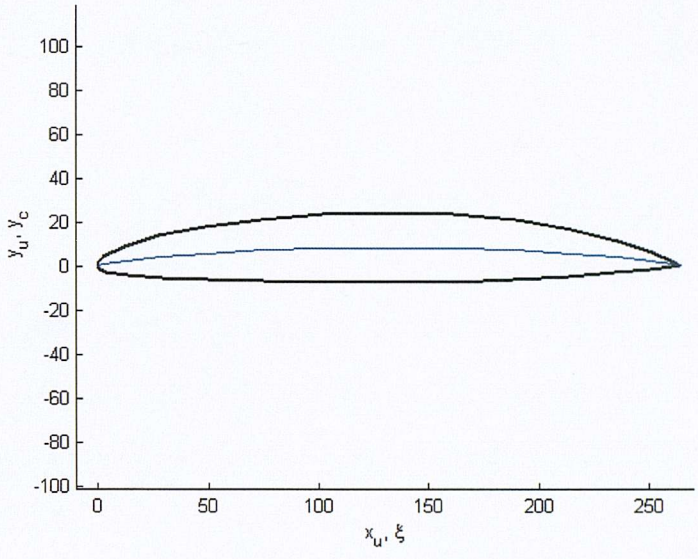

Figure 10.2 NACA 16-section profile at blade radius $2r_0 / D = 0.45$

Figure 10.2 shows the NACA 16-section profile at blade radius $2r_0 / D = 0.45$ obtained from Eqs.(10.5) and (10.6) below. The fine solid line between the upper- and lower-surface is the airfoil mean line. The NACA 16-section mean line is designed to obtain a uniform chordwise load distribution (mean-line designation $a = 1$). According to Abbott (1959) and Lindsey (1948), the mean line can be expressed as

$$y_c = -\frac{1}{4\pi} C_{li}\left[\xi \ln \xi + (1+\xi)\ln(1-\xi)\right] \tag{10.1}$$

where y_c is the mean-line ordinate normalised on the chord and ξ is the distance along the chord normalized on chord. The camber angle ϑ_0 is the gradient of y_c with respect to ξ, given by

$$\tan \vartheta_0 = \frac{dy_c}{d\xi} = -\frac{1}{4\pi} C_{li}\left[\ln \xi - \ln(1-\xi)\right] \tag{10.2}$$

The thickness distribution of the NACA 16-series airfoils was designed to produce a shape having very low induced velocities and thus having high critical Mach numbers. The ordinates for the basic (or symmetrical) profile of the 16-series airfoils can be obtained from the following equations

$$y_t = \frac{t}{c}\left(0.989665\xi^{1/2} - 0.239250\xi - 0.041000\xi^2 - 0.559400\xi^3\right), \quad \text{for } \xi \le 0.5 \tag{10.3}$$

$$y_t = \frac{t}{c}\left[0.01 + 2.325(1-\xi) - 3.42(1-\xi)^2 + 1.46(1-\xi)^3\right], \quad \text{for } \xi > 0.5 \tag{10.4}$$

where y_t is the ordinate non-dimensionalized on the chord measured normal to the camber line. If x_u and y_u represent, respectively, the abscissa and ordinate of a typical point of the upper surface of the airfoil section, the upper –surface coordinates are given by the following relations:

$$\begin{cases} x_u = \xi - y_t \sin\vartheta_0 \\ y_u = y_c + y_t \cos\vartheta_0 \end{cases} \tag{10.5}$$

The corresponding expressions for the lower-surface coordinates are

$$\begin{cases} x_l = \xi + y_t \sin\vartheta_0 \\ y_l = y_c - y_t \cos\vartheta_0 \end{cases} \tag{10.6}$$

In the following Section, the focus is placed on the tonal noise generation from the dipole source due to steady blade surface pressure. The thickness noise was assumed to be negligible for the reason discussed in the Section 1.2.3.

10.3 Reduction of the Far-field Formulation to Predict the Tonal Noise

The frequency-domain formulation of Eq. (9.23) is a general far-field formula that is valid for broadband noise prediction. It can also be used for tone noise prediction. The

tonal noise pressure due to the steady pressure distribution on the blade surface is given by Eq. (9.A.4). Fourier transforming Eq.(9.A.4) with respect to ω gives the radiated pressure in the time domain of the form

$$p(\mathbf{x},t) = \int_{-\infty}^{\infty} \overline{p}(\mathbf{x},\omega) e^{-i\omega t} d\omega = \sum_{l=-\infty}^{\infty} h_l(\mathbf{x},\omega) e^{iN_b l\Omega} \tag{10.7}$$

where

$$\begin{aligned} h_l(\mathbf{x},\omega) = \frac{i\mu N_b}{4\pi R_s} e^{i\mu(R_s - Mx_1)} e^{im(\theta' - \frac{\pi}{2})} \iint_{S_i} \Bigg\{ -n_1 \left[\frac{y_1 - x_1}{R_s} + M \right] \\ - n_r \beta^2 \left[r_0/R_s - i\sin\psi \left(\frac{m}{Z} - \frac{J_{m+1}(Z)}{J_m(Z)} \right) \right] + n_\theta \frac{\beta^2 m}{\kappa r_0} \Bigg\} \\ \times \overline{p}_t(\mathbf{y}^b) e^{i\mu(M - \cos\psi)y_1} e^{-iN_b l\theta_0} J_m(Z)\, dS(\mathbf{y}^b) \end{aligned} \tag{10.8}$$

where again $Z = \kappa r_0 \sin\psi$, $\mu = \kappa/\beta^2$, $\kappa = N_b l\Omega / c_0$, $m = N_b l$, and $\overline{p}_t(\mathbf{y}^b)$ is the steady pressure distribution on the blade surface. Most fans have a blade skew angle equal to zero, or at least very small. In this case $n_r << (n_1, n_\theta)$. The second term in the big bracket of Eq. (10.8) can therefore be ignored. Noting the Bessel function property $J_{-m}(-Z) = J_m(Z)$, we have the approximate result

$$h_{-l}(\mathbf{x},\omega) \approx h_l^*(\mathbf{x},\omega) \tag{10.9}$$

where the superscript "*" indicates the complex conjugate. The pressure at the l^{th} blade passing frequency is defined as

$$p_l = h_l e^{iN_b l\Omega} + h_{-l} e^{-iN_b l\Omega} = h_l e^{iN_b l\Omega} + h_l^* e^{-iN_b l\Omega} = 2\,\mathrm{Re}\{h_l e^{iN_b l\Omega}\} \tag{10.10}$$

The function h_l can be rewritten in the complex exponential form $h_l = |h_l| e^{i\delta}$. Equation (10.10) then becomes

$$p_l = 2|h_l|\cos(N_b l\Omega + \delta) \tag{10.11}$$

with the mean-square value given by

$$\overline{p_l^2} = \frac{1}{2}\left(2|h_l|\right)^2 = 2|h_l|^2 \tag{10.12}$$

The sound pressure level at the l^{th} blade passing frequency is therefore given by

$$SPL = 3 + 20\log_{10}\frac{|h_l|}{p_{ref}}, \qquad l = 1,2,3,\cdots \tag{10.13}$$

where $p_{ref} = 2\times10^{-5}\,Pa$. Note that h_l can be calculated numerically in the same way as the transfer function H_l discussed in Section 9.3 of Chapter IX.

10.4 Prediction of Steady Surface Pressure Distribution

In this Section we use Abbott's (1959) wing section theory and measured airfoil lift curves (Lindsey, Stevenson and Daley,1948) to determine the steady pressure distribution $\overline{p}_l(y^b)$ on the blade surface. This pressure distribution will be used in the next section to predict the tonal noise of an R212 propeller, which was measured by Trebble (1987a).

Trebble's investigations of R212 propeller noise were made at propeller rotational speeds n of 3750 and 8000 rev/min at axial stream speeds U of 30 m/s and 50 m/s for blade setting angles β_s of $9.3°, 17.3°, 22.4°, 27.3°$ and $34.9°$. Here we focus on the noise radiation at $n = 7000$ rev/min, $U = 50$ m/s and $\beta_s = 17.3°$. The blade setting angle β_s is defined as the twist angle at 0.70 radius station. The relation between pitch angle, twist angle and setting angle is

$$\beta_P = \beta_T + \beta_S \tag{10.14}$$

For $n = 7000$ rev/min, $U = 50$ m/s, $\beta_s = 17.3°$, we have $\Omega = 2\pi n / 60 = 733.0$ rad/s. The corresponding blade section Mach numbers $M(r_0) = U_0 / c_0$ and angles of attack $\alpha(r_0)$ are summarized in Table 10.2 below

blade station $2r_0 / D$	section Mach numbers $M(r_0)$	attack angles $\alpha(r_0)$ (degree)	section lift coefficients C_l
0.2	0.21	5.24	0.45
0.25	0.24	6.02	0.60
0.3	0.27	6.58	0.72
0.45	0.38	5.75	0.84
0.6	0.49	3.40	0.76
0.7	0.56	2.35	0.83
0.8	0.64	1.45	0.81
0.9	0.71	0.87	0.77
0.95	0.75	0.57	0.73
0.975	0.77	0.45	0.71
1.0	0.79	0.31	0.68

Table 10.2 Section Mach numbers, angles of attack and lift coefficients of R212 propeller

In Table 10.2, the section lift coefficients C_l at each blade section are obtained by interpolation of the measured airfoil lift curves (Lindsey, Stevenson and Daley, 1948) according to the section design lift coefficients, thickness ratios, Mach numbers and angles of attack.

According to Abbott's wing section theory (Abbott and Von Doenhoff, 1959), the velocity distribution due to steady non-uniform mean flow around an airfoil is considered to be composed of three independent components:

(1) The velocity distribution, v/U_0, corresponding to the velocity distribution over the basic thickness form at zero angle of attack. For different thickness ratios, values of v/U_0 can be obtained from the tabulated data in Appendix I of Abbott's book (Abbott and Von Doenhoff, 1959).

(2) The velocity distribution, $\Delta v/U_0$, corresponding to the load distribution of mean line at its ideal angle of attack, α_i. When $C_{li}=1.0$, $\alpha=0$, the velocity ratio $\Delta v/U_0=0.25$ is given in Appendix II of Abbott's (1959) book. For any other value of C_{li}, one should use $\Delta v/U_0=0.25C_{li}$.

(3) The velocity distribution, $\Delta v_a/U_0$, corresponding to the additional load distribution associated with non-zero angle of attack. For the lift coefficient $C_l=1.0$, values of $\Delta v_a/U_0$ are given in the tabulated data in Appendix I of Abbott's book (Abbott and Von Doenhoff, 1959). For $C_l\neq 1.0$, the ratio $\Delta v_a/U_0$ must be assigned some value by multiplying the originally calculated values (i.e. tabulated data for $C_l=1.0$) of this ratio by a factor C_l-C_{li}.

The velocity increment ratios $\Delta v/U_0$ and $\Delta v_a/U_0$ are added to the velocity ratio v/U_0 to obtain the total velocity at one point from which the pressure coefficient Π is obtained (Abbott and Von Doenhoff, 1959), thus

$$\Pi=\frac{p_a+0.5\rho_0U_0^2-\overline{p}_t}{0.5\rho_0U_0^2}=\left[\frac{v}{U_0}\pm\left(\frac{\Delta v}{U_0}+\frac{\Delta v_a}{U_0}\right)\right] \tag{10.15}$$

where $p_a=10^5\,Pa$ is the atmosphere pressure. In Eq. (10.15), the values of $\Delta v/U_0$ and $\Delta v_a/U_0$ are positive on the suction side and negative on the pressure side. When Eq.(10.15) is applied to a real propeller, the velocity increment ratios $\Delta v/U_0$ and $\Delta v_a/U_0$ should be multiplied by a correction factor f_c to include the effect of reduced angle of attack due to the induced velocity produced by the three-dimensional propeller

(Blake, 1986). The correction factor f_c should be adjusted so that the calculated thrust coefficient of the propeller is consistent with the measured thrust coefficient. After considering this correction factor, Eq. (10.15) becomes

$$\Pi = \left[\frac{v}{U_0} \pm f_c \left(\frac{\Delta v}{U_0} + \frac{\Delta v_a}{U_0} \right) \right] \tag{10.16}$$

Numerical tests show that the radiated propeller tone noise is not sensitive to the correction factor f_c. From Eq. (10.16), the steady pressure distribution $\overline{p}_t(y^b)$ can be calculated from

$$\overline{p}_t(\mathbf{y}^b) = p_a + 0.5\rho_0 U_0^2 (1 - \Pi) \tag{10.17}$$

Figure 10.3 below shows the mesh of the suction side of the R212 propeller used for making tone noise predictions. The propeller is meshed with 2596 triangle elements and 1320 nodes. Figure 10.4 shows the colour contour map of the pressure coefficient Π for the suction side of the R212 propeller. An enlarged map around the blade root part is shown in Figure 10.5 to allow a clearer view. Figure 10.6 is the colour contour map of the pressure coefficient Π for the pressure side with an enlarged view shown in Figure 10.7 around the blade root.

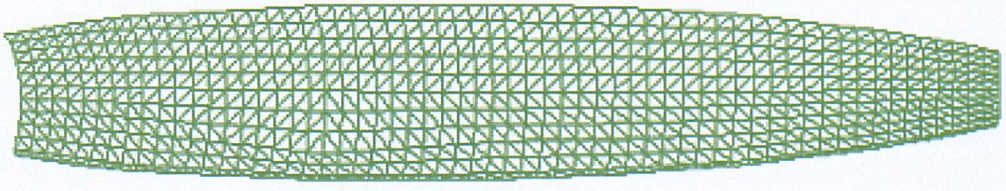

Figure 10.3 The mesh of suction side of R212 propeller

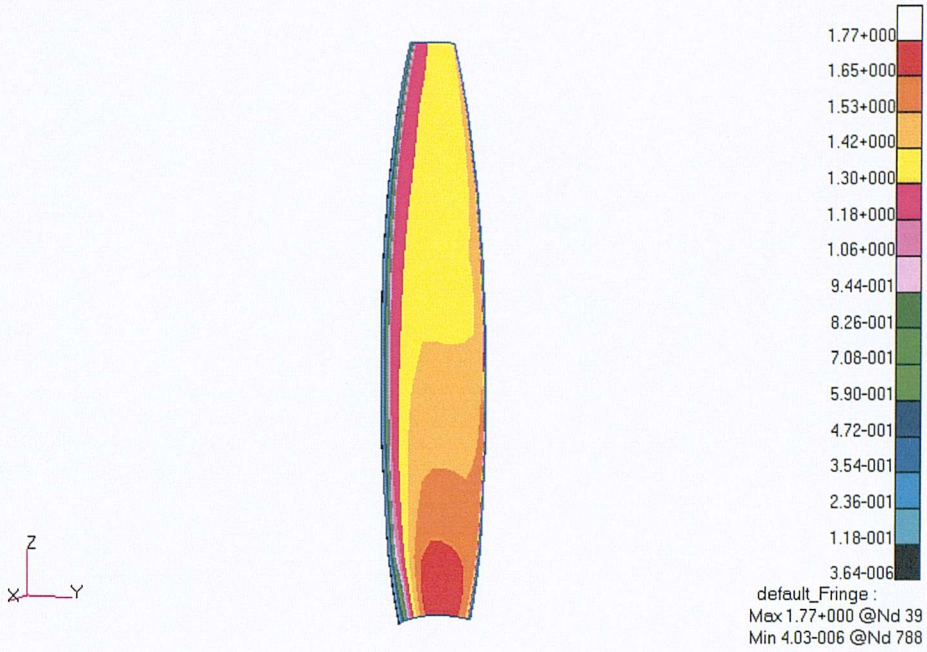

Figure 10.4 The colour contour map of the pressure coefficient Π for the suction side

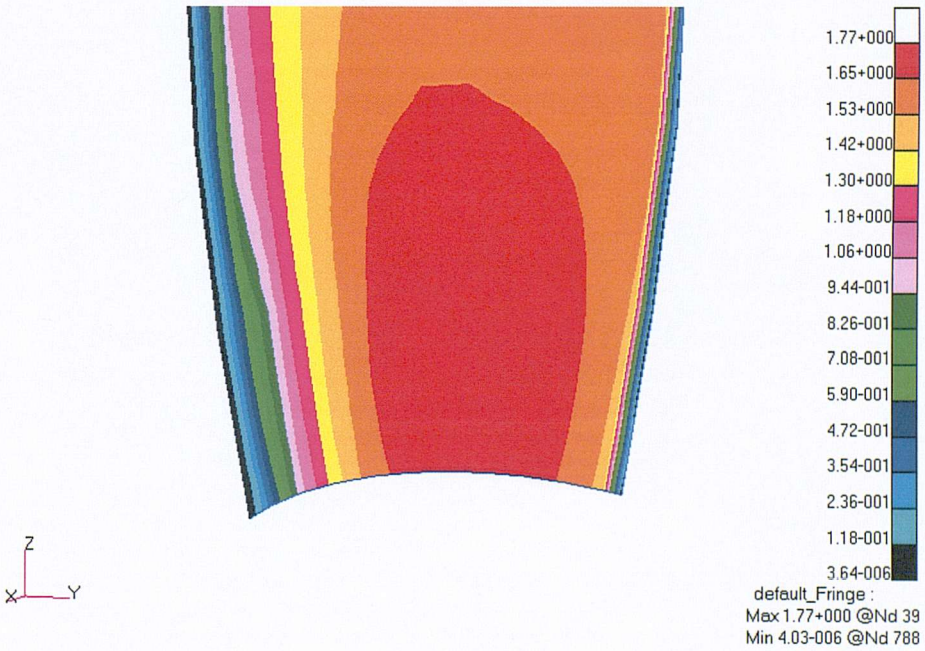

Figure 10.5 An enlarged map of Fig. 10.4 around blade root part to allow a clear view

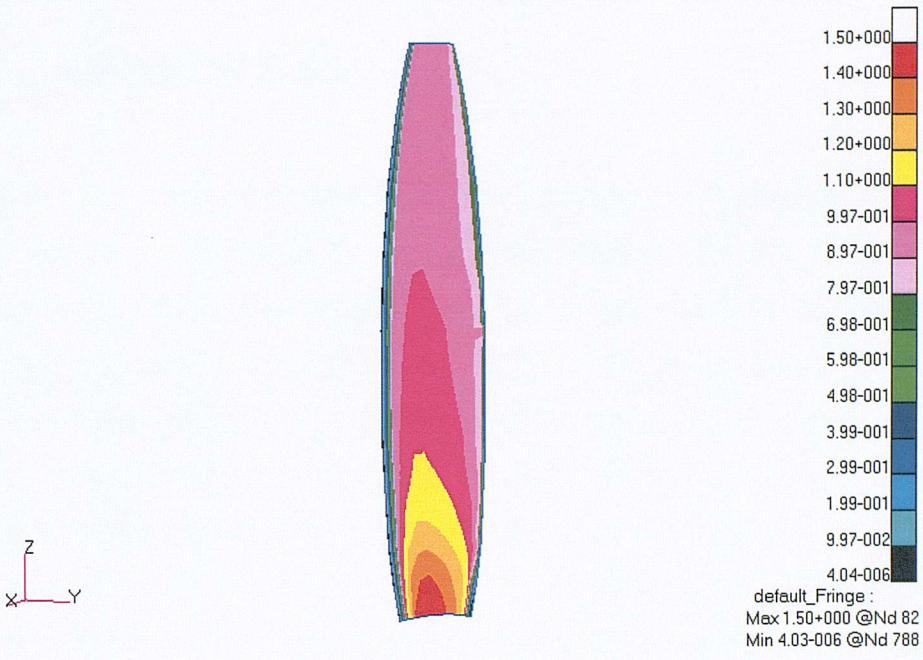

Figure 10.6 The colour contour map of the pressure coefficient Π for the pressure side

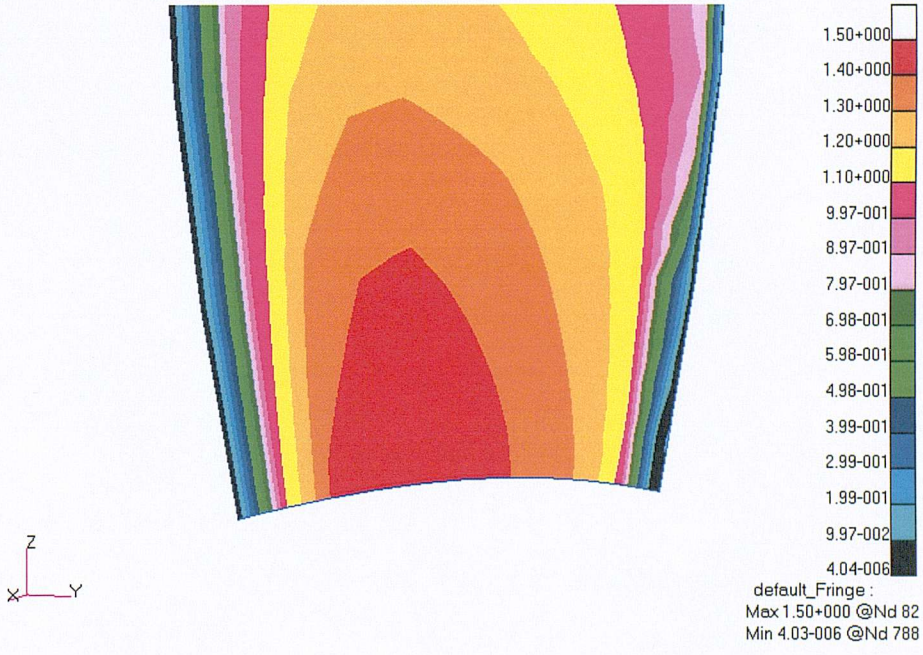

Figure 10.7 An enlarged map of Fig. 10.6 around blade root part to allow a clear view

10.5 Comparison of Tone Noise Predictions with Experimental Data

Noise measurements made by Trebble (1987a) were made in the plane of the propeller disc at a distance $2r = 4.17D$ from the propeller axis. Figure 10.8 shows the measured noise spectrum reproduced from Trebble's paper. The SPL value at the blade passing frequency and its harmonics are indicated. Table 10.3 is a comparison of the predicted sound pressure levels (SPL) with the measured SPL in dB for the first 11 blade passing frequencies. Figure 10.9 shows a comparison of the predicted and measured tone noise. For each blade passing frequency, the left red line is the predicted SPL, and the right black line is the measured SPL. Table 10.3 and Fig. 10.9 show that the error between the predicted SPL and measured SPL is generally within 2 dB except at the first-order blade passing frequency. This agreement provides reassuring verification of the far-field formulation. The over-estimated error at the first-order blade pass frequency may arise from the differences between the far-field assumption, on which the far-field formula is based, and the measurement point, which may not be far enough from the propeller to justify use of the far field approximation. Additional error is introduced by the use of two-dimensional airfoil theory to estimate the blade surface pressure, which does not include three- dimensional effects.

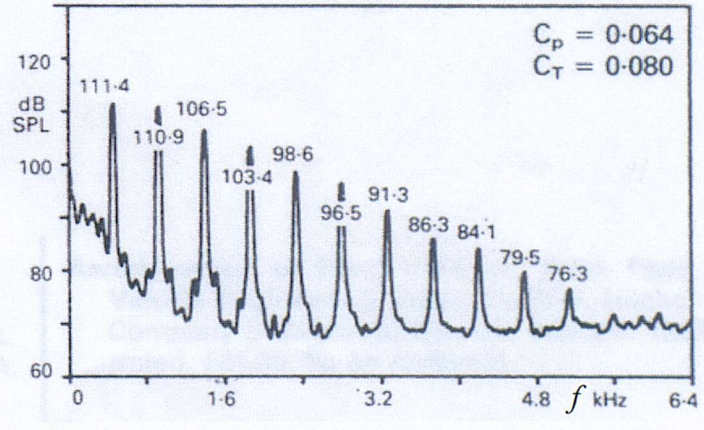

Figure 10.8 Measured noise spectrum at $2r/D = 4.17$, $\beta_s = 17.3^\circ$, $n = 7000$ **rev/min,** $U = 50$ **m/s.**

Blade pass frequency (kHz)	Predicted SPL (dB)	Measured SPL (dB)
0.467	118.9	111.4
0.933	112.7	110.9
1.400	107.8	106.5
1.867	103.5	103.4
2.333	99.3	98.6
2.800	95.3	96.5
3.267	91.3	91.3
3.733	87.3	86.3
4.200	83.4	84.1
4.677	79.4	79.5
5.133	75.3	76.3

Table 10.3 Comparison between predicted sound pressure levels (SPL) and the measured SPL

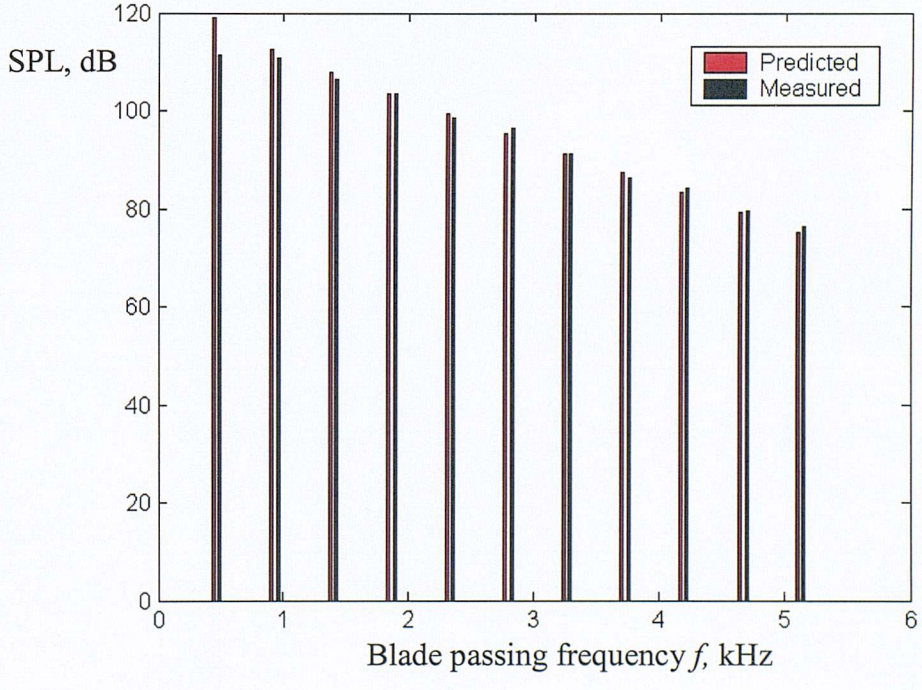

Figure 10.9 Tone noise comparison, left red line is the predicted SPL, right black line is measured SPL, $R_d = 1.522$ m

Figure 10.10 shows the predicted SPL directivity (in dB) of the line spectrum at blade passing frequencies of $f = 466.7\,\text{Hz}$, 1400.0Hz, and 2333.0Hz. The polar angle Ψ is measured from the x_1-axis (x_1 axis is opposite to forward flight direction), the observer distance $R_d = 50\,\text{m}$ is measured from the coordinate origin in the $x_2 = 0$ plane. The main lobes are in the direction vertical to the forward flight direction with null radiation occurring on the axis. The width of the main radiation lobe becomes increasingly narrow as the blade passing frequency increases. Similar directivity behaviour was predicted by Garrick and Watkins (1954).

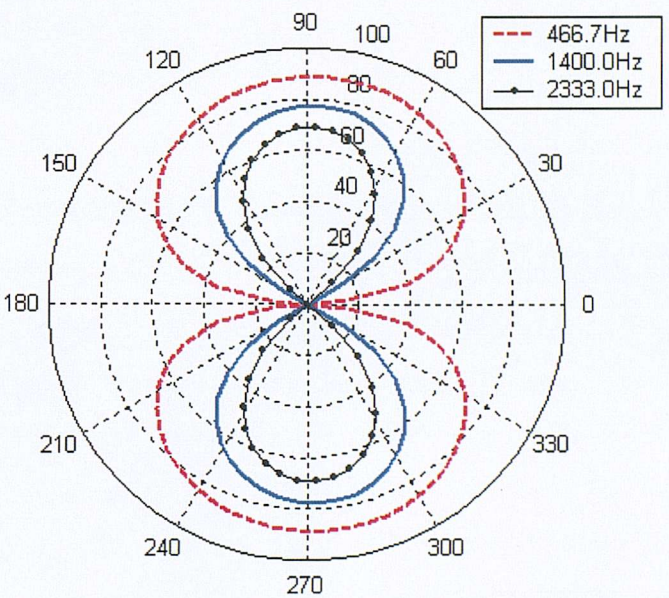

Figure 10.10 SPL directivity (in dB) of line spectrum of R212 1/5th scale model, $R_d = 50\,\text{m}$, U =50.0m/s, n =7000 rev/min.

Chapter XI:

Rotor Broadband Noise Prediction: Far-field Self Noise

11.1 Introduction

In this Chapter, the frequency-domain formulations of rotor noise presented in Chapter IX will be used to make self-noise predictions of the R212 propeller described in Chapter X. To validate the theoretical approach for broadband self-noise prediction, the predicted self-noise will be compared against the experimental data obtained by Trebble (1987b). The full-scale propeller shown in Fig. 11.1 will be used for comparison in this Chapter rather than the 1/5-scale model propeller discussed in Chapter X. This is because the self-noise radiation is higher due to a larger chord length in the full-scale propeller case. Parameter studies will also be presented in this Chapter, whereby the variation in self-noise is predicted against various blade

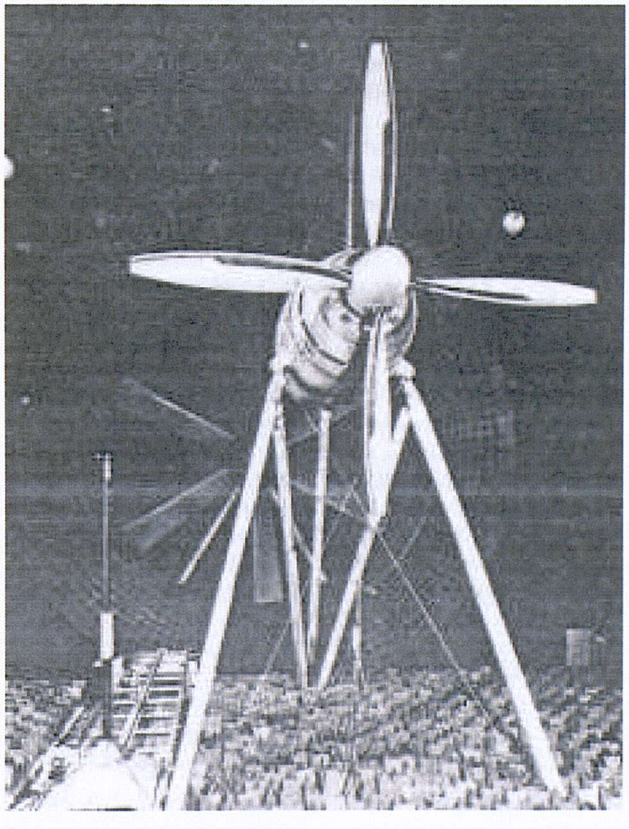

Figure 11.1. Test arrangement for R212 full-scale propeller, from Trebble (1987b)

setting angles, angles of attack, chord length, blade number, and blade tip Mach number.

The main geometric parameters of the full-scale propeller are identical to those of the 1/5-scale model propeller listed in Table 10.1, but with dimensions five times larger. The diameter of the full-scale propeller is $D = 3.66$ m. The blade geometry and angle of attack are described by Eqs. (10.5), (10.6), (10.14) and (7.7). To use Eq. (9.34) for numerical calculation, the tangent angle ϑ and the coordinate η_s of the NACA 16-series airfoil must first be determined. The tangent angle ϑ may be expressed in the form

$$\tan\vartheta = \frac{dy_u}{dx_u} = \frac{dy_u}{d\xi} \Big/ \frac{dy_u}{d\xi} \tag{11.1}$$

The necessary derivatives required in Eq. (11.1) may be obtained by performing the chain derivative of Eq. (10.5)

$$\frac{dy_u}{d\xi} = \tan\vartheta_0 + \frac{dy_t}{d\xi}\cos\vartheta_0 + y_t \frac{d\cos\vartheta_0}{d\xi} \tag{11.2}$$

$$\frac{dx_u}{d\xi} = 1 - \frac{dy_t}{d\xi}\sin\vartheta_0 - y_t \frac{d\sin\vartheta_0}{d\xi} \tag{11.2}$$

From Eqs. (10.3) and (10.4), we have

$$\frac{dy_t}{d\xi} = \frac{t}{c}\left(0.4948325\xi^{1/2} - 0.23925 - 0.082\xi - 1.6782\xi^2\right), \quad \text{for } \xi \le 0.5 \tag{11.3}$$

$$\frac{dy_t}{d\xi} = \frac{t}{c}\left[-2.325 + 6.84(1-\xi) - 4.38(1-\xi)^2\right], \quad \text{for } \xi > 0.5 \tag{11.4}$$

Finally,

$$\frac{d\cos\vartheta_0}{d\xi} = \frac{C_{li}}{4\pi}\frac{\tan\vartheta_0\cos^3\vartheta_0}{\xi(1-\xi)} \tag{11.5}$$

$$\frac{d\sin\vartheta_0}{d\xi} = -\frac{C_{li}}{4\pi}\frac{\cos^3\vartheta_0}{\xi(1-\xi)} \tag{11.6}$$

The corresponding expressions for the airfoil lower surface may be written as

$$\tan\vartheta = \frac{dy_l}{dx_l} = \frac{dy_l}{d\xi}\Big/\frac{dy_l}{d\xi} \tag{11.7}$$

where

$$\frac{dy_l}{d\xi} = \tan\vartheta_0 - \frac{dy_t}{d\xi}\cos\vartheta_0 - y_t\frac{d\cos\vartheta_0}{d\xi} \tag{11.8}$$

$$\frac{dx_l}{d\xi} = 1 + \frac{dy_t}{d\xi}\sin\vartheta_0 + y_t\frac{d\sin\vartheta_0}{d\xi} \tag{11.9}$$

The η_s - coordinate can be calculated from

$$\eta_s = c\int_1^{\xi}\sqrt{1+(dy_u/d\xi)^2}\,d\xi \quad \text{or} \quad \eta_s = c\int_1^{\xi}\sqrt{1+(dy_l/d\xi)^2}\,d\xi \tag{11.10}$$

Figure 11.2 below shows a pressure-side mesh ($\beta_s = 20.1°$) used to perform the

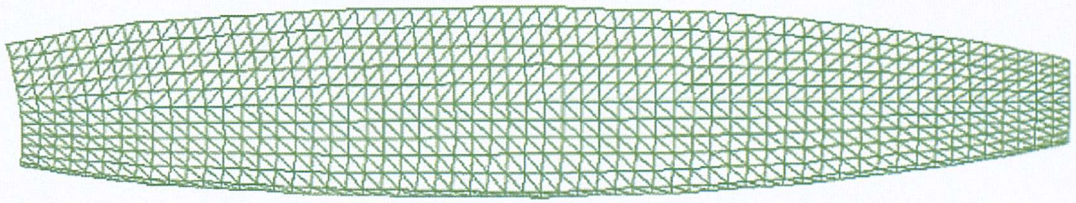

Figure 11.2. Mesh for numerical calculation of R212 Propeller, pressure side

numerical integration of Eq. (9.26). This mesh has 25mm maximum element dimension, which is valid for frequencies less than 1300Hz. This corresponds to 1298 triangle elements meshed on each side of the blade surfaces.

The unsteady blade loading, which constitutes the aerodynamic sound sources, is predicted using modifications to Amiet's thin aerofoil theory described in Chapter IV, in combination with the prediction of the boundary layer surface pressure frequency – wavenumber spectrum discussed in Chapter III. This is obtained by combining the wavenumber spectrum of Eq. (3.11) due to Corcos, the frequency spectrum of equations (3.23) and (3.24) due to Chou and George, and the boundary thickness prediction method of equations (3.33) to (3.35) due to Brooks given in Chapter III. For computational efficiency, the frozen gust assumption is made.

11.2 Comparison of Predicted SPL Spectrum with Experimental Data

In this section the theory developed in Chapter IX is compared against the experimental results reported by Trebble(1987b). Figure 11.3 below shows a comparison between the predicted SPL spectral density in the transverse plane (i.e., 90° to the axis), 5.49m from the axis (black broken line), and the measured noise spectrum (solid line). Also shown is the background noise spectrum (light broken line) to indicate the quality of the measured data. The calculations are taken at a rotational speed of $n = 1000$ rev/min, forward flight speed of $U = 30$ *m/s*, and a blade setting angle of $\beta_s = 20.1°$.

The sound pressure level (SPL) is defined in decibels referred to $p_{ref} = 2\times10^{-5}$ *Pa*, based on an analysis bandwidth Δf of 11 Hz

$$SPL(\mathbf{x}, f) = 10\log_{10}\frac{4\pi\Delta f\, S_{pp}(\mathbf{x}, \omega)}{p_{ref}^2} \tag{11.11}$$

where the factor 4π accounts for (i) converting to a single sided ($0 < \omega < \infty$) spectrum and (ii) converting from radian frequency to a 1 Hz bandwidth.

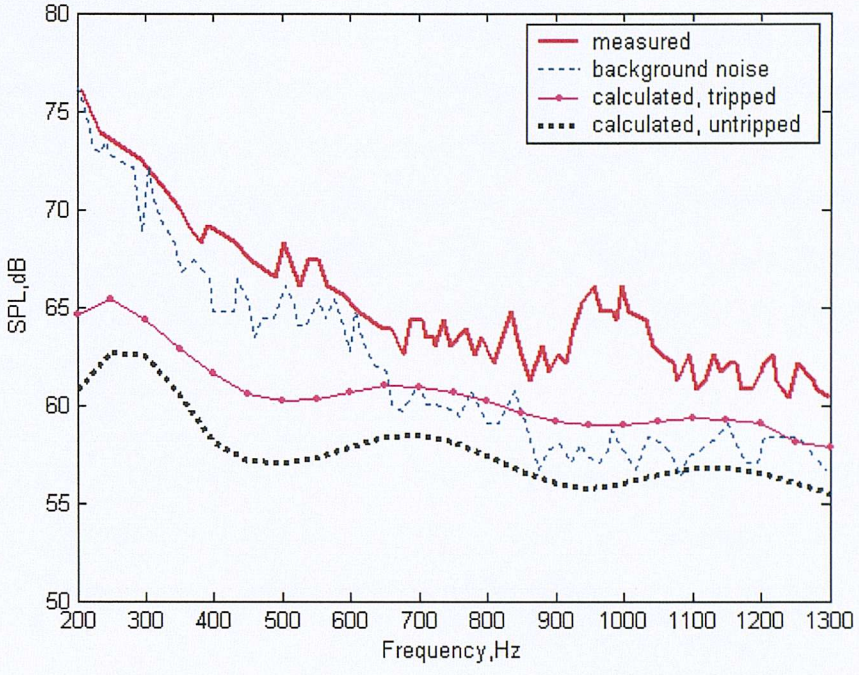

Figure 11.3. Comparison of measured and predicted broadband self-noise from a R212 propeller at $R_d = 5.49m$ from the axis in the plane of the propeller, with rotational speed $n = 1000$ rev/min, forward flight speed $U = 30$ *m/s*, blade setting angle $\beta_s = 20.1°$. Light broken line is the background noise spectrum.

Agreement between predictions and measurements at frequencies above about 700Hz are generally within 6dB. Below 700Hz, agreement is generally poorer. This may be due to the large background noise levels at these low frequencies. However, spectral shape is closely predicted. The underestimated error over the whole frequency range may be due to the differences between the far-field assumption, on which the far-field formula is based, and the measurement point, which may not be far enough from the propeller to justify the use of the far field approximation. Additional error is introduced by making the frozen turbulence assumption, which is now known to underestimate the radiated noise, as shown in Fig. 6.29. The third possible reason for the error is that the surface pressure spectrum and the boundary layer thickness, which determine the acoustic source on blade surface, are measured on NACA 0012 airfoil rather than NACA 16

series airfoil of which the R212 propeller is made. To assess the sensitivity of changes in the noise prediction to the source spectrum, the spectrum of the radiated pressure (dotted line) due to tripped boundary layer turbulence is also plotted in Fig 11.3. The tripped boundary layer thickness used here is that measured by Brooks, Pope and Marcolini (1989) for a NACA 0012 airfoil. Boundary layer turbulence tripping was achieved by placing random distributions of grit (nominal particle diameter of 0.29 mm with an application density of about 380 particles/cm^2) in strips from the leading edge to 20 percent chord. Figure 11.3 predicts a 3 dB increase in noise radiation due to tripping of the boundary layer turbulence. It indicates that the radiated noise is sensitive to the details of the boundary layer spectrum, for example, the location of the transition to turbulent flow.

Figures 11.4 and 11.5 show comparisons between the measured and predicted broadband self-noise for blade setting angles of $\beta_s = 17.3°, 22.4°$. In both cases, the agreement is better than 9dB above 700Hz, and better than 14dB below it.

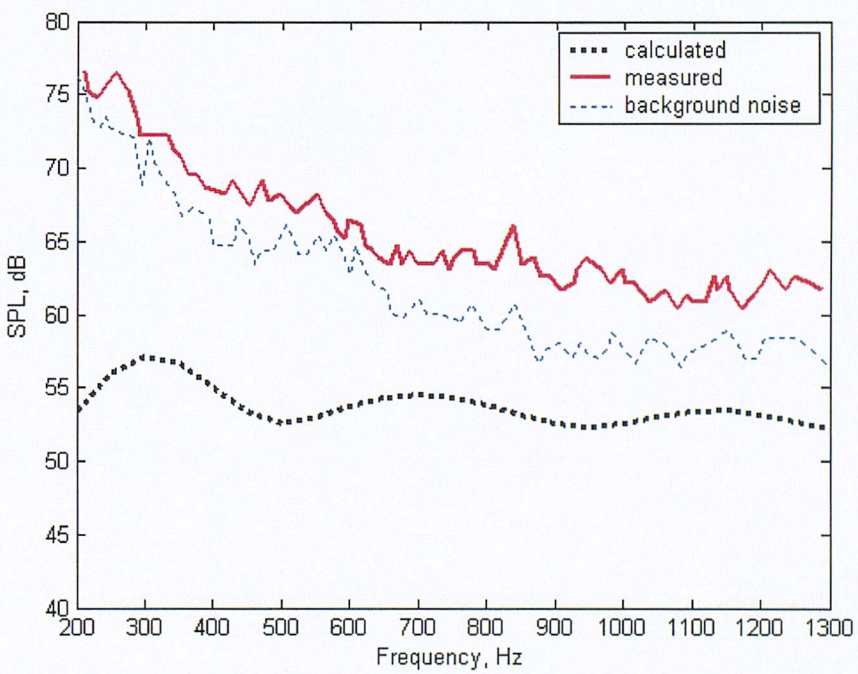

Figure 11.4. Comparison of measured and predicted broadband self-noise from a R212 propeller at $R_d = 5.49m$ from the axis in the plane of the propeller, with rotational speed $n = 1000$ rev/min, forward flight speed $U = 30$ *m/s*, blade setting angle $\beta_s = 17.3°$. Light broken line shows the background noise spectrum.

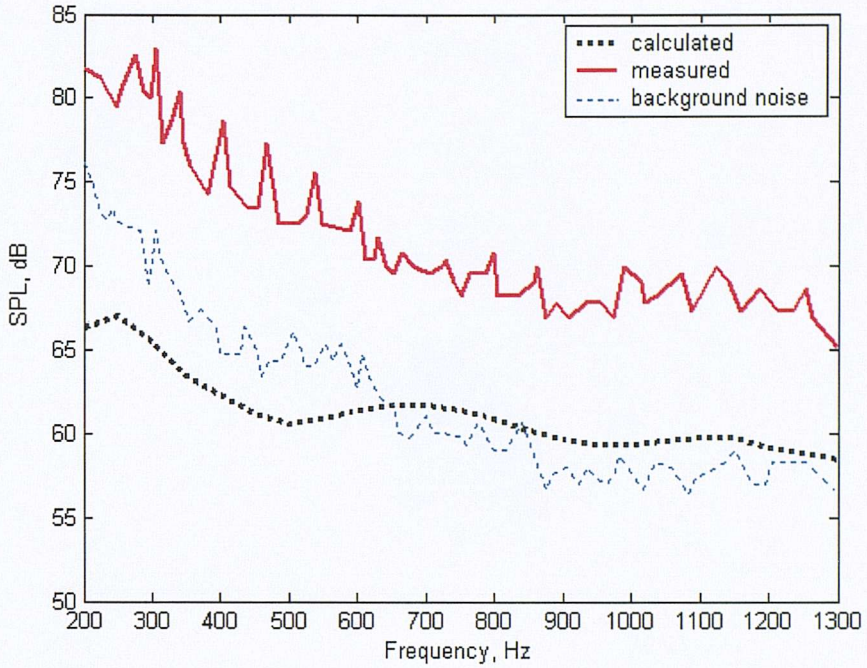

Figure 11.5. Comparison of measured and predicted broadband self-noise from a R212 propeller at $R_d = 5.49m$ from the axis in the plane of the propeller, with rotational speed $n = 1000$ rev/min, forward flight speed $U = 30$ *m/s*, blade setting angle $\beta_s = 22.4°$. Light broken line is the background noise spectrum.

11.3 Predicted Directivity of R212 Propeller Self-noise

In this section the theory in Chapter IX is used to predict the polar directivity of the broadband noise radiated by the propeller. The directivity is defined by

$$D(\Psi,\omega) = 10\log_{10}\left[\lim_{R_d\to\infty} {R_d}^2 \frac{4\pi S_{pp}(\mathbf{x},\omega)}{p_{ref}^2}\right] \tag{11.12}$$

where $\mathbf{x} = (R_d\cos\Psi, 0, R_d\sin\Psi)$ is the observation coordinates, Ψ is the polar angle measured from the x_1 axis, and the observer distance R_d is measured from the coordinate origin as shown in Fig.11.6. For numerical calculations, we take $R_d = 100\,\text{m}$. For a finite value of R_d, the directivity $D(\Psi,\omega)$ is related to the SPL spectrum of Eq.(11.11) by

$$D(\Psi,\omega) = SPL - 10\log_{10}\Delta f + 10\log_{10} R_d^{\,2} \tag{11.13}$$

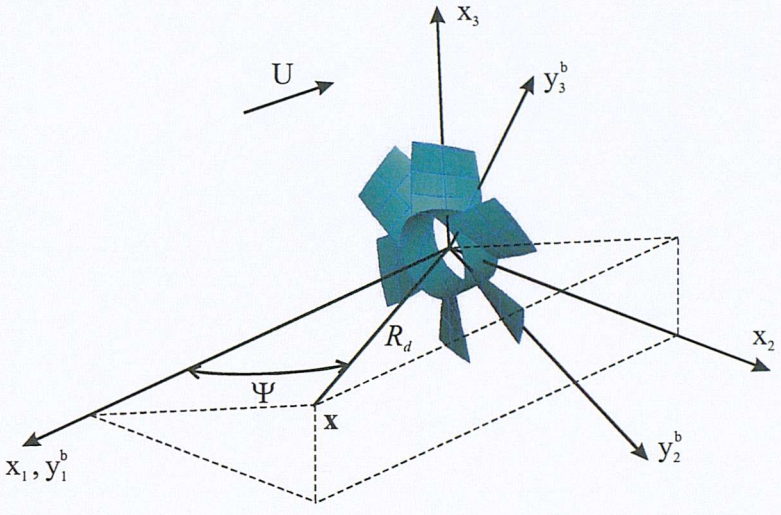

Figure 11.6. Observation distance R_d and polar angle Ψ.

Figures 11.7 to 11.9 show the self noise directivities in decibels of the R212 propeller in a 1Hz bandwidth with centre frequencies of 300Hz, 600Hz, and 900Hz respectively. In order to allow a clearer presentation of the directivities, the predicted values of $D(\Psi,\omega)$ are subtracted by 56, 52, 52dB respectively. Clearly, the broadband self-noise directivity is fundamentally different from the single-frequency directivities due to a steady body-force distribution shown in Fig. 8.1 and due to a steady blade surface pressure distribution shown in Fig. 10.10. In Figs. 11.7 to 11.9, the main lobes of the broadband self-noise directivities are located along the propeller axis, while the main lobes of the single-frequency directivities are in the direction transverse to the propeller axis. This may provide a way of discriminating the broadband self-noise from other sources of noise when processing propeller noise measurements. It also suggests that duct liners may be inefficient for reducing broadband self-noise radiation. On the other hand, the self-noise directivities exhibit greater omni-directional behaviour compared with that of tonal noise if one notes that the variation of $D(\Psi,\omega)$ in Figs 11.7 to 11.9 is less than about 15dB over the entire range of polar angles.

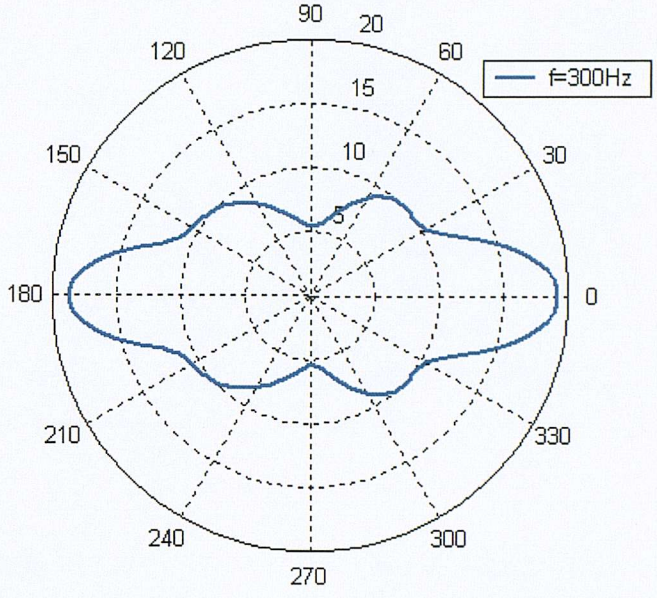

Figure 11.7. Directivity $D(\Psi,\omega)-56.0$ (in dB) at 300Hz of R212 propeller for an axial flow velocity U=30m/s, blade rotational speed of n = 1000 rev/min, $R_d = 100$ m, $\beta_s = 17.3°$

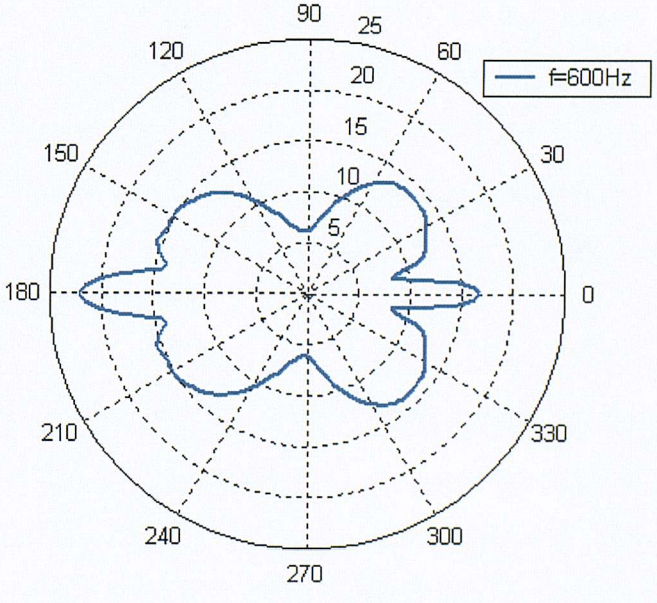

Figure 11.8. Directivity $D(\Psi,\omega)-52.0$ (in dB) at 600Hz of R212 propeller for an axial flow velocity U=30m/s, blade rotational speed of n = 1000 rev/min, $R_d = 100$ m, $\beta_s = 17.3°$

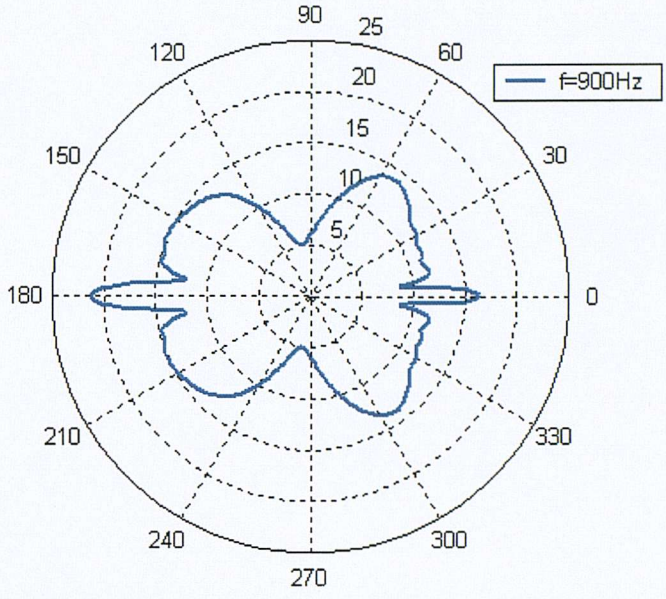

Figure 11.9. Directivity $D(\Psi,\omega)-52.0$ (in dB) at 900Hz of R212 propeller for an axial flow velocity U=30m/s, blade rotational speed of $n=1000$ rev/min, $R_d=100$ m, $\beta_s=17.3°$

11.4 Parameter Study of Propeller Broadband Self-noise

The theory in Chapter IX has been used to undertake a parametric study of the broadband self-noise radiation from propellers with variations in fan tip speed, number of blades, chord, and blade setting angles. Figure 11.10 shows a prediction of the pressure spectrum for various blade-setting angles at $R_d=5.49$m from the propeller axis, in the plane of the propeller.

Figure 11.10 shows that increasing the blade setting angle β_s increases self-noise radiation. This is simply because at a larger angle of attack, the boundary layer thickness is increased and hence the unsteady surface pressure is greater. For each degree of increase in the blade-setting angle, the noise is predicted to increase by about 1.4dB, except for the largest blade-setting angle of $\beta_s=32.1°$. This is because the flow will be separated at the highest blade angles and the radiated noise will be much higher than that predicted above, which assumes attached boundary layers.

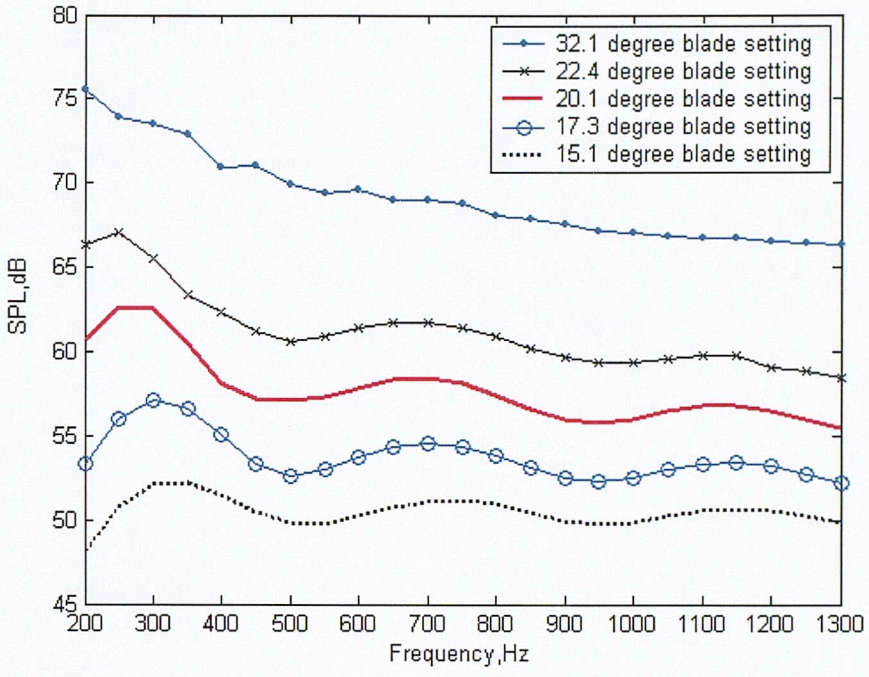

Figure 11.10. Predictions of the Broadband self-noise of R212 propeller at R_d =5.49m from propeller axis in the plane of the propeller. Axial flow velocity is U=30m/s, shaft rotational speed is n = 1000 rev/min, in an 11Hz analysis bandwidth

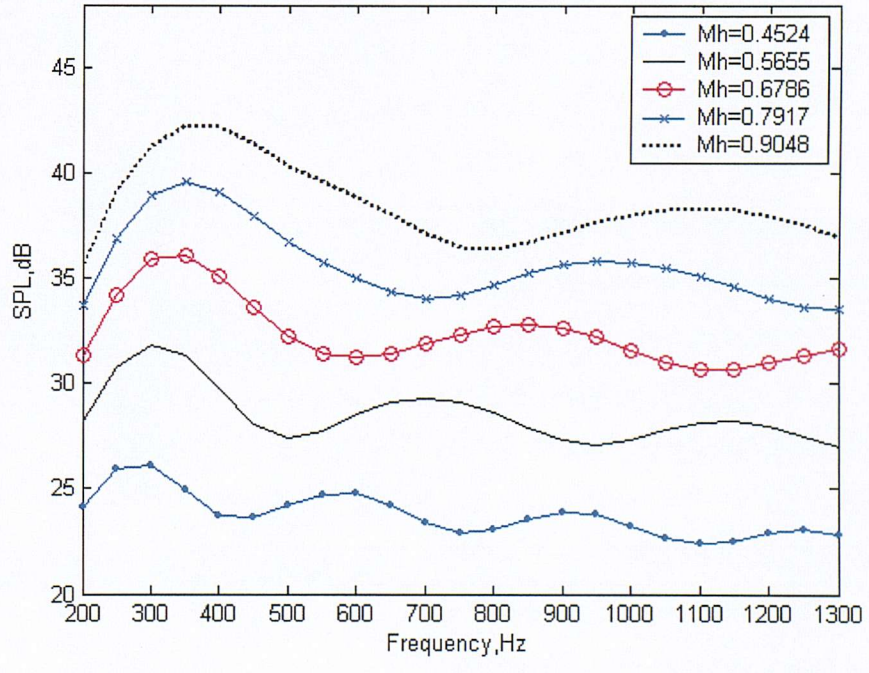

Figure 11.11. Predicted broadband noise of R212 propeller at R_d = 100 m for various blade tip Mach numbers M_h, in an 11Hz analysis bandwidth, β_s = 17.3°

Figure 11.11 shows the predicted dependence of the broadband noise frequency spectrum on the blade tip Mach number M_h for the R212 propeller. Note that in each case, the angular speed Ω of the propeller and the forward flight speed U are adjusted to keep the tip section attack angle unchanged at $\alpha = 2°$. Consistent with measurement and classical trailing edge noise theory, the mean square pressure is found to scale very closely with the fifth power of the blade tip Mach number.

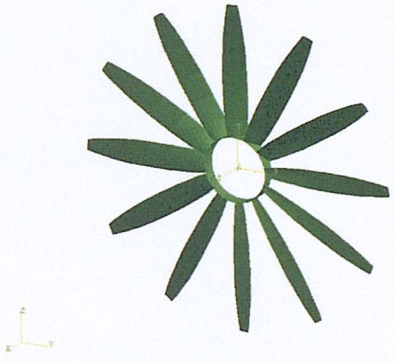

Figure 11.12. Geometry of one-chord propeller

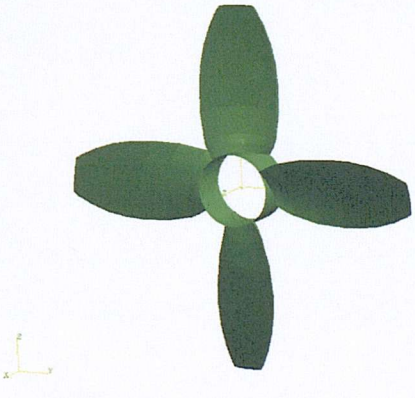

Figure 11.13. Geometry of three-chord propeller

We now consider self-noise radiation from two hypothetical propellers conceived specifically for the parametric study presented here. One has the same geometry as the R212 propeller discussed above but with the twist angle chosen such that a constant attack angle of four degrees is obtained at an axial flow velocity of U=30m/s and a shaft rotational speed n = 1000 rev/min. We refer to this geometry as the 'one-chord' propeller. The blade number of this one-chord propeller is $N_b = 12$. The other propeller has the same geometry with the same constant attack angle of four degree as the one-chord propeller, but with a chord length of three times greater than that of the one-chord propeller. We refer to as the 'three-chord' propeller. However this three-chord propeller has only 4 blades so that both the 'one-chord' propeller and the 'three-chord propeller' have approximately the same thrust area. Figures 11.12 and 11.13 show the geometry of these two propellers used in the calculation.

Since the two propellers have the same angle of attack, they should be able to provide roughly the same thrust. However their noise levels are predicted to differ appreciably, as shown in Fig. 11.14, where the dashed line shows the SPL for the twelve-blade 'one-chord' propeller and the solid line denotes the SPL of the four-blade 'three-chord' propeller. The calculations are made at $R_d = 5.49$m from the propeller axis in the plane

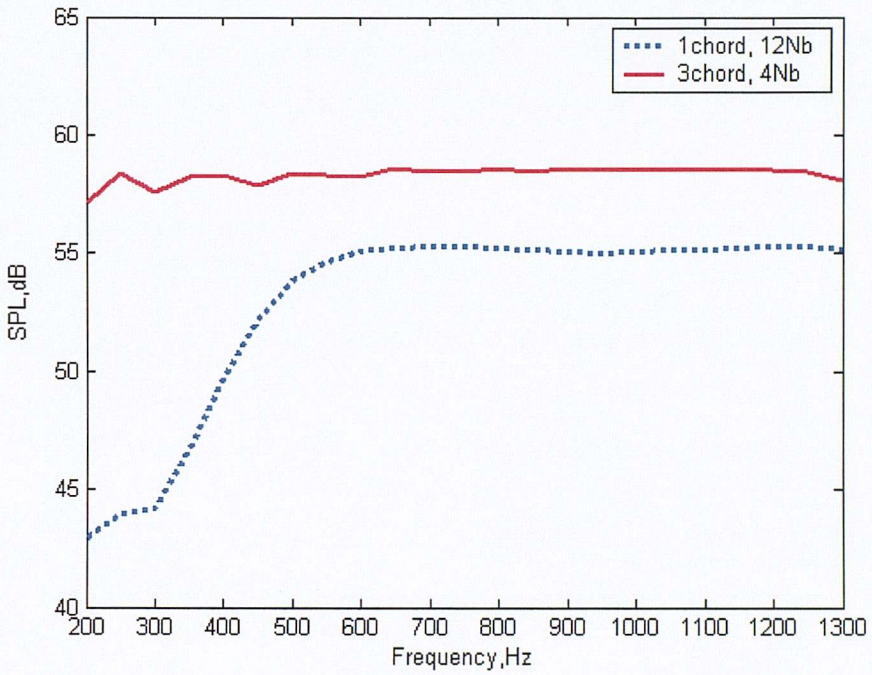

Figure 11.14. Self-noise comparison between one-chord propeller and three-chord propeller at $R_d = 5.49$ m from propeller axis in the plane of the propeller. Axial flow velocity is $U = 30$ m/s, shaft rotational speed is $n = 1000$ rev/min, in a 11Hz analysis bandwidth.

of the propeller with an axial flow velocity of U=30m/s, a shaft rotational speed of $n = 1000$rev/min, and an 11Hz analysis bandwidth. Figure 11.14 shows that the propeller with small chord and large blade number radiates lower noise, especially at the lower frequencies, where a difference in SPL of more than 10dB is observed.

The main difference between the R212 propeller and the 'one-chord' propeller is the blade twist angle. With the blade setting angle equal to $\beta_s = 17.3°$, the attack angle of the R212 propeller varies from $10.2°$ at the blade root to $2.0°$ at the blade tip for an axial flow velocity of U=30m/s and a shaft rotational speed $n = 1000$rev/min. The 'one-chord'

propeller, however, has a constant attack angle of 4.0°. Noting that the blade tip section has a higher speed than the root section, and that the airfoil lift depends on both the attack angle and the airfoil velocity, these two propellers should deliver roughly the same thrust if the 'one-chord' propeller has the same number of blades (equal to four) as the R212 propeller. Figure 11.15 shows a comparison between the self-noise due to this change of attack angle at an observation distance of $R_d = 5.49$m from the propeller axis in the plane of the propeller. The sound pressure level is calculated in an 11 Hz bandwidth. The propeller with constant angle of attack is predicted to radiate a SPL of 4 to 6dB lower at low frequencies, and about 2 dB lower noise levels at higher frequencies.

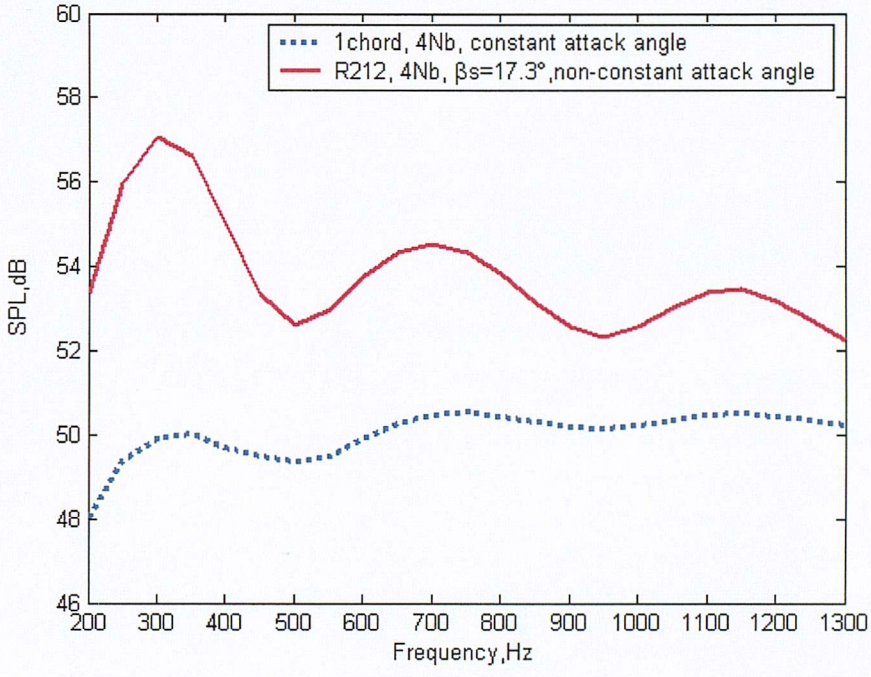

Figure 11.15. Self-noise comparison between propellers of constant angle of attack and non-constant angle of attack at $R_d = 5.49$ m from propeller axis in the plane of the propeller. Axial flow velocity is $U = 30$ m/s, shaft rotational speed is $n = 1000$ rev/min, in a 11Hz analysis bandwidth.

The computation time for numerical prediction presented above is 256.2 minutes per frequency per observation point for the four-blade three-chord propeller while for the four-blade one-chord propeller, the computation takes only 67 minutes per frequency per observation point on a 1.2 GHz PC. However for the twelve-blade one-chord propeller, the computation takes 27.7 minutes per frequency per observation point. The computation code was written in FORTRAN 90.

It is useful to make a study to see which part of the blade source makes large contribution to the self-noise radiation. If it turns out that the blade tip source is dominant due to the higher Mach number near to the blade tip, then a large saving in computation time will be possible for a small loss in accuracy. Figure 11.16 shows a comparison of the blade surface source contribution for a R212 propeller with the same parameters used in Fig. 11.4. The dotted line and the line with circles show the noise contribution from the pressure side and the suction side respectively. Note that the R212

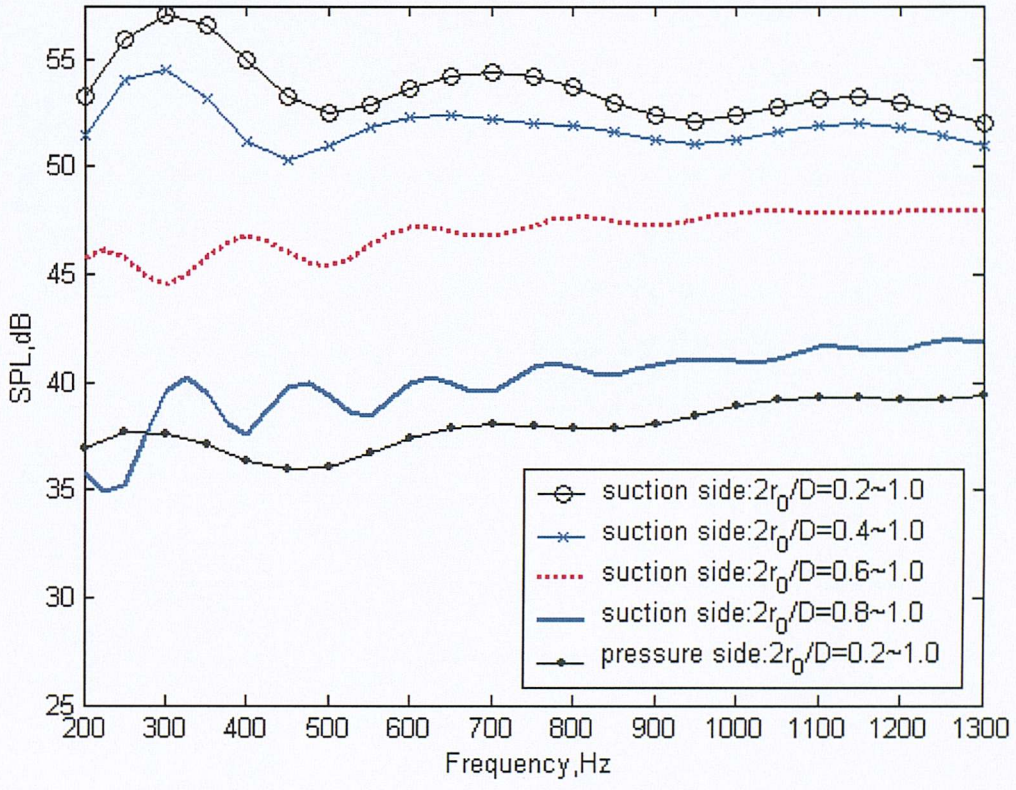

Figure 11.16. Comparison of blade surface source contribution for a R212 propeller at $R_d = 5.49m$ from the axis in the plane of the propeller, with rotational speed $n = 1000$ rev/min, forward flight speed $U = 30$ *m/s*, blade setting angle $\beta_s = 17.3°$, the propeller has hub radius $2r_0 / D = 0.2$.

propeller has hub radius $2r_0 / D = 0.2$. More than 10 dB differences between these two curves indicate that the contribution from the suction side is dominant. The line with crosses, the dashed line and the solid line show the noise contributions from the blade segments on the suction side between non-dimensional radii $2r_0 / D =$ 0.2~1.0,

$2r_0 / D = 0.6 \sim 1.0$, and $2r_0 / D = 0.8 \sim 1.0$ respectively. It can be seen that the tip segment between $2r_0 / D = 0.8 \sim 1.0$ makes a noise contribution that is at least 8 dB lower than the complete suction-side surface. This draws no conclusion that the noise contribution from the blade tip segment is dominant because the large attack angle (see Table 10.2 on page 163) produces thick boundary layer turbulence at the blade root therefore a large source contribution. However the conclusion that the main source contribution comes from the suction side is useful for the saving in computation time. The computation time saved by computing the source contribution from only suction side is 24 minutes per frequency per observation point on a 1.0 GHz PC.

Chapter XII

Conclusions

12.1 Acoustic Source Prediction

An engineering model for the determination of the acoustic source due to boundary layer turbulence developed on an airfoil or blade surface has been developed. In this model, the relationship between the spectrum of scattered pressure due to the trailing edge and the spectrum due to the incident pressure is clearly established. The unsteady blade loading, which constitutes the aerodynamic sound sources, is predicted by combining single-airfoil theory, the representation of the turbulence wavenumber spectrum proposed by Corcos (1963), and the measured boundary layer turbulence parameters (that is boundary layer frequency spectrum of point pressure on the blade surface, boundary-layer- turbulence integral scales, and boundary layer thickness). Using the measured pressure spectrum as an input quantity forms an important basis for a robust, accurate engineering model on the rotor self-noise prediction. Accuracy of the model depends on how the boundary-layer-turbulence parameters are measured. Ideally they should be measured on the rotating blade surface with adjacent blades present. When these parameters are measured on a single airfoil surface, a cascade model in which the effects of adjacent airfoils are included may be more pertinent than the single-airfoil theory presented in this thesis. However the use of a cascade model may not allow a concise closed-form solution for airfoil surface pressure prediction, which is crucial for reducing the computation time to reasonable limits when making rotor broadband noise prediction.

12.2 Airfoil Self-noise Prediction

A frequency domain formulation has been developed for making airfoil self noise predictions. It is valid for arbitrary airfoil geometries at small, but non-zero angles of attack. Moreover, the solution is valid in both near and far fields. It is shown to reduce to Amiet's analytic solution when the airfoil collapses to a flat plate with large span and the measurement point is taken to the far field.

A numerical scheme for the evaluation of the integral formula on an arbitrary airfoil surface has been presented. Numerical predictions of broadband self-noise show reasonable agreement with Brook empirical prediction, which is based on experimental data. Broadband self-noise predictions are made for both frozen and non-frozen boundary layer turbulence. Non-frozen turbulence is shown to generate higher noise radiation than frozen turbulence at high frequency. However, the difference is generally less than 3 dB, suggesting that the frozen-gust assumption is a reasonable assumption for broadband noise predictions

Broadband noise directivity has been predicted for a flat-plate, a NACA 0012 and a NACA 0024 airfoil. The directivities are asymmetric due to the non-zero angle of attack assumed in the study. The results reveal that Mach number has an important influence on the magnitude and directivity of broadband self-noise radiation. The directivity predictions due to a single harmonic component of turbulence for a flat plate airfoil are shown to be in excellent agreement with Amiet's analytic solution.

12.3 Rotor Self-noise Prediction

A generalized frequency domain formulation has been developed for making rotor broadband noise predictions. It can be used for making broadband and tonal noise predictions, and is valid in both the near field and the far field. This general formulation has been validated by comparison with the analytic solution of the 3rd CAA benchmark problem of the far field noise due to a prescribed source distribution of a rotating body force.

A simplified expression for the self-noise radiation in the far field has been derived. This frequency domain formulation is computationally far more efficient than the general formulation. It can be used for frozen and non-frozen turbulence. The far-field formulation is shown to reduce to the classic Gutin solution of propeller tonal noise prediction when the steady surface pressure distribution is confined to the propeller-projected disc.

These two formulations provide insight into the mechanisms by which the unsteady surface pressure is shifted by the blade passing frequency to radiate a continuous pressure spectrum. The main difference from previous work is that the source distribution is integrated over the real blade surface to provide more accurate prediction. Previous theory for broadband noise prediction performed source integration over the projected disk of the rotating blades only. Although Hanson's helicoidal surface theory (Hanson, 1983), which was used for tone noise prediction, may be potentially extended to broadband noise prediction, the source integration is confined mean-chord surface. This leads to significant phase error at high frequency near the propeller axial direction (Hanson, 1980). However, broadband self-noise has shown to be important in the axial direction with source frequency shifted by the blade passing frequency.

The numerical method for making airfoil noise predictions is extended to rotating blades. The validation is performed from predictions of the measured broadband noise from an R212 propeller. Absolute sound pressure level predictions are generally better than 10 dB. Good agreement between the spectral shapes of the measured and predicted noise spectrum is obtained. The tonal noise predicted by the method also shows very good agreement with the R212 propeller experimental data.

The broadband self-noise directivity is predicted to be significantly different from the pure-tone noise directivities. The main lobe of broadband self-noise directivity is in the direction of the propeller axis while the main lobe of the pure-tone noise directivity is normal to the propeller axis.

Parameter studies on rotor self-noise prediction show that a propeller with large blade number and constant attack angle along the blade radius radiates lower self-noise

compared with propellers with small blade number and non-constant attack angle. A prediction of the pressure spectrum in the plane of the propeller for various blade-setting angles shows that for each degree of increase in blade-setting angle, the sound pressure level increases by 1.4 dB. The predicted dependence of the broadband noise frequency spectrum is predicted to scale very closely with the fifth power of the blade tip Mach number.

List of references

Abbott I.H., Von Doenhoff A.E. (1959). Theory of Wing Section. 2nd Edition, Dover publication, INC., New York.

Amiet R.K. (1975). Acoustic Radiation from an Airfoil in a Turbulent Stream. Journal Of Sound And Vibration **41:4**,407-420.

Amiet R.K. (1976a). Noise due to Turbulence Flow past a Trailing Edge. Journal of Sound and Vibration **47:3**, 387-393.

Amiet R.K. (1976b). High Frequency Thin-airfoil Theory for Subsonic Flow. AIAA Journal, **14:8**, 1076-1082.

Amiet R.K. (1978). Effect of the Incident surface Pressure Field on Noise Due to Turbulence Flow Past a Trailing Edge. Journal of Sound and Vibration **47:3**, 387-393.

Amiet, R.K., Simonich, J.C. and Schlinker, R.H. (1990) Rotor Noise due to Atmospheric Turbulence Ingestion — Part II: Aeroacoustic Results. Journal of Aircraft, Vol. **27**, No. **1**, 15-22.

Atassi, H. and Akai, T.J. (1979). Aerodynamic Force and Moment on Oscillating Airfoils in Cascade. AIAA paper, 78-GT-181.

Blake, W.K. (1986). Mechanics of Flow-induced Sound and Vibration. Volume II, Academic Press.

Brooks T.F. and Hodgson T.H. (1980). Prediction and Comparison of Trailing Edge Noise Using Measured Surface Pressures. AIAA paper 80-0977.

Brooks, T.F. and Hodgson T.H. (1981). Trailing Edge Noise Prediction from Measured Surface Pressures. Journal of Sound and Vibration, **78:1**,69-117.

Brooks, T.F. (1983). Progress in Rotor Broadband Noise Research. Vertica, **7:4**, 287-307.

Brooks T.F., Pope D.S. and Marcolini M.A. (1989). Airfoil Self-noise and Prediction. NASA Reference Publication 1218.

Carley, M. (1999). Sound Radiation From Propellers in Forward Flight. Journal of Sound and Vibration, **225:2**, 353-374.

Carley, M. and Fitzpatrick, J. A. (2000). Spectral Conditioning of Propeller Noise From Broadband Sources. Journal of Sound and Vibration, **238:1**, 31-49.

Casper J. and Farassat F.(2002). Broadband Noise Prediction Based On A New Aeroacoustic Formulation. AIAA Paper No.2002-0802.

Category 2—Rotor Noise (1999). Proceeding of the 3th Computational Aeroacoustics (CAA) Workshop on Benchmark Problems, Cleveland, Ohio, Nov 8-10 1999, NASA/CP-2000-209790, 7-9.

Chandiramani, K.L. (1974). Diffraction of Evanescent Waves With Applications to Aerodynamically-scattered Sound and radiation From Unbaffled Plates. Journal of the Acoustical Society of America, **55**, 19-29.

Chapman, C.J. (1993). The Structure of Rotating Sound Fields. Proceedings of the Royal Society of London A, **440**, 257-271.

Chase, D.M. (1972). Sound Radiated by Turbulent Flow off a Rigid Half-plane as Obtained from a Wavenumber Spectrum of Hydrodynamic Pressure. Journal of the Acoustical Society of America, **52**, 1011-1022.

Chase, D.M. (1975). Noise Radiated From an Edge in Turbulent Flow. AIAA Journal, **13**, 1041-1047.

Chase D.M. (1980). Modeling the Wavevector-frequency Spectrum of Turbulent Boundary Layer Wall Pressure. Journal of Sound and Vibration **70:1**,29-67.

Chase, D.M. (1987). The Character of the Turbulent Wall Pressure Spectrum at Subconvective Wavenumbers and a Suggested Comprehensive Model. Journal of Sound and Vibration **112:1**,125-147.

Chou S.T. and George A.R.(1984). Effect of Angle of Attack on Rotor Trailing-Edge Noise. AIAA Journal **22:12**, 1821-1823.

Corcos G.M. (1963). Resolution of Pressure in Turbulence. Journal of the Acoustical Society of America **35**, 192-199.

Corcos, G.M. (1964). The Structure of the Turbulent Pressure Field in Boundary Layer Flows. J. Fluid Mech. **18**, 353-377.

Crighton D.G., Dowling A.P., Ffowcs Williams J.E., Heck M. and Leppington F.G. (1992). Modern Methods in Analytical Acoustics, Springer-Verlag London Limited.

Cumpsty, N.A. (1977). A Critical Review of Turbomachinery Noise. Journal of Fluid Engineering, Transaction of the ASME, **99**, 278-293.

Curle N. (1955). The Influence of Solid Boundaries upon Aerodynamic Sound. Proceedings of the Royal Society **A231**,505-514.

Demming, A. F.(1938). Noise from Propellers with Symmetrical Sections at Zero Blade Angle, II. NACA TM 679.

Dowling, A.P.(1992). Flow Noise on Surface, Chapter 16. Modern Methods in Analytical Acoustics by Crighton D.G., Dowling A.P., Ffowcs Williams J.E., Heck M. and Leppington F.G. Springer-Verlag London Limited.

Eckert E.R., and Drake J_R. R.M. (1959). Heat and Mass Transfer, New York: McGraw-Hill Book Company,Inc. See P.144.

Ernsthausen, W. (1936). The Source of Propeller Noise. Luftfahrtforschung, **8**, 433-440. Translated as NACA TM 825, 1937.

Farassat, F. (1981). Linear Acoustic Formulas for Calculation of Rotating Blade Noise. AIAA Journal, **19**, 1122-1130.

Ffowcs Williams, J.E. (1965). Surface-pressure Fluctuations Induced by Boundary-layer Flow at Finite Mach Number. J. Fluid Mech. **22**, 507-519.

Ffowcs Williams J.E. and Hawkings D.L. (1969a). Theory Relating to the Noise of Rotating Machinery. Journal of Sound and Vibration, **10:1**, 10-21.

Ffowcs Williams J.E. and Hawkings D.L. (1969b). Sound Generated by Turbulence and Surfaces in Arbitrary Motion. Philosophical Transactions of the Royal Society, Series **A 264**,321-342.

Ffowcs Williams J.E. and Hall L.H. (1970). Aerodynamic Sound Generation by Turbulence Flow in the Vicinity of a Scattering Half Plane. Journal of Fluid Mechanics **40**, 657-670.

Garrick, I. E. and Watkins,C. E. (1954). A Theoretical Study of the Effect of Forward Speed on the Free-space Sound Pressure Field Around Propellers. NACA Report 1198.

Gennaretti M. and Morino L. (1992). A Boundary Element Method For The Potential, Compressible Aerodynamics Of Bodies In Arbitrary Motion. The Aeronautical Journal **96:951**,15-19.

Goldstein M.E. (1976). Aeroacoustics, McGraw-Hill Book Company, New York.

Goldstein, M.E. and Atassi, J.A. (1976). A Complete Second-order Theory for the Unsteady Flow About an Airfoil due to a Periodic Gust. Journal of Fluid Mechanics, **74**, 741-765.

Gradshteyn I.S. and Ryzhik I.M. (1965). Table of Integrals, Series, and Products(P710,P979), Academic Press, New York and London(Translated from the Russian by Scripta Technica,Inc).

Gutin, L. (1936). On the Sound Field of a Rotating Propeller. Zhurnal Technicheskoi Fiziki, **6**, 889-909 (in Russian). Translated as NACA Tech. Memo 1195 (1948).

Gutin, L.(1942). On the 'Rotational Sound' of an Airscrew. Zhurnal Technicheskoi Fiziki, **12**, 76-83 (in Russian). Translated as British National Lending Library for Science and Technology RTS 7543, 1942.

Hanson, D.B. and Fink, M.R. (1979). The Importance of Quadrupole Sources in Prediction of Transonic Tip Speed Propeller Noise. Journal of Sound and Vibration, **62**, 19-38.

Hanson D.B. (1980). Helicoidal Surface Theory for Harmonic Noise of Propellers in the Far Field. AIAA Journal, **18:10**, 1213-1220.

Hanson D.B. (1983). Compressible Helicoidal Surface Theory for Propeller Aerodynamics and Noise. AIAA Journal **21:6**, 881-889.

Hanson, D.B. (1995). Sound From a propeller at Angle of Attack: a New Theoretical Viewpoint. Proceedings of the Royal Society of London, Series A, Vol. **449**, No. **1936**,.315-328.

Homicz, G.F. and George, A.R. (1974) Broadband and Discrete Frequency Radiation From Subsonic Rotors. Journal of Sound and Vibration, Vol. **36**, No. **2**, 151-177.

Howe M.S. (1978). A Review of the Theory of Trailing Edge Noise. Journal of Sound and Vibration **61:3**, 437-465.

Howe M.S. (1998). Acoustics of Fluid-structure Interaction, Cambridge University Press, Cambridge, UK.

Howe M.S. (1999). Trailing Edge Noise at Low Mach Numbers. Journal of Sound and Vibration **225:2**, 211-238.

Hubbard H.H. (1991). Aeroacoustics of Flight Vehicles: Theory and Practice, Vol.1: Noise Sources, NASA Reference Publication 1258, Vol.1, WRDC Technical Report 90-3052.

Kraichnan, R.H. (1956a). Pressure Fluctuations in Turbulent Flow Over a Flat Plate. Journal of the Acoustical Society of America, **28:3**, 378-390.

Kraichnan, R.H. (1956b). Pressure Field Within Homogeneous Anisotropic Turbulence. Journal of the Acoustical Society of America, **28:1**, 64-72.

Landahl M. (1961). Unsteady Transonic Flow. New York: Pergamon Press, Inc. 27-30.

Langanelli, A.L. and Wolfe, H (1989). Prediction of Fluctuating Pressure in attached and Separated Turbulent Boundary Layer Flow. AIAA paper 89-1064.

Lighthill M. J. (1952). On Sound Generated Aerodynamically. I. General Theory. Proceedings of the Royal Society, **211A**, 1107, 564-587.

Lighthill M. J. (1954). On Sound Generated Aerodynamically. II. Turbulence as a Source of Sound. Proceedings of the Royal Society, **222A**, 1148,1-32.

Lindsey W.F., Stevenson D.B. and Daley B.N. (1948). Aerodynamic Characteristics of 24 NACA 16-series Airfoils at Mach Numbers between 0.3 and 0.8. NACA Technical Note No. 1546, Langley Aeronautical Laboratory.

Lowson, M. W. (1965). The Sound Field for Singularities in Motion. Proceedings of the Royal Society, Series **A 286**, 559-572.

Mani, R. (1999). The Radiation of Sound From a Propeller at angle of Attack. Proceedings of the Royal Society of London, Series A, Vol. **431**, No. **1882**, 203-218.

Manoha, E., Delahay, C., Sagaut, P. and Mary, I. (2001). Numerical Prediction of the Unsteady Flow and Radiated Noise From a 3D Lifting Airfoil. AIAA paper 2001-2133, 7th AIAA/CEAS Aeroacoustics Conference, 28-30 May 2001, Maastricht Netherlands.

Mawardi, O.K. (1955). On the Spectrum of Noise From Turbulence. Journal of the Acoustical Society of America, **27:3**, 442-445.

McAlpine, A., Nash, E.C. and Lowson, M.V. (1999). On the Generation of Discrete Frequency Tones by the Flow Around an Aerofoil. Journal of Sound and Vibration, **222:5**, 753-779.

Meecham, W.C. and Tavis, M.T. (1980). Theoretical Pressure Correlation Functions in Turbulent Boundary Layer. Physics of Fluids, **23**, 1119-1131.

Metzger, F.B., Magliozzi,B., Towle,G. and Gray,L. (1969). A Study of Propeller Noise Research. Aerodynamic Noise, 371-386, Ribner, H.S. ed., University of Toronto Press.

Morfey, C.L. (1973). Rotating Blades and Aerodynamic Sound. Journal of Sound and Vibration, **28:3**, 587-617.

Morino, L. (1993). Boundary Integral Equations in Aerodynamics. Applied Mechanics Reviews, **46:8**, 445-466.

Oberai, A.A., Roknaldin, F., and Hughes, T.J.R. (2002). Computation of Trailing-Edge Noise due to Turbulent Flow Over an Airfoil. AIAA Journal, **40:11**, 2206-2216.

Peake, N. and Crighton, D.G. (1991). Lighthill Quadrupole Radiation in Supersonic Propeller Acoustics. Journal of Fluid Mechanics, **223**, 363-382.

Phillips, O.M. (1956). On the Aerodynamic Surface Sound From a Plane Turbulent Boundary Layer. Proc. R. Soc. London, Ser. A **234**, 327-335.

Powell, A. (1960). Aerodynamic Noise and the Plane Boundary. Journal of the Acoustical Society of America, **32:8**, 982-990.

Roger M. (2002). Trailing Edge Noise Measurements and Prediction for Subsonic Loaded Fan Blades. AIAA paper 2002-2460.

Schwartzschild K. (1902). Die Beugung und Polarisation des Lichts Durch Einen Spalt-I. Mathematische Annalen **55**, 177-247.

Tam C. K.W. (1999). Rotor Noise: Category 2 Analytical Solution. Proceeding of the 3th Computational Aeroacoustics (CAA) Workshop on Benchmark Problems, Cleveland, Ohio, Nov 8-10 1999, NASA/CP-2000-209790, 41-46.

Trebble W.J.G.(1987a). Investigations of the Aerodynamic Performance and Noise Characteristics of a 1/5th Scale Model of Dowty Rotol R212 Propeller. The Aeronautical Journal **91:905**,225-236.

Trebble W.J.G.(1987b). Investigations of the Aerodynamic Performance and Noise Characteristics of a Dowty Rotol R212 Propeller at Full-scale in the 24ft Wind Tunnel. The Aeronautical Journal **91:906**,275-284.

Van de Vooren, A. I. and Zandbergen, P. J. (1963). Noise Field of a Rotating Propeller in Forward Flight. AIAA Journal, **1**, 1518-1526.

Whitehead, D.S. (1962). Force and Moment Coefficients for Vibrating Aerofoils in Cascade. Aeronautical Research Council (London), R. & M. No. 3254.

Widnall, S.E. (1969). A Correlation of Vortex Noise Data From Helicopter Main Rotors. Journal of Aircraft, **6**, 279-281.

Willmarth W.W. and Roos F.W. (1965). Resolution and Structure of the Wall Pressure Field beneath a Turbulent Boundary Layer. Journal of Fluid Mechanics **22**, 81-94.

Willmarth W.W. (1975). Pressure Fluctuations beneath Turbulent Boundary Layers. Ann. Rev. Fluid Mech. **7**, 13-38.

Wright, S.E. (1976). The Acoustic Spectrum of Axial Flow Machines. Journal of Sound and Vibration, **45**, 165-223.

Yu, J.C. and Joshi, M.C. (1979). On Sound Radiation From the Trailing Edge of a Isolated Airfoil in a Uniform Flow. AIAA Paper No. 79-0603.

Yu, J. C. and Tam, C.K.W. (1978). An Experimental Investigation of the Trailing-edge Noise Mechanism. AIAA Journal, **16**, 1048-1052.